Self-assembly of viologen molecules at metal/electrolyte interfaces under *non-reactive* and *reactive* conditions

Pham Duc Thanh

DBV

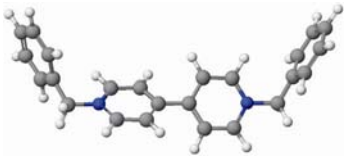

DPV

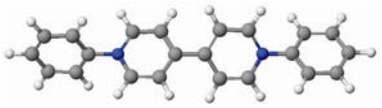

Non-reactive

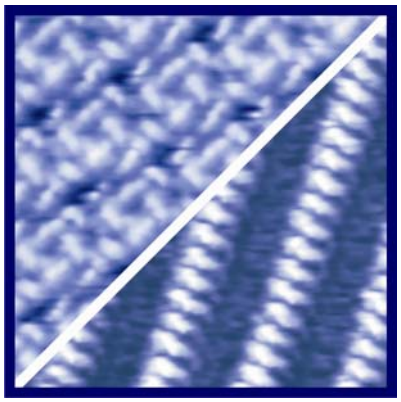

Reactive

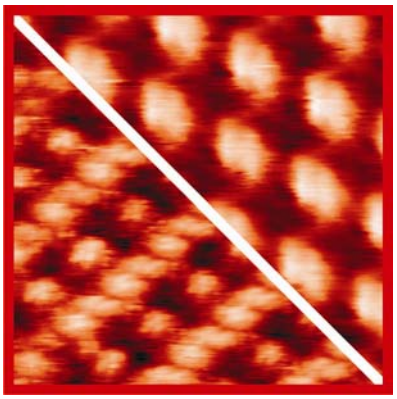

Self-assembly of viologen molecules at metal/electrolyte interfaces under *non-reactive* and *reactive* conditions

Dissertation
zur Erlangung des Doktorgrades (Dr. rer. nat.)
der
Mathematisch-Naturwissenschaftlichen Fakultät
der
Rheinischen Friedrich-Wilhelms-Universität Bonn

vorgelegt von
Pham Duc Thanh
aus
Hanoi, Viet Nam

Bonn 2011

Angefertigt mit Genehmigung der Mathematisch-Naturwissenschaftlichen Fakultät der Rheinischen Friedrich-Wilhelms-Universitat Bonn

1. Referent: Prof. Dr. Klaus Wandelt
2. Referent: PD Dr. Peter Broekmann

- Tag der Promotion: 24.08.2011
- Erscheinungsjahr: 2001

dedicated to my family, especially my lovely **Linh Dan**

Contents

List of abbreviations

BE	Bonding Energy
CDR	Copper Dissolution Reaction
CE	Counter Electrode
CV	Cyclic Voltammetry
DBV	Dibenzyl-Viologen
DPV	Diphenyl-Violgen
E	Working potential *vs* RHE
EC-STM	Electrochemical Scanning Tunneling Microscopy
fcc	face-centered cubic
FWHM	Full Width at Half Maximum
HER	Hydrogen Evolution Reaction
HOPG	Highly Ordered Pyrolytic Graphite
I_t	Tunneling current
IHP	Inner Helmholtz Plane
LDOS	Local Density of State
LEED	Low-Energy Electron Diffraction
LUMO	Lowest Unoccupied Molecular Orbital
ML	Monolayer
NND	Nearest Neighbor Distance
OHP	Outer Helmholtz Plane
RE	Reference Electrode
RHE	Reversible Hydrogen Electrode

SoLiAS	Solid/Liquid Interface Analysis System
SXPS	Synchrotron X-ray Photoelectron Spectroscopy
U_b	Bias voltage
UHV	Ultra High Vacuum
WE	Working Electrode
XPS	X-ray Photoelectron Spectroscopy

List of Figures

Part I

Introduction and outline

Chapter 1

Introduction and outline

Organic adsorbates play an important role in a number of electrochemical processes, e.g. as organic additives for metal plating. Furthermore, electrochemical deposition of thermally unstable molecules may also be a promising route towards functional organic layers. Detailed investigations are mandatory in order to acquire profound knowledge of the structural and electronic properties of these layers parallel and perpendicular to the surface, and to achieve a deeper mechanistic understanding of the kinetics of involved charge transfer reactions taking place at the metal/organic interface in the electrochemical environment [1].

Viologens are certainly among the most intensively studied organic adsorbates, especially as molecular building-blocks in supramolecular chemistry [2]. They have attracted much attention in the field of surface electrochemistry within the last few decades due to their widespread applications as chromophores, electron-transfer mediators, and most recently as gating molecules in model systems for electronic devices that are based on molecular architectures. Their main advantage lies in their low-lying LUMOs and an almost ideal reversibility of the electron-transfer reaction. Their solution electrochemistry is well documented in the literature [3, 4]. However, far less is known about the surface redox-chemistry and the related phase behavior of adsorbed viologens.

Therefore, the aim of this work is to investigate the processes of viologen adsorption occurring within the solid/liquid interface at the atomic/molecular level. Two particular viologens, the 1,1'-dibenzyl-4,4'-bipyridinium or Dibenzyl-Viologen (DBV) and the 1,1'-diphenyl-4,4'-bipyridinium or Diphenyl-Viologen (DPV) are chosen to study. In spite of the difference of the outer organic group, i.e. benzyl vs. phenyl, attached to the bipyridinium core, the two

viologens have similarities in their molecular size and their redox chemical properties which makes them a good pair to compare concerning their structure formation and phase behavior at the surface. Note that the adsorption of DBV molecules on chloride modified Cu(100) has been previously studied by C. Zörlein [5], however in the framework of this thesis, the comparison between DBV and DPV adsorption as well as the discovery of new structures under "reactive adsorption" conditions results in new contributions to the understanding of viologen layers at metal/electrolyte interfaces.

This work combines classical Cyclic Voltammetry (CV) studies with *in-situ* Electrochemical Scanning Tunneling Microscopy (EC-STM) and *ex-situ* X-ray Photoelectron Spectroscopy (XPS) experiments in order to probe the surface structures and the influence of the electrode potential on the electrochemical processes at the solid/liquid interface. On the one hand, the *in-situ* EC-STM provides direct images of structural changes within the adsorbed viologen films even in the course of electron transfer reactions. On the other hand, the *ex-situ* XPS supplements information on the chemical composition analyses of the viologen adsorption layers.

The previous study proved an enhanced DBV adsorption on the chloride modified Cu(100) "template" due to the electrostatic interaction and good conformation between the negatively charged chloride layer and the viologen cations [5]. Therefore this thesis focuses mostly on the viologen adsorption on that surface. In addition, the DBV adsorption is also performed on an inert HOPG substrate in order to firstly evaluate the influence of the preadsorbed anions and secondly to search for other redox states of DBV species at more negative potentials.

The outline of this work is as follows:

This thesis is organized in five parts. Part I - "Introduction and outline" presents the motivation for doing this work and the outline of the thesis. In Part II - "Experimental and theoretical background", a short overview about the electrochemistry at the solid-liquid interface, the tunneling effect, the principle of *ex-situ* XPS as well as the experimental setups are described in Chapter 2. The two solid substrates used in this thesis, the inert HOPG and the more active anion modified copper surface, are described in Chapter 3. Then an overview about supramolecular chemistry and self-assembly of Viologens is given in Chapter 4 focusing on DBV and DPV molecules. Part III concentrates

on the results and discussions of the "non-reactive" adsorption of the viologens on the different substrates including three chapters devoted to DBV, DPV and their comparison, respectively. While Chapter 5 characterizes intensively the DBV molecules adsorbed on chloride modified Cu(100) and compares it with the adsorption on the HOPG surface, Chapter 6 focuses especially on the DPV molecules on the chloride modified Cu(100) substrate. In this part, the redox chemistry, structural morphology and phase behavior of the adsorption and self-assembly of the two molecules are investigated systematically and, as a matter of course, the comparison between DBV and DPV adsorption will then be given in Chapter 7. Part IV or Chapter 8 discusses the DBV adsorption on the chloride modified Cu(100) under "reactive" conditions in which the surface morphology and the phase behavior shows interesting differences from the "non-reactive" adsorption, namely the formation of new but metastable structures. Furthermore, appealing results on tip-induced structural transitions of these metastable structures are also presented here. The final Part V comes with the conclusion of all results for this work.

Part II

Experimental and theoretical background

Chapter 2

Methods

2.1 Electrochemistry at solid-liquid interfaces

2.1.1 Introduction

The structure and composition of electrified solid-liquid interfaces as well as their electrical charge distribution is of great fundamental interest in electrochemistry. Many scientifically and technologically relevant processes occur at these interfaces, i.e. corrosion, electro-catalysis, compound formation and galvanic deposition, e.g. the copper damascene process (electroplating). Therefore, an atomic-scale understanding of the interfacial structure is mandatory in order to control the fabrication of new surface structures and materials. In this chapter, the conventional structure models of electrified solid-liquid interfaces are presented. Furthermore, the cyclic voltammetry as one of the most important methods to characterize the solid/liquid interface is described.

2.1.2 Solid-liquid interfaces

The electrical double-layer is associated with an ideally polarized electrode which is an electrode at which no charge transfer can occur regardless of the potential imposed by an external voltage source. The specific nature of the structure and the interactions within the electrical double-layer should be considered in the interpretation of electroanalytical data. Various models have been proposed describing the interphasial region near the electrode surface.

Helmholtz envisaged a "double layer" in which the excess charge on the metal would be neutralized by a monomolecular layer of ions of opposite charge to that on the metal phase. Considering a metal surface which is exposed to an electrolyte solution, such a double layer is composed of a charged metal surface and an interfacial regime in the electrolyte phase containing an excess of ionic particles

counterbalancing the charge at the electrode q_e. A positively charged electrode, for instance, attracts a layer of negative ions. The overall interface must be neutral with $q_e + q_s = 0$ where q_s is the excess charge of ions in the nearby solution. The surface charging can be carefully controlled by the applied "Galvani" potential to the electrode [6]. However, this model did not account for the possible specific adsorption or random motion of ions.

The Gouy-Chapman-Stern-Grahame (GCSG) model

The development of theoretical models of the electrolytic double layer until today is considered in a detailed review article [7]. A more modern model of the charge density distribution near metals is the GCSG model which accounts for the finite size of ions and their thermally activated motion, as illustrated in Fig. 2.1. The double layer can be roughly divided on the electrolyte side by two planes, the Inner and the Outer Helmholtz Plane (IHP or OHP), into three regions, the inner Helmholtz layer, the outer Helmholtz layer and the diffuse double layer.

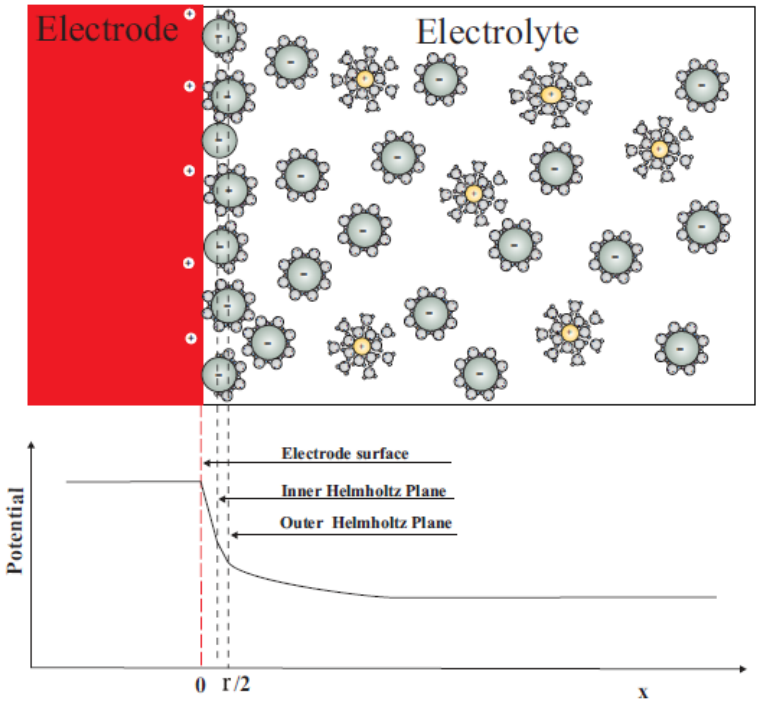

Figure 2.1: The Gouy-Chapman-Stern-Grahame (GCSG) model.

Inner Helmholtz layer: It is based on the assumption that a single layer of specifically adsorbed anions which are desolvated maintain direct contact with the electrode surface in the inner Helmholtz layer. A rigid double layer is formed with one-by-one matching of the charges on the metal surface and in the ion layer. The arrangement resembles a plate capacitor with separation of d = r/2 between the two

plates, where r equals the diameter of the unsolvated anions. The ionic particles are directly bound to the metal surface atoms [8]. This phenomenon occurs primarily with anions and is often accompanied by the formation of periodically ordered adsorbate layer [9].

Outer Helmholtz layer: The outer Helmholtz layer is formed by solvated ions. In this case the hydration shell is bound more strongly and is not even partially removed upon adsorption. The solvated ions interact through the hydration sphere more weakly and purely electrostatically with the electrode surface. The outer Helmholtz plane is thus at a distance of a/2, where a is the radius of a solvated ion.

The Helmholtz layer is then followed by the diffuse double layer region, which is disordered due to the thermal motion of the ions. A preliminary calculation of the electrochemical potential in the diffuse double layer under the simplistic view of the ions as point charges shows an exponential decrease of the potential $\phi(z)$ and the space charge density $\rho(z)$ with the distance z to the electrode surface: [10, 11]

$$\phi(z) = \frac{\sigma}{\varepsilon\varepsilon_0\kappa} e^{-\kappa.z} \tag{2.1}$$

$$\rho(z) = -\sigma\kappa e^{-\kappa.z} \tag{2.2}$$

with ρ represents the charge density,

ε the dielectric constant of water,

ε_0 the dielectric constant of vacuum,

e the electron charge,

κ the inverse Debye length.

Here the quantity κ provides the length scale for the screening and $1/\kappa$ is associated with the thickness of the diffuse double layer regime and is called the Debye length.

As the result, the potential decreases exponentially with increasing distance to the surface. An increase of the salt concentration leads to a steeper drop and thus to a shorter Debye length.

$$\kappa = \sqrt{\frac{2n_0 z^2 e^2}{\varepsilon\varepsilon_0 kT}} \tag{2.3}$$

with n_0 the total ion concentration,

k the Boltzmann's constant,

Within the IHP specific adsorption can be observed i.e. the ions loose partially or completely their hydration shell. The OHP contains only ions that are solvated. Both Helmholtz layers represent compact layers. The potential drops in the IHP and the OHP respectively are linear, the drop in the diffuse layer is exponential. The capacitance of the double layer consists of a combination of the capacitance of the compact layers in series with that of the diffuse layer. For two capacitors in series, the total capacitance is given by:

$$\frac{1}{C} = \frac{1}{C_H} + \frac{1}{C_{diff}} \tag{2.4}$$

The specific adsorption of anions on a metal surface

Besides the intrinsic electrostatic interaction between the charged electrode surface and ions in the electrolyte as described above by the GCSG-model, there is also chemical interaction between anions such as iodide, sulfate etc. and the electrode surface. In this case, these anions loose their hydration shell completely and adsorb directly and strongly on the electrode surface. This phenomenon is called specific adsorption. In many cases, specific anion adsorption leads to the formation of a dense anion layer. The model of this specific adsorption of anions on a metal surface is presented in Fig. 2.2.

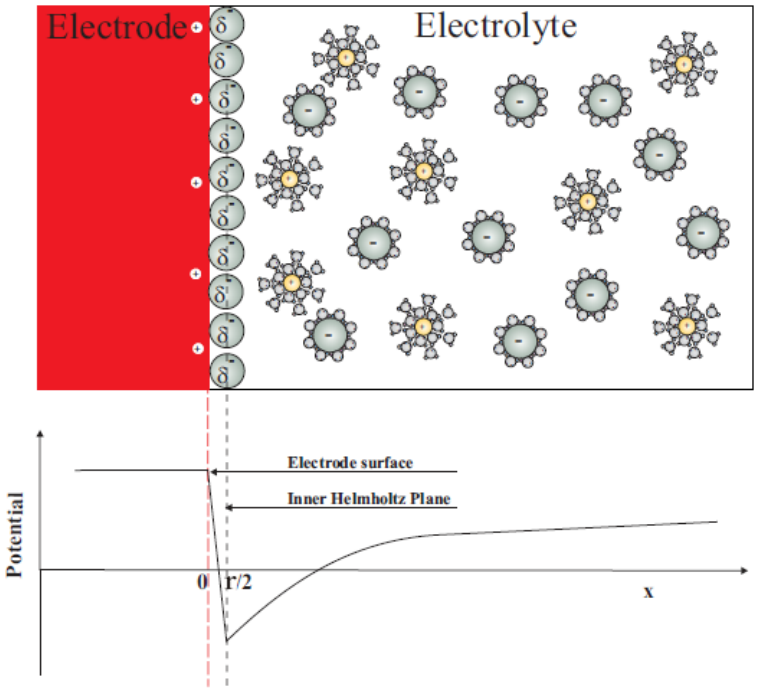

Figure 2.2: The specific adsorption of anions on a metal surface.

The potential decreases linearly between the electrode surface and the IHP, i.e. the plane through the centers of dehydrated ions, and then re-increases exponentially towards the bulk solution.

The specifically adsorbed anions bind strongly to the electrode surface and thereby form a dense, laterally ordered and immobilized layer which can be well observed by microscopic methods such as the EC-STM.

Interestingly, such a specific adsorbate layer can be used as template for the immobilization of molecules on electrode surfaces, especially for positively charged organic cations as will, for example, be demonstrated for viologens in this thesis. The model can be seen in Fig. 2.3.

Structure of the electrode surface: The Jellium model

All models presented so far only describe one part of the double layer, namely the interfacial regime in solution by neglecting the interfacial structure of the solid electrode surface.

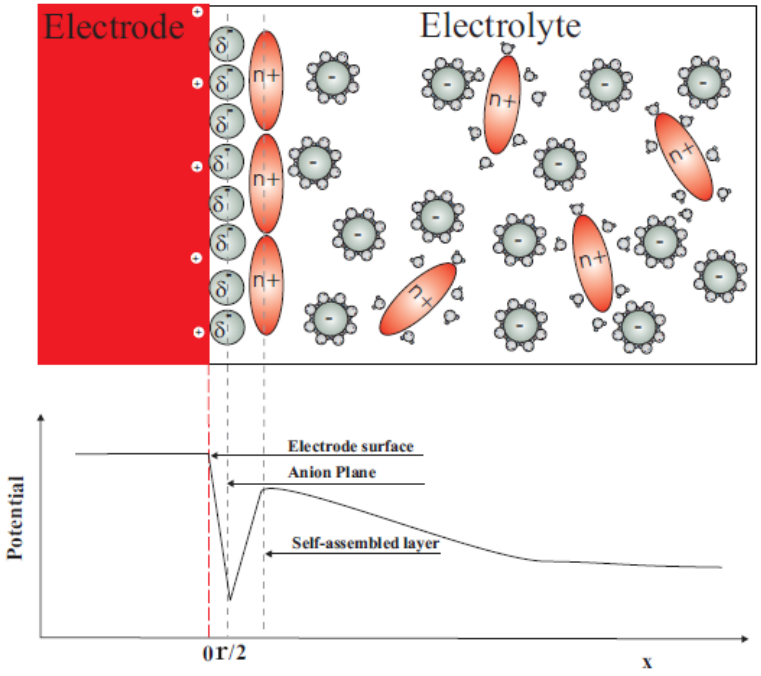

Figure 2.3: The self-assembly of organic cations on a specifically adsorbed anion layer.

With respect to the bulk, the structural and electronical properties of a metal surface are strongly modified. There is a simple model to illustrate some fundamental properties of the electronic structure of surfaces, namely the so-called Jellium model. In this model, the positive charge of the ion cores is spread uniformly over the solid (jellium) while the valence electrons move in the potential produced by this jellium.

At the surface, the positive background charge terminates abruptly (jellium edge) but the electron density does not. Instead, the electron density oscillates near the surface (Friedel oscillations) before decaying exponentially outside the solid (see Fig. 2.4). This distribution of charge density produces an electrostatic dipole layer at the surface. This dipole attracts electrons to the surface and produces a step in the surface potential [12-14], which contributes to the work function which electrons have to overcome when leaving the metal through the surface.

The electrostatic potential including the surface dipole depends on the roughness of the surface, i.e. its atomic scale structure. Fig. 2.5 shows the so-called "Smoluchowski smoothing" at steps which introduces dipoles at the surface. Therefore, the work function depends on the crystallographic orientation of the face of the crystal. For instance, the work function of Cu (fcc) is 4.94 eV, 4.59 eV and 4.48 eV for the (111), (100) and (110) surface, respectively [13].

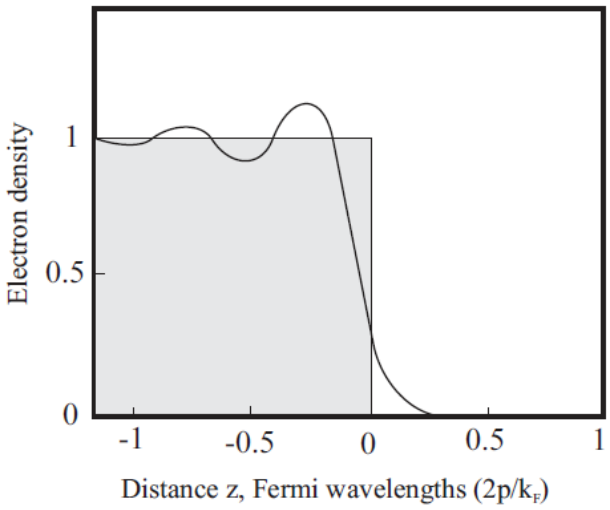

Figure 2.4: Charge density as a function of the distance from the surface in Fermi wavelengths as predicted by the jellium model [12].

The presence of adsorbates on the electrode surface can introduce two different dipolar contributions to the work function. The first contribution comes from the charge transfer between the surface and the adsorbate. When an electropositive adsorbate such as an alkali metal forms a chemical bond with a transition metal surface the alkali metal tends to donate charge into the metal which causes a decrease of the work function. Contrary to that, an electronegative adsorbate, such as oxygen, sulfur or halogens, withdraws charge from the metal and thereby increases the work function. The second contribution arises when a molecular adsorbate has an intrinsic dipole. Whether this contribution increases or decreases the work function depends on the relative orientation of the molecular dipole with respect to the surface [12].

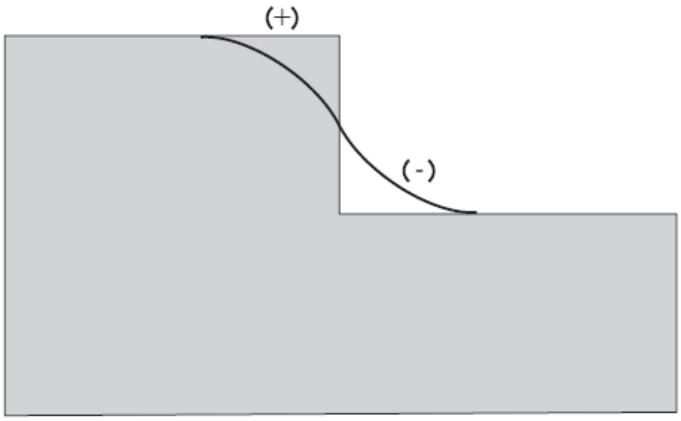

Figure 2.5: Smoluchowski smoothing effect: The electrons at a step attempt to smooth out the discontinuity of the step [12].

2.1.3 Cyclic voltammetry

The cyclic voltammetry (CV), one of the voltammetric methods, is the most commonly used technique for acquiring qualitative and quantitative information about electrochemical reactions. It was first reported in 1938 and described theoretically in 1948 by Randles and Sevcik [15]. This technique consists of scanning linearly the potential of a stationary working electrode between two chosen limits using a triangular potential waveform at a known sweep rate, υ (Fig. 2.6).

Depending on the information sought, single or multi-cycles can be used. During the potential sweep, the potentiostat measures the current resulting from the applied potential. The resulting plot of current versus potential is termed a cyclic voltammogram.

Cyclic voltammetry (CV) is used throughout this thesis in order to characterize the general electrochemical behavior of the systems under investigation.

In order to be sensitive to the potential drop between electrode and bulk solution a so-called three electrode arrangement is used, consisting of a working electrode, a counter electrode and a reference electrode. The latter one is mandatory to measure potentials being not affected by current flowing through the working and counter electrodes. Kinetic as well as thermodynamic data can be obtained by scan rate dependent CV measurements.

CV is often the first experiment performed in an electro-analytical study because it offers a rapid determination of redox potentials of electroactive species and a convenient evaluation of the effect of media upon the redox process. CV can provide considerable information on the thermodynamics of redox processes, on the kinetics of heterogeneous electron transfer reactions, and on coupled chemical reactions or

adsorption processes. Moreover, this method is not only used for evaluating the interfacial behavior of electroactive compounds such as organic molecules etc., but also widely used for the characterization of the adsorption/desorption process of anions on metal surfaces.

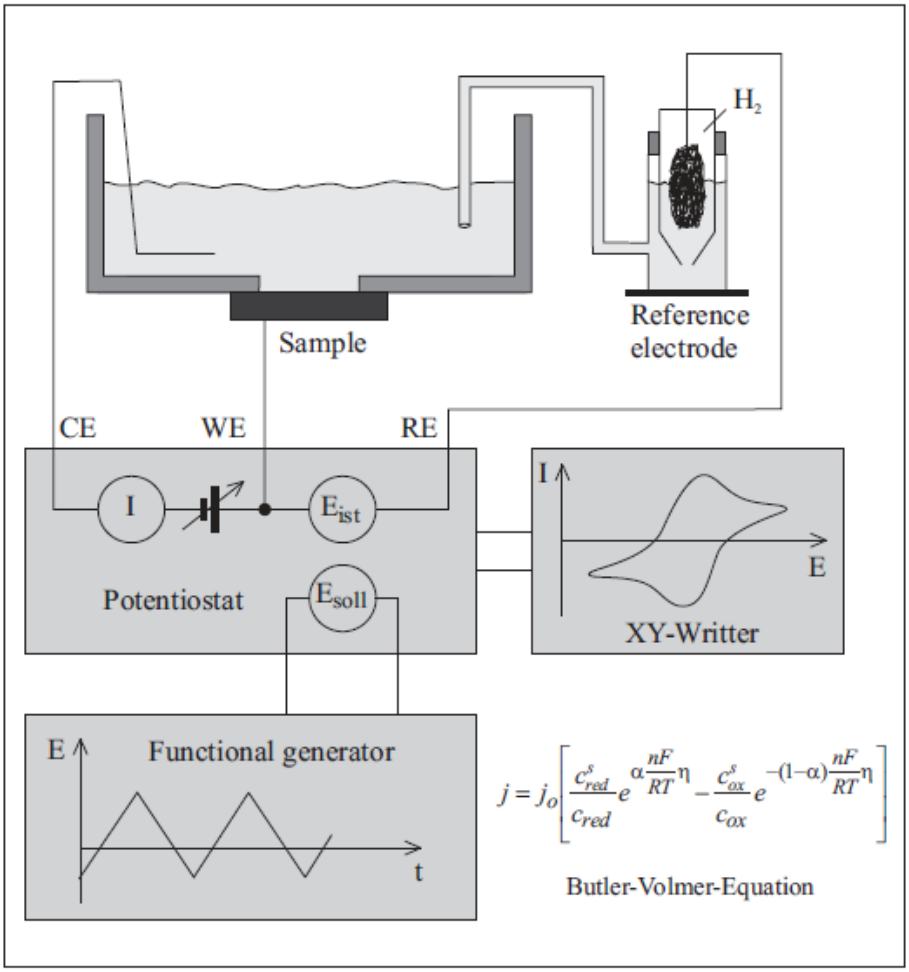

Figure 2.6: Working principle of cyclic voltammetry with the three electrode arrangement, CE: counter electrode; WE: working electrode; RE: reference electrode.

2.2 Microscopy at the solid-liquid interface – EC-STM

2.2.1 Introduction

The invention of the first Scanning Tunneling Microscope (STM) by Binnig and Rohrer in 1982 [16-18] for which they won the Nobel Prize for Physics in 1986 has revolutionized the field of surface science since it allows the direct imaging of surface structure and dynamics on the atomic scale.

The STM has been first used in an ultra high vacuum environment (UHV) and has been extensively used to investigate the surface properties of various inorganic conducting materials. Although much of the early STM work has focused on surfaces in vacuum, the STM, in fact, can also be used to obtain images of surfaces in contact with liquids or air. The first STM working at solid-liquid interfaces has been introduced by Sonnenfeld and Hansma in 1986 [19]. From that time on, the so-called Electrochemical Scanning Tunneling Microscopy (EC-STM) has attracted more and more attention.

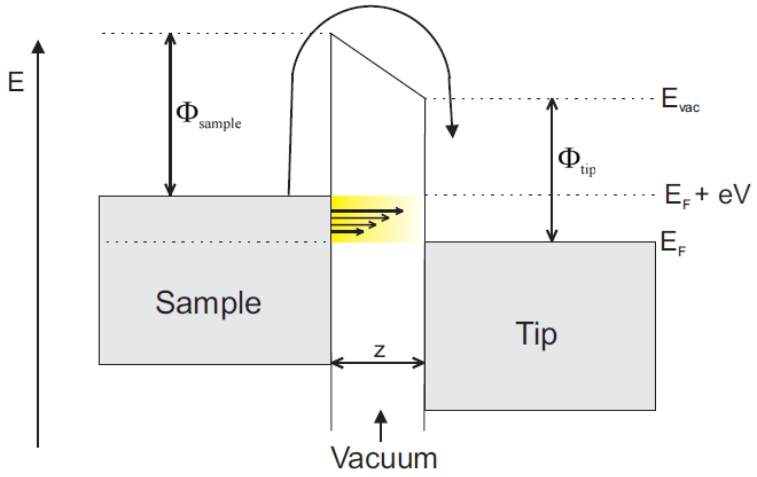

Figure 2.7: Energy level diagram of a tunneling junction.

These STMs are able to image directly the electrode surface in solution (*in-situ*). The ability to offer structural information on the atomic level makes it highly suitable for *in-situ* studies of time dependent electrochemical processes, such as corrosion, electrodeposition, adsorption, as well as surface modification and passivation. In the following the physical background of the tunneling effect, the working principle of the STM and, in particular, the experimental set-up will be presented.

2.2.2 Tunneling effect

Tunneling is a quantum-mechanical effect. An electron with energy E can penetrate a potential barrier $\Phi > E$. The wave function ψ decays exponentially in the classically forbidden region according to:

$$\psi(z) = \psi(0)\exp\frac{-\sqrt{2m(\Phi - E)}z}{\hbar} \qquad (2.5)$$

where m is the mass of the electron, $\hbar = h/2\pi = 1.05 \times 10^{-34} Js$ where h is the Planck constant, Φ is the barrier height in eV and z is the width of the barrier.

In the STM set-up, a metallic tip approaches the sample to a distance z of only some Å, so that the wave functions of the electrons in the tip and the sample overlap within the vacuum gap (see Fig. 2.7). When a small bias voltage V is applied, only electronic states very near the Fermi level are excited. The excited electrons can tunnel across the barrier from the tip into the sample or vice versa depending on the polarity of the bias voltage. In other words, tunneling occurs mainly with electrons of energies near the Fermi level.

However, tunneling does require that there is an empty level of the same energy as that of the electron tunneling to the other side of the barrier. It is because of this that the tunneling current can be related to the density of available or filled states in the sample. The current due to an applied voltage V (assume tunneling occurs sample to tip) depends on two factors: 1) the number of electrons between E_F and eV (a product of electron charge and voltage, not to be confused here with electronvolt unit) in the sample, and 2) the number among them which have corresponding free states to tunnel into on the other side of the barrier at the tip. The higher density of available states the greater the tunneling current. When V is positive, electrons in the tip tunnel into empty states in the sample; for a negative bias, electrons tunnel out of occupied states of the sample into the tip [20].

The tunneling current I_t can be calculated by taking into account the density of states at the Fermi edge of the sample, $\rho(E_F)$, according to [20]:

$$I_t \propto V\rho(E_F)\exp[-2\frac{\sqrt{2m(\Phi - E)}z}{\hbar}]\rho V\rho(E_F)e^{-1.025\sqrt{\Phi}z} \qquad (2.6)$$

Here the tunneling current is a complex convolution of the electronic properties of the tip and the sample as well.

Various theories on STM were developed in recent years which deal with a realistic surface-tip system in three dimensions [21]. One of them was introduced by Tersoff and Hamann [22-24]. Following this, the tunneling current is proportional to the surface local density of states (LDOS) at the Fermi level evaluated at the location of the tip. This theory is based on assumptions such as a small bias, a low temperature and a tip which is represented by an s-wave function. The relation between the tunneling current and the bias voltage V as well as the distance between tip and sample z is given by:

$$I_t \propto Ve^{-kz\sqrt{\Phi}}\rho(\vec{r_0}, E_F) \qquad (2.7)$$

Here the tunneling current decreases exponentially with the separation between tip and sample. This result leads to an extremely high vertical resolution of STM. A change of the distance by 1 Å results in a tunneling current change by one order of magnitude. If the current varies within 2%, the distance remains constant to within 0.01%. For the lateral resolution, about 90% of the tunneling current flow through

the gap between the outermost atom of the tip and the closest atom of the surface. Then surface atoms with an atomic separation down to ~ 2 Å can be resolved [25].

The main advantage of the Tersoff and Hamann approach consists in the fact that the electronic properties of the local probe (the tunneling tip) can be neglected. The tunneling current depends only on the local density of states of the surface but not on the tip anymore.

2.2.3 Working principle of the STM

The STM contains essentially an atomically sharp metal tip which scans over the conductive surface under investigation (Fig. 2.8). The metal tip is fixed into a scanner - a piezo tube containing three components: P_x, P_y, P_z. The piezoelectric ceramic material is used as electromechanical transducer which converts electric signals V_x, V_y and V_z of 1 mV to 1 kV applied to the P_x, P_y and P_z electrode with respect to an electrode inside the tube into mechanical motion in the range from fractions of an Å to a few µm. A feedback electronics is used to control the tip-sample distance. The voltage applied to the P_z electrode is controlled by the feedback system so that I_t remains constant when scanning the tip with P_x and P_y over the surface. At constant work function ϕ, $V_z(V_x, V_y)$ yields the "topography" of the surface, $z(x, y)$. A computer system is needed to control the tip position, to acquire data, and to convert data into an image. In addition, further auxiliary components are necessary, namely a coarse positioning system in order to bring the tip into the tunneling regime, and a vibration isolation system [24-26].

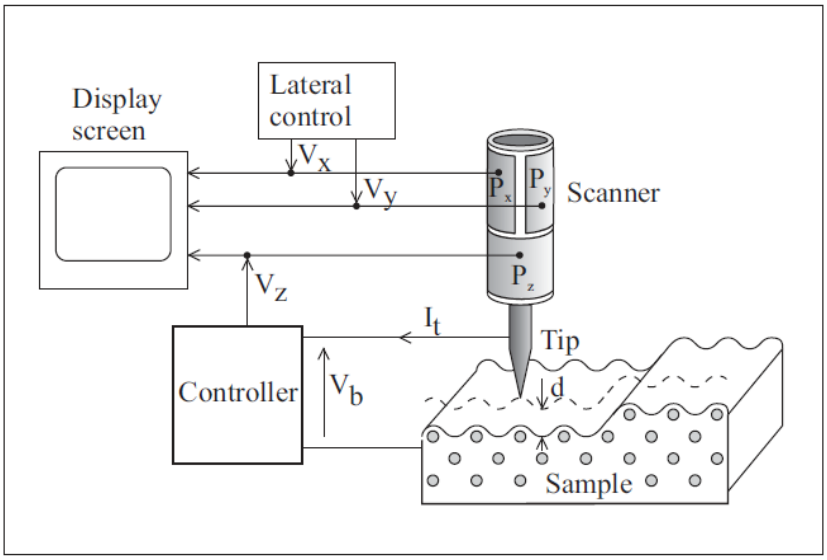

Figure 2.8: Working principle of the STM, V_b: bias voltage, I_t: tunneling current, V_x: lateral controller voltage, V_y: lateral controller voltage, Vz: vertical controller voltage [24].

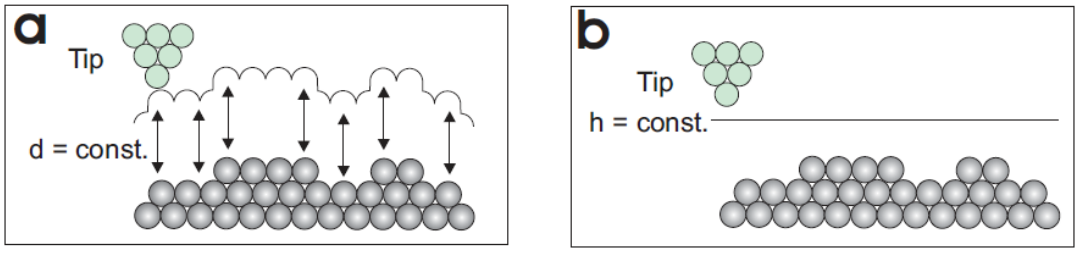

Figure 2.9: STM operation modes. a) Imaging a surface in the constant current mode. The surface contour plot is obtained by the z-signal (voltage that has to be applied for the positioning) upon scanning; b) Imaging the surface in the constant height mode. The tunneling current is recorded.

In principle, there are two operating modes: the constant current mode and the constant height mode [16, 25-26] (see Fig. 2.9):

• **The constant-current mode:** *I* and *V* are kept constant, *x* and *y* are varied by rastering the tip, and the *z*-signal is measured as a function of *x* and *y*. In this mode, comparatively large and rough sample areas can be imaged without any damage of the tip or the sample surface (”tip crash”). However, the scan rate must be kept quite slow allowing the feedback system to control the z-position of the tunneling tip.

• **The constant-height mode:** *z* and *V* are kept constant, *x* and *y* are varied by rastering the tip, and I is measured as a function of *x* and *y*. Higher scan rates can be applied which is advantageous to eliminate thermal drift effects in high resolution imaging. However, large scan sizes should be avoided since ”tip crashs” are possible, because the feedback loop is switched off.

2.2.4 The STM setup at the solid-liquid interface

The electrochemical tunneling microscopy (EC-STM) combines the STM with a potentiostat and an electrochemical cell, so that it can work in an electrochemical environment. It appears more complicated than an STM working in UHV since the EC-STM must deal with a complex tip-sample-electrolyte system. The potentio-dynamic EC-STM presented in this thesis is a home-built system designed by Wilms et al. [24, 27]. This system is developed as a special Besocke type STM instrument [28] in combination with an electrochemical cell and has various advantages over most commercial systems. Technical details about this EC-STM can be found in refs. [24, 27, 29]. Here only a brief description is presented.

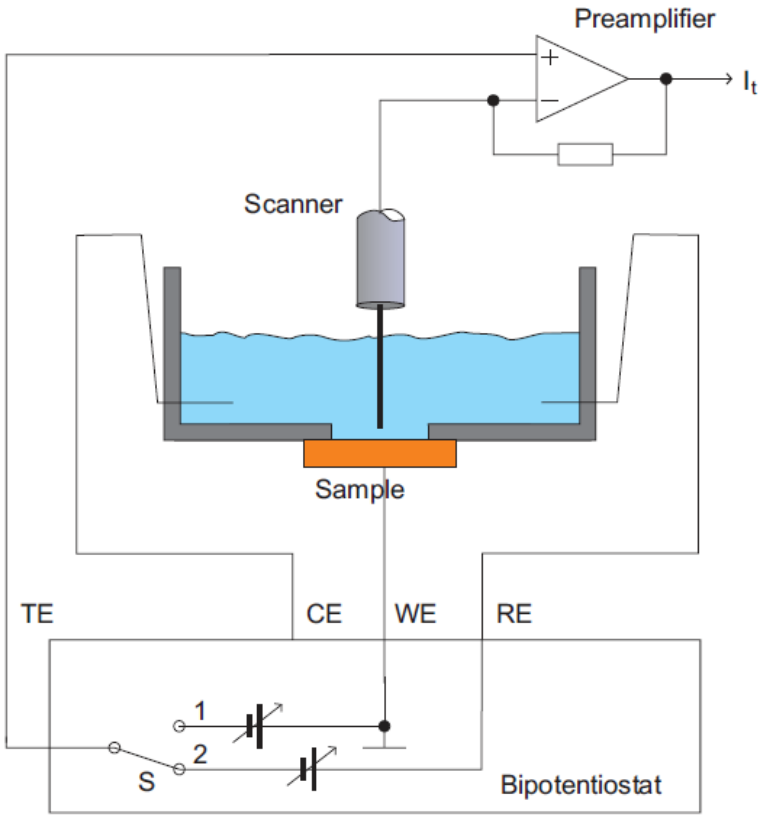

Figure 2.10: Principle of the potential control for potentiostatic and potentiodynamic imaging with the EC-STM. TE: tip electrode; CE: counter electrode; WE: working electrode; RE: reference electrode; S: switch; I_t: tunneling current [24].

The working principle of the potentiodynamic EC-STM system is displayed in Fig. 2.10. The three-electrode configuration (WE, CE, RE) controlled by a potentiostat can be used separately to investigate the electrochemical properties of the sample-electrode. In combination with the STM, the tunneling tip has to be considered as a second working electrode resulting in a four-electrode arrangement controlled by a bipotentiostat. (The control of the sample potential is independent from the tip potential). The tip potential has to be chosen so that the Faradaic current through the tip is minimal because it is superimposed to the tunneling current and could, hence, disturb the proper tip height control. Such a system is able to measure:

1. Cyclic voltammograms as in the case of a normal three electrode arrangement.
2. Potentiostatic STM images when the switch S is in position 1, and the tip potential can be adjusted to a value where the Faradaic current disappears.
3. Potentiodynamic STM images when the switch S is in position 2 and the tip potential is adjusted and held constant versus the reference electrode. Hence, the sample potential is varied while the tip potential remains unaffected.

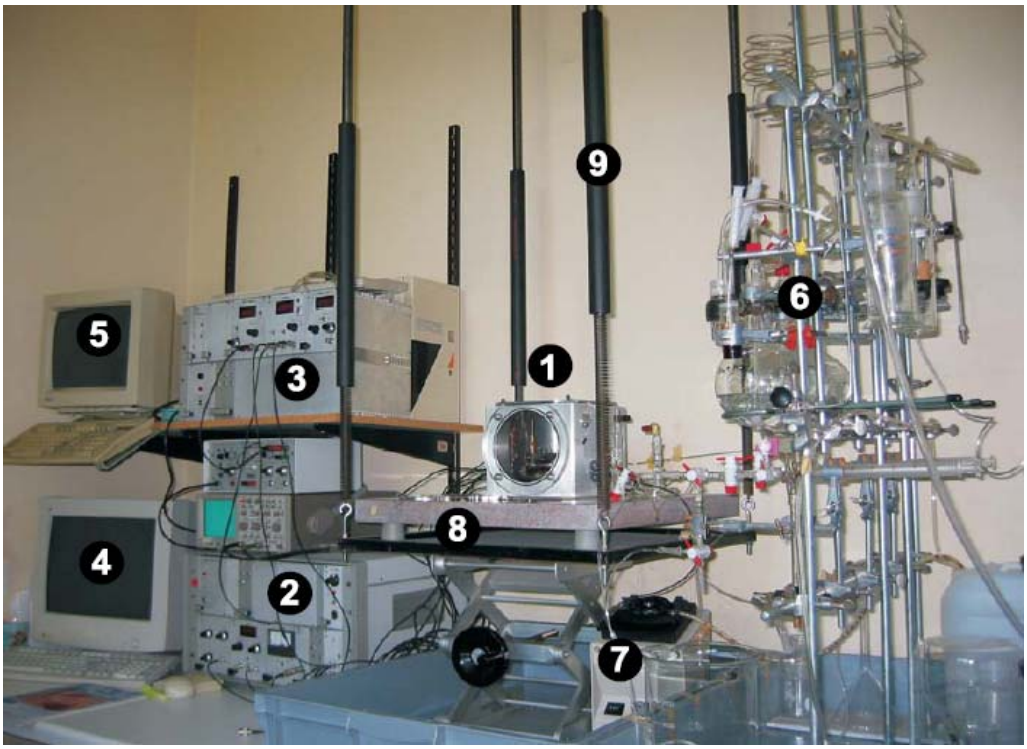

Figure 2.11: Photo of the EC-STM: 1) aluminum chamber for the STM; 2) STM control unit; 3) bipotentiostat; 4) computer for controlling the STM unit and displaying STM images; 5) computer for displaying the cyclic voltammograms; 6) electrolyte supply and gas purification system; 7) hose pump; 8) heavy granite plate; 9) steel springs connected with the ceiling.

An overview of the complete EC-STM system is shown in Fig. 2.11. The most important part of the EC-STM is the tunneling unit and an electrochemical cell which are placed within an aluminum chamber (1). This aluminum chamber can be filled with a protective Argon gas atmosphere and additionally serves as a shielding against acoustic and electromagnetic noises. In order to damp higher frequencies larger than 100 Hz the STM is placed inside the aluminum chamber on a stack of brass plates separated by rubber pieces. The chamber is placed on a heavy granite plate (8) suspended with steel springs (9) from the ceiling. This damping stage has a resonance frequency of less than 1 Hz and effectively protects the STM from outer vibrations in the low frequency regime. The protective gas is purified by using a gas purification system before filling it into the aluminum chamber. The electrolyte from the electrolyte supply system (6) is degassed by the purified protective Ar gas and then fed into the electrochemical cell. The hose pump (7) is used to adjust the circulation of the electrolyte through the electrochemical cell. The STM controller (2) is used for controlling the STM unit and a computer (4) for controlling the movement of the scanner and displaying the STM images. The operation of the electrochemical cell is controlled by a bipotentiostat (3) and the cyclic voltammograms are recorded by the second computer system (5).

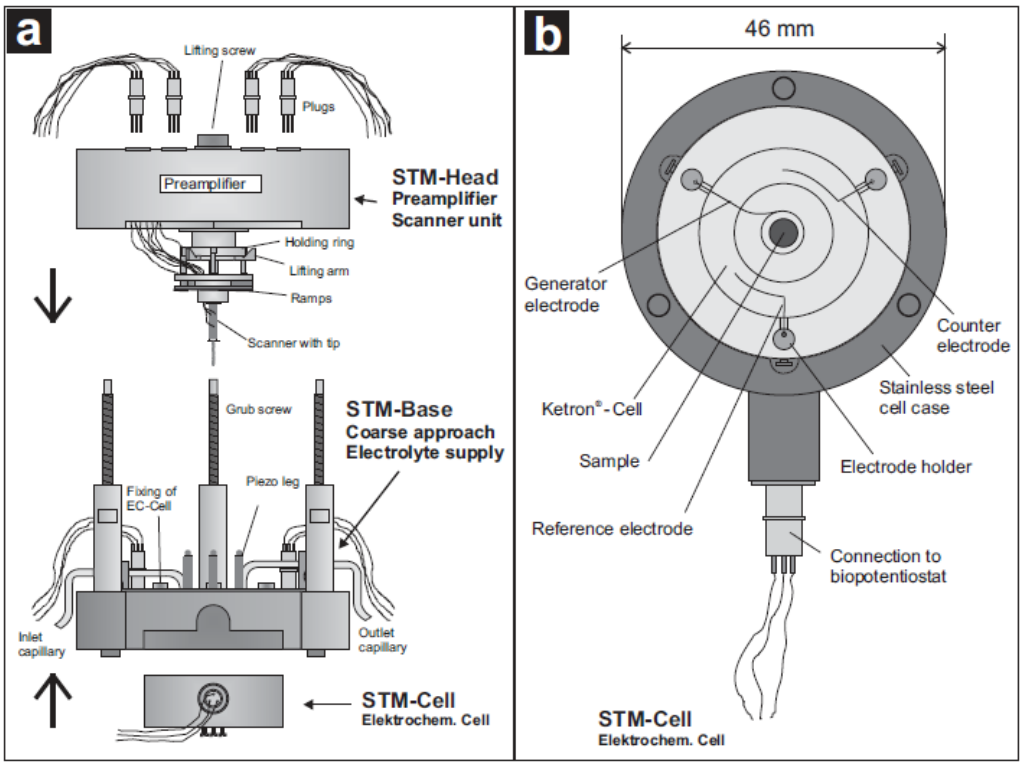

Figure 2.12: (a) Sketch of the home-built EC-STM; (b) Electrochemical cell [24].

Fig. 2.12 shows the mechanical setup of the STM (disassembled) (a) and the top view of the electrochemical cell (b). For each measurement, the sample must be prepared as described below (see Sec. 2.2.6). Afterwards, the sample is mounted into the electrochemical cell (Fig. 2.12b). This cell is then fixed into the STM-base (Fig. 2.12a) and filled with the electrolyte under potential control. The tip is installed in the scanner and adjusted to have the right length. The STM head, which carries the scanner unit and the preamplifier, is put down onto the three grub screws. After the electrical connections are made, the scanner unit is lowered down by turning the lifting screw thereby setting down the ramped ring with the scanner freely resting on the piezolegs. Scanner and tip are now mechanically decoupled from the scanner head. The STM unit is then isolated within the aluminum chamber and the granite plate is suspended freely from the ceiling. From now the scanner can be controlled by the STM control unit and the computer in order to approach the tip to the sample. After the tunneling tip reaches the tunneling regime, all the fine movements and the image recording can be controlled by the computer system. The potential applied to the sample is under control and adjusted by the bipotentiostat unit.

2.2.5 Tunneling tips

The geometry and material of the tunneling tip plays a key role in producing STM images with atomic resolution. A blunt tip will usually deliver poor images. Tunneling tips can be produced by etching or tearing a thin metal wire.

In all measurements presented in this thesis, tips have been made from tungsten using an electrochemical etching method.

The tunneling tips were electrochemically etched from a 0.25 mm diameter tungsten wire. The tungsten wire was pierced through a thin lamella of mM solution suspended by a loop of a Pt wire. Then a potential with an amplitude of ±4 V and a frequency of 100 Hz was applied between the tip and the loop electrode for a total of 3 minutes while the electrolyte was exchanged every minute. After that, the amplitude of the alternating voltage was reduced to ±2 V, and the etching process continued until the free end of the tungsten wire fell off. The tip was carefully rinsed with high purity water. After the tip became dry it was coated by passing it through a drop of hot glue [24, 30, 31]. Due to its high curvature the very tip remains uncovered.

2.2.6 Sample preparation

In order to perform useful STM measurements the surfaces have to be reproducibly well prepared and well defined. In order to study the interplay between the structure and reactivity of the surface, many well-defined single crystalline surfaces especially with low indexes have been used in electrochemical STM-studies, e.g., Au, Ag, Pt, Cu, etc. [29, 32]. Depending on the nature of the electrode material, particular preparation recipes have to be chosen. Typical methods to prepare samples for electrochemical measurements are [32]:

- **Flame-annealing and quenching method:** This method was introduced by Clavillier in 1980. A Pt single crystal was annealed in an oxygen flame and quenched in pure water. This method can be applied for Pt [33, 34], Au [35], Ir [36], Rh, Pd [37] and Ag [38].

- **Electrochemical etching method:** Flame annealing, however, can not be applied for less noble metals such as Cu, Ni, Fe, Co because these metals are easily oxidized in a flame, in air and even in contact with only trace amounts of oxygen. However, they can be very well prepared by the electrochemical etching method, i.e. electropolishing.

- **UHV-EC:** The surfaces are cleaned in UHV by cycles of Ar-ion bombardment and high temperature annealing. This method can basically be applied to any metal also such as Pt, Au, Pd [39, 40].

In this thesis, Cu(100) samples were used and prepared by the electropolishing procedure which was first introduced by Brisard et al. [41].

The Cu(100) samples were cut from a single-crystal rod, oriented by Laue diffraction and first mechanically polished using a diamond paste with different grain sizes down to 0.25 μm. A surface orientation of less than 0.5^0 off the (100) plane was required to guarantee a reproducibly smooth surface. Since copper is a quite reactive metal, a thick oxide layer is formed at the surface when this metal is exposed to air. In order to remove this native oxide layer, the sample must be electropolished prior to each STM experiment. The single crystal was electro-polished in a separate cell for about 40 s in 50% orthophosphoric acid at an anodic potential of 2 V. The surface used should be held parallel to the electrolyte surface and waved gradually in order to obtain a regularly electropolished surface. The copper surface was then rinsed with the supporting electrolyte (HCl) to remove the phosphoric acid and was covered with a drop of purged electrolyte in order to protect the copper surface against oxygen re-adsorption. After that the electrode was mounted into the electrochemical cell which was then protected in the aluminum chamber filled with Ar atmosphere. In order to check the quality of the copper surface, CVs and STM images were recorded under potential control first in the pure supporting electrolyte [24, 29, 30].

2.3 Synchrotron X-ray photoelectron spectroscopy

2.3.1 Introduction

X-ray photoelectron spectroscopy (XPS), one of the most frequently used methods for surface analysis, is a quantitative spectroscopic technique in UHV which can measure the elemental composition, as well as the chemical and electronic state of the elements that exist within a material. Furthermore it can be applied to examine samples of quite a variety of materials: metals and alloys, oxides, ceramics, organic solids, polymers and biological material. The depth of information is just in the range up to a few nanometers from the surface and the analysis area is routinely in a range from only 0.5 to 1 mm^2.

The XPS technique was used as an *ex-situ* method providing additional information on the chemical composition to the in-situ EC-STM structural results of the solid/liquid interface.

In this work, in order to get this information of the viologen adlayers on the surface, synchrotron XPS, which is highly monochromatic and has high intensity and resolution, was applied. The used solid/liquid interface analysis system (SoLiAS) installed at the synchrotron facility BESSY in Berlin which enables transferring safely the electrochemically processed surfaces into the XPS analyzer chamber will be described in more detail in the following.

2.3.2 Working principle of XPS

The technique was first known by the acronym ESCA (Electron Spectroscopy for Chemical Analysis). Surface analysis by XPS involves irradiating a solid under UHV condition with monoenergetic soft X-rays and analyzing the emitted electrons by energy. A detailed presentation of the photoelectron spectroscopy and its application can be found in [42, 43].

The spectrum is obtained as a plot of the number of detected electrons per energy interval versus their kinetic energy. Each element has a unique spectrum and in a mixture of elements, the spectrum is approximately the sum of the peaks of the individual constituents. Because the mean free path of electrons in solids is very small, the detected electrons originate from only the top few atomic layers, making XPS a surface-sensitive technique for chemical analysis. Quantitative data can be obtained from peak heights or peak areas, and identification of chemical states often can be made from exact measurements of peak positions and separations on the energy scale, as well as from certain spectral features.

Because the energy of a particular X-ray wavelength is known, the electron binding energy (BE) of each of the emitted electrons can be determined by using an equation that is based on the work of Ernest Rutherford (1914):

$$E_{binding} = E_{photon} - (E_{kinetic} + \phi) \tag{2.8}$$

where E_{binding} is the binding energy of the electron, E_{photon} is the energy of the X-ray photons being used, E_{kinetic} is the kinetic energy of the electron as measured by the instrument and ϕ is the work function of the spectrometer (not the material).

XPS is routinely used to analyze inorganic compounds, metal alloys, semiconductors, polymers, elements, catalysts, glasses, ceramics, paints, papers, inks, woods, plant parts, make-up, teeth, bones, medical implants, bio-materials, viscous oils, glues, ion modified materials and many others.

XPS can be used to measure

- elemental composition of the surface (top 1–10 nm usually),
- elements that contaminate a surface,
- chemical or electronic state of each element in the surface,
- uniformity of elemental composition across the top surface (line profiling or mapping),
- uniformity of elemental composition as a function of ion beam etching (depth profiling).

Therefore, XPS can be used to determine:

- The nature and the quantity of those elements that are present within ~10 nm of the sample surface,
- Contaminants, if any, existing in the surface or the bulk of the sample,
- The chemical state identification of one or more of the elements in the sample,
- The binding energy (BE) of one or more electronic states,
- The thickness of one or more thin layers (1–8 nm) of different materials within the top 10 nm of the surface,
- The density of electronic states.

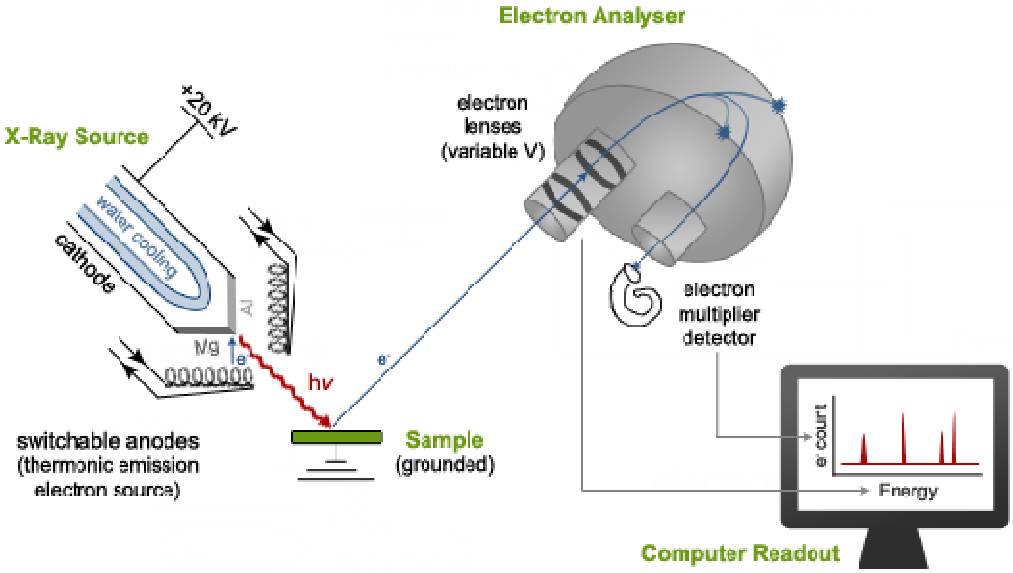

Figure 2.13: Scheme of an X-ray photoemission spectrometer. [44]

Fig. 2.13 shows the scheme of a typical XPS, including the main following components:

- A source of X-rays (X-ray gun or synchrotron radiation),
- An ultra-high vacuum (UHV) stainless steel chamber with UHV pumps,
- An electron collection lens,
- An electron energy analyzer,
- Magnetic field shielding,
- A vacuum sample introduction chamber,
- Sample holders and manipulators,
- A computer with software for data acquisition, storage, presentation and analysis.

The quantitative accuracy of the XPS method depends on several parameters such as: signal-to-noise ratio, peak intensity, accuracy of relative sensitivity factors, correction for electron transmission function, surface and volume homogeneity, correction for energy dependency of electron mean free path, and degree of sample degradation due to irradiation. Under optimum conditions, the quantitative accuracy of the atom % values calculated from the major XPS peaks is 90-95% of the atom % values of each major peak. If a high level quality control protocol is used, the accuracy can be further improved. Under work conditions, where the surface is a mixture of contamination and expected material, the accuracy ranges from 80-90% of the value reported in atom % values. The quantitative accuracy for the weaker XPS signals, that have peak intensities 10-20% of the strongest signal, are 60-80% of the true value.

The analysis area depends on the instrument design. The minimum analysis area ranges from 10 to 200 micrometres. Largest size for a monochromatic beam of X-rays is 1–5 mm. Non-monochromatic beams are 10–50 mm in diameter. Spectroscopic image resolution levels of 200 nm or below have been achieved on latest imaging XPS instruments using synchrotron radiation as X-ray source.

XPS can be performed using either a commercially built XPS system, a home built XPS system or a synchrotron-based light source combined with an electron analyzer. Commercial XPS instruments in the year 2005 used either a highly focused 20 to 200 micrometer beam of monochromatic aluminium Kα X-rays or a broad 10-30 mm beam of non-monochromatic (polychromatic) magnesium X-rays. A few, special design XPS instruments can analyze volatile liquids or gases, materials at low or high temperatures or materials at roughly 1 torr vacuum, but there are relatively few of these types of XPS systems.

Quantitative analysis is possible because the photoionization cross sections for core electrons are largely independent of the chemical bond. The intensity I_A of the escaping photoelectrons for a species A is given by:

$$I_A \sim \sigma_A(h\nu)\, D(E_A)\, L_A(\gamma)\, N_A\, \lambda_M(E_A)\, \cos\Theta \tag{2.9}$$

$\sigma_A(h\nu)$ photoionization cross section of the incident photon energy $h\nu$,

$D(E_A)$ efficiency of the detector at the electron energy E_A,

$L_A(\gamma)$ photoelectron emission probability of an atom A at the angle γ of the incident photon,

N_A density of atom A in the analyte,

$\lambda_M(E_A)$ inelastic mean free path of electrons with energy E_A in the matrix M,

Θ angle between the surface normal and the direction to the spectrometer.

Because of the difficulties to determine experimentally most of the parameters, the equation 2.9 can be simplified by disregarding the angular dependence $L_A(\gamma)$ and the mean free path $\lambda_M(E_A)$, and using tabulated atomic sensitivity factors (ASF), e.g. [42, 45]. Thus a simple relationship between intensity and the number of emitters can be identified:

$$I_A \sim ASF_A N_A \tag{2.10}$$

The ratio of the photoelectron intensities of two components is given by:

$$\frac{I_A}{I_B} \approx \frac{ASF_A N_A}{ASF_B N_B} \tag{2.11}$$

Alternatively, the apparent mole fraction of a component:

$$X_A \approx \frac{\frac{I_A}{ASF_A}}{\sum_i \frac{I_i}{ASF_i}} \tag{2.12}$$

In order to quantify the XP-spectra the intensity is defined as the peak area. Since part of the emitted photoelectron undergoes scattering processes within the solid resulting in electrons with lower kinetic energy, each XP-peak is superimposed on an increasing background. Therefore a subtraction of this background before further analysis of the spectra is essential.

2.3.3 Synchrotron XPS (SXPS) and SoLiAS setup

The development of synchrotron radiation sources has enabled highly monochromatic, high resolution and high intensity studies to be carried out with radiation spanning a much wider and more complete energy range (5 - 5000 eV). SXPS has a continuously variable excitation energy, enabling variation of the cross section and mean free path for the specific measurement.

The SoLiAS station is operated on the TGM 7 as well as on the U49/2-PGM2 beamline at BESSY in Berlin, providing excitation energies in the range 20-130 and 86-1400 eV, respectively.

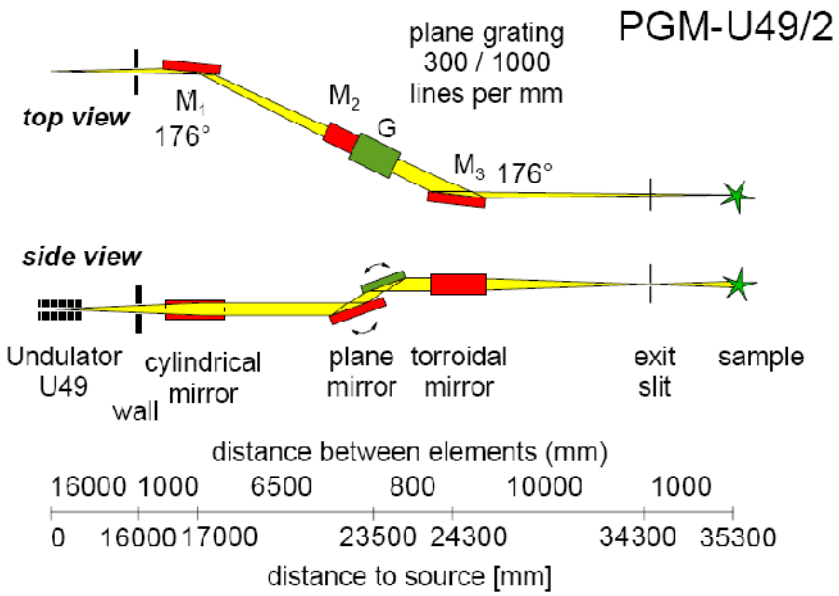

Figure 2.14: Schematic optical layout of beamline PGM-U49/2 (BESSY – Berlin).

The SoLiAS system is a six-chamber system, described in Fig. 2.15, consisting of:

1. EC cell for sample preparation under electrochemical control,
2. Buffer cell for pumping out the remaining moisture and transferring the sample from the electrochemistry cell to the vacuum system,
3. Adsorption chamber with evaporators or more sample preparation facilities using molecular beam epitaxy (not applicable in these measurements),
4. Analysis chamber including a LEED optics, an XPS electron analyser (SPECS Phoibos 150) and radiation source,
5. UHV preparation like sputtering and annealing the sample,
6. Load lock.

The buffer chamber enables sample transfer without contact to ambient air. If we want to analyze atomically thin surface layers with highest surface sensitivity and spectroscopic resolution, very special measures have to be taken in order to avoid contamination by ambient air or ubiquitous hydrocarbons. Therefore it is required to carry out the entire wet processing under normal pressure in a high purity inert gas atmosphere in a system directly attached to the UHV system. The SoLiAS system fulfills these demands. Without contact to ambient air, the sample is transferred via a buffer chamber vented with high purity inert gas as well.

SoLiAS also allows to deposit thin films within the UHV chamber in order to provide clean substrates or to prepare reference samples in the studies.

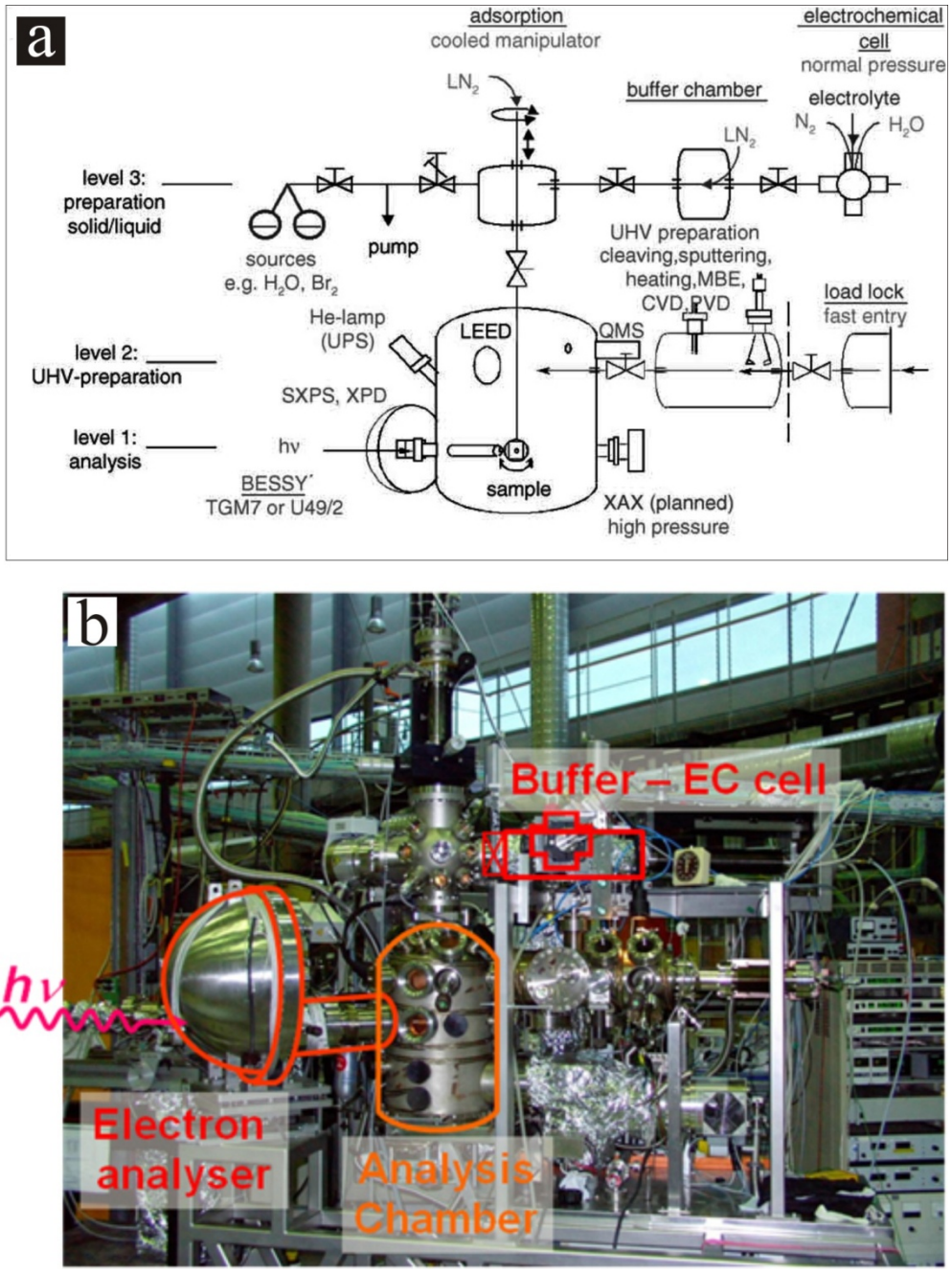

Figure 2.15: The SoLiAS: (a) schematic drawing, (b) photo.

The chamber system of the SoLiAS station permits an almost contamination-free transfer of the sample from UHV into the electrochemical cell. All parts of the SoLiAS station, and the electrochemical cell are separated by plate valves from each other and each part is evacuated by its own magnetically levitated turbo pump. The base pressure of the analysis chamber amounts to $1 * 10^{-10}$ mbar. The structure of the electrochemical cell is further explained below. The actual electrochemical cell is

housed in a Teflon holder at the bottom of a 3-dimensional glass cross with six equivalent openings. Both the Teflon holder as well as all other attachments are secured with plastic clips. Fig. 2.16a shows the 3-dimensional glass cross, including the electrochemical cell, the magnetic thrust rod with sample holder and sample for sample transfer into the analysis chamber, and the capillary for drying the sample after emersion. The electrochemical cell consists of a Teflon holder, in the actual glass cell (Fig. 2.16b) an internal reference electrode can be used.

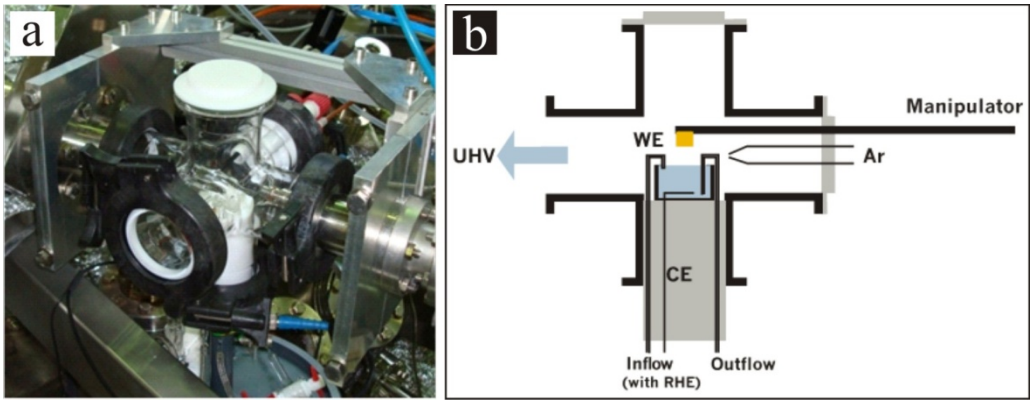

Figure 2.16: Glass cross with electrochemical cell: (a) photo, (b) schematic drawing.

2.3.4 Sample preparation and XPS measurements

The photoemission studies were performed using the solid/liquid interface analysis system (SoLiAS) experimental station at the undulator beamline U49/2-PGM2 at the synchrotron light source BESSY II [46], which enables spectroscopy of electrochemically processed surfaces. Electrochemical processing was performed in an atmospheric pressure inert-gas cell using a classical hanging meniscus configuration followed by a transfer of the electrode into the vacuum via a buffer chamber. Photoelectron spectra were obtained using a Phoibos 150 MCD 9 analyzer (SPECS). All spectra were recorded in normal emission and are referenced to the respective Fermi level of the metallic substrate. Thus, the displayed energy scales in the XPS spectra correspond to binding energies (BE). The total experimental resolution including the energy width of the photon beam and the detector resolution amounts to 100 meV. XPS data obtained from the solid di-chloride salts of the respective viologens, which were deposited on a clean gold foil under ambient conditions, served as references for the XPS spectra of the electrochemically processed, i.e. viologen covered surfaces.

Chapter 3

Substrates

3.1 Introduction

In an EC-STM, the substrate not only acts as the working electrode where electrochemical reactions take place, it is also the adsorption surface for the self-assembly processes. Therefore, the adsorbed supra-molecular structures depend strongly on the 2D-structure of the substrate surfaces and their electrochemical properties. Substrates are usually made of well defined surfaces of single crystals. In this thesis, only HOPG and Cu(100) have been used.

HOPG (Highly Oriented Pyrolytic Graphite) is a popular electrode used in electrochemistry, because HOPG has a very broad potential window and easy cleaving properties. The reason of using HOPG as a substrate in this work is at first to compare the cyclic voltammogram with those of the other surfaces, and furthermore to find out the influence of the anion layer template on the adsorption and self-assembly of supramolecular structures. Because, different from copper substrates, HOPG does not form a 2D-ordered anion adsorption layer, therefore molecules interact directly with its surface.

On the other hand, the choice of copper is due to its higher reactivity in comparison with that of noble metals such as Au, Ag, Pt. The potential window of copper is also more negative than that of those metals. These aspects are expected to offer a number of undiscovered interesting phenomena concerning the electro-chemistry and the self-assembly of supramolecular structures on the surfaces under reactive condition.

It is worthy to note that the presence of an anion adlayer on a copper surface acts as an interface where the adsorption of molecules takes place. Therefore it is the anion adlayer which is supposed to determine the structure of the building-blocks not only by their conformation but also by enhancing the adsorption due to electrostatics. And the anion adlayers lead to anion modified templates which will be described in a special sub-chapter.

3.2 HOPG surface

"Usual" graphite, especially natural one, exhibits a quite imperfect structure due to plenty of defects and inclusions. A number of technologies are developed for the preparation of perfect graphite samples to take advantage of its unique structure. Of these, pyrolysis of organic compounds is the most common and effective. Thus HOPG is a highly-ordered form of high-purity pyrolytic graphite (impurity level is of the order of 10 ppm ash or better) [47].

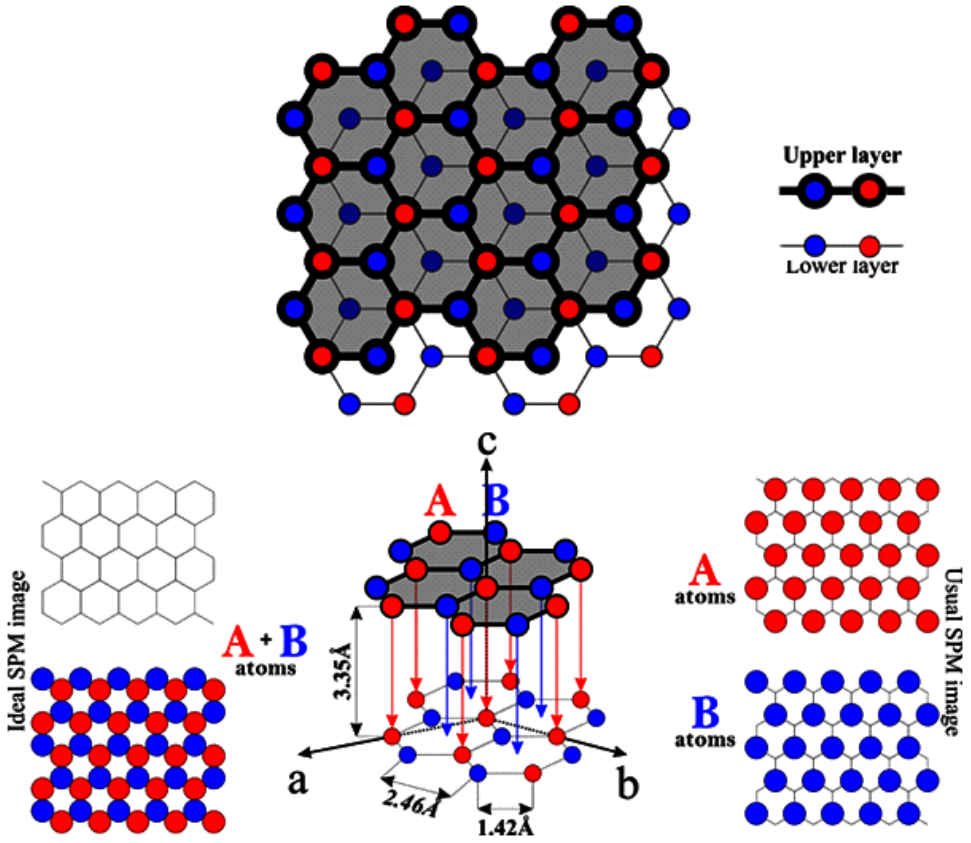

Figure 3.1: Schematic structural representation of the bulk hexagonal graphite crystal. The dashed lines show the axes of the bulk unit cell. Side insets: top view of the basal plane of graphite and schematic representation of the surface structure (carbon atoms) of graphite mostly viewed by STM, where every other atom is enhanced (right-side inset) and viewed under ideal conditions, where every single atom is seen (left-side inset) [47].

In particular, HOPG is highly oriented with respect to the layer-stacking direction. Its preferable orientation is the (0001) basal plane, because its crystal structure is characterized by an arrangement of carbon atoms in stacked parallel layers – the two-dimensional and single-atom thick form of carbon that is called graphene.

Each graphene layer is composed of a planar arrangement of fused hexagonal benzene rings. Therefore, graphite is highly anisotropic and hydrophobic. The trigonal bonding within each graphene sheet involves overlap of carbon sp^2 hybrid orbitals in the plane, whereas the overlap of carbon $2p_z$ orbitals produces delocalized rings of π electrons lying above and below each benzene ring, which makes graphite a good electrical conductor. The graphene layers are bonded to each other by weak van der Waals forces, so that they can easily slide over one another, which is why graphite is soft and slippery, and used as lubricant.

As shown in Fig. 3.1, the lattice of graphite consists of two equivalent inter-penetrating triangular carbon sublattices A and B, each one contains half of the carbon atoms. The lattice of graphite thus has two types of carbon atoms, designated A and B, per unit cell, and is invariant under 120° rotation around any lattice site. The network of carbon atoms connected by the shortest bonds looks like a honeycomb and in each layer the atoms form a grid of correct hexagons with distances between atoms equal to 0.1415 nm. The vertical distance between layers is equal to 0.3354 nm that gives a theoretical value of density $\rho = 2.265$ g/cm^3.

Because of being easily cleaved to expose a fresh surface with an extreme smoothness, HOPG terminated with a graphene layer is an excellent tool for using it in scanning probe microscopy. It has an ideal atomically flat surface. This is vital for SPM measurements that require uniform, flat, and clean substrates where elemental analysis is to be done. In addition, atomic-level images of HOPG can be used to calibrate the STM for high-resolution imaging.

3.3 Copper surfaces

Copper, one important transition metal, has several attractive properties: it is an excellent electrical conductor, ductile, etc. so that it is widely used both in everyday life and in technology. Since longtime, it is used as an electrical conductor (wires), as a building material (roofing, tubing, etc.), and as a component of various alloys [48]. Recently, copper has been considered as one of the key materials of the twenty-first century due to its application as wiring material in the state-of-the-art chip design replacing the former aluminum technology. Damascene Cu electroplating for on-chip metallization which has been developed in the early 1990s and is, for instance, central to IBM's Cu chip interconnection technology [49-51], etc..

However, the application of this material at the nanometer scale requires a more sophisticated understanding of the relevant interface properties and processes of those devices containing reactive materials like copper. An atomic scale understanding of corrosion phenomena, corrosion inhibition by organic molecules, oxidation, anodic dissolution and the formation of passivating films on copper is thus

of vital interest. In this thesis work, the Cu(100) substrate was used in order to study the self-assembly of supramolecular structures with anion adlayers serving as templates.

Surface lattice and STM image of the bare Cu(100) are presented in Fig. 3.2. The nearest neighbor distance (NND) of Cu-Cu is a_{Cu} = 2.56 Å.

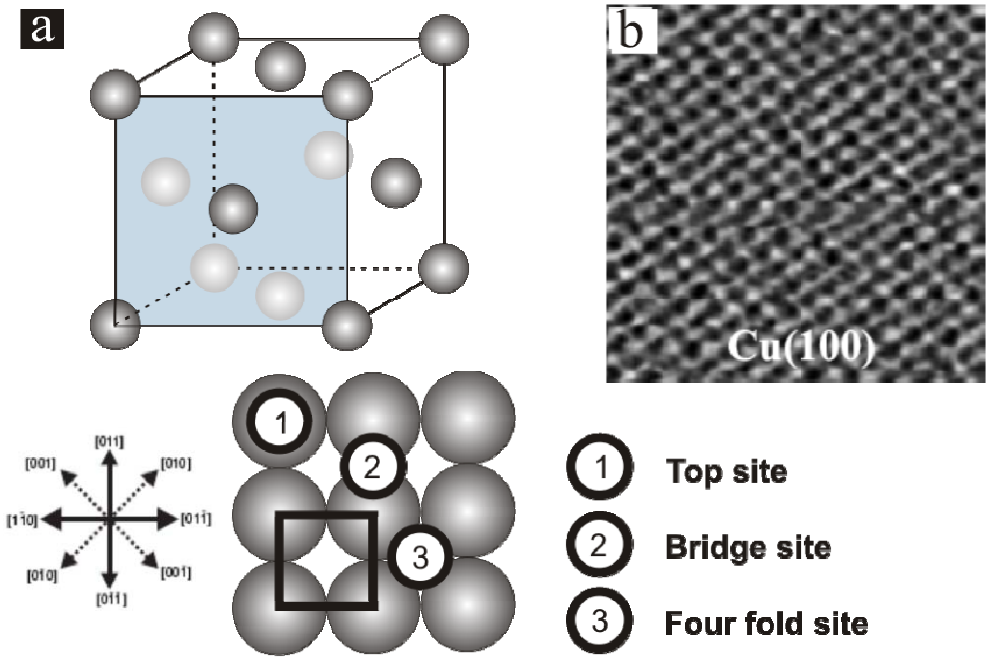

Figure 3.2: (a) (100) plane of the face-centered cubic (fcc) lattice of a copper crystal; (b) STM-image of a Cu(100) surface in diluted sulfuric acid 3.8 nm × 3.8 nm, U_b = 35 mV, I_t = 5 nA, E = 90 mV [52].

3.4 Anion modified copper surfaces

3.4.1 Overview of anion modified metal surfaces

Ion adsorption is certainly one of the most prominent and therefore one of the most intensively studied phenomena in electrochemistry. It is well-known from various electrochemical processes such as in galvanic deposition, etching, corrosion and electro-catalysis that the presence of specifically adsorbed anions can significantly affect the electrochemical reactivity of metal electrodes.

When a metal surface is in contact with aqueous electrolytes, the tendency towards specific anion adsorption increases in the sequence [53]:

Anions with strongly bound solvation shells such as F–, ClO^-_4, PF^-_6 interact with the electrode surface by pure electrostatic forces and are not specifically adsorbed on the metal surfaces. Whereas weakly solvated anions such as SO^{-4}_2, Cl^- , Br^-, I^-, can strip a part of their solvation shell and form chemical bonds with the metal surfaces [9]. As a consequence, these anions can specifically adsorb and can form close-packed, ordered adlayer structures on electrode surfaces.

The characterization of the adlayer structures was done first using an ex-situ approach that allowed the transfer of electrochemically processed electrodes into the UHV. However, the drawback of this approach lies in the possibility of a potential loss upon emersion of the electrode out of the electrolyte. But as a major breakthrough for the surface electrochemistry, the invention of the STM and then EC-STM [16, 17, 19] has revolutionized the field of surface electrochemistry allowing in-situ studies of the interfacial structure. Various ordered structures of halides, pseudohalides and oxoanions have been observed in in-situ studies on single crystal electrode surfaces of the fcc metals: Au, Ag, Cu, Pt, Pd, Ni [9, 24, 29, 30, 32, 54-72]. Especially, the specific adsorption of these anions on the reactive copper surfaces was intensively studied by Wandelt's group [54-62], Itaya's group [32, 63, 67] and others [9, 70-72].

3.4.2 Chloride modified Cu(100) surface

For most parts of this thesis, the chloride modified Cu(100) surface serves as the substrate for the adsorption of cationic organic molecules, therefore, it will be described in more detail in this part, including some experiment results.

At the interface between Cu(100) and a dilute hydrochloride acid (HCl 10mM) within the double layer, chloride adsorbs spontaneously on Cu(100) and forms a highly ordered adlayer that is stable within the potential range between copper dissolution and close to the on-set of the hydrogen evolution reaction (HER) (see Fig. 3.5). Fig. 3.3 displays the surface morphology and atomic scale structure of the Cu(100) electrode exposed to the pure supporting electrolyte. In 10mM HCl solution, the adlayer lattice is square and commensurate with respect to the substrate lattice. The adlayer can be described by a $(\sqrt{2}\times\sqrt{2})R45^o$ or c(2×2) unit cell [71-73]. The chloride species reside in four-fold hollow sites on the Cu(100) lattice [74]. The surface coverage of the chloride adlayer is 0.5 ML and the NND is $a_{Cl} = \sqrt{2}a_{Cu} = 0.362$ nm.

As known from the literature [9, 71, 72, 75] the presence of the chloride adlayer induces a preferential alignment of steps parallel to the substrate [100] directions along the close-packed chloride rows. Upon the chloride adsorption/desorption the steps reversibly change their shape from a random orientation and fuzzy appearance to predominantly [010]- and [001]-oriented steps with strongly reduced mobility of copper atoms at steps. As a consequence, typical angles between steps of 90^o can be

seen in the presence of chloride. Especially, the deposition or dissolution of copper proceeds by the subsequent addition or removal of primitive $(\sqrt{2} \times \sqrt{2})R45^{o}$ units along these edges (i.e. along [010] or [001]). Step faceting is a result of a copper mass transport in the course of the so-called "electrochemical annealing" that is facilitated in the presence of complex chloride species. This morphological feature serves as a safe indication for the presence of an intact chloride lattice with chloride coverage close to saturation.

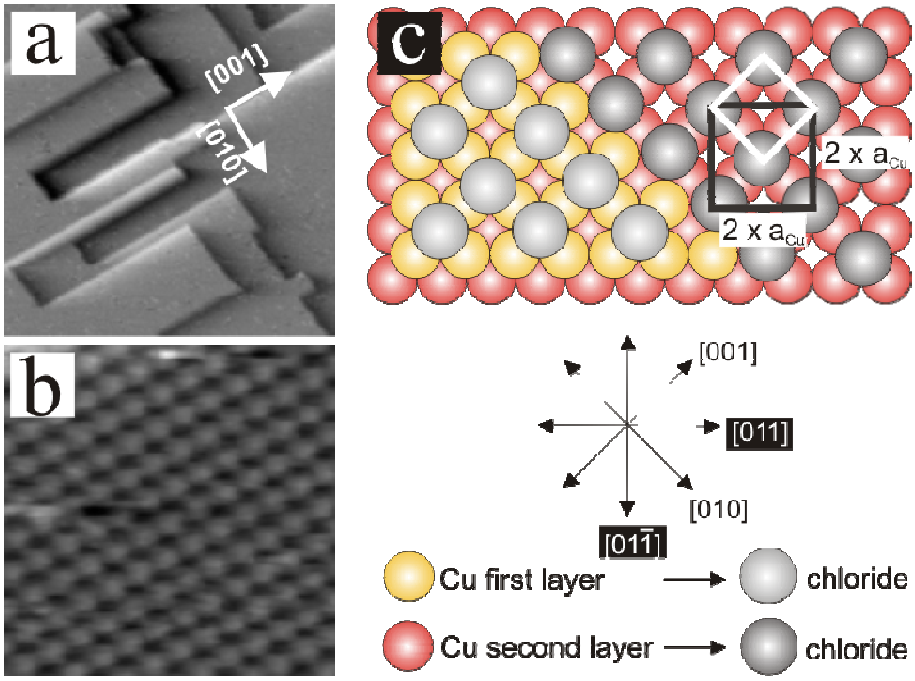

Figure 3.3: (a) Morphology of the Cu(100) electrode in the presence of the c(2 x 2)-Cl layer, 87 nm x 87 nm, I_t = 5 nA, U_b = 27 mV, E = +100 mV; (b) atomic structure of the c(2 x 2)-Cl phase, 3.9 nm x 3.9 nm, I_t = 5 nA, U_b = 25 mV, E = +100 mV; (c) Hard sphere model of the chloride modified Cu(100).

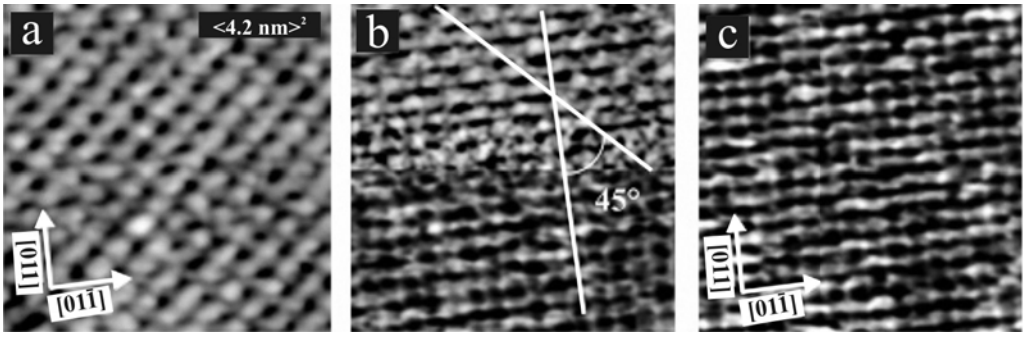

Figure 3.4: Relating the c(2x2)-Cl adlayer to the Cu(100) substrate; (a) U_b = 3 mV, I_t = 8.9 nA; (c) U_b = 3 mV, I_t = 50 nA; (b) comparison between (a) and (c).

A convenient method of the in-situ STM approach to determine the structure of halide phases is based on a systematic variation of the tunneling parameters thus allowing not only to image the covering chloride layer at moderate tunneling conditions but also the underlying copper substrate at more drastic tunneling conditions (low bias voltage, high tunneling current). At the same scanning area, Fig. 3.4a firstly shows the c(2 x 2)-Cl adlayer on the Cu(100) substrate, then, by applying higher tunneling current, it reveals the p(1 x 1)-Cu of the bulk lattice underneath (Fig. 3.4b,c).

Recent *in-situ* surface x-ray scattering experiments indicate that chloride anions remain to a large extent negatively charged upon adsorption on Cu(100). This could be concluded from the huge interlayer spacing between the chloride lattice and the topmost copper layer of 0.196 nm and an outward relaxation of the topmost copper layer by 2.2% with respect to the respective bulk value of d_{Cu-Cu} = 0.181 nm [74].

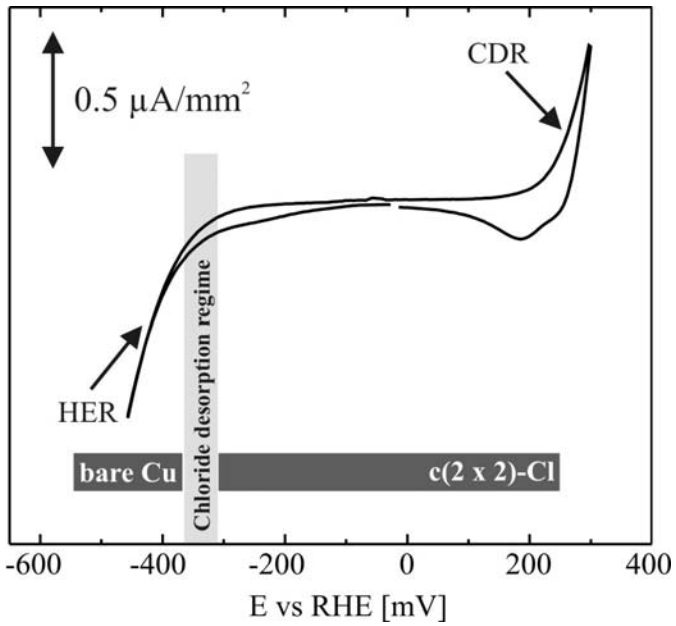

Figure 3.5: CV of Cu(100) in 10 mM HCl and specification of the surface morphology depending on the potential regimes.

From previous STM studies it is known that the chloride anions form a c(2 x 2)-Cl adlayer on Cu(100) which is stable in the potential range between copper dissolution (CDR) and close to the onset of the hydrogen evolution reaction (HER), i.e. from +250 mV to -300 mV *vs* RHE, as shown in Fig. 3.5. But sweeping further to a negative potential near the hydrogen evolution regime, a phase transition or chloride desorption occurs on the surface, starting from about -300 mV and completing around -380 mV. After complete desorption, STM results show the bare Cu(100) surface.

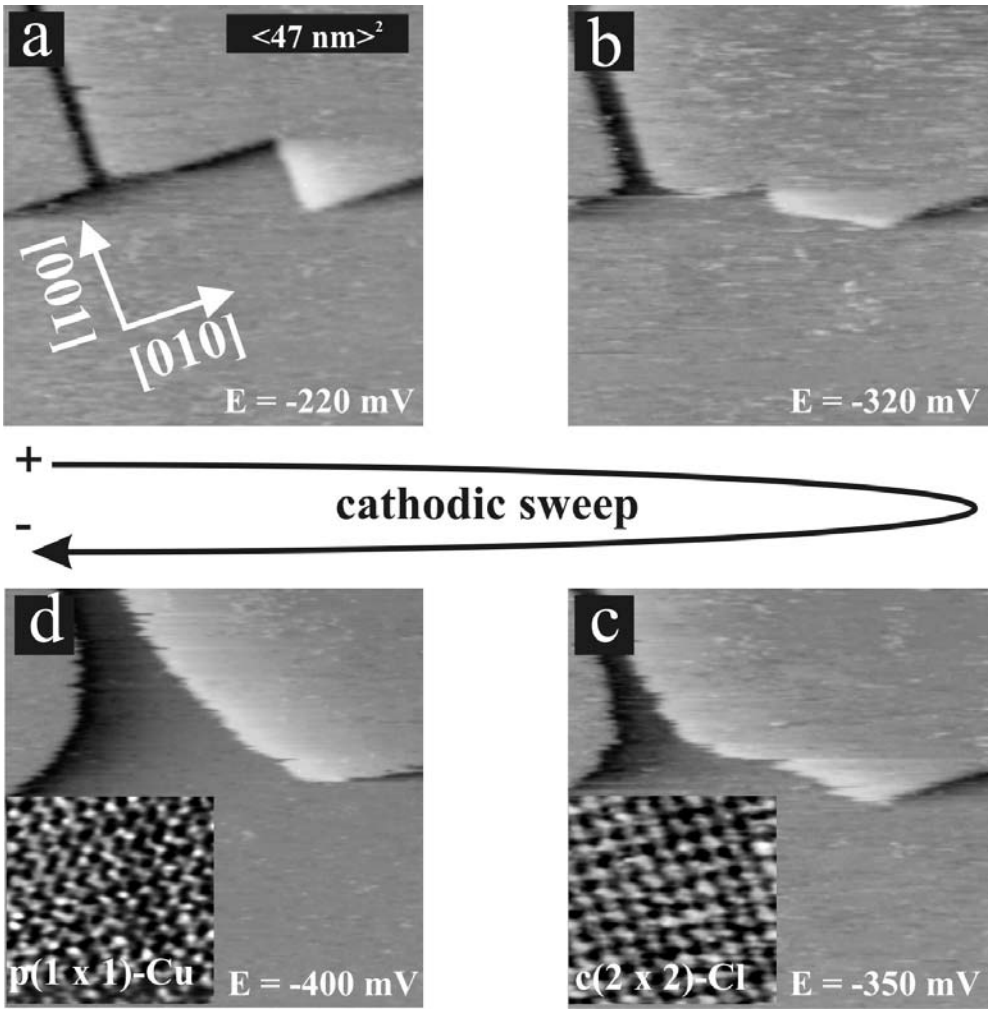

Figure 3.6: Potential dependent series of STM images showing morphological changes upon chloride desorption from Cu(100) in 10mM HCl supporting electrolyte on Cu(100), 47nm x 47nm, I_t = 1.7 nA, U_b = 255 mV. The inset in (c) represents a 3 nm x 3nm section of the lower copper terrace showing the c(2 x 2)-Cl adlayer. The inset in (d) represents a 3 nm x 3nm section of the lower copper terrace showing the bare Cu(100) surface.

As reported by Magnussen and co-workers [9, 72], the c(2 x 2)-Cl adlayer induces a "step faceting" along the closely packed chloride rows parallel to the [100] substrate directions due to significant changes in kink and step energies in the presence of this chloride adlayer, thus resulting in a new surface equilibrium morphology. In turn, the starting chloride desorption causes the corresponding "defaceting" resulting in randomly oriented substrate steps.

Such a process is exemplarily shown in Figs. 3.6a-d, which is largely consistent with the results of Magnussen et al. [9, 72]. Note that in 10 mM HCl chloride desorption starts at about E ≈ -300 mV. With higher potential sweep rates, small cathodic and anodic current features appear in the CV at potentials before reaching

the HER regime. These were assigned to the chloride desorption and adsorption processes and related order-disorder transitions [72, 76]. While substrate steps are preferentially aligned parallel to the [100] directions in the presence of c(2 x 2)-Cl under saturation conditions (Figs. 3.6c-d), these steps tend to round off in Figs. 3.6b-d, which already represents a chloride submonolayer coverage ($\theta < 0.5$ ML) at E = -320 mV. While Magnussen et al. correlate the step defaceting with a disorder-order transition within the c(2 x 2)-Cl adlayer [76], we still observe ordered c(2 x 2)-Cl patches on extended substrate terraces while step edges are already noticeably rounded off (Fig. 3.6c) in this initial stage of chloride desorption. Chloride desorption obviously starts from step edges, most likely from their lower sites. The breakdown of the chloride mediated step alignment is the consequence of an enhanced mobility of copper species diffusing along these step edges in the absence of chloride. Such a step edge diffusivity is significantly lowered under chloride saturation conditions only. Similar morphological phenomena are known from ultra-high-vacuum studies dealing with the dissociative adsorption of halogens on Cu(100) [77, 78]. At potentials below E = -380 mV, only the bare Cu(100)-(1 x 1) lattice could be imaged (see inset in Fig. 3.6d). Hence, hydrogen evolution on Cu(100) in 10 mM HCl is expected to take place on an almost halide free copper surface.

Chapter 4

Supramolecular chemistry and self-assembly of Viologens

4.1 Introduction

Nowadays, supramolecular chemistry has been well established as a major part of modern chemistry dealing with the design, fabrication and characterization of complex molecular architectures of nanometer sizes [2, 79-81]. A particular challenge for supramolecular chemists is to find artificial model systems allowing them to study the working principles of nano-sized devices, machines and actuators [82]. A successful strategy towards nano-scale molecular architectures is based on the so-called bottom-up approach. Here, supramolecular structures self-assemble from simpler molecular building-blocks via non-covalent weak forces which often reveal a directional character. As a result molecular architectures are obtained which exhibit a significantly higher complexity than the individual molecular building-blocks following Lehn‘s definition of supramolecular chemistry as the ‘‘chemistry beyond the molecule’’ [79, 80]. Supramolecular structures are the result not only of additive but also of cooperative interactions, including hydrogen bonding, hydrophobic effects and metal coordination. Their properties differ from the sum of the properties of the individual component [83].

A promising approach to direct the ordering process of supramolecular architectures takes advantage of well defined surfaces of single crystals which can act as electronic and/or geometric templates due to the presence of specific adsorbate–substrate interactions. These are modulated according to the symmetry and periodicity of the substrate surface. Whereas in solution and in the 3D solid-state only the specific and directional intermolecular interactions govern the assembly of supramolecular architectures we find on surfaces, by contrast, a complex interplay of competing adsorbate-adsorbate and adsorbate-substrate interactions controlling the 2D phase behavior. Therefore, it does not astonish that structure motifs and intermolecular spacings of supramolecular ensembles are observed on surfaces which are known neither from the solution phase nor from the 3D solid-state [84].

The surface can be regarded as an effective template in the course of the 2D ordering of molecular building-blocks if enhanced adsorbate-substrate interactions are governing the 2D phase behavior. However, surfaces are not only potential binding partners for these molecular building blocks. The surface can also act as a reactant in terms of an electron-donor or electron-acceptor provided an electrochemical environment is used.

In a new text book [83], Ariga and Kunitake subdivided supramolucular chemistry in three categories related to the size of the molecular target system:

(1) The molecular recognition chemistry or the chemistry associated with a molecule recognizing a partner molecule. Molecular recognition as the basis of supramolecular chemistry has been defined as "a process involving both binding and selection of a substrate by a given receptor molecule as well as possibly a specific function". Two types of receptors are: (i) endo-receptors are host molecules that have binding sites insides their molecular structures (inner surface) and (ii) exo-receptors are host molecules with binding sites on their outer surfaces [83, 85].

(2) The chemistry of molecules built to specific shapes: It is possible to build molecules of medium size which have unique geometric features and provide the key to many tailored supramolecular topologies. For example, fullerenes are like "molecular soccer ball", carbon nanotubes, etc.. One can design one-dimensional supramolecular objects, rectangles, squares, three dimensional cages, molecular branching such as dendrimers (molecular tree), molecular rings, etc. [81, 83, 86-90].

(3) The chemistry of molecular assembly from numerous molecules: Supermolecules can also be programmed from a huge number of components producing a supramolecular self-assembly with a defined shape and structure. For example, supramolecular crystals, micelles, monolayers and Langmuir-Blodgett films on the surface of water, self-assembled monolayers on solid surfaces, etc. [83, 85, 90-93]. Here the concept of self-assembly is used for the spontaneous assembly of several molecules into a single, highly structured supramolecular aggregate [94]. The intermolecular interactions within supramolecules are non-covalent and quite diversified such as:

- *Electrostatic interaction* occurs between charged species, is relatively strong compared to other non-covalent interactions, and is non-directional.
- *Hydrogen bonding* occurs only when the interacting functional groups are properly oriented, and is weak and directional.
- *Coordinative bonding* occurs between a metal ion and electron-rich atoms, and is of moderate strength and directional.

- *The van der Waals interaction* is weak, non-directional and less specific than other interactions described above, it acts between all kind of matter.
- *Hydrophobic "interaction"* occurs between hydrophobic molecules and is the major driving force for hydrophobic molecules to aggregate.
- $\pi - \pi$ *interactions between aromatic rings* are present when the aromatic rings face each other, and the overlap of π-electrons results in an energetic gain.

The formation of supramolecular architectures may be due to one kind of these interactions or a combination of them. By mastering these interactions, one can control the building of supramolecular architectures which have particular forms and specific functions [83]. Therefore, the development of supramolecular chemistry has opened a wide range of promising application in many fields, especially in nanotechnology [81, 82, 85, 91, 95-100].

However, the new supramolecular chemistry as mentioned above is mostly applied and explored in solution or in 3D crystals, but not yet fully exploited in 2D. Because of the increasing demand to produce surface pattern and devices with nanometer dimensions using the promising "bottom-up" technique, the autonomous ordering and self-assembly of atoms and molecules on atomically well-defined surfaces is receiving more and more attention. That is the reason why the self-assembly of supramolecules on solid surfaces has been intensively studied only over the past few years. In addition, the invention of the scanning probe techniques has facilitated the studies because of their ability to visualize molecules in real space [84, 91].

Actually, the self-assembly of supramolecular entities on solid surfaces can be divided into two groups:

(1) Self-assembly of molecules on solid surfaces in ultrahigh vacuum (UHV):
   - Interactions between molecules (intermolecular interactions),
   - Interaction between the molecule and the substrate (adsorbate-substrate interactions).

(2) Self-assembly of molecules on solid surfaces at the solid/liquid interface:
   - Interactions between molecules (intermolecular interactions),
   - Interaction between the adsorbed molecules and the substrate,
   - Interaction between the molecules and the solvent.

The self-assembly of supramolecules on surfaces is quite complex and is a result of a delicate balance among all these interactions [101]. It can be also restricted to the monolayer regime or may extend to multilayers. The concept of self-assembled

monolayers (SAMs) was discovered in the case of chemisorption of thiolates on gold [81]. However, it is clearly seen nowadays that self-assembled monolayers can be formed in a wide range of systems with different supramolecules on different solid surfaces.

The present work focuses on the self-assembly of molecules at the solid/liquid interface using viologen molecules as building blocks. The adsorption of viologens could be found to form highly ordered self-assembled monolayer, sub-monolayer, multilayer or even disorder phases. These structures of the viologen adsorption on copper surfaces can be controlled by changing the adsorbate-substrate interactions, i.e. by changing the electrode potential in the case of electrostatic interaction, etc.

4.2 Viologen molecules

4.2.1 Introduction

The common name of "viologen" derives from Michaelis who noted the violet colour formed when 1,1'-dimethyl-4,4'-bipyridilium underwent a one electron reduction to form a radical cation (as dimer). Then, the term "viologen" was used widely to mean a compound or salt of anion X^- and 4,4'-bipyridine to form 1,1'-disubstituted-4,4'-bipyridine (Fig. 4.1), whatever its redox-state. The bipyridine group has one single nitrogen atoms per ring and reveals a rotational degree of freedom along their connecting C-C axis. Therefore, the two pyridine rings are not always coplanar but are skewed with an inter-plane angle (dihedral angle) of certain degrees depending on their redox-state [4].

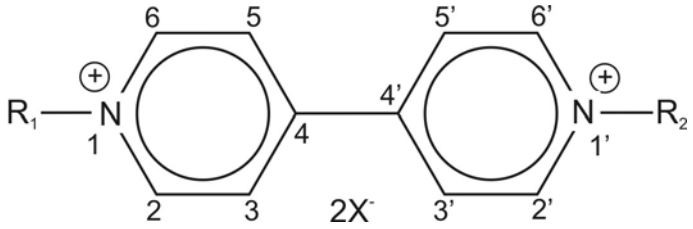

Figure 4.1: Molecular scheme of a viologen dication, R_1, R_2 ligands, X^- counter anion.

Because of the two nitrogen atoms, viologens have three redox-states: dication, radical cation and uncharged molecules. All three common viologen redox-states can be converted into each other in an electrochemical environment by two single electron transfer reactions (Fig. 4.2). The bipyridinium dication is the most stable of the three common redox forms, and is the usual starting material for a study.

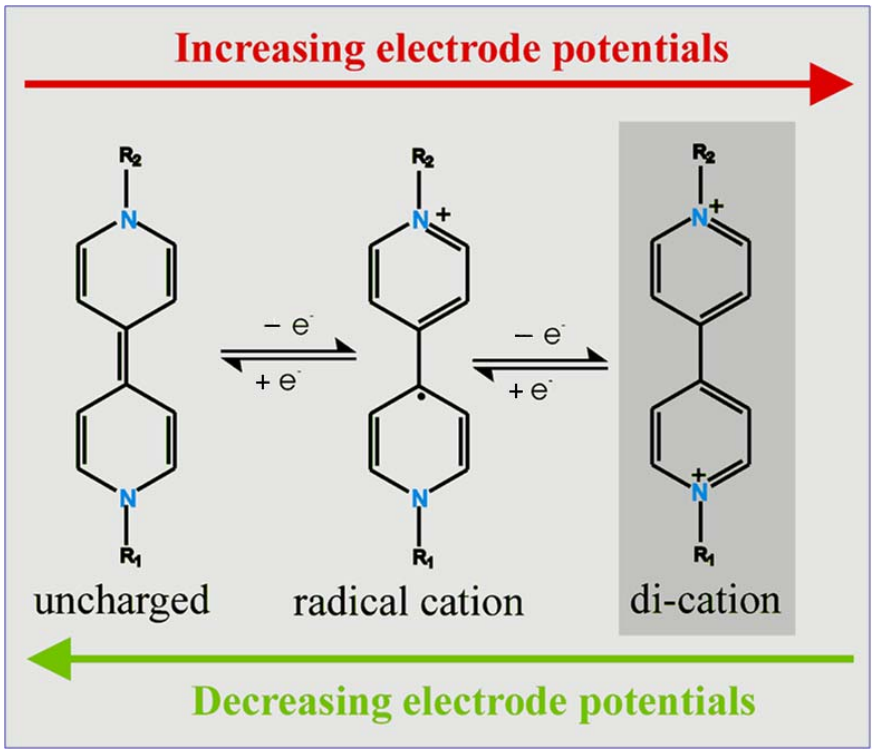

Figure 4.2: The three common redox forms of viologens and their electron transfer reactions.

In order to understand the particular phase behavior of adsorbed viologens on the chloride modified copper surface depending on their redox-state one has to consider in particular the *intra-molecular conformal changes* that occur upon the charge transfer. These structural changes have been exemplarily studied for isolated viologen molecules by DFT calculations. *Ab initio* calculations have been performed by Hoffmann and Nagy Felsobuki [102, 103] to analyse the way electron density from the cationic centres is delocalized around the ring. They investigated the effect of the redox-state upon the dicatonic and radical cation structure, their results implying that the bipyridinium radical cation is almost flat. By contrast, the dicaton is not planar but skewed in the ground state, exhibiting a much larger interplane angle of more than 40°. This result is presumed to be similar to a (low-pressure) gas-phase value since it presupposes the absence of any external forces on the molecule.

As mentioned in the "Introduction and outline" part, viologens are certainly among the most intensively studied molecular building-blocks in supramolecular chemistry. Their solution electrochemistry is well documented in the literature [3, 4]. Certain attention was paid to the surface chemistry of viologens using standard electrochemical methods such as cyclic voltammetry (CV) [104, 105] and various spectroscopic methods, e.g. Raman spectroscopy [106-110] or UV reflectance spectroscopy [111, 112] in order to derive information about adsorption geometries depending on the particular redox-state. Characteristically, the reduction of pre-

adsorbed viologen dications to the corresponding adsorbed radical mono-cation takes place at potentials more positive than the redox-processes of the corresponding solution species giving rise to the appearance of characteristic pre-peaks in the CV. Their appearance has been rationalized in terms of pure kinetic effects since reaction rates are usually higher for adsorbed reactants than for the corresponding solution species [4]. For the reaction of adsorbed species no diffusion limitations are expected. This phenomenon has been demonstrated for various viologens adsorbed on Hg [105, 113, 114] and HOPG [105, 115, 116] electrodes. In the present work we focus on the surface redox chemistry and the related phase behavior of adsorbed viologens by employing not only ‘‘integral’’ methods averaging over the entire surface but also scanning tunneling microscopy (STM) as a structure-sensitive local probe technique providing direct access to structural changes within adsorbed viologen films in the course of electron transfer reactions. The two viologens studied in this thesis are dibenzyl-viologen (DBV) and diphenyl-viologen (DPV).

4.2.2 Dibenzyl-Viologen (DBV)

The chemical model of DBV molecules is displayed in Fig. 4.3. The core of the molecules consist of a 4,4’-bipyridinium group with an intramolecular distance of 0.71 nm between the nitrogen atoms, and the extra methylene group separates the phenyl groups from the central bipyridinium unit, forming two benzyl groups as outer chains. Due to the methylene groups as connectors, the outer chain of DBV molecules can bend as shown in Fig. 4.3, and the total length of isolated DBV molecules is about 1.55 nmm.

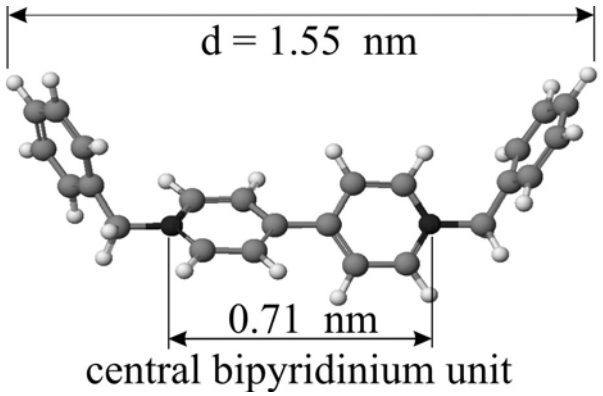

Figure 4.3: The chemical model of DBV molecules.

The quantum chemical optimization of the molecular viologen structures the density functional and *ab initio* programs provided by the TURBOMOLE 5.1 suite has also been done by Kirchner and Kossmann [117].

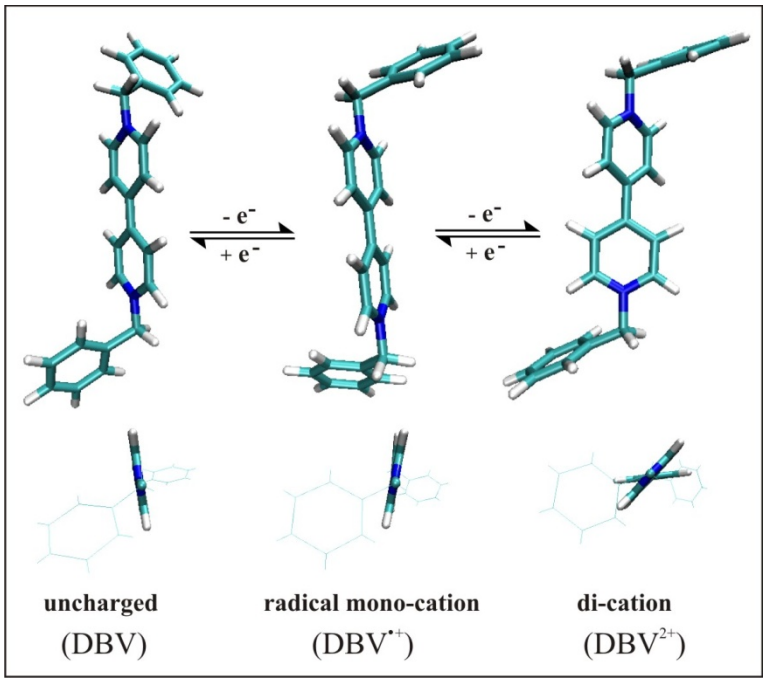

Figure 4.4: DFT based structure optimization of the isolated DBV^{2+}, $DBV^{\bullet+}$ and the uncharged DBV^{0} molecules.

Fig. 4.4 displays the result of the quantum chemical structure optimization obtained for the isolated di-cationic DBV^{2+}, the radical mono-cation $DBV^{\bullet+}$ and the uncharged DBV^{0} species in the gas phase. As expected, the DBV^{2+} exhibits a pronounced non-zero interplanar dihedral-angle between the two pyridinium rings of $\Phi(DBV^{2+}) = 40.11°$. However, it is reported for the solution phase that counter ions with electron donor capabilities can undergo CT (charge transfer) interactions with viologen dications leading to a significant decrease of the dihedral angle. The same trend is observed for the reduction of the isolated DBV^{2+} to the corresponding radical mono-cation with a resulting dihedral angle $\Phi(DBV^{\bullet+}) = -5.41°$ (Fig. 4.4). For the uncharged DBV^{0} molecule the dihedral angle is close to zero with $\Phi(DBV^{0}) = -0.11°$. These changes of the intramolecular structure become obvious from a side-view of the viologens along their main molecular axis (Fig. 4.4). All three common viologen redox-states can be converted into each other in an electrochemical environment by two single electron transfer reactions. At least the first electron transfer process reducing the di-cation DBV^{2+} to the radical mono-cation $DBV^{\bullet+}$ is considered as reversible.

Although the C-C bond length between the two pyridine rings in $DBV^{\bullet+}$ decreases by 4.2% during reduction, the effects of increased steric repulsion between ortho hydrogens is less than the stability gained by increasing the extent of conjugation between the two rings.

4.2.3 Diphenyl-Viologen (DPV)

The chemical model of DPV molecules is displayed in Fig. 4.5. The core of the DPV molecules is also a 4,4'-bipyridinium group with an intramolecular distance of 0.71 nm between the nitrogen atoms, however, DPV molecules lack the methylene group in comparison with DBV, and therefore the conjugated π-system of DPV molecules extends over the entire molecule (Fig. 4.5) causing the higher total length of isolated molecules of about 1.77 nmm.

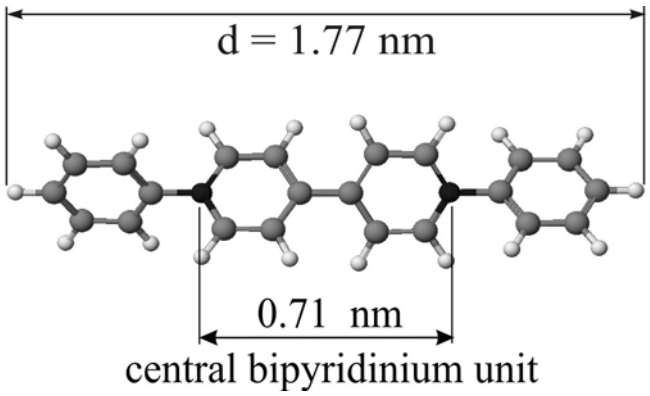

Figure 4.5: The chemical model of DPV molecules.

Fig. 4.6 displays the result of the quantum chemical structure optimization obtained for the isolated DPV molecule, also containing three redox-states: the di-cationic DPV^{2+}, the radical mono-cation $DPV^{\bullet+}$ and the uncharged DPV^{0} species, respectively [117]. The DPV^{2+} exhibits a pronounced non-zero interplanar dihedral-angle between the two pyridinium rings of $\Phi(DPV^{2+}) = 44{,}15°$. The reduction of the isolated DPV^{2+} to the corresponding radical mono-cation $DPV^{\bullet+}$ also results in a significant decrease of the dihedral angle. The dihedral angle of radical mono-cation $DPV^{\bullet+}$ is close to zero, and particularly the two outer phenyl chains are arranged coplanar with the bipyridinium core (Fig. 4.6 radical mono-cation), therefore, concerning the radical mono-cation species, we expect the fully conjugated π-system of the $DPV^{\bullet+}$ to stabilize more effectively than that of the $DBV^{\bullet+}$ with its "isolated" π-system of the central bipy unit. Going further to negative potential, the radical mono-cation $DPV^{\bullet+}$ is reduced to the uncharged DPV^{0} species with the similar dihedral angle close to zero. However the difference between $DPV^{\bullet+}$ and DPV^{0} species is the arrangement of the phenyl groups. While in radical mono-cation $DPV^{\bullet+}$ the two phenyl groups are coplanar with the bipyridinium core, in uncharged DPV^{0}, they turn by an angle of about 40° with respect to the bipyridinium core (Fig. 4.6).

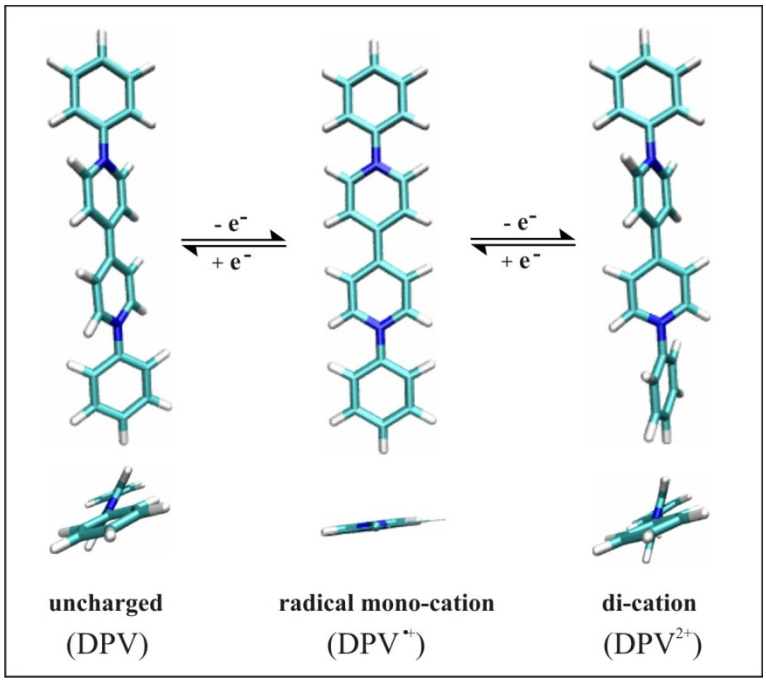

Figure 4.6: DFT based structure optimization of the isolated DPV^{2+}, $DPV^{\bullet+}$ and the uncharged DPV^{0} molecules.

The small structural difference by the methylene groups between DBV and DPV, however, significantly affects both the viologen solution redox-chemistry and the phase behavior of the adsorbed viologen species which are discussed in detail in the next chapters.

4.3 Viologen adsorption

Traditionally, adsorption is "the taking up of one substance on to the surface of another". In electrochemistry, the material taken up is almost always in solution prior to adsorption, and the surface on to which the material is taken (the electrode) is usually a liquid (mercury) or a metallic solid, and the adsorbing species adhere to the substrate between the inner and outer Helmholtz planes [4].

However, in the modern supramolecular chemistry, a promising approach to direct the ordering process of supramolecular architectures takes advantage of well defined surfaces of single crystals which can act as electronic and/or geometric templates due to the presence of specific adsorbate–substrate interactions. These are modulated according to the symmetry and periodicity of the substrate surface. Whereas in solution and in the 3D solid-state only the specific and directional intermolecular interactions govern the assembly of supramolecular architectures we find on surfaces, by contrast, a complex interplay of competing adsorbate–adsorbate

and adsorbate–substrate interactions controlling the 2D phase behavior. Therefore, it does not astonish that structure motifs and intermolecular spacings of supramolecular ensembles are observed on surfaces which are known neither from the solution phase nor from the 3D solid-state [84]. The surface can be regarded as an effective template in the course of the 2D ordering of molecular building-blocks if enhanced adsorbate–substrate interactions are governing the 2D phase behavior. Furthermore, surfaces are not only potential binding partners for these molecular building blocks. The surface can also act as a reactant in terms of an electron-donor or electron-acceptor provided an electrochemical environment is used. This applies to the adsorption of viologens on metal substrate.

However, to achieve both the right adsorption geometry and a large extent of lateral order within the organic film, one has to tune carefully the balance between adsorbate-substrate interactions on the one hand and adsorbate-adsorbate interactions on the other hand. These can be obtained by alternatively using anion-modified metal surfaces as substrates in an electrochemical environment. In this case, the negative charge of the anion adlayer can enhance the viologen adsorption due to electrostatic interaction [5]. In this work, chloride is chosen as pre-adsorption layers resulting in modified metal surface templates.

The compounds used here are highly soluble dibenzyl- and diphenyl-viologen dichloride salts. It should be noted that the electron transfer processes do not necessarily take place at the bare metallic electrode surface but on the chloride modified surface. Therefore, the adsorption from aqueous chloride solutions on these metal surfaces is even more complex due to the superposition of several processes involving both “solution-” and “surface-limited” reactions as proposed below:

1. The first reversible transition from di-cationic species (V^{2+}) into their corresponding radical mono-cations ($V^{\bullet+}$) via a one-electron transfer step, can occur:

a. as surface limited reduction/oxidation of adsorbed viologen species according to

$$V_{(ads)}^{2+} + e^{-} \leftrightarrow V_{(ads)}^{\bullet+} \tag{4.1}$$

which might be accompanied by the subsequent dimer formation at the surface according to

$$2V_{(ads)}^{\bullet+} \leftrightarrow [V_2]_{(ads)}^{2+} \tag{4.2}$$

or even oligomer or polymer formation at the surface according to

$$nV_{(ads)}^{\bullet+} \leftrightarrow [V_n]_{(ads)}^{n+} \tag{4.3}$$

Oligomeric and polymeric reaction products tend to accumulate preferentially on the electrode surface while the dimer species often remain water soluble [3, 4].

b. as reduction/oxidation of viologen solution species according to

$$V^{2+}_{(aq)} + e^- \leftrightarrow V^{\bullet+}_{(aq)} \tag{4.4}$$

which might be accompanied by the subsequent dimer formation in solution according to

$$2V^{\bullet+}_{(aq)} \leftrightarrow [V_2]^{2+}_{(aq)} \tag{4.5}$$

c. as film formation/dissolution of radical mono-cation chloride salts according to

$$nV^{\bullet+}_{(aq)} + nX^- \leftrightarrow [V^{\bullet+}X^-]_n \downarrow \tag{4.6}$$

2. The second single electron transfer step transforms the radical mono-cation into the fully uncharged viologen species according to:

$$V^{\bullet+} + e^- \leftrightarrow V^0 \tag{4.7}$$

This latter transition has to be considered as less reversible than the first electron transfer process [3, 4]. Furthermore, the two sequential electron transfer steps in the viologen redox-chemistry can interfere with an additional conproportionation reaction between the uncharged and the di-cationic viologen species to the corresponding radical mono-cation according to:

$$V^0 + V^{2+} \leftrightarrow 2V^{\bullet+} \tag{4.8}$$

Since the reduction from their radical cation to uncharged species is supposed to lie within the regime of massive hydrogen evolution of the copper substrate at even more negative potentials only two redox species, the dication and radical cation, have been studied within the potential window of the copper substrates. However, the potential window of the HOPG surface is much broader than that of copper. Thus, for this substrate we expect to observe both electron transfers related to consecutive reductions from dication to radical mono-cation and to uncharged species.

4.4 Preparation method

4.4.1 Viologen adsorption on chloride modified Cu(100)

The studies of viologen adsorption on the chloride modified copper substrate presented in this thesis consist of three systems:

- “Non-reactive” adsorption of DBV
- “Reactive” adsorption of DBV

- Adsorption of DPV

Focusing on a chloride modified template, all three systems use 10 mM HCl as supporting electrolyte. The working electrolyte is a mixture of the supporting electrolyte and soluble viologen dichloride salts. For most of the experiments the concentration of the viologen was chosen to be 0.1 mM, however the concentration of 1 mM was also used for CV experiments in order to distinguish between bulk and surface processes in CV curves. The preparation for the viologen adsorption on chloride modified Cu(100) is performed as follows.

After the initial electro-polishing process as mentioned in Sec. 2.2.6 the copper surface was rinsed with the deoxygenated supporting electrolyte (10 mM HCl), mounted into the electrochemical cell and fixed into the STM unit which is placed in the aluminum chamber filled with Ar gas. The electrochemical cell was then filled with the 10 mM HCl by the electrolyte supply system (see Fig. 2.6) and the electrode was kept under potential control by the bipotentiostat. In order to check the quality of the copper surface, CVs and some STM images were recorded. Within the double layer regime chloride specifically adsorbs and forms a monolayer on the copper surface as shown in Sec. 3.4.2. When the quality of the chloride modified surface was affirmed, the supporting electrolyte was replaced by the working electrolyte containing viologen molecules which was also deoxygenated before use.

The potential where the working electrolyte exchanges the pure supporting electrolyte to initiate the viologen adsorption is called the initial potential. For the system of DBV "non-reactive" adsorption, the initial potential was chosen in the double layer or unreactive regime (from E = 0 to 100 mV vs. RHE). On the other hand, for the system of DBV "reactive" adsorption, the initial potential was chosen within the reduction peak P1 (transforming dication DPV^{2+} into the corresponding radical mono-cation $DPV^{\bullet+}$ species) from E = -130 to -250 mV vs. RHE (see Fig. 5.2).

4.4.2 DBV adsorption on HOPG

Although there is no pre-adsorption of halide on HOPG, the pure supporting electrolyte of 10 mM HCl was still used in order to unify the experimental conditions of DBV adsorption. The working electrolyte is a solution of 0.1 mM DBV in supporting electrolyte.

The electrochemical characterization of the viologens was also done by the use of an inert HOPG electrode. Since anions do not specifically adsorb on HOPG, the redox-chemistry of organic molecules can be studied in the absence of adsorbed anion layers. Furthermore, HOPG offers a potential window of -500 to 2200 mV vs. RHE that is significantly broader than that of the potential window of copper surfaces, thus allowing to study redox processes at even more positive potentials than accessible

with copper as electrode material. HOPG is simply prepared by peeling off graphite layers using an adhesive tape. After introducing HOPG into the electrochemical cell and to the aluminum chamber, the cell was filled with the supporting electrolyte and the reference CVs were then recorded. After the supporting electrolyte was replaced by the working electrolyte, CVs were also recorded to characterize some electrochemical properties of viologens and STM can then be applied to image the surface's sample.

Part III

“Non-reactive” adsorption of Viologens – Results and discussion

Chapter 5

DBV adsorption on chloride modified Cu(100) and on HOPG

5.1 Introduction

This chapter characterizes the adsorption behavior and surface redox-chemistry of DBV^{2+} that is adsorbed on an chloride modified Cu(100) electrode surface under non-reactive condition.

For this not only the cyclic voltammetry method averaging over the entire surface and the bulk solution is employed, but also STM as a structure-sensitive local probe technique providing direct access to structural changes within adsorbed viologen films in the course of electron transfer reactions.

As mentioned in the previous general part, there are three redox-states of DBV molecules: the dication DBV^{2+}, the radical mono-cation $DBV^{\bullet+}$ and the uncharged DBV^{0}. In normal form or in open circuit condition, DBV molecules exist as dicationic DBV^{2+} species even in solid salt form or in the electrochemical electrolyte. It was proven in the literature [4] that the standard electrode potentials are of $E^{0}(DBV^{2+}/DBV^{\bullet+})$ = -330 mV vs. RHE and $E^{0}(DBV^{\bullet+}/DBV^{0})$ = -548 mV vs. RHE for the first and the second electron transfer step, respectively. Therefore within the potential window of copper (about -450 to 250 mV), the first reduction of di-cationic DBV^{2+} to the corresponding radical mono-cationic $DBV^{\bullet+}$ species takes place, the second reduction can occur within the HER regime of copper substrate. Because of the massive hydrogen evolution reaction, the STM is not able to image the adsorption of uncharged DBV^{0} species, however for the first reduction, it is important to notice that the structures of the DBV adsorption layer depends strongly on the initial potential where the DBV^{2+} containing electrolyte is filled into the electrochemical cell. In this chapter, all adsorption experiments were performed under “non-reactive” potential conditions, i.e. the DBV^{2+} containing electrolyte was exposed at a double layer potential around 0 mV, far away from the DBV^{2+} reductive reaction regime.

5.2 Electrochemistry

5.2.1 CV of Cu(100) in DBV containing acidic solution

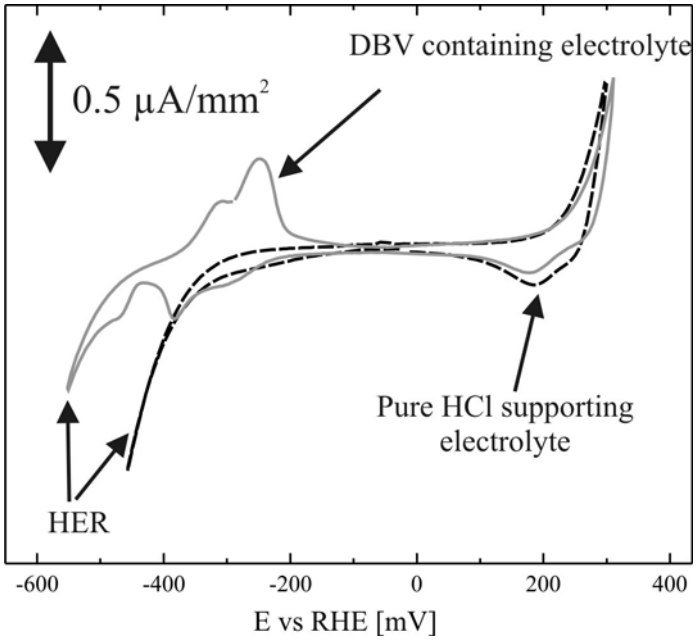

Figure 5.1: Black dotted curve: CV in the pure supporting electrolyte (10 mM HCl). Grey curve: CV of Cu(100) in the DBV^{2+} containing electrolyte (10 mM HCl, 0.1 mM $DBVCl_2$), dE/dt = 10 mV s^{-1}.

Fig. 5.1 shows representative steady-state CVs of Cu(100) in the absence (black dotted curve) and the presence (grey curve) of viologen species. The potential window of the Cu(100) electrode in the pure supporting electrolyte (10 mM HCl) is limited by two chemical reactions, the oxidative copper dissolution reaction (CDR) at the anodic limit and the reductive hydrogen evolution reaction (HER) at the cathodic limit.

After exchanging the pure supporting electrolyte for the one containing the redox-active DBV^{2+} species we observe drastic changes in the CV curve. The presence of the DBV^{2+} layer has impact also on the oxidative copper dissolution and the reductive copper deposition, i.e. the on-set potential of the dissolution reaction is shifted to higher potentials. However, this blocking effect is much less pronounced than that at the HER regime where there is a considerable shift of the HER ($\Delta E \approx$ -140 mV) towards lower potentials pointing to a pronounced inhibiting effect of viologens on the HER. Apparently, viologens are still present at the surface under these reductive conditions thereby blocking reactive sites for the HER such as substrate steps. If it is supposed that the DBV^{2+} exists as adlayer in the regime of copper

dissolution/redeposition and transforms into the corresponding radical mono-cation $DBV^{\bullet+}$ in the HER regime (see Secs. 5.3, 5.4), it can be concluded that 2D films of reduced viologen species block the copper substrate steps as the reactive sites for the hydrogen reduction/reoxidation reaction even more effective than the di-cationic species. It will be shown later that this is consistent with the molecular packing density of the respective layers.

A further deviation from the CV of the pure supporting electrolyte concerns the appearance of several anodic and cathodic current waves at potentials close to the HER regime. These additional current features have to be assigned to viologen-related redox processes. Typically, the shape of the CV in the presence of the viologen species depends strongly on the chosen cathodic potential limit. A precise correlation of the cathodic to the respective anodic current waves in the reverse potential scan is achieved by a systematic variation of the cathodic potential limit as shown in Fig. 5.2.

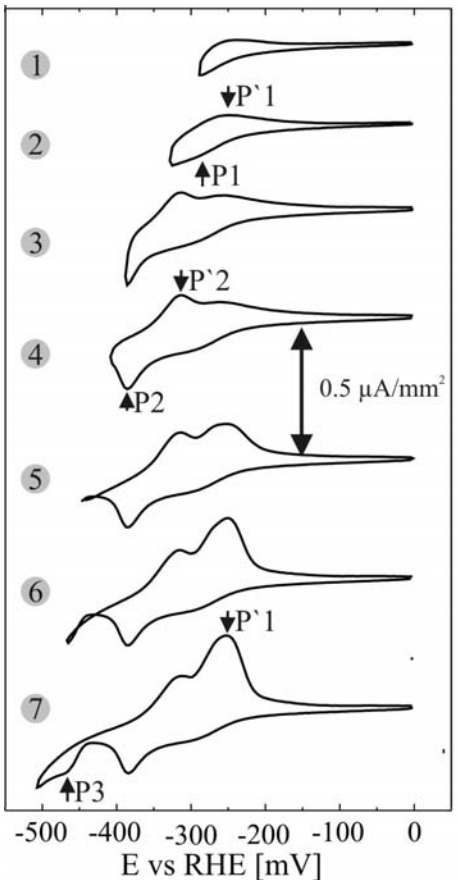

Figure 5.2: Appearance of anodic and cathodic current waves in the CV of Cu(100) in the DBV^{2+} containing electrolyte upon changing the cathodic potential limit

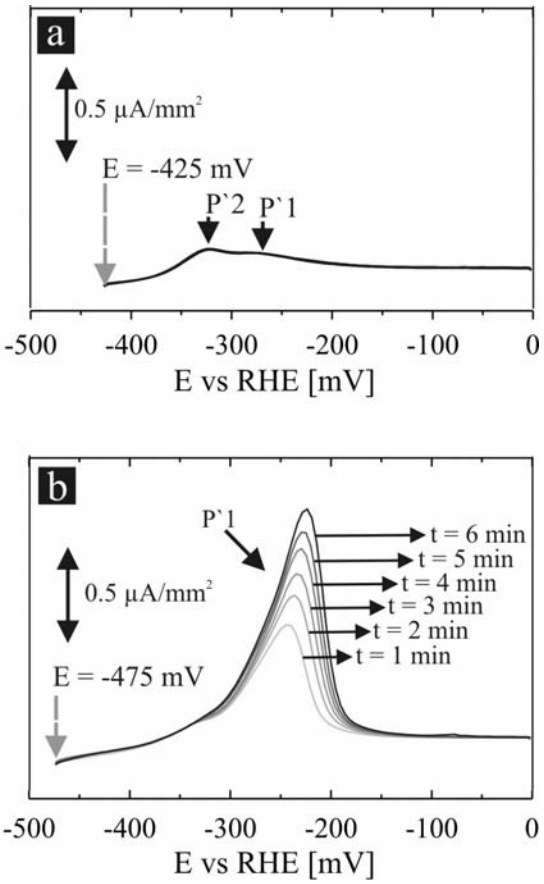

Figure 5.3: (a) Set of anodic potential sweep curves after holding the potential at E = -425 mV for 1 to 4 min, (b) Set of anodic potential sweep curves after holding the potential at E = -475 mV for 1 to 6 min, respectively.

By restricting the cathodic potential limit to E = -330 mV only the small peak pair P1/P'1 ($P1_{max}$ = -290 mV, $P'1_{max}$ = -260 mV) appears in the CV (CV2 in Fig. 5.2). Extending the potential limit further to E = -410 mV causes the appearance of P2/P'2 ($P2_{max}$ = -380 mV, $P'2_{max}$ = -318 mV, CV4 in Fig. 5.2) revealing a slightly greater hysteresis of ΔE = 62 mV than for peak pair P1/P'1. If the cathodic potential limit exceeds a critical value E = -430 mV we initiate not only the HER but also a further process related to the viologen redox-chemistry which is represented by P3. With the presence of P3, peak P'1 increases in line with the shift of the cathodic potential limit (CV5–7 in Fig. 5.2). Besides the potential hysteresis there is also another remarkable difference between P1/P'1, P2/P'2 on the one hand and P3 on the other hand as demonstrated in Fig. 5.4. In this experiment the potential scan was stopped in the cathodic potential sweep at E = –425 mV after passing P1 and P2 (Fig. 5.3a) and at P3, E = -475 mV (Fig. 5.3b), respectively. After a well defined hold-time at these potentials only the anodic potential scans were recorded. Obviously, there is no dependence of P'1 and P'2 on the potential hold time at E = -425 mV since all 4 curves (t_{hold}= 1–4 min) in Fig. 5.4a are identical. In contrast to that P'1 shows a strong dependence on the hold time at E = -475 mV (Fig. 5.3b). Peak height and the FWHM (full width at half maximum) increase with increasing hold time at E = -475 mV. Furthermore the peak maximum of P'1 is shifting towards higher potentials with increasing hold time. Now arises the question which reactions or processes relate to the peaks P1/P1', P2/P2', P3 and where the P'3 is.

The set of equations (from Eq. 4.1 to 4.6) describing the superposition of several processes involving "solution-" as well as "surface-limited" reactions now can be assigned more in detail for this system to:

1. The surface limited reduction/oxidation of pre-adsorbed viologen species according to:

$$\mathrm{DBV}^{2+}_{(\mathrm{ads})} + e^- \leftrightarrow \mathrm{DBV}^{\bullet+}_{(\mathrm{ads})} \tag{5.1}$$

$$2\,\mathrm{DBV}^{\bullet+}_{(\mathrm{ads})} \leftrightarrow \left[\mathrm{DBV}_2\right]^{2+}_{(\mathrm{ads})} \tag{5.2}$$

or even an oligomer or polymer formation at the surface according to

$$\mathrm{n\,DBV}^{\bullet+}_{(\mathrm{ads})} \leftrightarrow \left[\mathrm{DBV}_\mathrm{n}\right]^{\mathrm{n}+}_{(\mathrm{ads})} \tag{5.3}$$

2. The reduction/oxidation of viologen solution species according to:

$$\mathrm{DBV}^{2+}_{(\mathrm{aq})} + e^- \leftrightarrow \mathrm{DBV}^{\bullet+}_{(\mathrm{aq})} \tag{5.4}$$

which might be accompanied by the subsequent dimer-formation in solution according to:

$$2\,DBV^{\bullet+}_{(aq)} \leftrightarrow \left[DBV_2\right]^{2+}_{(aq)} \tag{5.5}$$

3. The film formation/dissolution of radical mono-cation chloride salts according to:

$$n\,DBV^{\bullet+}_{(aq)} + n\,Cl^- \leftrightarrow \left[DBV^{\bullet+}\,Cl^-\right]_n \downarrow \tag{5.6}$$

4. The second single electron transfer step transforms the radical mono-cation into the fully uncharged viologen species according to:

$$DBV^{\bullet+}_{(aq)} + e^- \leftrightarrow DBV^{0}_{(aq)} \tag{5.7}$$

It is known that the redox processes of solution DBV^{2+} on Cu(100) interfere with the redox processes of the preadsorbed species and related surface phase transitions. However, extra "prepeaks" that appear at potentials more positive than the main redox-current waves are not observed in this particular case. For example, spike-like prepeaks were reported for various dialkylated viologens interacting with Hg[105, 113, 114] or highly oriented pyrolytic graphite (HOPG)[105, 115, 116] electrode surfaces. This phenomenon was explained in terms of a Faradaic process of adsorbed viologen species coupled with 2D phase transitions between gaslike adsorption phases of the oxidized and more condensed 2D films of the corresponding reduced viologen species. The involvement of redox processes of solution species in the observed peak system P1/P1' can be clearly proven by concentration-dependent CV measurements. Peak current densities of P1/P1' scale up almost linearly with the viologen concentration in solution as predicted by the Randles-Sevcik equation [1] (Eq. 5.8).

$$J_p = -0.44nF\left(\frac{nF}{RT}\right)^{1/2} D^{1/2}\nu^{1/2}c_0A^{-1} \tag{5.8}$$

where J_p is the peak current density, D the viologen diffusion coefficient, ν the potential sweep rate, c_0 the viologen concentration in the bulk solution, A the area of the electrode surface, T the temperature, n the number of transferred electrons, F the Faraday constant, and R the gas constant.

Fig. 5.4 displays the concentration dependence of the peak pairs P1/P1' and P2/P2'. As long as we restrict the cathodic potential limit in the CV experiment to potentials of E > -425 mV, we only have to deal essentially with the first electron-transfer step of the viologen redox system, the quasi-reversible reduction of the dications (DBV^{2+}) to the radical monocations ($DBV^{\bullet+}$), and the corresponding oxidation reaction (Eq. 5.1).

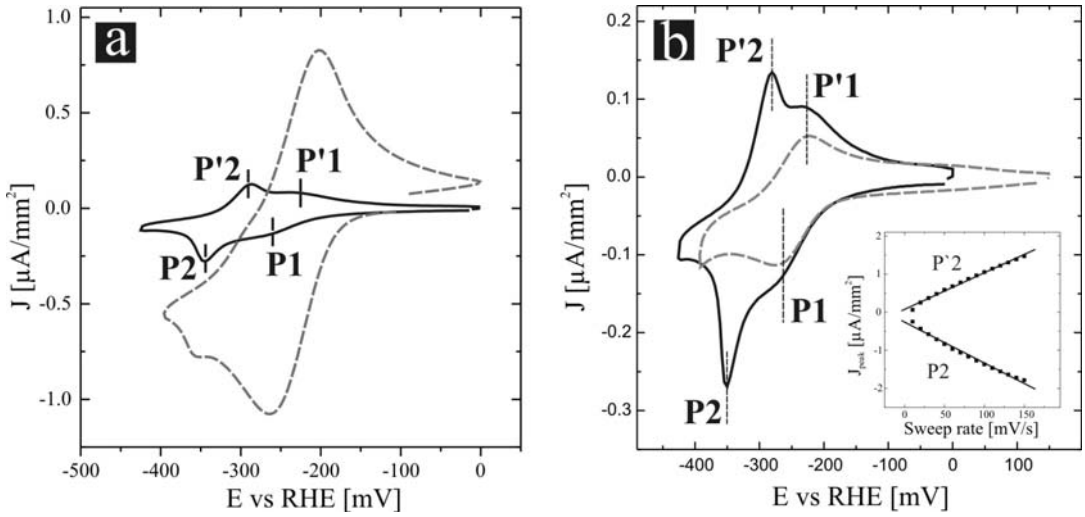

Figure 5.4: (a) CVs of Cu(100) in 10 mM HCl/0.1 mM $DBVCl_2$ (black line) and Cu(100) in 10 mM HCl/1 mM $DBVCl_2$ (grey dashed line), dE /dt = 10 mV s^{-1}, (b) CVs of Cu(100) in 10 mM HCl/0.1 mM $DBVCl_2$ (black line) and Cu(100) in 5 mM H_2SO_4/10 mM KBr/0.1 mM $DBVCl_2$ (grey dashed line), dE /dt = 10 mV s^{-1}. The inset shows the linear dependence of the peak current of P2/P2' on the potential sweep rate.

By increasing the viologen concentration by a factor of 10 in Fig. 5.4a, we noted an increase in the peak maximum of P1 from J_{P1} = -0.13 µA/cm² (black curve) to J_{P1} = -1.1 µA/cm² (gray dashed curve). The concentration dependence of P1/P1' indicates the dominance of bulk solution redox processes in the voltammetric behavior in the 10 mM HCl/1 mM $DBVCl_2$ solution. Therefore, we assign the peak system P1/P´1 to the reduction of di-cationic DBV^{2+} from solution to the corresponding radical mono-cationic $DBV^{\bullet+}$ species. Due to different conditions of the RHE reference electrodes the CVs reported here are shifted by -40 mV compared to those presented in reference [4].

At this point, it should be noted that the peak heights of P2/P2' are almost independent of the viologen concentration in solution. In the CV obtained for the 10 mM HCl/1 mM $DBVCl_2$ solution P2/P2' appears only as a small shoulder at the "cathodic" tail of the peak system P1/P1'. The peak positions of P2/P2' are slightly downward shifted in the 10 mM HCl/1 mM $DBVCl_2$ solution by about $\Delta E \approx 15$ mV. As it will be argued below we can attribute this effect to the slight increase of the chloride concentration (note that the DBV^{2+} is added as chloride salt to the solution). The use of even higher viologen concentrations, for example 10 mM HCl/10 mM $DBVCl_2$, leads to a complete suppression of the peak system P2/P2' due to the dominance of P1/P1'. In the following, we will discuss in detail the origin of the peak system P2/P2'. In particular, it will be demonstrated that these current waves do not correspond to the redox processes of any adsorbed or solution DBV species but to a quasi-reversible order-disorder transition coupled with chloride desorption

/adsorption processes through a condensed viologen monolayer film. A first experimental hint supporting this idea comes from a comparison of the voltammetric behavior of DBV in chloride and bromide containing electrolytes (Fig. 5.4b). Although bromide anions also form a c(2 x 2) adlayer on Cu(100) [57, 77, 78], the Cu-Br bond is stronger, and the bromide anions desorb from the electrode surface at more negative potentials [57]. While chloride desorption in 10 mM HCl starts already at E ≈ -300 mV (Fig. 5.1), bromide desorption takes place at potentials E < -350 mV, which is already within the regime of massive hydrogen evolution. Note that the observed downward shift of the bromide desorption potential is not only due to the stronger copper-halide interaction but it is also further promoted by the weaker trend toward solvation in the case of bromide compared to that of chloride anions. Assuming that P2/P2' (black curve in Fig. 5.4b) indeed involve chloride desorption/adsorption and related order/disorder transitions of the c(2 x 2) adlayer and following the reasoning above we would not expect such a pair of peaks for the bromide containing electrolyte, at least within the given potential range. The CV obtained for the bromide containing solution (grey dashed curve in Fig. 5.4b) reveals only the peak pair P1/P1' that corresponds to the electron-transfer reaction and there is no peak pair P2/P2' pointing to bromide desorption/ readsorption and related order-disorder transitions. Interestingly, the peak maxima of P1 and P1' are almost at the same potentials as those in the chloride containing electrolyte suggesting that in this particular case there is no significant impact of the nature of the halide counterion on the DBV redox potentials. This kind of anion effect on the viologen redox potentials is well known, for instance, from anions revealing electron donor capabilities [3, 4, 118]. A further observation pointing to a chloride desorption/adsorption process is the slight downward shift of P2/P2' by ΔE ≈ 15 mV when the chloride concentration is increased upon changing the DBV solution concentration. The inset in Fig. 5.4b indicates a linear dependence of the peak current density of P2/P2' on the potential sweep rate also suggesting that P2/P2' is most likely related to a surface process. Typically, the peak position of P2 is less affected by the sweep rate (dE/dt) than that of P2'. By increasing (dE/dt) from 5 to 150 mV/s, we observe a downward shift of only 12 mV for P2 while P2' reveals an upward shift of about 70 mV, suggesting that the latter process is even more hindered than the one represented by P2 (the graph not shown here).

A further electron-transfer reaction is not expected for the potential regime where P2/P2' appears in the CV. This becomes obvious from a comparison of CVs of Cu(100) in 10 mM HCl/1 mM $DBVCl_2$ obtained for two different cathodic limits (Fig. 5.5). Only if we decrease the cathodic potential limit, for example, from E = -395 mV (black curve in Fig. 5.5) to E = -630 mV (grey dashed curve in Fig. 5.5), we initiate the second electron-transfer reaction (see Eq. 5.7) that can be correlated with the appearance of P3 at E = -440 mV (cathodic sweep). The current features in the corresponding anodic potential sweep appear more complex.

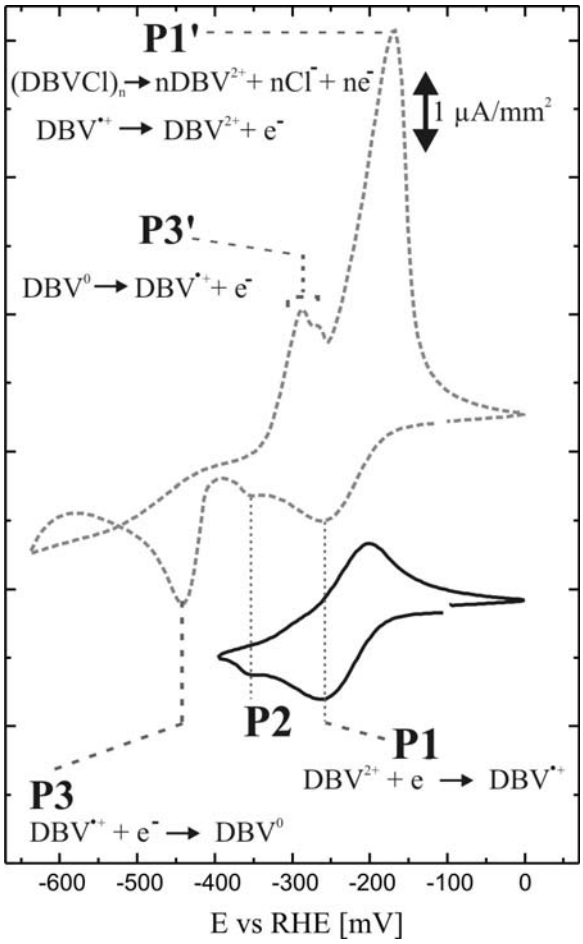

Figure 5.5: CVs of Cu(100) in 10 mM HCl/1 mM $DBVCl_2$, dE /dt = 10 mV s^{-1}.

The CV in high concentration of DBV containing electrolyte in Fig. 5.5 interestingly reveals the peak P3' which appears very close to the chloride readsorption surface peak P'2 (see Fig. 5.4a). By increasing the concentration, the intensity of the solution peak system P3/P'3 increase while the surface peak system P2/P'2 of the chloride desorption process remains unchanged, indicating that the peak P'3 is concealed by P'2 for the low concentration CVs (Fig. 5.2). The peak system P3/P'3 corresponds to the reoxidation of the uncharged species to the corresponding radical monocations (Eq. 5.7). The huge peak P1' has been assigned to the oxidation of the radical monocations from the $(DBV^{\bullet+} + Cl^-)_n$ precipitate that is most likely formed upon the conproportionation reaction between the uncharged DBV^0 formed below E = -440 mV and the dicationic DBV^{2+} solution species [3, 4]. Recent experiments evidenced that at potentials below E = -475 mV a colored film appears at the surface, most likely due to the precipitation of the radical mono-cationic chloride salt (Eq. 5.6) as a consequence of massive reduction of $DBV^{2+}_{(aq)}$ solution species (Eq. 5.4). Hence, the increasing of P'1 of CV5-7 in Fig. 5.2 might be associated with the oxidation of that film.

5.2.2 CVs of HOPG in DBV containing acidic solution

The HOPG potential window regime extends broadly from about -800 mV to +2300 mV. Since the reduction and oxidation processes of dicationic DBV^{2+} and radical mono-cationic $DBV^{\bullet+}$ species take place within the copper potential window regime (from about -500 mV to +200 mV) in this part we focus on CV current waves of the DBV redox behavior on HOPG in comparison with those on Cu(100). All CVs are kept at anodic potential limit of 150 mV despite the very broad potential window of HOPG substrate because there are no DBV redox processes at potentials higher than that limit.

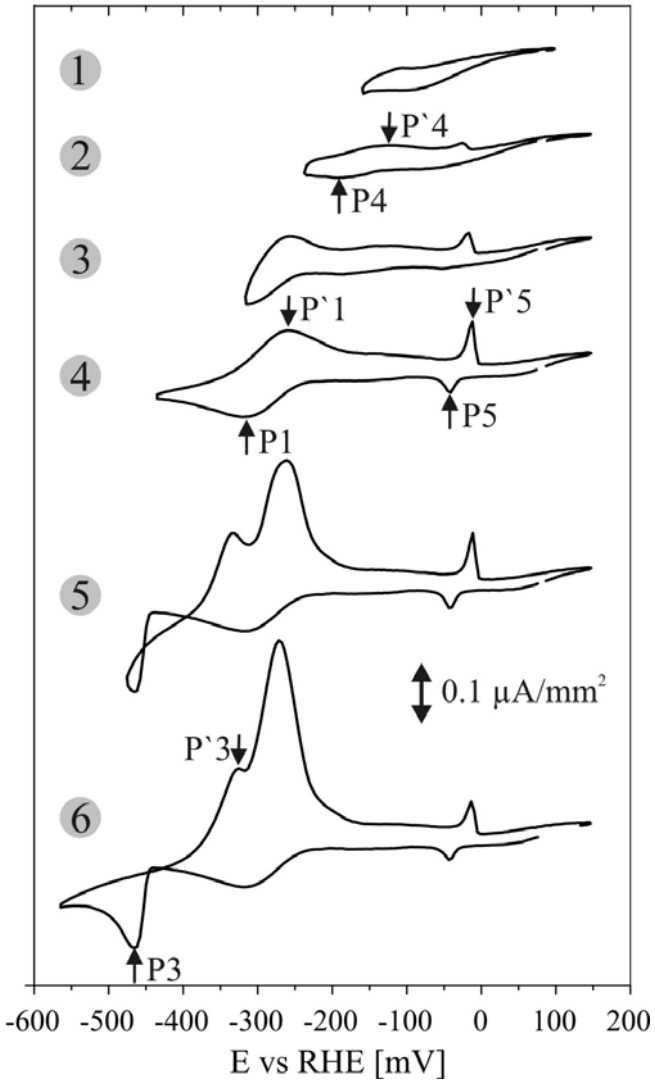

Figure 5.6: Appearance of anodic and cathodic current waves in the CV of HOPG in a DBV^{2+} containing electrolyte (10 mM HCl, 0.1 mM $DBVCl_2$) upon changing the cathodic potential limit, $dE/dt = 10\ mV\ s^{-1}$

The measurement started with the 10 mM HCl supporting electrolyte, then the 10 mM HCl/0.1 mM $DBVCl_2$ solution was added (the concentration of DBV was chosen the same as in the copper case). After exchanging the pure supporting electrolyte for the one containing the redox-active DBV^{2+} species we observe drastic changes in the CV curve. Typically, the shape of the CV in the presence of the viologen species depends strongly on the chosen cathodic potential limit. A precise correlation of the cathodic to the respective anodic current waves in the reverse potential scan is achieved by a systematic variation of the cathodic potential limit as shown in Fig. 5.6.

The CV4 and CV6 in Fig. 5.6 have quite similar shapes and peak pair potentials to the corresponding CVs of the Cu(100) substrate in Fig. 5.2. Therefore, we assume that similar to the Cu(100) substrate, the peak pair system P1/P'1 relates to the reduction of di-cationic DBV^{2+} to the corresponding radical mono-cationic $DBV^{\bullet+}$ species and the reverse reoxidation, and peak pair P3/P'3 corresponds to the reduction of the radical monocations to the uncharged species and the reverse reoxidation. Moreover, the huge peak P1' in CV6 has been also assigned to the oxidation of the radical monocations from the $(DBV^{\bullet+} + Cl^-)_n$ precipitate that is most likely formed upon the conproportionation reaction between the uncharged DBV^0 formed and the dicationic DBV^{2+} solution species (like in Fig. 5.5). Noted that HOPG is an inert surface, chloride cannot adsorb to form an anion adlayer as in the case of Cu(100), thus it does not exist the peak pair P2/P'2 of chloride desorption/readsorption in the CVs of HOPG substrate.

However, CVs of DBV on HOPG appear more complex than in the case of the copper surface. By restricting the cathodic potential limit to E = -240 mV, the potential within the double layer regime of DBV on copper, the CV2 on HOPG shows a small peak pair P4/P'4 ($P4_{max}$ = -193 mV, $P'4_{max}$ = -120 mV) with the potential hysteresis of ΔE = 73 mV. The CV2 also reveals a new oxidation peak P'5 whose pair peak will appear more obvious after sweeps to more cathodic potentials. The presence of peak pair P4/P'4 and P5/P'5 was not observed on the copper substrate. The underlying processes are not understood yet. Even the STM results in the last part of this chapter do not help in interpreting these processes. Therefore, in the framework of this thesis, the origin of these two pair peaks remains still unknown.

Extending the potential limit further to E = -410 mV causes the appearance of P1/P'1 (CV4 in Fig. 5.6). As mentioned above, the peak pair corresponds to the reduction of di-cationic DBV^{2+} to the corresponding radical mono-cationic $DBV^{\bullet+}$ species and the reverse reoxidation because of its similarity to the case of the copper substrate. It also has the $P'1_{max}$ = -260 mV, however $P1_{max}$ is at more negative potential, i.e. -320 mV, in spite of -290 mV on copper, indicating the weaker interaction of DBV to the inert HOPG substrate. At this cathodic potential limit, the peak pair P5/P'5 appears completely with $P5_{max}$ = -41 mV, $P'5_{max}$ = -12 mV in CV4 of

Fig. 5.6. Due to the fact that the peak pair does not always appear in every CV measurements, the origin of the peak pair P5/P'5 is still unclear.

In a more cathodic scan, reaching close to HER on HOPG, the CV6 reveals the peak pair P3/P'3 similar to the copper substrate with the exact value $P3_{max}$ = -466 mV which is very close to that on Cu(100). Therefore, the peak P3 is also assigned to the second reduction of DBV from the radical cation $DBV^{\bullet+}$ species to the uncharged DBV^0 molecules. Notice that on Cu(100) the small oxidation peak P'3 is superimposed on the chloride readsorption peak P'2 causing an unclear appearance, on the other hand on HOPG the P'3 appears clearly (without the presence of P'2) with $P'3_{max}$ = -325 mV.

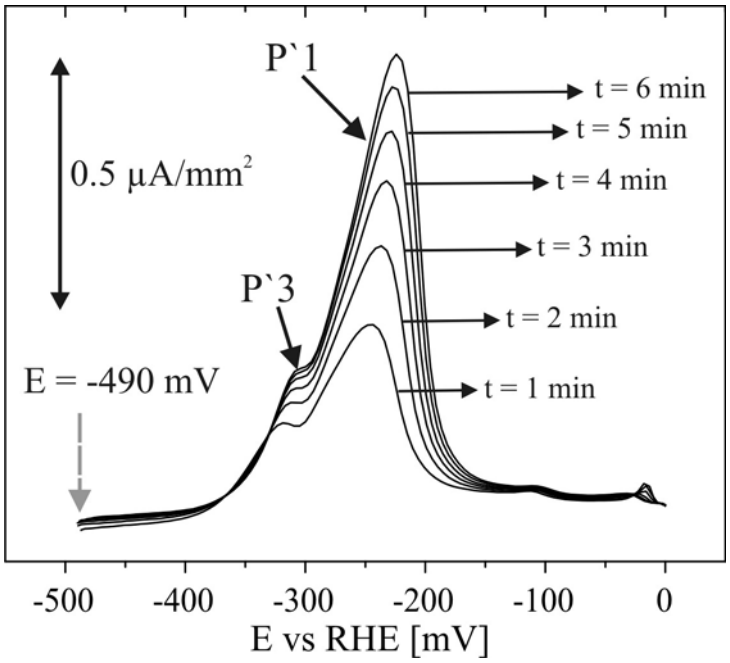

Figure 5.7: Appearance of anodic and cathodic current waves in the CV of HOPG in the DBV^{2+} containing electrolyte upon changing the cathodic potential limit.

Repeating the experiment by stopping the cathodic potential scan after passing P3 (chosen value E = -490 mV), and then changing the hold-time, the same trend is observed similar to that in the case of the copper surface. Peak heights and the FWHMs (full width at half maximum) of both P'3 and P'1 increase with increasing hold time at E = -490 mV. And the peak maximum of these two peaks is also shifting towards higher potentials with increasing hold time simultaneously. Thus, one can conclude that the massive reduction of $DBV^{\bullet+}$ species to DBV^0 forming a thick colored film of an adsorbed multilayer can not only take place on an active copper substrate but also on an inert substrate like HOPG.

5.3 Structural determination

Following the discussions in the previous part, the electrochemical characteristics of DBV adsorption on Cl modified Cu(100) can be divided into four regimes within the Cu potential window. They are listed below according to the potential from positive to negative regimes:

1. The adsorption of the dication DBV^{2+} at the CDR where the Cu dissolution reaction takes place causing the change of surface morphology.
2. The adsorption of dicationic DBV^{2+} on the Cl modified Cu(100) template at the potential regime from CDR until reaching P1 (reduction peak transforming the dication DBV^{2+} into the radical cation $DBV^{\bullet+}$ species), where STM images show a so-called cavitand phase.
3. The adsorption of radical cations $DBV^{\bullet+}$ on the Cl modified Cu(100) template at the potential regime after passing P1 until reaching P2 (chloride desorption process), where STM images reveal a stripe phase.
4. The adsorption of an amorphous radical cation $DBV^{\bullet+}$ phase on the Cl modified Cu(100) template at the potential regime after passing P2 to further negative potential at HER.

Each regime has its own characteristics of redox behavior and structural surface morphology. Within the boundaries of these regimes they reveal changes of structures or phase transitions. The adsorption structures of DBV species at these regimes will be described in the following sub-parts and the phase transitions among these structures will be then discussed in the next part.

5.3.1 Cavitand phase

The exposure of a chloride-modified Cu(100) surface to the DBV^{2+} containing electrolyte within the double-layer potential regime leads instantaneously to the adsorption and subsequent lateral ordering of DBV^{2+} species at the surface. Surface morphology and molecular structure in the presence of DBV_{ads}^{2+} are displayed in Fig. 5.8. Obviously, the DBV_{ads}^{2+} phase has no significant impact on the surface morphology which remains governed by the interaction of the specifically adsorbed chloride anions with the underlying copper lattice. In the presence of the DBV^{2+} adlayer the copper steps are still oriented parallel to the substrate [100] directions and thus parallel to the main symmetry axes of the chloride c(2 x 2) phase (Fig. 5.8a). The DBV_{ads}^{2+} adlayer occurs in two mirror-domains denoted as I and II and each domain forms a “checker-board” structure (Fig. 5.8a).

The structure of the DBV^{2+}_{ads} adlayer was investigated and described in detail in the doctoral thesis of C. Zörlein [5]. It can be summarized as follows.

Four DBV^{2+} molecules build up one single square-shaped molecular assembly with a cavity in the center. Therefore, the structure has been called "cavitand" phase. Occasionally, some isolated molecular assemblies consist of only three (arrow in Fig. 5.8b) instead of four of these rod-shaped subunits. Even single subunits can occasionally be observed within the DBV^{2+} adlayer.

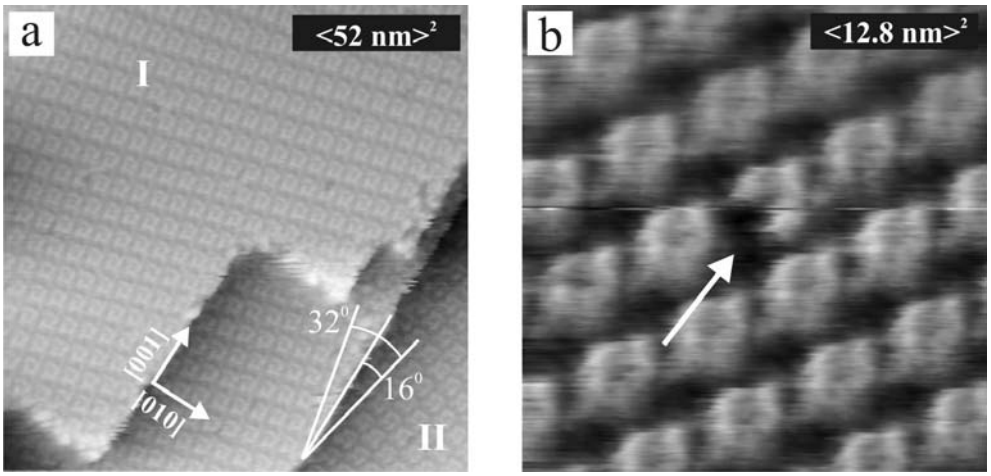

Figure 5.8: Surface morphology and surface structure of Cu(100) in the presence of DBV^{2+}_{ads}, (a) I_t = 0.25 nA, U_b = 174 mV, E = -135 mV; (b) I_t = 0.1 nA, U_b = 390 mV, E = 0 mV.

The structural relation of the DBV^{2+}_{ads} adlayer to the chloride lattice underneath could be achieved by a careful variation of the tunneling conditions. While under moderate tunneling conditions (high bias voltage, low tunneling current) the covering viologen film is imaged, the underlying chloride lattice becomes visible by applying more drastic tunneling conditions (low bias voltage, high tunneling current). In this latter case the tunneling tip penetrates into the organic film which leads to the local removal of viologen molecules upon scanning. These kinds of experiments suggest an interaction between the viologen film and the chloride lattice which is weaker than the chemisorptive Cu-Cl interaction. Note, the chemisorbed chloride layer cannot be removed by the tunneling tip. And the graphical superposition of two STM images showing the cavitand structure of the DBV^{2+}_{ads} film and the chloride lattice underneath is presented in Fig. 5.9a,b. With the c(2 × 2)-Cl phase serving as internal calibration lattice the DBV^{2+}_{ads} unit-cell can be described either by a transformation matrix according to

$$\begin{pmatrix} a_{vio} \\ b_{vio} \end{pmatrix} = \begin{pmatrix} 2 & 7 \\ \overline{7} & 2 \end{pmatrix} \begin{pmatrix} a_{Cl} \\ b_{Cl} \end{pmatrix}$$

or in Wood-notation by a ($\sqrt{53} \times \sqrt{53}$)R15.9° unit-mesh with lattice constants of $|\vec{a}| = |\vec{b}|$ = 2.6 nm ± 0.02 nm enclosing an angle of 90° ± 2° (see model in Fig. 5.9c). Alternatively, the two-dimensional DBV^{2+}_{ads} array can be directly related to the copper substrate assuming a ($\sqrt{106} \times \sqrt{106}$)R29.05° unit-mesh or a matrix transformation according to

$$\begin{pmatrix} a_{vio} \\ b_{vio} \end{pmatrix} = \begin{pmatrix} 5 & 9 \\ \bar{9} & 5 \end{pmatrix} \begin{pmatrix} a_{Cu} \\ b_{Cu} \end{pmatrix}$$

This results in a DBV^{2+}_{ads} surface coverage of Θ = 0.075ML with respect to the intermediate chloride c(2 x 2) layer or Θ = 0.0375 ML with respect to the copper substrate.

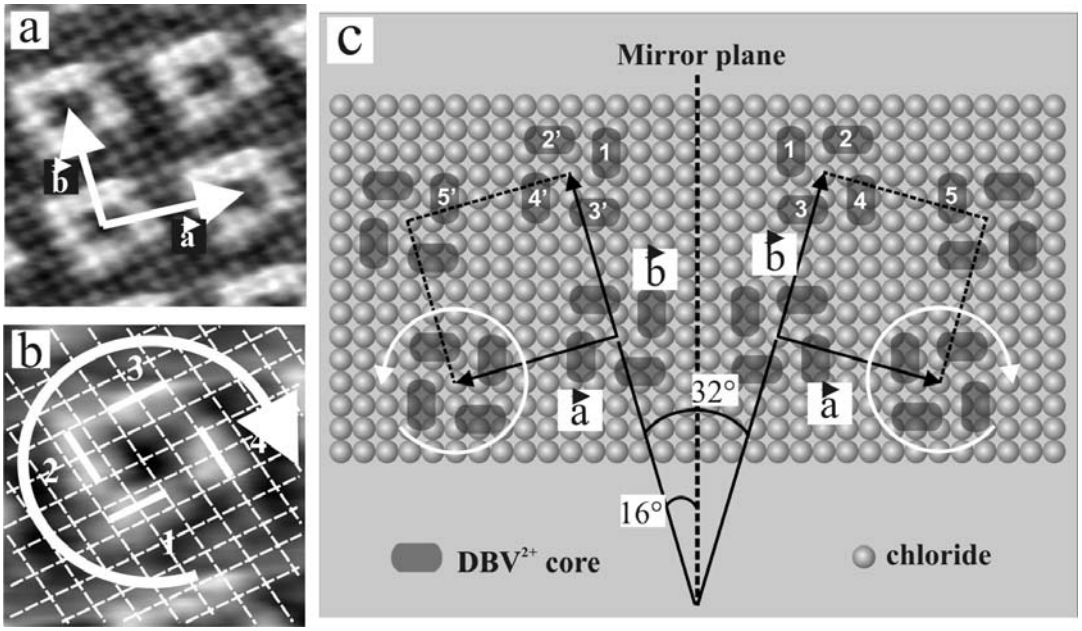

Figure 5.9: (a) "Transparent" superposition of the atomically resolved chloride lattice with the DBV^{2+}_{ads} adlayer, $(5.6\ nm)^2$; (b) circular chirality of the DBV^{2+}_{ads} cavitand ensemble indicated by the white arrow; the white grid represents the chloride lattice, $(3.1\ nm)^2$, I_t = 0.25 nA, U_b = 86 mV, E = +50 mV; (c) tentative structure model of the cavitand phase reflecting the STM imaging contrast [5].

The cavitand phase structure model explains the unit cell of the DBV^{2+}_{ads} adlayer with respect to the lattices underneath and even predicts the chirality of the DBV^{2+}_{ads} cavitand ensembles which was actually proved by STM observations. However, following the structure model (Fig. 5.9c) one can see that the space between cavitand ensembles is large enough to absorb more species. And as reported by Zörlein, apart from this cavitand-like structure motif, STM images sometimes show further visible

satellite spots between the cavitands which, however, appear only under certain tunneling conditions and their origin is still under discussion. One reasonable explanation assumes further adsorbed DBV^{2+}_{ads} species residing in different adsorption sites and geometries than those constituting the cavitand ensemble. An alternative interpretation assumes a further co-adsorption of anions and/or water molecules within the viologen layer as origin of the satellite spots in the STM experiment. The aim of the following explanations is to answer this question.

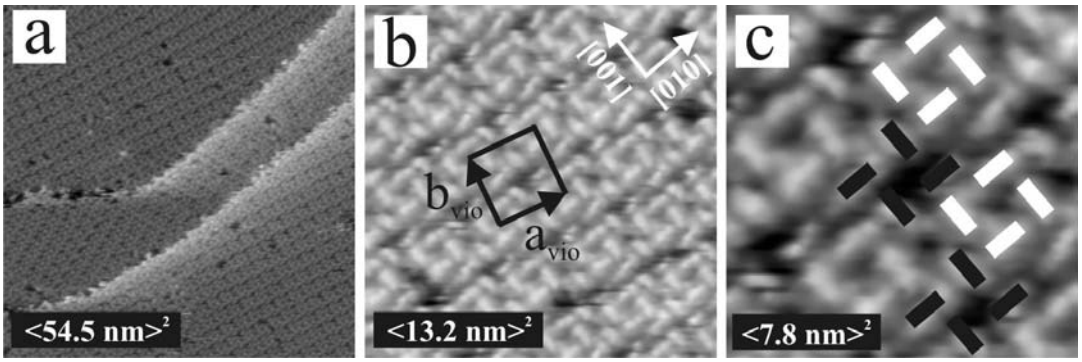

Figure 5.10: Cavitand DBV^{2+}_{ads} phase adsorbed on the c(2 x 2)-Cl/Cu(100) surface: (a)-(c) I_t = 1.1 nA, U_b = 350 mV, E = -150 mV.

Most of the STM measurements were carried out under normal tunneling condition showing the cavitand phase as seen in Fig. 5.8 which agrees with the structure model in Fig. 5.9c. However, under different tunneling condition or in some specific cases, STM images reveal some different structures. As one such example, Fig. 5.10 shows STM results of a cavitand DBV^{2+} phase with different resolutions. As we can see, besides the cavitand-like ensembles marked by 4 white lines in Fig. 5.10c, there are also other ordered adsorbed species (satellites) marked by black lines. From this STM result, the satellites look a little bit different from DBV^{2+}_{ads} molecules concerning their size and brightness. The following STM images, however, will prove that these satellites are also DBV^{2+}_{ads} molecules.

Fig. 5.11 shows two STM images of the cavitand phase at the same area (the defect is marked with the white circle), under the same potential control, but with different tunneling conditions (inverted bias voltage). The structure of DBV^{2+}_{ads} in Fig. 5.11a under normal tunneling condition is the cavitand-like phase as seen by Zörlein [5]. However, by inverting the bias voltage, the STM image changes to Fig. 5.11b with satellites similar to Fig. 5.10c. Therefore, it can be concluded that the well-ordered satellites are present even when the surface is observed as a normal cavitand-like phase. The STM images in Fig. 5.11 also lead to the fact that by inverting the bias

voltage, some of the molecules on the metal surface can be imaged inversely due to the electronic interaction between their orbitals and the STM tip.

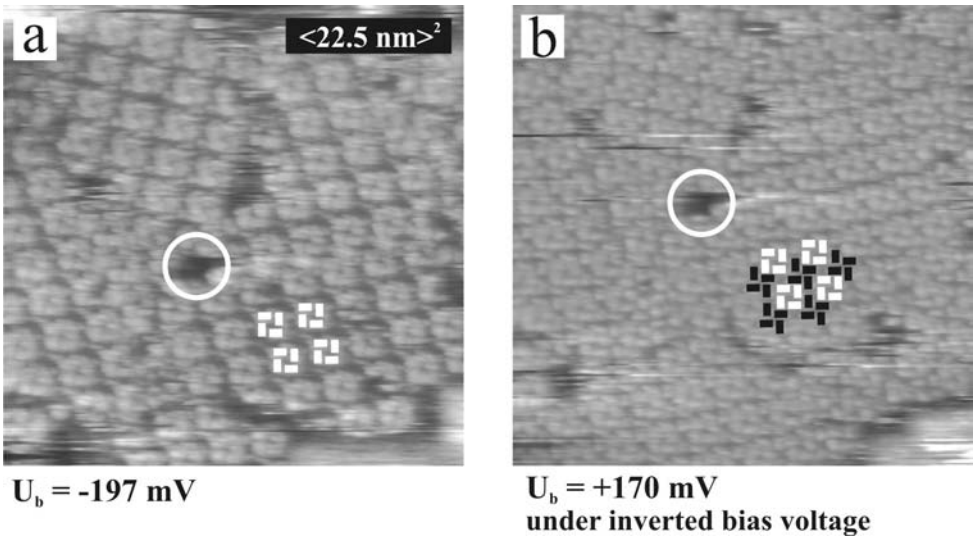

Figure 5.11: Structure of cavitand phase under different tunneling conditions, E = +10 mV, a) It = 0.3 nA, Ub = -197 mV; b) I_t = 0.4 nA, U_b = +170 mV,

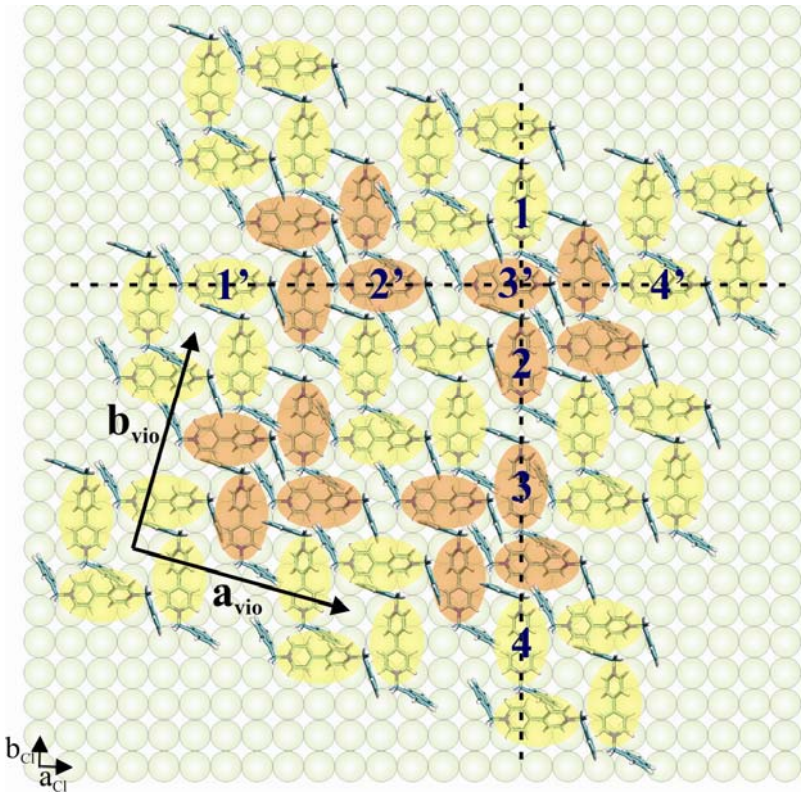

Figure 5.12: New structure model of the cavitand phase

With the new structure of DBV_{ads}^{2+} adsorbed on c(2 x 2)-Cl/Cu(100) which has been seen in Figs. 5.10 and 5.11b, a new structure model is proposed as shown in Fig. 5.12. This model has the same unit cell as Safarowsky's. The improvement is that besides the groups of four molecules building a cavitand ensemble (brighter group), there are also groups of four other molecules in the space between the cavitands (darker group). Obviously, in order to fit into this small space, the molecules of the dark groups gather in a different order than in the bright cavitand group. This model is based on the assumption of knowing the correlation between DBV_{ads}^{2+} and the chloride lattice underneath. It assumes that the bipyridine group of DBV_{ads}^{2+} molecules is packed parallel to the [100] direction of c(2 x 2)-Cl layer. Therefore a DBV^{2+} molecule can absorb between two adjacent chloride atom rows. From this assumption and the description of the model in Fig. 5.12, one can observe that DBV^{2+} molecule in adjacent dark and bright groups have to be aligned as exemplified by the molecules 1 - 4 and 1' - 4' in Fig. 5.12. If the condition above cannot be guaranteed, the ordering of the DBV_{ads}^{2+} adlayer will be affected. Following the new model, we determine a DBV_{ads}^{2+} surface coverage of about Θ = 0.15 ML with respect to the chloride lattice or Θ = 0.075 ML with respect to the bare Cu(100)-(1 × 1). The area required for each $DBV_{ads}^{\bullet+}$ molecule on c(2 x 2)-Cl/Cu(100) amounts to 0.864 nm^2. The surface coverage amounts to twice that proposed by Zörlein [5].

This new model can be supported even further by the following STM results concerning translational domain boundaries of the cavitand phase.

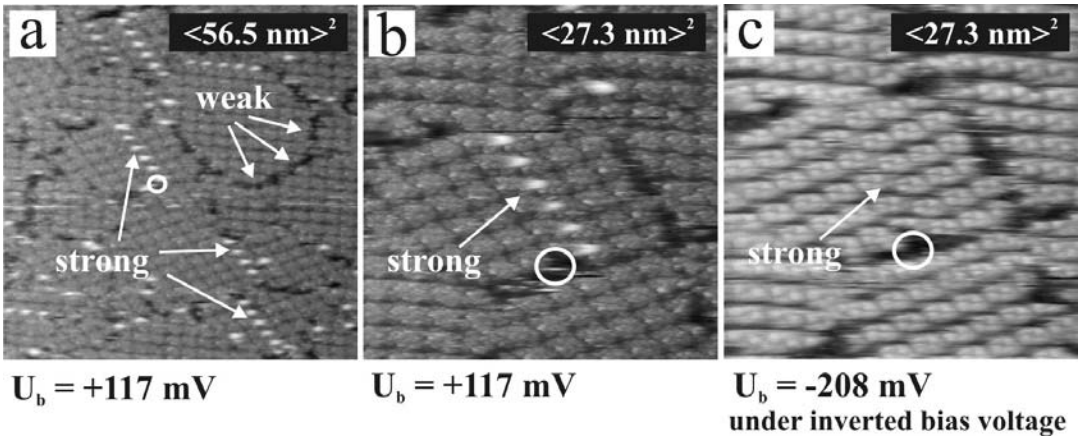

Figure 5.13: The two types of translational domain boundaries of the cavitand phase.

The STM image of Fig. 5.13a shows a full DBV_{ads}^{2+} mono-adlayer on c(2 x 2)-Cl/Cu(100), revealing two typical distinct translational domain boundaries: one with bright dots along the boundary which is quite stable within a definite potential regime, thus called strong domain boundary, and on the contrary, one with hollows or

defects between domains which is much less stable, therefore called weak domain boundary. The instability of the weak domain boundary can be seen in Fig. 5.14 at which the DBV^{2+} molecules are quite mobile causing the movement of the weak boundary under the same electrochemical control. It is impossible to observe such movement with the strong domain boundary.

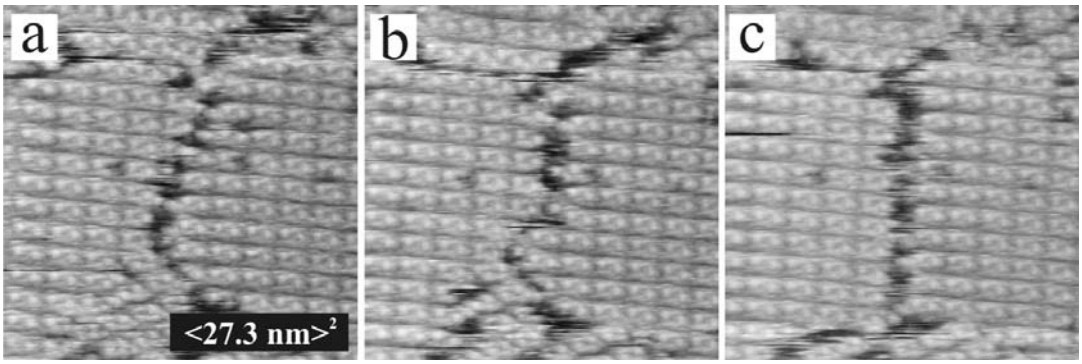

Figure 5.14: STM series showing the dynamics of DBV^{2+} molecules at a "weak" translational domain boundary, I_t = 1.1 nA, U_b = -209 mV, E = +36 mV.

It is noteworthy that in Fig. 5.14, the dynamics of the weak domain boundary takes place at high positive potential of 36 mV where the viologen molecules are supposed to be more active at the surface. And the DBV^{2+}_{ads} cavitand phase within domains tends to attain a more ordered structure so that the weak domain boundary becomes more and more straight.

Interestingly, by inverting the bias voltage, the bright dots along strong domain boundaries disappear (see Fig. 5.13b,c). This raises the big question "what are the bright dot?". Only using the new structure model of the cavitand phase, we can interpret the nature of the two translational domain boundaries.

As mentioned above, there is such a condition that DBV^{2+} molecules form ordered assemblies, such that there is straight alignment of DBV^{2+} molecules along and between two adjacent chloride rows. Note that only one DBV^{2+} molecule can be fitted in a chloride row, and in the same domain, DBV molecules align as indicated in Fig. 5.12, therefore there are only two possibilities for alignment between two adjacent domains: shifted by two chloride rows ("even-shift") e.g. between domain I and II in Fig. 5.15 (see dotted lines) or shifted by an odd number (1 or 3) of chloride tows ("odd shift"), e.g. between domain I and III in Fig. 5.15. From the model, we can see, at even shift, the space at the domain boundary is large enough so that each group of four molecules at the domain boundary can share one molecule. The bipyridine groups of the two shared molecules at a domain boundary of "even shift" are closer than within the domain, resulting in a bright dot in the STM image and forming a stable and "strong" domain boundary. On the other hand, the odd

alignment cannot meet the distance condition to form a strong enough interaction, therefore this domain boundary is "weak", consisting of spaces of bare chloride layer, thus DBV^{2+} molecules at this boundary should be much more mobile and easy to remove. And there are only these two translational domain boundary types in DBV^{2+} adsorption on chloride modified Cu(100) substrate.

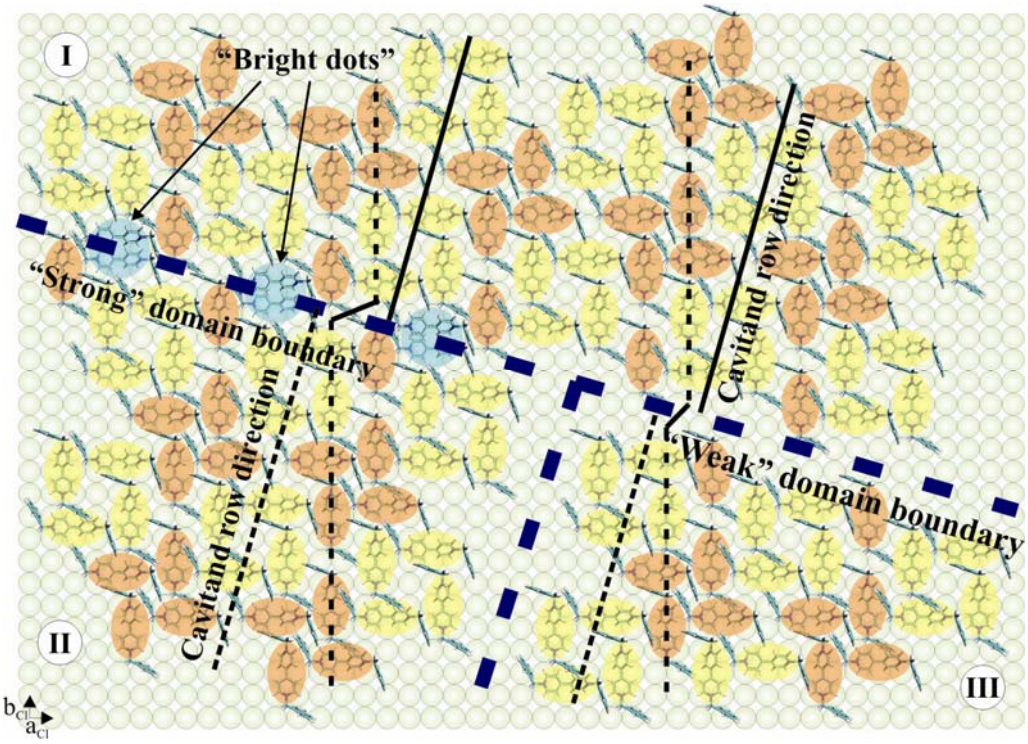

Figure 5.15: Schematic drawing of DBV^{2+} adsorbed on c(2x2)-Cl/Cu(100), showing the difference between the "strong" and "weak" translational domain boundaries.

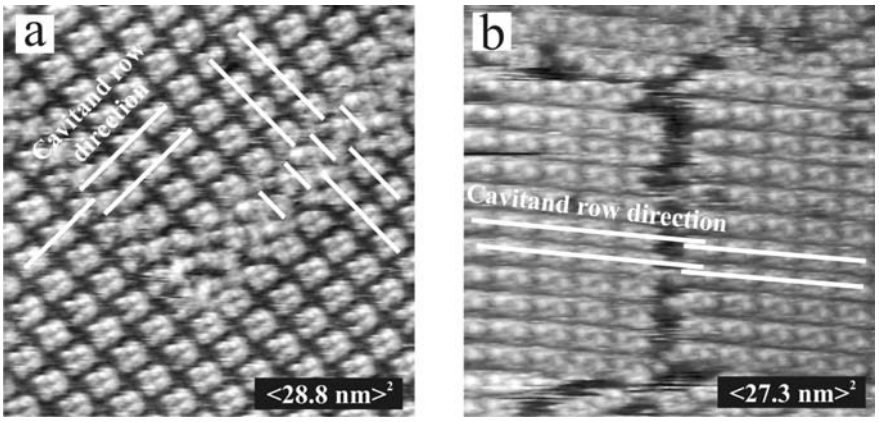

Figure 5.16: STM images showing two types of translational domain boundaries corresponding to a shift between two domains of the DBV^{2+} cavitand phase, (a) "strong" domain boundaries, I_t = 0.3 nA, U_b = 214 mV, E = -141 mV, (b) "weak" domain boundaries, I_t = 1.1 nA, U_b = -209 mV, E = +36 mV.

Fig. 5.16 displays the shift between two domains determining the characteristics of the domain boundary. An “odd shift” appears in Fig. 5.16b corresponding to a weak domain boundary. And an “even shift” appears in Fig. 5.16a resulting in a strong domain boundary. Fig. 5.16a also includes the realization of two adjacent strong domain boundaries.

This part discussed the structural behavior of DBV adsorption at potentials more positive than needed for the reductive reaction. The next part will focus on the same aspect but in the potential regime after passing the reduction peak P1 (see Fig. 5.2), i.e. the structure of the $DBV_{ads}^{\bullet+}$ species.

5.3.2 Stacking phase

Passing P1 of CV2 in Fig. 5.2, the reduction of DBV_{ads}^{2+} to $DBV_{ads}^{\bullet+}$ is complete. The surface morphology of adsorbed $DBV_{ads}^{\bullet+}$ is shown in Fig. 5.17, i.e. the stripe pattern of the stacking phase. The gross surface morphology is still dominated by substrate steps that are parallel to the [100] directions (Fig. 5.17). The presence of the viologen adlayer apparently gives rise to an additional increase of the activation barrier for the chloride desorption. From these results it becomes evident that the electron transfer from the metal to the redox-active species occurs through the “inner Helmholtz plane” of specifically adsorbed chloride anions (Fig. 5.17).

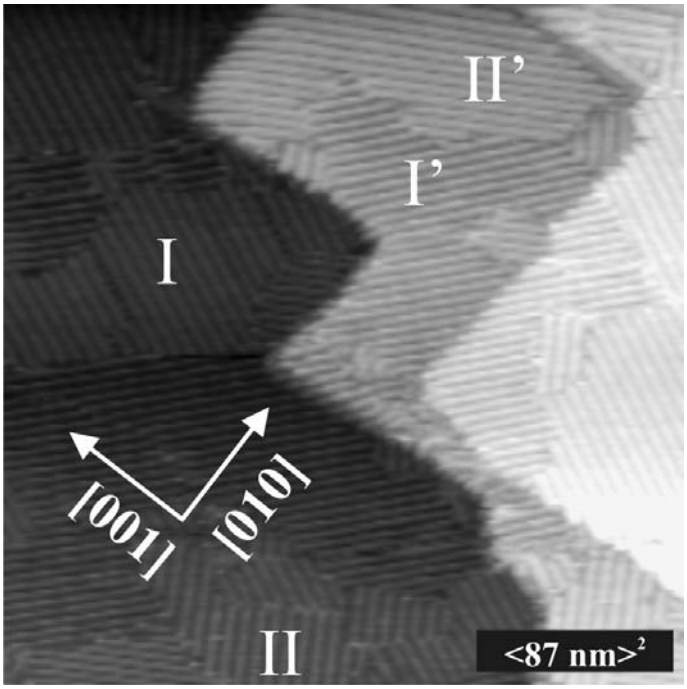

Figure 5.17: Surface morphology of the stacking phase on c(2 x 2)-Cl/Cu(100), I_t = 0.4 nA, U_b = 176 mV, E = -321 mV.

On a mesoscopic length scale, these $(DBV^{\bullet+}_{ads})_n$ polymer chains arrange themselves into extended rotational and mirror domains (Fig. 5.17). Individual $DBV^{\bullet+}_{ads}$ molecules within the $(DBV^{\bullet+}_{ads})_n$ oligomer and polymer chains are often imaged as elongated "discs" with an intermolecular spacing of 3.6 ± 0.2 Å within and 1.82 nm between adjacent $(DBV^{\bullet+}_{ads})_n$ chains (Fig. 5.18a). However, the particular imaging contrast sensitively depends on the applied tunneling conditions. A selective imaging of the more conductive bipyridinium redox-centers is obtained in Fig. 5.18b. The structural correlation to the chloride lattice is achieved by the local removal of the viologen layer upon scanning under drastic tunneling conditions (Fig. 5.18c).

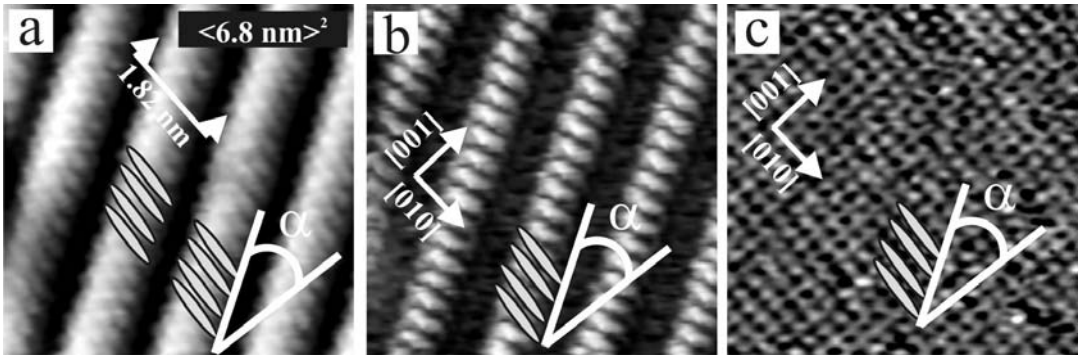

Figure 5.18: Structural correlation between the stacking phase and the c(2 x 2)-Cl/Cu(100) lattice underneath by a systematic variation of the tunneling conditions, (a) I_t = 0.2 nA, U_b = 93 mV, E = -200 mV; (b) I_t = 40 nA, U_b = 28 mV, E = -200 mV; (c) I_t = 9 nA, U_b = 1 mV, E = -130 mV

For the stacking phase we propose in Fig. 5.19 a structure model for only one of the possible mirror domains with individual $DBV^{\bullet+}_{ads}$ molecules residing with their main molecular axes parallel to the surface in a side-on adsorption geometry. The stripe propagation direction encloses a characteristic angle of α = 37° with one of the main symmetry axes of the chloride lattice. The bright stripes in Figs. 5.18a, b are assigned to bipyridinium cores arranged in an almost face-to-face orientation. Benzyl groups are expected to lie within the dark ditches revealing a reduced STM imaging contrast. Essential for the formation of such a 1D polymer chain with a nearest neighbor distance of only 3.6 ± 0.2 Å is the almost planar conformation of the bipyridinium cores in the reduced state. A dihedral-angle of Φ = 40.1° as predicted for the DBV^{2+} species (Fig. 4.4) would not allow such a small intermolecular distance within the 1D polymer chain. A further sterical requirement for the stabilization of the 1D polymer chains consists in the slight side-shift of adjacent $DBV^{\bullet+}_{ads}$ molecules and explains the slight deviation from an ideal face-to-face arrangement. As a consequence of that, the propagation direction of the 1D polymer chain is not exactly perpendicular to the main molecular axes of the $DBV^{\bullet+}_{ads}$ molecules (Figs. 5.18 and 5.19) but rotated by an angle α. On c(2 x 2)-Cl/Cu(100) we determine a $DBV^{\bullet+}_{ads}$

surface coverage of about Θ = 0.2 ML with respect to the chloride lattice or Θ = 0.1 ML with respect to the bare Cu(100)-(1 × 1). The area required for each $DBV^{\bullet+}_{ads}$ molecule on c(2 x 2)-Cl/Cu(100) amounts to 0.648 nm².

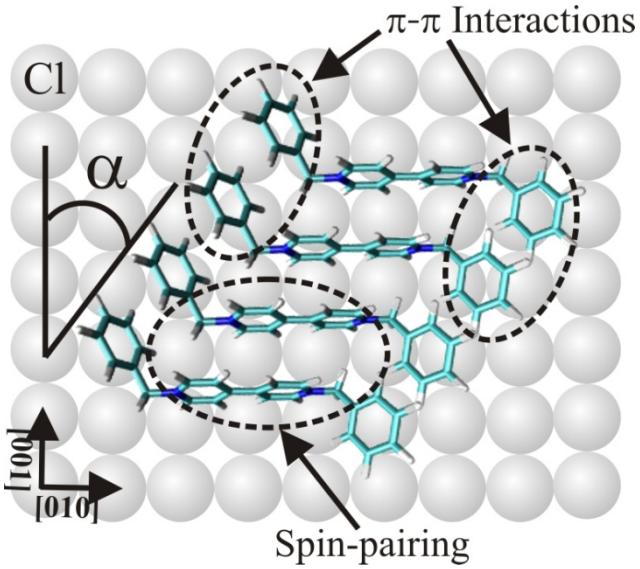

Figure 5.19: Structure model of one possible mirror domain of the stacking phase on c(2 x 2)-Cl/Cu(100).

The driving forces for the formation of the observed polymeric $(DBV^{\bullet+}_{ads})_n$ stacking chains are intermolecular *π-π* interactions between neighboring benzyl groups and even stronger interactions between neighboring reduced bipyridinium moieties, probably due to spin pairing [3, 4]. It should be stressed that such an effective π-π-interaction between adjacent $DBV^{\bullet+}_{ads}$ molecules can only be realized on the surface if the benzyl groups take up a trans-conformation. Attractive intermolecular interactions apparently overcome the repulsive electrostatic interactions of positively charged monocations within this compact film. Note that the nearest neighbor distance (NND) within the $(DBV^{\bullet+}_{ads})_n$ stacking chains amounts only to 0.36 nm.

This value is typical for *π*-stacking assemblies of aromatic systems and has also been observed, for example, for 2,2'- bipyridine phases on Au(111) [119] and Au(100) [120]. Strong attractive intermolecular interactions as the driving force for *dimerization* of open-shell planar aromatic species *in aqueous solutions* were first reported by Hausser and co-workers in 1957 [121]. The face-to-face orientation of adjacent radical species allows an overlap of the singly occupied *π** orbitals of the neighboring aromatic ring systems. It is assumed that the redox-active (reduced) bipyridinium moieties are imaged as bright and elongated dots under these tunneling conditions while the benzyl groups are supposed to lie within the dark ditches

exhibiting a lower imaging contrast (Fig. 5.18b). This phenomenon is known not only for viologens [122] but also for reduced naphtyl [123], anthracyl [123], and pyridinium [124] derivatives in aqueous solution. The formation of a dimer species is also discussed for viologen radical monocations that were immobilized before reduction on electrode surfaces via thiol or disulfide functional groups [109, 125]. In these SAM-like films, the dimerization is favored over the extended polymerization due to the lack of lateral mobility of the covalently immobilized viologens. Note that the STM image in Fig. 5.18b was obtained by using a tunneling current of I_t = 40 nA and a bias voltage of U_b = 28 mV. This extraordinary stability can be clearly attributed to the presence of the anionic chloride layer under the polycationic $(DBV^{\bullet+}_{ads})_n$ stacking phase.

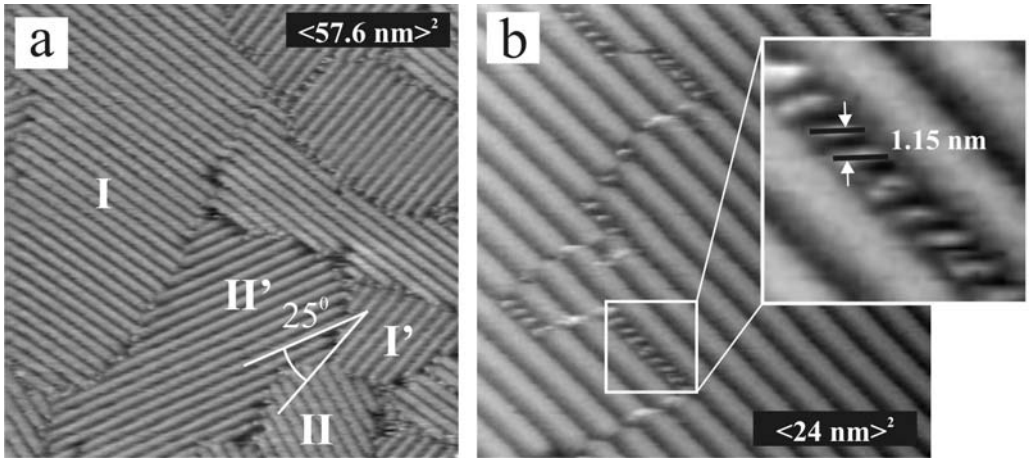

Figure 5.20: Surface morphology of $(DBV^{\bullet+}_{ads})_n$ stacking phase showing: (a) the four domains, I_t = 0.2 nA, U_b = 268 mV, E = 380 mV; (b) translational domain boundary, I_t = 0.15 nA, U_b = 174 mV, E = -330 mV.

Fig. 5.20 shows more details about the 4 domains of the $(DBV^{\bullet+}_{ads})_n$ stacking phase including 2 extended rotational domains rotated by 90° with respect to each other and 2 mirror domains. The angle between 2 mirror domains of the $(DBV^{\bullet+}_{ads})_n$ stacking phase is defined to be 25^0. The areas at the domain boundaries appear to be hollow sites or a combination of disordered $DBV^{\bullet+}_{ads}$ species which will then act as active sites for the nucleation of phase transitions. However, STM results also reveal the typical translational domain boundary of ordered $DBV^{\bullet+}_{ads}$ species (Fig. 5.20b) where the $(DBV^{\bullet+}_{ads})_n$ stacking chains shift by half the distance between two chains. This type of domain boundary is much more stable than those in Fig. 5.20a. The translational domain boundary between two parallel stacking chains provides surely not enough space to fit for a full stacking chain, however it accommodates an ordered row of separated $DBV^{\bullet+}_{ads}$ species (the zoom-in image in Fig. 5.20b). The distance between these entities in the translational domain boundaries is about 1.15 nm

(nearly equal to three times of the 0.36 nm distance value between two adjacent $DBV^{\bullet+}$ molecules in the typical stacking chain). The half-distance of 0.91 nm at the translational domain boundary is less than the theoretical length of 1.55 nm of isolated DBV molecule (Fig. 4.3). Therefore, the adsorption of the ordered row in the translational domain boundary is assumed to associate with a flexible twist of the methyl group in the DBV molecule so that at the translational domain boundaries only the bipyridinium groups appear while the benzyl groups can twist and raise perpendicular to the surface in order to fit into the narrow area of the boundaries.

It should be mentioned that even these translational domain boundaries are generally stable but at moderate tunneling condition or in a very active potential regime, these boundaries can be dynamic to move and also act as active sites for the nucleation of phase transitions.

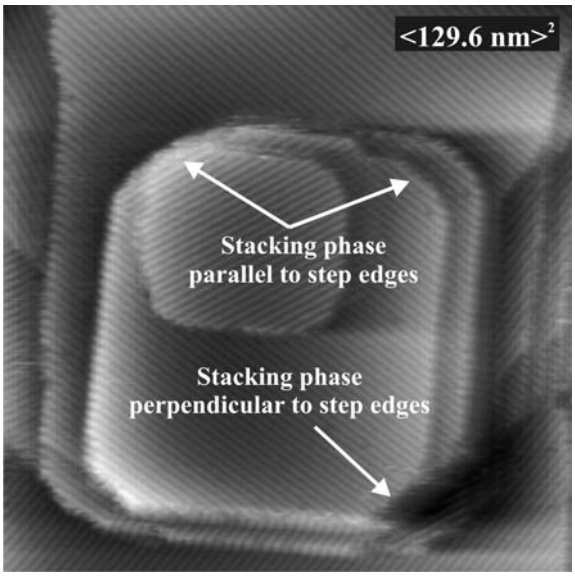

Figure 5.21: STM image shows the $(DBV^{\bullet+}_{ads})_n$ stacking phase at the on-set of the chloride desorption process, I_t = 0.2 nA, U_b = 219 mV, E = -320 mV.

As shown in Fig. 5.17, in the surface morphology of $(DBV^{\bullet+}_{ads})_n$, normally, the stacking phase does not arrange parallel to the [100] directions of the typical 90^0 step edges. However, at the potential of -320 mV or the on-set of the chloride desorption process, it initiates the removal of the adlayer starting from step edges, described as the obtuseness of the step edge angle in Fig. 5.21. Hereby, the adsorbed $(DBV^{\bullet+}_{ads})_n$ stacking chains are now parallel or perpendicular to the decayed step edges at some places.

Fig. 5.21 also represents the possibility to form a very well-ordered assembly of the $(DBV^{\bullet+}_{ads})_n$ stacking phase even on a mesoscopic length scale.

5.3.3 Amorphous phase

After passing P2 of CV4 in Fig. 5.2, the DBV species both in solution and on the surface is still the radical cation $DBV^{\bullet+}$, however the surface morphology does not appear as the stacking phase but as another disordered phase of radical cation $DBV^{\bullet+}$ adsorption, called amorphous phase describe in Fig. 5.22a.

The amorphous DBV phase represented in Fig. 5.22a seems to be composed of randomly distributed and immobilized entities. The immobilization of DBV species is assumed to be related to the chloride desorption through the $DBV^{\bullet+}$ adlayer. This hypothesis is further supported by a tip induced local removal of the disordered viologen layer as demonstrated in Fig. 5.22b.

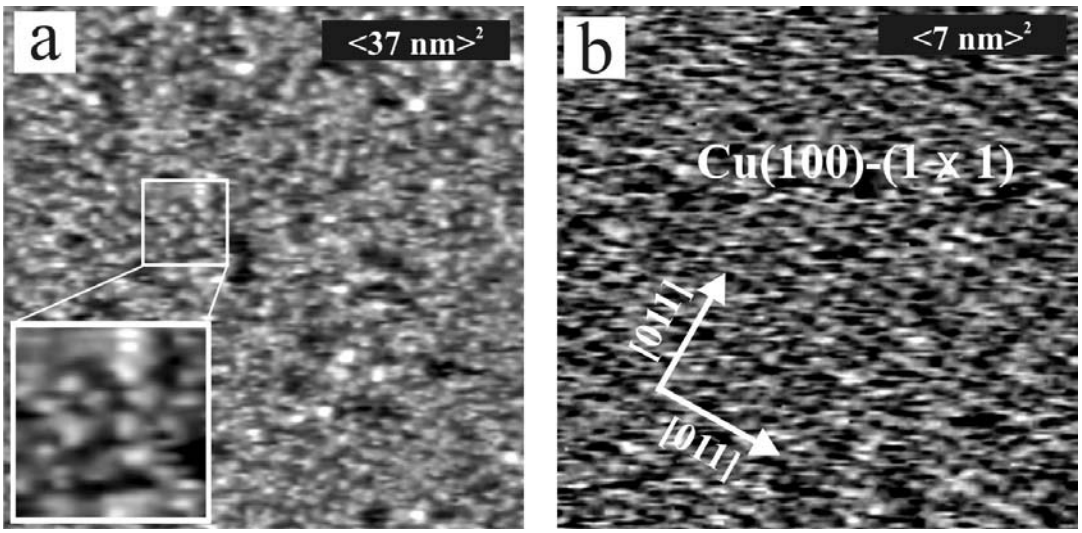

Figure 5.22: (a) Amorphous $DBV^{\bullet+}$ layer imaged under moderate tunneling conditions, I_t= 0.2 nA, U_b = 286 mV, E = -415 mV, (b) Cu(100)-(1x1)-lattice imaged under more drastic tunneling conditions, I_t= 1.7 nA, U_b = 1 mV, E = -500 mV.

While the disordered viologen phase could be obtained under moderate tunneling conditions (Fig. 5.22a), it is possible to image a square lattice using more drastic tunneling conditions (Fig. 5.22b). An NND = 0.25 nm gives clear evidence for the presence of the bare Cu(100)-(1 x 1) lattice under the amorphous phase. Apparently, the $DBV^{\bullet+}_{ads}$ molecules do not accompany the desorbing chloride anions into the bulk of the solution. Such an anion "carrier effect" is, for instance, known from polycationic porphyrin layers adsorbed on an ordered sulfate/water coadsorption layer on Cu(111) [126]. Here, the sulfate desorption leads to a co-desorption of the cationic porphyrin molecules. In turn, sulfate adsorption initiates the coadsorption of the polycationic porphyrins again resulting in a laterally ordered paired anion-cation layer. In the present case, by contrast, the cationic organic

molecules remain on the bare metal surface after anion desorption. The missing lateral order within the viologen layer right after (partial) chloride desorption points to a strongly reduced diffusivity of the radical monocations on the bare metal surface. Two reasons can be assumed causing that effect:

(1) Radical monocations interact much stronger with the metallic copper substrate than with the anionic chloride lattice thus preventing a lateral mobility of the viologens.

(2) It can further be assumed that the chloride desorption is not fully completed even in the presence of the disordered phase.

In this scenario a disordered chloride submonolayer still in contact with the copper prevents a lateral ordering of the viologens on the metallic copper substrate (Fig. 5.23b). How the starting chloride desorption/adsorption process affects the polycationic viologen film is illustrated in Fig. 5.23.

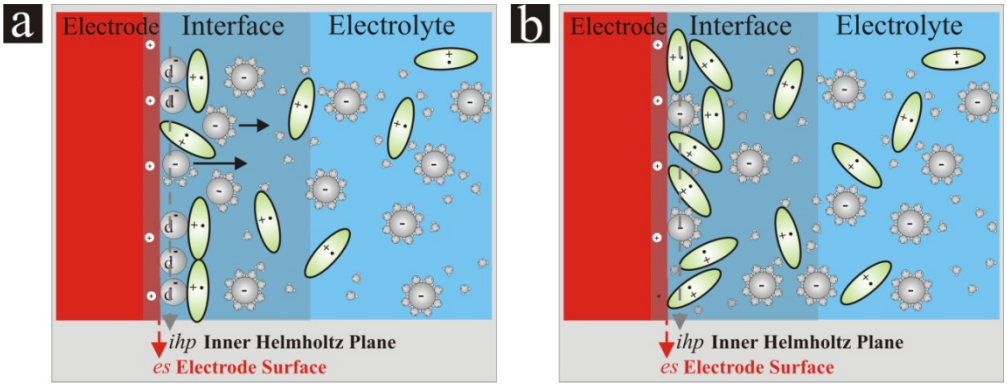

Figure 5.23: Schematic drawing showing (a) the chloride desorption through the polycationic organic layer; (b) the disordered $DBV^{\bullet+}$ layer after (partial) chloride desorption.

5.4 Phase transitions

5.4.1 Cavitand/Stacking phase transition

The DBV^{2+}_{ads} related cavitand structure and the $DBV^{\bullet+}_{ads}$ stripe phase on c(2 x 2)-Cl/Cu(100) are displayed in Fig. 5.24 again. The cavitand phase is stable only down to potentials of about -240 mV. Reaching the potential regime where P1 appears in the CVs (Fig. 5.2) we initiate the reduction of the viologen di-cation to the corresponding radical mono-cation which leads to a slow decay of the DBV^{2+}_{ads} cavitand phase as demonstrated in Fig. 5.25.

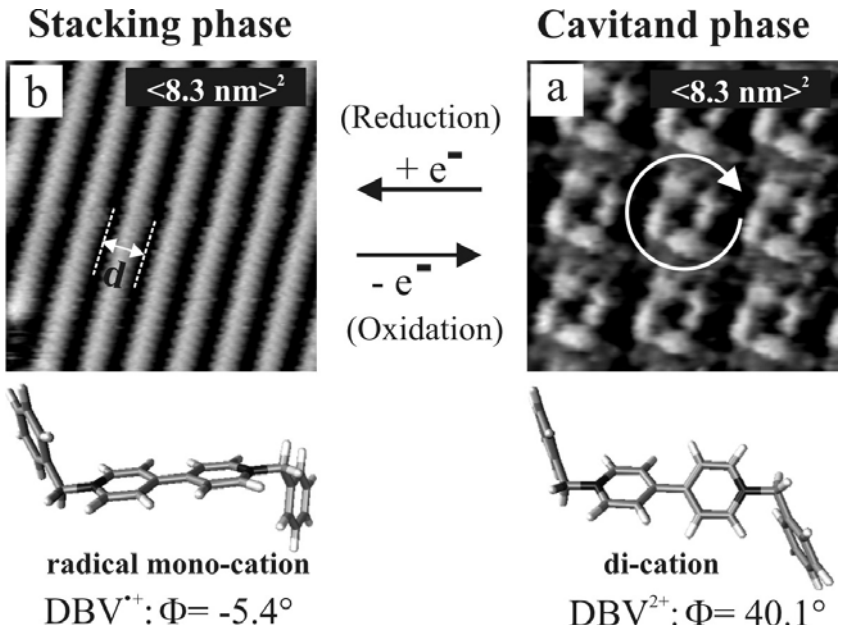

Figure 5.24: Structure motifs of DBV adlayers on c(2 x 2)-Cl/ Cu(100) depending on the viologen redox-state resulting in a quasi-reversible phase transition from (a) cavitand phase to (b) stacking phase; Φ = dihedral angle of DBV in the recspective redox state.

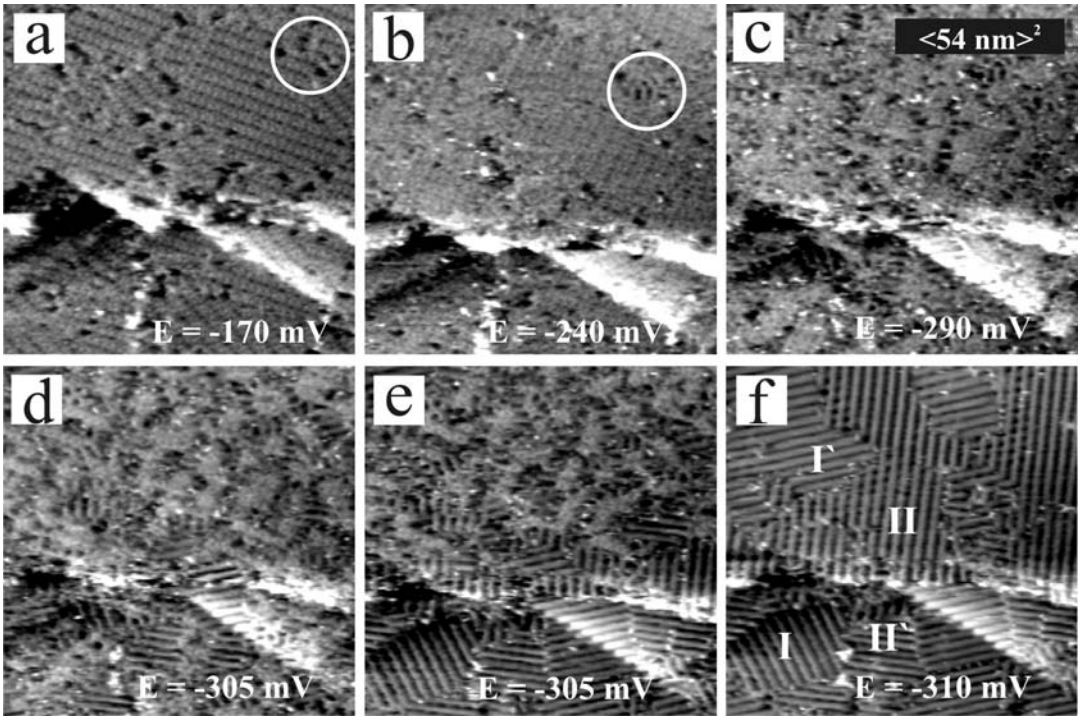

Figure 5.25: Series of STM images showing the phase transition upon reduction of the DBV^{2+}_{ads} to the corresponding $DBV^{\bullet+}_{ads}$ species, (a)-(f) I_t = 0.1 nA, U_b = 200 mV.

This process is accompanied by the nucleation and subsequent growth of the stacking phase that occurs in two mirror and two further rotational domains (Fig. 5.25f). Defects such as translational or mirror domain boundaries within the pre-existing DBV^{2+}_{ads} cavitand phase serve as preferential nucleation centers for this growth process (see white circles in Figs. 5.25a and b). Due to the slow transition kinetics there is a wide potential range of co-existence of both phases in the cathodic potential sweep ranging from E = –240 mV to E = –320 mV. The phase transition is fully completed at about E = -330 mV.

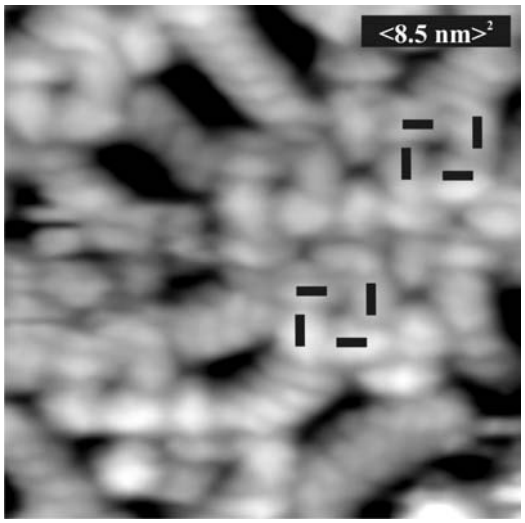

Figure 5.26: Coexistence of the DBV^{2+}_{ads} and $DBV^{\bullet+}_{ads}$ species at the surface, I_t = 0.38 nA, U_b = 161 mV, E = -315 mV.

It should be stressed that the electron-transfer reaction does not come to a standstill after completion of the surface phase transition presented in Fig. 5.25. Fig. 5.26 shows a molecularly resolved STM image obtained in this potential regime of coexistence with isolated DBV^{2+}_{ads} cavitands surrounded by short chains of the stacking phase. Their lateral order and structural relation to the substrate is still poor in this intermediate regime. Ongoing ripening processes after the initial nucleation and growth lead to an overall improvement of the lateral order of this stacking, the increase of domain sizes and to a significant decrease of the domain boundary density indicating that the presence of these domain boundaries is energetically unfavorable. After completion of these ripening processes individual domains of the stacking phase often extend over entire substrate terraces (Fig. 5.25f).

Apparently, the ongoing electron-transfer reaction does not seriously affect the structural integrity of the $(DBV^{\bullet+}_{ads})_n$ stacking phase on top of the chloride lattice, at least in a solution of 10 mM HCl and 0.1 mM $DBVCl_2$. Solvated ($DBV^{\bullet+}_{solv}$) monomers or $(DBV^{\bullet+}_{solv})_2$ dimers as reaction products are transported back into the bulk of the

solution. Their solubility in the chloride containing electrolyte is still sufficient to prevent a thick film formation of chloride salts of the radical monocations, at least at these low reaction rates. From STM experiments alone it cannot be concluded where and how this further reaction takes place, either by an electron transfer through the paired anion-cation layer at terraces ((1) in Fig. 5.27), which might involve electron transfer via electronic states of the viologen moiety, or at defect sites such as domain boundaries of the viologen stacking layer and substrate step edges ((2) in Fig. 5.27) or via an exchange process of an already reduced $DBV^{\bullet+}_{ads}$ by an oxidized DBV^{2+}_{solv} species followed by its reduction directly on top of the chloride layer ((3) in Fig. 5.27).

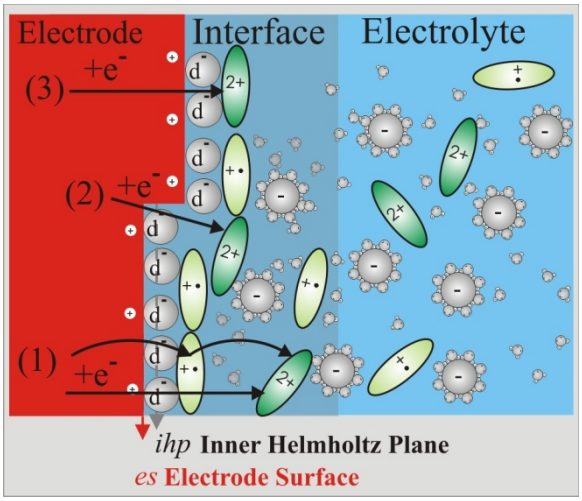

Figure 5.27: Out-of-plane structure model of the interface in the presence of the paired anion-cation layer.

In principle, the transition of the DBV^{2+}_{ads} cavitand to the stacking phase can be regarded as a quasi-reversible process. Sweeping the potential back towards the double layer regime converts the stacking back into the DBV^{2+}_{ads} cavitand phase (Fig. 5.28). This transition preferentially starts again at defect sites, e.g. at mono-atomically high substrate steps which serve as natural domain boundaries of the stacking phase. Comparing Fig. 5.28a and f it becomes evident that the appearance of both mirror domains of the DBV^{2+}_{ads} cavitand phase is independent on the pre-orientation of the stacking rows. Both mirror domains of the DBV^{2+}_{ads} cavitand phase can originate from the same mirror domain of the stacking phase.

Since we change the delicate balance between the substrate-adsorbate and the adsorbate-adsorbate interactions by the electron transfer a resulting change in the lateral ordering within the viologen film appears plausible. For the resulting $DBV^{\bullet+}_{ads}$ film we expect both, reduced repulsive electrostatic interactions due to the reduced positive charge on the adsorbed viologens and increased intramolecular interactions.

From the solution phase chemistry of viologens it is known [4, 104] that the paramagnetic radical mono-cations reveal a strong tendency towards dimerization in particular in an aqueous environment resulting in highly soluble and spin-paired $(DBV_2)^{2+}_{aq}$ species (see Eq. 5.5). Driving forces for such a spontaneous dimerization in solution are enhanced π-π-interactions between bipyridinium cores and the tendency towards spin-pairing in the reduced redox-state which can even overcompensate the repulsive electrostatic interactions between those radical mono-cations [4]. The Standard Free Gibb's Enthalpy for the exergonic dimerization of $DBV^{\bullet+}_{ads}$ species in an aqueous and chloride containing solution amounts to ΔG^0 = -16.81 kJ/mol [4]. Blandamer et al. even report an oligomerization of di-alkylated radical mono-cations in solution [4, 127]. A similar tendency towards oligomerization and polymerization is observed here on the electrode surface (Figs. 5.24 and 5.25). The observed stacking formation can be understood in terms of the 2D ordering of the adsorbed $DBV^{\bullet+}_{ads}$ species to 1D oligomer and polymer aggregates $(DBV_n)^{n+}_{ads}$ according to Eq. 5.3. Here, "polymerization" does not imply a covalent bonding as it has been reported for a $DBV^{\bullet+}$ polymer being irreversibly formed by a "prolonged electrolysis of an aqueous solution" [4, 128, 129]. The stacking phase on c(2 x 2)-Cl/Cu(100) can be quasi-reversibly transformed back into the DBV^{2+}_{ads} cavitand phase by applying potentials in the double layer regime as evidenced in Fig. 5.28.

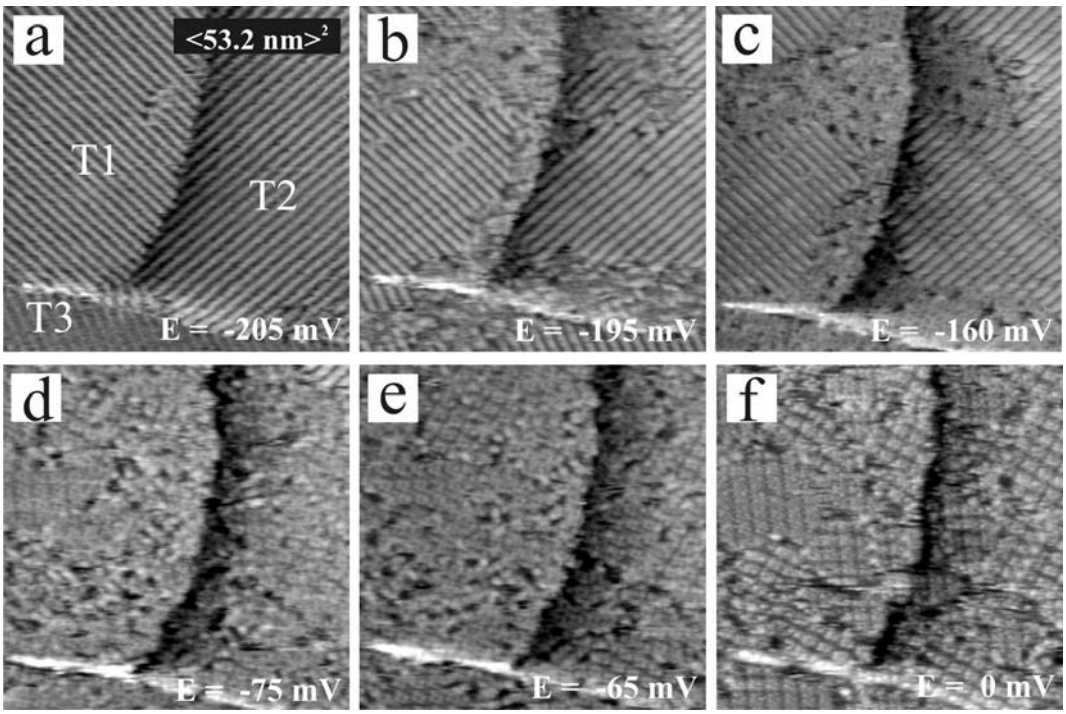

Figure 5.28: Series of STM images showing the phase transition from $(DBV^{\bullet+}_{ads})_n$ stacking phase to the DBV^{2+}_{ads} cavitand structure upon increasing potentials, (a)–(f) I_t = 0.15 nA, U_b: ranging from 228 mV to 310 mV.

While the first electron transfer step in the viologen redox-chemistry of solution species is often considered as a fast and fully reversible process the related surface phase transitions of the adsorbed viologen species are slow and therefore reveal a considerable potential hysteresis which arises from additional activation barriers. These might originate from the required positional and conformational changes of viologen molecules within the condensed 2D layer in the course of the phase transition. Note, the restoration of the DBV_{ads}^{2+} cavitand phase in the anodic potential sweep is completed only at E = 0 mV (Fig. 5.28f). In particular the transition from the stacking to the DBV_{ads}^{2+} cavitand phase seems to be kinetically hindered. Such a kinetical hindrance appears plausible considering that intermolecular π-π-bonds have to be broken upon this phase transition.

5.4.2 Chloride desorption/adsorption phase transition

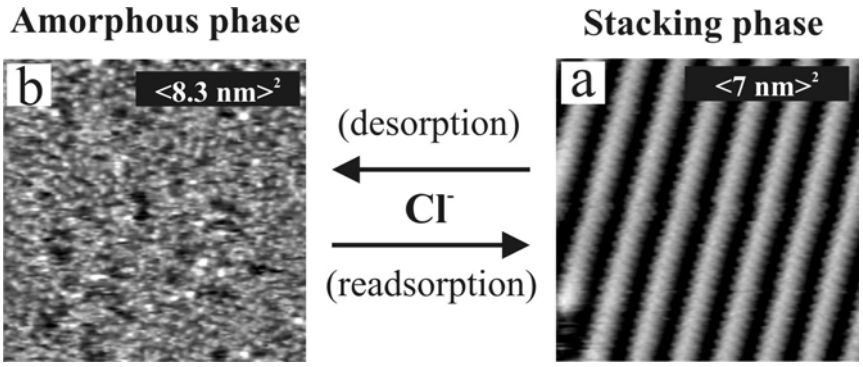

Figure 5.29: Quasi-reversible order/disorder phase transition from (a) DBV stacking phase to (b) DBV amorphous phase due to chloride desorption/readsorption.

Previous STM studies already gave clear evidence for a surface phase transition from cavitand to stacking phase upon reaching the CV-peak P1 (cathodic potential sweep in Fig. 5.2, CV2). A further decrease of the electrode potential upon reaching P2 causes a reversible order/disorder transition within the $(DBV_{ads}^{\bullet+})_n$ stacking phase related to the chloride desorption/readsorption process (Fig. 5.29).

Fig. 5.30 shows an STM series of this quasi-reversible phase transition. The surface process starts at defects or domain boundaries of the stacking phase (marked by the circles in Fig. 5.30a). Obviously, the activation free energy for the dissolution at these defects is significantly lower than the one necessary to create new point defects within intact domains. The structural transition is completed after passing P2 (Fig. 5.2, CV4). In contrast to the reported order-disorder transitions of organic films, it is not a “gaseous”, an “expanded-liquid”-, or a “condensed-liquid”-like phase of laterally mobile organic molecules that is left behind after completion of the phase transition.

Instead, the amorphous viologen phase seems to be composed of randomly distributed and *immobilized* entities (Fig. 5.30d).

A further deviation from the reported examples of defect mediated dissolution processes is the respective underlying driving force. While it is usually a temperature or potential induced reorientation of adsorbed molecules that might be associated with the partial desorption/adsorption of the organic molecules initiating these transitions [130], here, it is the starting chloride desorption though the organic film that drives the observed order-disorder transition.

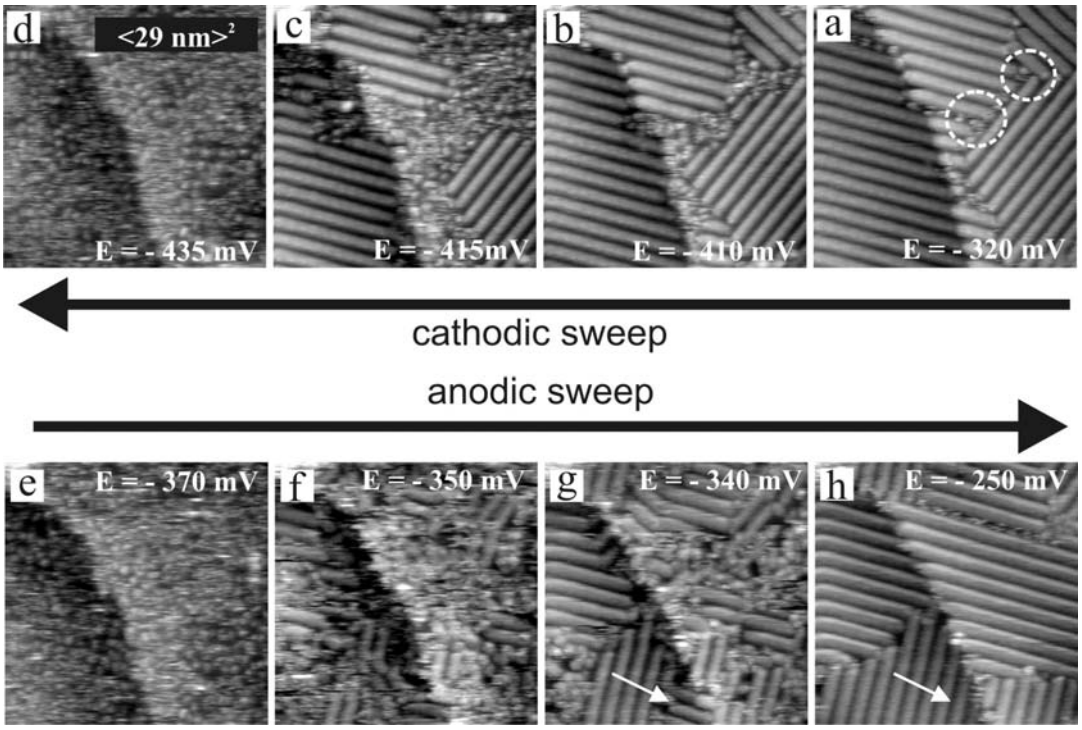

Figure 5.30: Series of STM images showing the reversible potiential dependent decay and formation of the $(DBV^{\bullet+}_{ads})_n$ stacking phase at very negative potentials: (a)-(h) I_t = 0.1 nA, U_b = 151 mV.

In general, the observed order-disorder transition is quasi-reversible with a remarkably small potential hysteresis of about $\Delta E_{hyst} \approx 70$ mV. In the reverse potential sweep, chloride anions are forced to readsorb onto the copper surface once potentials close to P2' (Fig. 5.1) are reached. Therefore, chloride anions have not only to penetrate into the disordered viologen film but also displace $DBV^{\bullet+}_{ads}$ molecules from the metallic copper surface, which then order themselves again into patches of the c(2 x 2)-Cl phase in the presence of the disordered viologen phase. In this sense, the chloride anions "crawl" under the polycationic amorphous viologen layer. Driven by the chloride readsorption two coupled disorder-order transitions take place

successively. The first one affects the ordering of chloride anions that are in contact with the metallic substrate, and the other one affects the viologen overlayer. The lateral diffusivity of $DBV^{\bullet+}_{ads}$ molecules is again enhanced on top of the chloride lattice compared to that on the bare metal surface, thus allowing the fast recombination of $DBV^{\bullet+}_{ads}$ molecules into the $(DBV^{\bullet+}_{ads})_n$ stacking phase on top of the locally restored c(2 x 2)-Cl phase (Figs. 5.30e-g). The reorganization of the c(2 x 2)-Cl phase is considered as rate determining. Sweep-rate dependent CV measurements as discussed in part 5.2.1 suggest a kinetical hindrance that is stronger for the disorder-order transition (P2') than for the preceding order-disorder transition (P2). In general, the chloride mediated disorder-order transition also complies with the typical 2D nucleation and growth behavior and the coexistence of two discernible phases (disordered/2D-ordered) within a certain potential regime between P2 and P2'. Ongoing nucleation during the disorder-order transition combined with a relatively slow growth of the stable 2D nuclei leads to the appearance of a high number of growing patches of the $(DBV^{\bullet+}_{ads})_n$ stacking phase and consequently to a high density of energetically unfavorable line and point defects. However, postgrowth ripening effects tend to reduce the total length of domain boundaries (white arrows in Figs. 5.30g-h).

It should be mentioned that the electrode is still under reactive conditions even after chloride desorption. Ongoing electron-transfer processes now take place either through the disordered viologen layer or at defects in the disordered viologen film at the bare metal surface (Fig. 5.23b). Not only the chloride desorption has an influence on the lateral order of the $(DBV^{\bullet+}_{ads})_n$ stacking phase but also the presence of the viologen layer affects the chloride desorption/adsorption process. Compared to the pure supporting electrolyte (Fig. 5.1), the chloride desorption is shifted toward lower potentials in the presence of the viologen by up to $\Delta E_{\mathrm{desorp}} \approx 90$ mV. While chloride desorption in the pure supporting electrolyte has already started at $E \approx$ -320 mV (see Fig. 3.6), both the $(DBV^{\bullet+}_{ads})_n$ stacking phase and the chloride lattice underneath are still largely intact at E = -410 mV in the DBV containing electrolyte as evidenced in Fig. 5.30b. The observed downward shift of the chloride desorption can simply be understood in terms of an additional activation barrier for chloride desorption when the covering viologen film is present. While chloride desorption in the pure supporting electrolyte exclusively starts at the step edges, we observe, in addition, chloride desorption from terraces in the presence of the viologen film with line and point defects in the covering $(DBV^{\bullet+}_{ads})_n$ stacking phase, which act as active sites for that process. It should also be noted that the shift of the chloride desorption potential depends on the structural quality of the covering viologen film. A high defect density within the viologen film generally leads to a smaller shift of the chloride desorption.

Passing P2 (Fig. 5.1) in the cathodic potential sweep, STM measurements normally showed only the disorder phase covering the whole sample surface, but occasionally they revealed also ordered structures as indicated by the white arrows

in Figs. 5.31e-f. Obviously, the orientation of the new stacking phase is not the orientation of any $(DBV_{ads}^{\bullet+})_n$ stacking phase domains (compare angles in Figs. 5.31b and 5.31e). Furthermore, the orientation of the new stacking structure is about 44° in relation with that of the adlayer DBV stacking phase on c(2 x 2)-Cl (similar with the 45° angle of main symmetry axes between c(2 x 2)-Cl and Cu(100)-(1 x 1)), it is supposed that $DBV_{ads}^{\bullet+}$ molecules can now directly interact with the metallic copper substrate, giving more evidence about the chloride desorption process. The reorganization of the $DBV_{ads}^{\bullet+}$ species to 1D oligomer or polymer chains now on-top of the bare copper is much slower than on the chloride modified electrode surface. The stacking structure of adsorbed $DBV_{ads}^{\bullet+}$ species on bare copper is shown in the enlarged image in Fig. 5.31f as stripes of separated molecules.

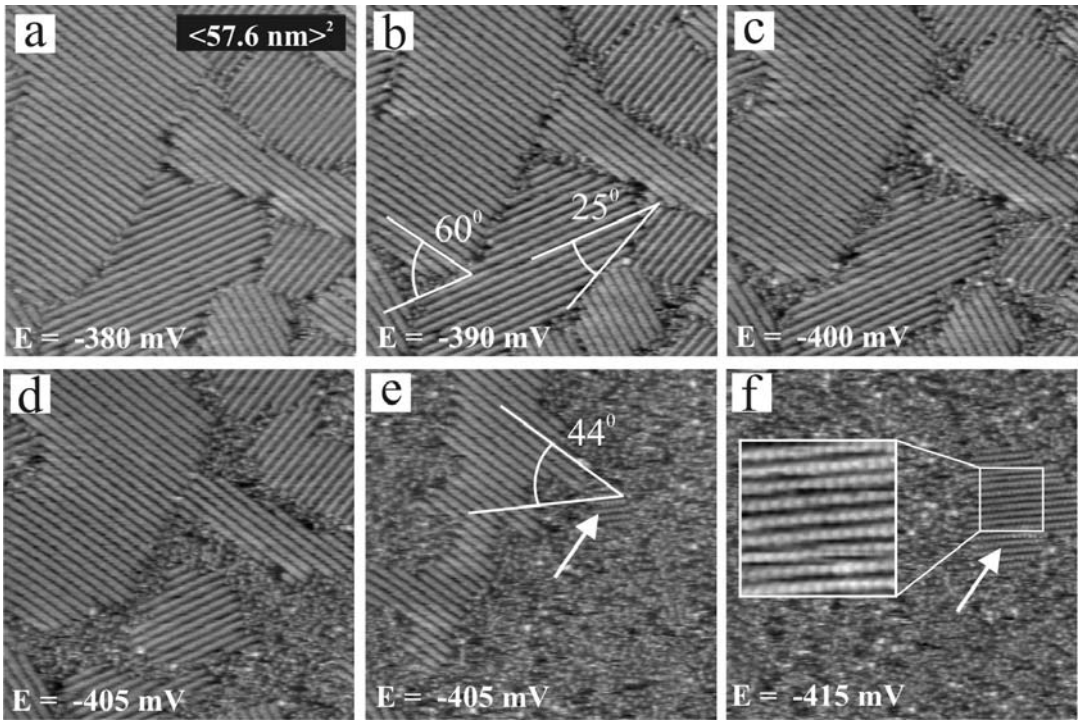

Figure 5.31: Decay of the stacking phase due to chloride desorption, (a)-(f) I_t = 0.2 nA, U_b = 268 mV, the inset in (f) shows local structure of $DBV_{ads}^{\bullet+}$ on bare copper lattice.

In brief, the role of the chloride anions in the course of the lateral ordering of $DBV_{ads}^{\bullet+}$ molecules is not a templating one in the sense of controlling the $DBV_{ads}^{\bullet+}$ ordering process due to strongly modulated adsorbate-substrate interactions. The chloride layer acts here more as a "buffer layer" between the $DBV_{ads}^{\bullet+}$ film and the metallic copper substrate. This allows the $DBV_{ads}^{\bullet+}$ entities to self-organize at the surface.

5.5 Copper dissolution in the presence of DBV adlayer

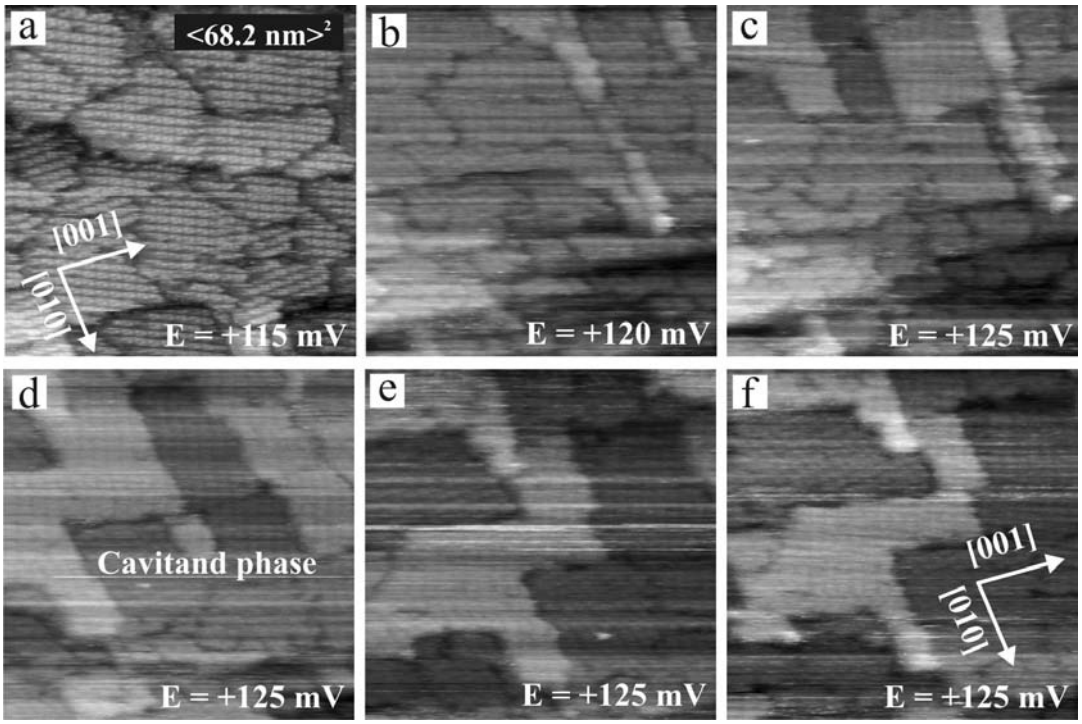

Figure 5.32: Series of STM images showing the adsorbed DBV_{ads}^{2+} cavitand phase at the on-set of CDR, (a)-(f) I_t = 1.1 nA, U_b = 290 mV.

Fig. 5.32 shows the series of STM images at the on-set of the copper dissolution reaction (CDR), beginning with a full monolayer of DBV_{ads}^{2+} cavitand phase (Fig. 5.32a) the surface morphology changes due to the dissolution reaction of the copper lattice underneath. The copper dissolution reaction starts at the potential of +120 mV. With the copper dissolution reaction, the surface terraces decay preferential parallel to the [100] orientation of the Cl lattice (Fig. 5.32f). However, the DBV_{ads}^{2+} cavitand phase still adsorbs as a full monolayer even under the destructive process of the copper dissolution reaction (Fig. 5.32d).

5.6 DBV adsorption on HOPG

In previous parts, we discussed the adsorption of DBV on the chloride modified Cu(100) substrate. On this surface the adsorption of cationic DBV species is enhanced by electrostatic attraction from the anionic chloride template. As a result with decreasing potential the structures of the cavitand phase, stacking phase and an amorphous phase related to the dication DBV^{2+} and reduced radical cation $DBV^{\bullet+}$

species, respectively, are observed. The phase transitions between these phases were observed in specific potential regimes.

However, the presence of the anionic chloride adsorbed on the electrode surface is not mandatory for the adsorption of DBV molecules. On an HOPG substrate there is no specifically adsorbed chloride layer present. Here, the phase formation of the viologen species takes place directly on the unmodified HOPG surface. Furthermore, the much broader potential window of the HOPG substrate gives a chance to investigate the viologen adsorption at more anodic or cathodic potentials than this is possible on the copper substrate, especially at more negative potentials where the reduction from the radical $DBV^{\bullet+}$ to uncharged species takes place.

In order to study the adsorption of DBV on the HOPG surface the DBV^{2+} containing electrolyte was added to the electrochemical cell at a potential of 0 mV. The corresponding CV was shown in Fig. 5.6. In the positive potential regime before reaching the reduction peak P1, the CV shows two unknown peak pairs P4/P'4 and P5/P'5, however, DBV adsorption on the HOPG surface can be observed with STM. Passing P1 of CV4 in Fig. 5.6 causes the reduction of viologen molecules from dication DBV^{2+} to the corresponding radical cation $DBV^{\bullet+}$ species. Then the adsorption of DBV can be observed by STM, revealing a new structure as shown in Fig. 5.33. Obviously, the structure of adsorbed $DBV^{\bullet+}$ on HOPG is different from the stacking phase of $DBV^{\bullet+}_{ads}$ on chloride modified Cu(100) (see Fig. 5.18).

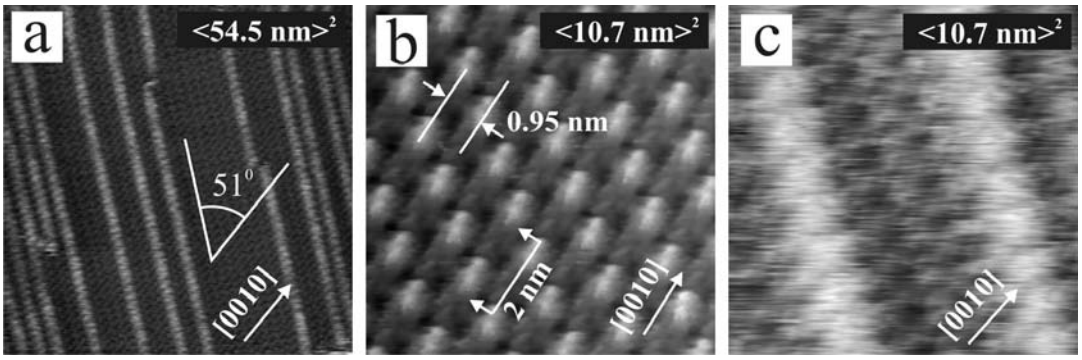

Figure 5.33: STM images of $DBV^{\bullet+}_{ads}$ double layer stripe phase obtained on HOPG, (a)-(c) I_t = 0.2 nA, U_b = 350 mV, E = -350 mV.

This new structure is composed of stripes of separated $DBV^{\bullet+}_{ads}$ species (Fig. 5.33b) in the first layer and further stripes adsorbed on top of the first layer (Figs. 5.33a,c). In Fig. 5.33b, the bright dots are assigned to the bipyridinium cores and the benzyl groups are assumed to lie within the darker area between these bright stripes. By using tip-induced removal of the DBV adlayer revealing the HOPG substrate underneath, it is found that the bipyridinium cores are arranged along the [1000]

direction of the HOPG lattice (Fig. 5.34). The second stripes are assigned to stay on top and in between the $DBV^{\bullet+}_{ads}$ stripes of the first layer therefore showing up brighter in Fig. 5.33a. The stripe propagation direction encloses a characteristic angle of 51° with one of the main symmetry axes of the HOPG lattice (Fig. 5.33a). The nearest neighbor distance between molecules within the stripe is 0.95 ± 0.05 nm, and the distance between adjacent stripes is 2.0 ± 0.1 nm (Fig. 5.33b). Both the distance between the entities and their size in Fig. 5.33b are so high that these adsorbed $DBV^{\bullet+}_{ads}$ species are assumed to lay flat down on the substrate, unlike the face-to-face polymeric $DBV^{\bullet+}_{ads}$ stacking phase known from Cl/Cu(100).

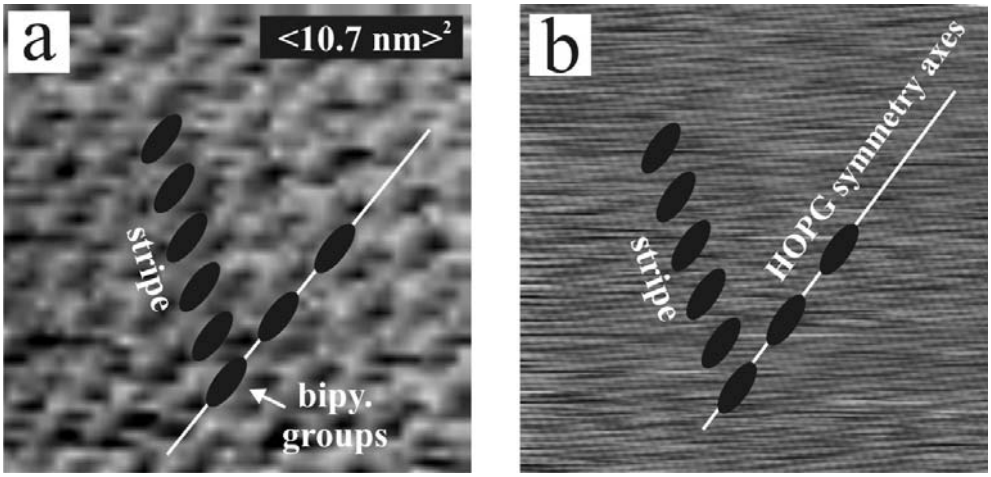

Figure 5.34: STM images of the first $DBV^{\bullet+}_{ads}$ stripe layer in comparison with the HOPG lattice underneath at the same position, (a) $DBV^{\bullet+}_{ads}$ stripe phase under moderate tunneling conditions, I_t = 0.2 nA, U_b = 350 mV, (b) HOPG lattice imaged under more drastic tunneling conditions, I_t = 1 nA, U_b = -1 mV.

Going further to negative potential, as mentioned in the CV part 5.2.2, the peak P3 is assigned to the second reduction of DBV from the radical cation $DBV^{\bullet+}$ species to the uncharged DBV^0 molecules. In the case of a copper substrate, the hydrogen evolution reaction already takes place in the potential regime of P3. Therefore STM images cannot show the surface covered with the DBV adsorption adlayer. On the other hand, due to the broader potential window of the HOPG substrate the hydrogen evolution reaction does not taken place yet at P3, giving a chance for STM experiments to observe the adsorption of uncharged DBV^0 molecules. In fact, starting from the $DBV^{\bullet+}_{ads}$ double layer stripe phase on the HOPG substrate and going to more negative potentials than P3, a phase transition of the DBV adlayer appears on the unmodified HOPG substrate. Surprisingly, the observed structure of the adsorbed uncharged DBV^0 molecules is a stacking phase (similar to the $DBV^{\bullet+}_{ads}$ stacking phase on chloride modified copper surface). This structure is described in Fig. 5.35.

The structural motifs of the uncharged DBV^0 stacking phase has a nearest neighbor distance (NND) of 0.37 nm which is almost identical with the $(DBV^{\bullet+}_{ads})_n$ stacking phase on copper. Therefore, this structure represents a face-to-face polymeric $(DBV^0_{ads})_n$ stacking phase adsorbed directly on the HOPG surface. The stacking chain propagation direction encloses an angle of α = 65° with one of the main symmetry axes of the HOPG lattice (Fig. 5.35).

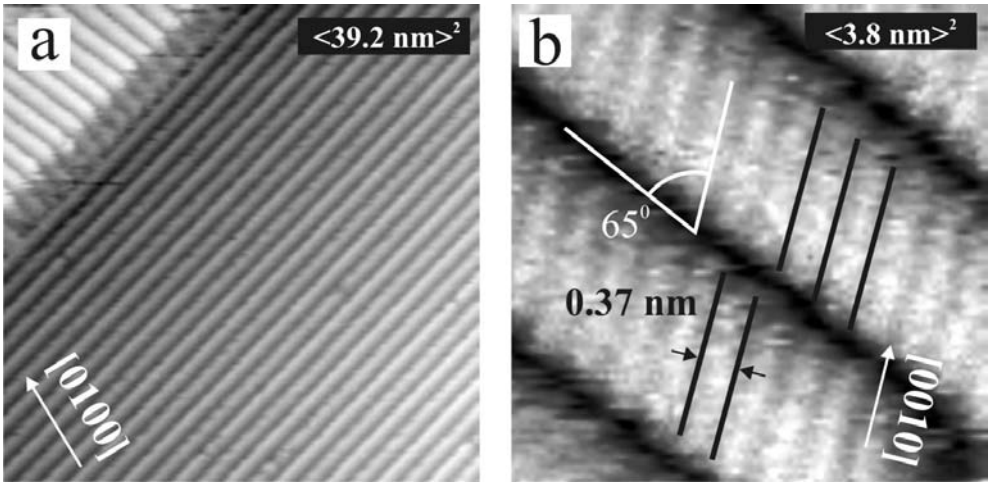

Figure 5.35: Uncharged $(DBV^0_{ads})_n$ stacking phase obtained on HOPG, (a)-(b) I_t = 0.2 nA, U_b = 337 mV, E = -510 mV.

Thus, on copper the face-to-face polymeric stacking phase formation appears even with $DBV^{\bullet+}_{ads}$ species, while the stacking phase on HOPG can only be observed after the reduction to the corresponding DBV^0_{ads} molecules. It is noteworthy that the NNDs within stacking chains on copper is smaller (0.36 nm) than on HOPG (0.37 nm). Therefore the chloride-covered Cu-template apparently enhances the attractive intermolecular interaction of $DBV^{\bullet+}_{ads}$ species and reduces the repulsive electrostatic interactions of the positively charged monocations within this compact film. On the other hand, on HOPG without the enhancement of any anionic template, the mere intermolecular interactions of $DBV^{+\bullet}$ species cannot overcome the repulsive electrostatic interactions to form the polymeric stacking phase until the reduced uncharged molecules are formed. Another evidence proving the enhancement of the chloride template on the adsorption of DBV lies in their stability and robustness against externally induced mechanical stress, for instance, by the tunneling tip upon scanning. While on HOPG the stacking phases of adsorbed DBV_{ads} are extremely fragile and, hence, often are destroyed upon scanning even at moderate tunneling conditions, by contrast, even drastic tunneling conditions for the imaging of the $(DBV^{\bullet+}_{ads})_n$ stacking phases on c(2 x 2)-Cl/Cu(100) can be applied without destroying them (see Fig. 5.18b).

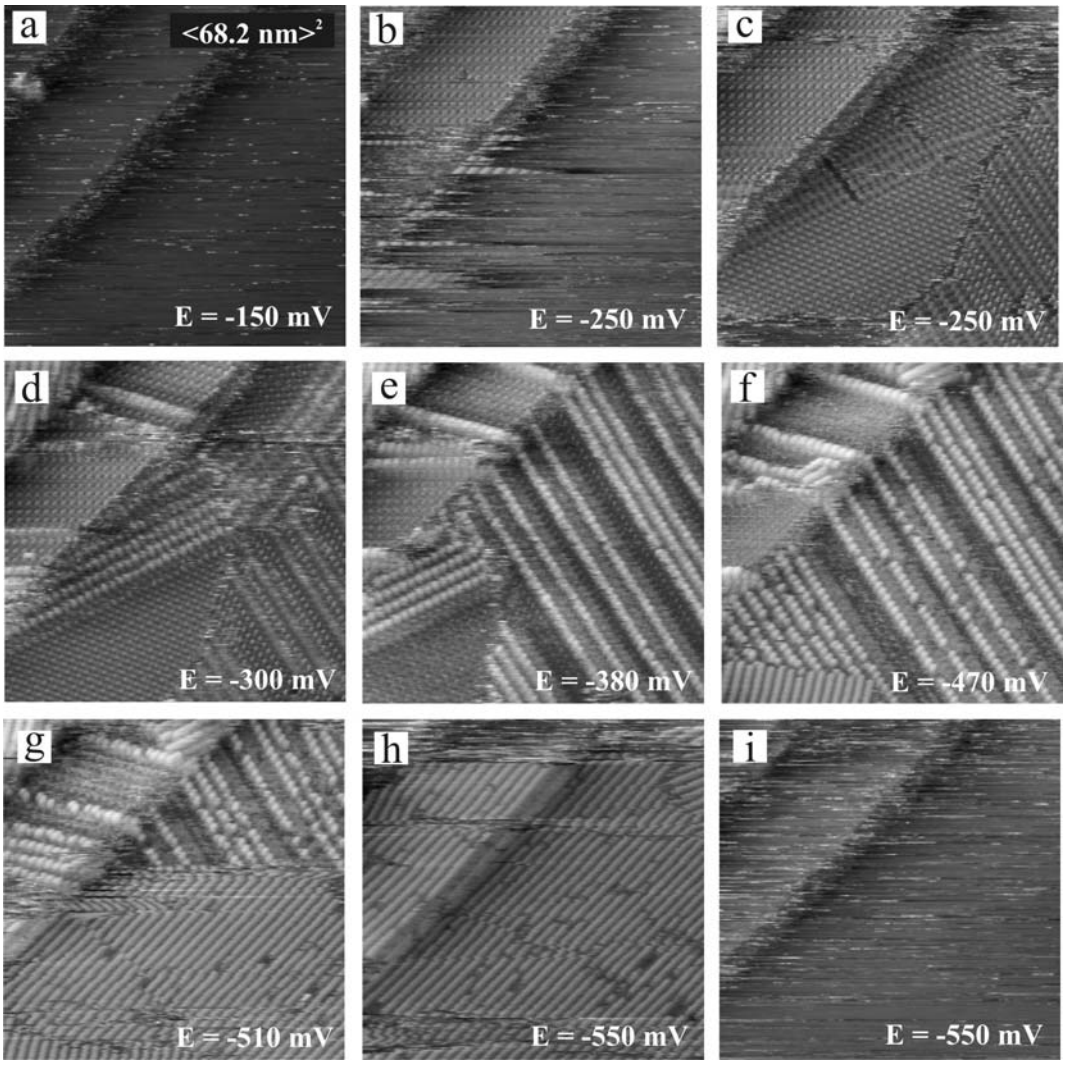

Figure 5.36: Series of STM images showing the phase transition from $DBV^{\bullet+}_{ads}$ double layer stripe phase to $(DBV^{0}_{ads})_n$ stacking phase on HOPG upon scanning towards negative potential regime, (a)-(f) I_t = 0.2 nA, U_b = 373 mV.

Fig. 5.36 represents a potential-dependent series of STM images showing the surface morphology upon going towards negative potentials. Starting with the initial potential of 0 mV, the HOPG substrate does not adsorb dicationic DBV^{2+} in a broad potential regime reaching until P1 of CV4 in Fig. 5.6 (Fig. 5.36a). Reaching P1 at the potential of -250 mV where the dications DBV^{2+}_{aq} start to be reduced to the corresponding radical cation $DBV^{\bullet+}_{aq}$ causes immediately the adsorption of the $DBV^{\bullet+}_{ads}$ double layer stripe phase on the bare HOPG substrate (Figs. 5.36b,c). The $DBV^{\bullet+}_{ads}$ double layer stripe phase persists towards more negative potential before reaching P3 of CV6 in Fig. 5.6 (Fig. 5.36d,e). Note that the change of working potential causes also a change of the tunneling conditions, therefore, the same structures of the $DBV^{\bullet+}_{ads}$ double layer stripe phase in Figs. 5.36b-e appears in different contrast.

Reaching P3 at the potential of -470 mV, in Fig. 5.6, CV6, together with the reduction from $DBV^{\bullet+}$ to DBV^{0}, the phase transition from the $DBV^{\bullet+}_{ads}$ double layer stripe phase to $(DBV^{0}_{ads})_n$ stacking phase takes place (Fig. 5.36f,g). Right after the completion of the phase transition at -550 mV (Fig. 5.36h), the whole DBV adlayer desorbs due to the hydrogen evolution reaction (Fig. 5.36i).

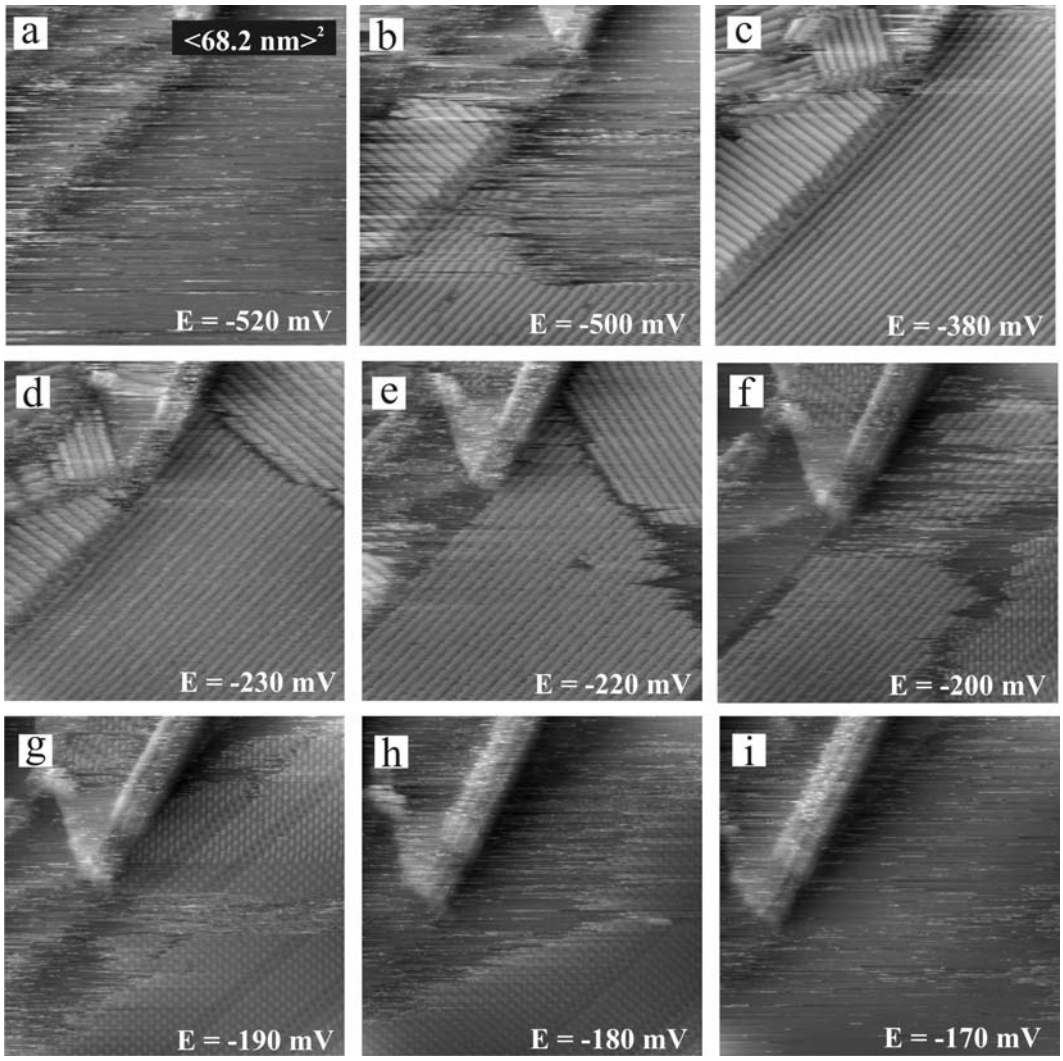

Figure 5.37: Series of STM images showing the phase transition from $(DBV^{0}_{ads})_n$ stacking phase back to $DBV^{\bullet+}_{ads}$ double layer stripe phase upon scanning towards positive potential regime, (a)-(f) I_t = 0.2 nA, U_b = 373 mV.

These phase transition processes are reversible. Fig. 5.37 represents a potential-dependent series of DBV phase transitions on HOPG upon scanning back towards positive potentials. Starting from the uncovered surface within the HER regime the $(DBV^{0}_{ads})_n$ stacking phase readsorbs at -500 mV (Fig. 5.37b). This process takes place

gradually until forming a full monolayer at the potential of -380 mV. Further change towards positive potentials through both solution oxidation peaks P'3 and P'1 of CV6 in Fig. 5.6, the $(DBV^{0}_{ads})_n$ stacking phase remains stable on the surface (Fig. 5.37d). Only until totally passing P'1 at the potential of -220 mV or the completion of the oxidation from $DBV^{\bullet+}_{aq}$ back to DBV^{2+}_{aq} species in solution, the reverse phase transition from $(DBV^{0}_{ads})_n$ stacking phase back to $DBV^{\bullet+}_{ads}$ double layer stripe phase takes place (Figs. 5.37e,f). However, due to the lack of $DBV^{\bullet+}_{aq}$ in solution, this phase of $DBV^{\bullet+}_{ads}$ double layer stripes is only a sub-monolayer (Fig. 5.37g) which decays to expose the bare HOPG substrate (Figs. 5.37h,i). In comparison with the transition in the negative-scan in Fig. 5.36, in which the phase transition takes place almost simultaneously with the corresponding processes of the solution species, the reverse transition in Fig. 5.37 starts at much more positive potential than the corresponding solution peak P'3. Therefore, the phase transitions between $DBV^{\bullet+}_{ads}$ double layer stripe phase and $(DBV^{0}_{ads})_n$ stacking phase result in a very high hysteresis of $\Delta E \approx 250$ mV, indicating the extremely high stability of the $(DBV^{0}_{ads})_n$ stacking structure.

Going further to positive potentials, into the solution dication regime, the $DBV^{\bullet+}_{ads}$ double layer stripe phase decays until there is again no DBV adsorption observed (Figs. 5.37h,i).

5.7 Summary

In this chapter, the non-reactive adsorption of DBV molecules on chloride modified Cu(100) and on HOPG has been investigated systematically by using the combination of two methods, CV and EC-STM. Although the system of DBV adsorbed on the chloride template has been partly studied in the doctoral thesis of Zörlein [5], the present work adds new information about this system.

From the CV experiments, we can conclude on the reactions or processes corresponding to the peak pairs P1/P'1, P2/P'2 and P3/P'3 appearing in the CVs of Figs. 5.2 and 5.5. According to the results, the peaks P1 and P3 are *solution* peaks assigned to the first and the second electron transfer reduction from the dication DBV^{2+} to the corresponding radical cation $DBV^{\bullet+}$ species, and then to the uncharged DBV^{0+} molecules, respectively. P'1 and P'3 are their corresponding reoxidation peaks. On the other hand, the P2 and P'2 peaks correlate with the chloride desorption/readsorption processes on the *surface*. The above conclusions fit well with the CV results on an inert HOPG substrate where the preadsorbed anion layer is not present. Indeed, CVs on HOPG in Fig 5.6 show the similar solution peak systems P1/P'1 and P3/P'3 in corresponding potential regimes without the presence of the peak system P2/P'2 of the chloride desorption process. It is noteworthy that in the

CVs of the HOPG substrate also some small peak systems P4/P'4 and P5/P'5 appear at high potentials, however, these peaks have not been identified yet.

The corresponding STM experiments on the copper substrate show clear results which provide complementary information about surface structures and phase transitions as suggested by the CV data.

First of all, under non-reactive adsorption at high initial potential, the surface morphology represents a very well-ordered cavitand phase of DBV^{2+} species which is characterized by a square-shaped structure of DBV^{2+} species with "strong" as well as dynamic "weak" boundaries between different structural domains. A new structural model is proposed for the cavitand phase which agrees with the obtained high resolution STM images and the explanation of the two types of translational domain boundaries.

Passing the first reduction peak P1 of the CV a phase transition from the dication DBV^{2+}_{ads} cavitand phase to the radical cation $(DBV^{\bullet+}_{ads})_n$ stacking phase is observed on the surface. The stacking phase is characterized by the polymerization of face-to-face $DBV^{\bullet+}$ species forming stripes which enclose an angle of 37° with one of the main symmetry axes of the chloride lattice.

At even more negative potentials, passing the chloride desorption peak P2, the stacking phase transforms into a disordered amorphous phase which suggests that the chloride desorption occurs through the organic adlayer. The presence of the amorphous phase causes also an inhibition effect shifting the hydrogen reduction reaction (HER) in the DBV containing electrolyte to much more negative potentials.

The two phase transitions are reversible with different hysteresis as presented in the result sessions. However, it is noteworthy that with every phase transition the number of defects or the perfectness of ordering may decreases.

In addition, STM experiments have been done on an HOPG substrate with a broader potential window into the more negative regime revealing different structures from those observed on the copper surface. At first, at high potentials the DBV^{2+} species do not form an ordered structure to be observed by STM. In the radical cation regime of the CV, the $DBV^{\bullet+}$ species orders on the HOPG lattice, however, the obtained structure does not appear as a stacking phase but as a double layer stripe phase of separated $DBV^{\bullet+}_{ads}$ species. Passing the second reduction peak P3, a phase transition takes place from the $DBV^{\bullet+}_{ads}$ double layer stripe phase to the polymeric $(DBV^{0}_{ads})_n$ stacking phase. The phase transition is also reversible, however the $(DBV^{0}_{ads})_n$ stacking phase is so stable that a very high hysteresis of $\Delta E \approx 250$ mV between cathodic formation and anodic decay results.

Chapter 6

DPV adsorption on chloride modified Cu(100)

6.1 Introduction

The goal of this chapter is to discuss the redox chemistry and the structural phase behavior of adsorbed Diphenyl-viologen (DPV) on a Cu(100) surface. Since the molecules (see Fig. 4.5) are dissolved as cations in aqueous electrolytes, a negatively charged metal surface like the chloride modified Cu(100) surface is expected to be a good template for the self-assembly of this kind of molecules.

Like DBV, the DPV molecules have three redox states: dication, radical cation and uncharged molecule. All three common viologen redox-states can be converted into each other in an electrochemical environment by two single electron transfer reactions (see Sec. 4.2), however, within the Cu potential window, we expect only the transition from the dication DPV^{2+} to the radical cation $DPV^{\bullet+}$ following the first election transfer reaction.

The main difference between DPV and DBV consists in the lack of the extra methylene group separating the phenyl groups from the central bipyridinium unit as in case of the DBV (see Figs. 4.3 and 4.5), therefore the conjugated π-system of the DPV molecule extends over the entire molecule. In the following, it will be demonstrated that this small structural difference significantly affects both the viologen solution redox chemistry and the structural phase behavior of the adsorbed viologen species. The fully conjugated π-system of the DPV can be expected to stabilize the radical mono-cation more effectively than the 'isolated' π-system of the central bipyridinium unit as in the case of DBV.

6.2 Cyclic Voltammetry

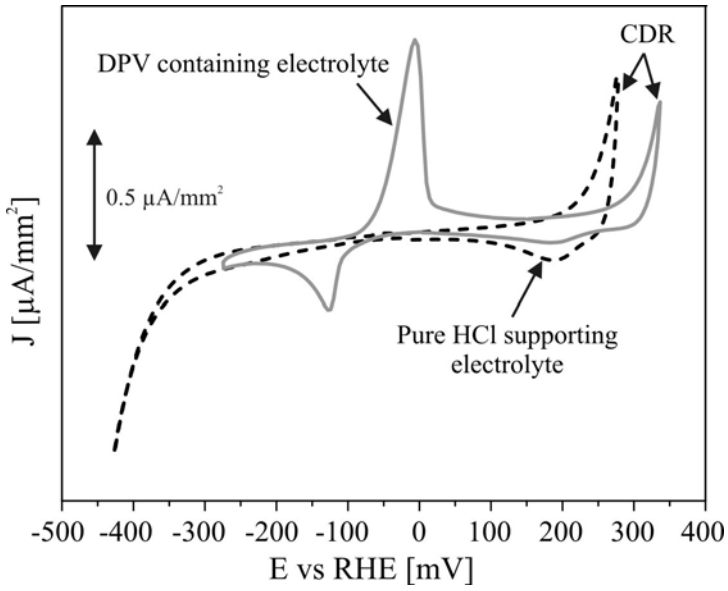

Figure 6.1: Black dotted curve: CV of Cu(100) in the pure supporting electrolyte (10 mM HCl). Grey curve: CV of Cu(100) in the DPV^{2+} containing electrolyte (10 mM HCl, 0.1 mM $DPVCl_2$), dE/dt = 10 mV s^{-1}.

Fig. 6.1 shows representative steady-state CVs of Cu(100) in the absence (black dotted curve) and the presence (grey curve) of DPV species in the supporting electrolyte 10 nM HCl. After exchanging the pure supporting electrolyte by the one containing the redox-active DPV^{2+} species we observe drastic changes in the CV curve, namely the appearing of a pair of peaks in the potential regime from about -200 to 50 mV. Unlike DBV, the presence of the DPV layer has almost no impact on the chloride modified Cu(100) surface at the HER regime, however, the DPV layer has strong impact on the oxidative copper dissolution regime (CDR), manifested by the fact that the potential of the dissolution reaction is considerably shifted to higher potentials (Fig. 6.1) ($\Delta E \approx 60$ mV). That points to a pronounced inhibition effect of DPV on the CDR. Obviously DPV molecules are still present at the surface even under the copper dissolution conditions thereby blocking reactive sites for the CDR such as substrate steps. It is worth to note that also in the case of DBV, the molecules have also a blocking effect on CDR but with much lower efficiency. In the case of DBV the blocking adlayer is the dicationic DBV^{2+} layer (see chapter 5 and 7), however at CDR the adsorbed DPV species is not the dication. That strong DPV blocking effect will be explained in the next part of STM results.

Towards negative potentials, the CV in DPV containing electrolyte shows some anodic and cathodic current waves. These additional current features have to be assigned to viologen-related redox processes. Typically, the shape of the CV in the presence of the viologen species depends strongly on the chosen cathodic potential limit. A precise correlation of the cathodic to the respective anodic current waves in

the reverse potential scan is achieved by a systematic variation of the cathodic potential limit as shown in Fig. 6.2.

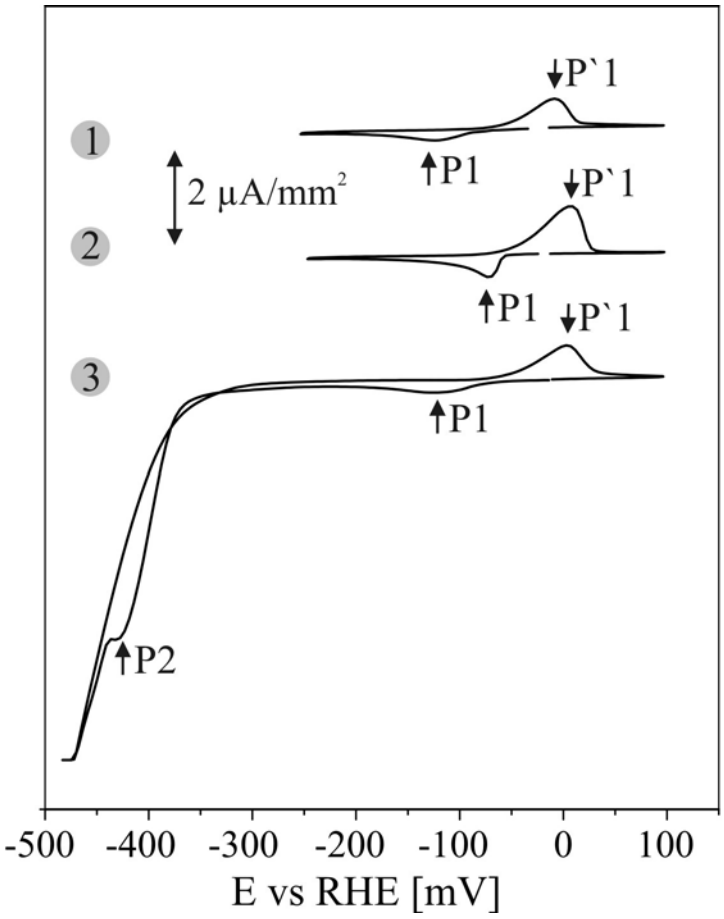

Figure 6.2: Appearance of anodic and cathodic current waves in the CV of Cu(100) in the DPV^{2+} containing electrolyte upon changing the cathodic potential limit

In Fig. 6.2, by restricting the cathodic potential limit to E = -250 mV, a peak pair P1/P'1 ($P1_{max}$ = -120 mV, $P'1_{max}$ = -10 mV) appears in the CV1. In CV2, extending the potential a bit further than -250 mV to about -300 mV and then even back to the cathodic potential limit of -250 mV, the peak pair P1/P'1 becomes considerably higher and shifts towards positive potentials ($P1_{max}$ = -80 mV, $P'1_{max}$ = +10 mV). Towards a more negative regime, if the cathodic potential limit exceeds a critical value E = -450 mV we initiate not only the HER but also a further process which is represented by P2 (CV3 Fig. 6.2). The small oxidation peak P'2, i.e. the counterpart of P2, can still be within the HER regime and does not appear clearly in the CV of DPV. CV3 of Fig. 6.2 also shows surprisingly that the peak system P1/P'1 is now not at the same positions as in CV2 but seems to shift back close to that of CV1 in both respects, intensity and position.

It is worth mentioning that when restricting the cathodic potential to values higher than -250 mV (CV1 Fig. 6.2), the peak pair P1/P'1 does not represent a perfect steady state during continuous scans. Fig. 6.3 shows a set of potential sweep curves while the cathodic potential limit is kept at -250 mV showing the instability of the peak pair P1/P'1. During scans, that peak pair shifts towards negative potentials and the height of the reduction peak P1 becomes higher while the height of the oxidation peak P'1 becomes lower continuously. However, if scanning further than -250 mV, the peak pair P1/P'1 in CV2 of Fig. 6.2 becomes a steady state CV and remains extremely stable. Both P1 and P'1 shift to positive potentials with the peak heights becoming almost double than in the former case. Following these CV results, it is expected that ongoing scanning to negative potentials further than the onset of HER, there should be 3 different reactions or processes related to the adsorption of DPV on the chloride modified Cu(100) surface:

- A reaction of DPV giving rise to P1/P'1,
- the process happening when passing below -250 mV,
- and the reaction or process related to P2.

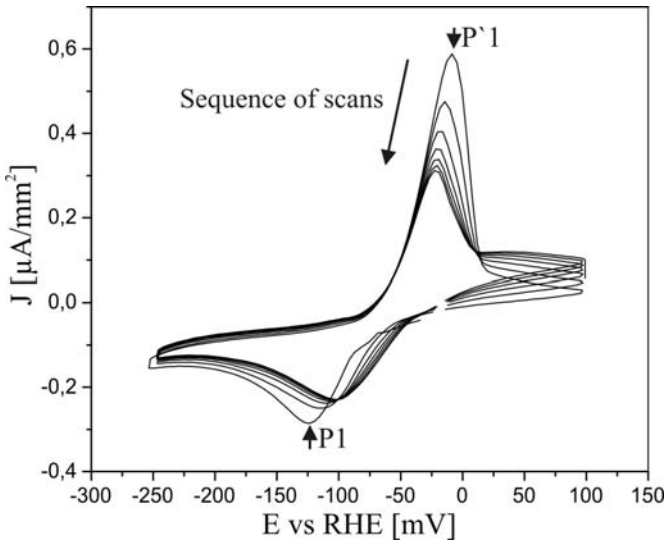

Figure 6.3: Set of continuous CV scans while the cathodic potential limit is kept at -250 mV.

Similar to the case of DBV, the redox behavior of adsorbed DPV adsorption on chloride modified Cu(100) might be described in more detail below by the set of Eqs. 6.1 to 6.4 involving "solution-" as well as "surface-limited" reactions:

1. The surface limited reduction/oxidation of pre-adsorbed viologen species according to:

$$\mathrm{DPV}^{2+}_{(\mathrm{ads})} + e^- \leftrightarrow \mathrm{DPV}^{\bullet+}_{(\mathrm{ads})} \qquad (6.1)$$

or even a polymer formation at the surface according to

$$n\,DPV^{\bullet+}_{(ads)} \leftrightarrow \left[DPV_n\right]^{n+}_{(ads)} \tag{6.2}$$

2. The reduction/oxidation of viologen solution species according to:

$$DPV^{2+}_{(aq)} + e^- \leftrightarrow DPV^{\bullet+}_{(aq)} \tag{6.3}$$

3. And the film formation/dissolution of radical mono-cation chloride salts according to:

$$n\,DPV^{\bullet+}_{(aq)} + n\,Cl^- \leftrightarrow \left[DPV^{\bullet+}\,Cl^-\right]_n \downarrow \tag{6.4}$$

Note from CV3 in Fig. 6.2 that the HER regime in the DPV containing electrolyte comes so early that the second single electron transfer step transforming the radical mono-cation into the fully uncharged DPV species does not take place within the potential window.

Firstly, the peak pair P1/P'1 is similar to that in the CV of a DBV containing electrolyte. Therefore we assign the peak system P1/P´1 to the reduction of di-cationic DPV^{2+} to the corresponding radical mono-cationic $DPV^{\bullet+}$ species. However, the STM results in the next part show that DPV adsorption leads exclusively to a stacking phase of mono-reduced species or $(DPV^{\bullet+}_{ads})_n$ across the whole potential window. This indicates that at the surface DPV dications are so active that they undergo the reductive reaction already before P1(DPV) even when their species in bulk solution is still stable DPV^{2+}_{aq}. Therefore, the peak pair P1/P'1 is only related to the reduction/oxidation process of the solution species described by Eq. 6.3.

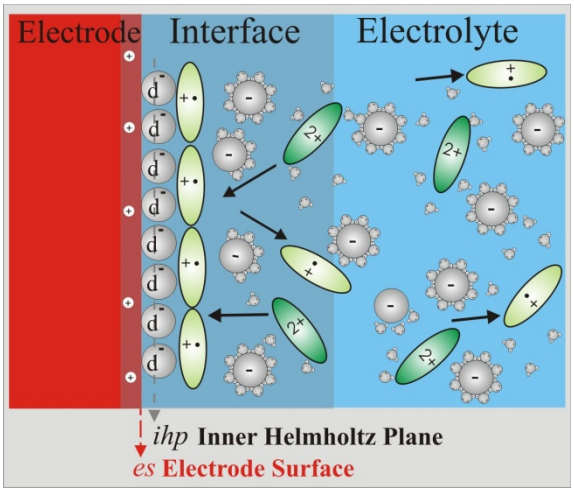

Figure 6.4: Out-of-plane structure model of the interface in the presence of the reductive reaction of dication DPV^{2+}_{aq} species in bulk solution to radical cation $DPV^{\bullet+}_{aq}$ through the stable preadsorbed $(DPV^{\bullet+}_{ads})_n$ adlayer.

The surface reactions of Eqs. 6.1 and 6.2 take place prior to P1 and do not appear in the CV. The reduction taking place at P1 is illustrated in the structure model of the interface in Fig. 6.4. P1 is supposed to be a fast reduction of molecules from the liquid layer near the surface (or "interface" layer in Fig. 6.4). With the presence of the preadsorbed $DPV^{\bullet+}$ adlayer on the surface, the DPV^{2+} species in solution come to the interface layer to be reduced to $DPV^{\bullet+}$ species. After consumption of molecules from the "interface" layer, further dication DPV^{2+} species in solution have to diffuse towards the surface which leads to a reduced reaction current of P1. The process is correlated with the re-oxidation process at P'1.

Secondly, after passing -250 mV, the process which leads to the increase and the shift of the peak system P1/P'1 is assumed to be related to a stable double adlayer formation. That can explain why P1 and P'1 have almost double heights compared to those in the stacking monolayer phase.

Thirdly, similar to the DBV experiment, P2 is attributed to the chloride desorption process, starting just at the onset of the HER regime (about -350 mV) and completing at a potential of about -420 mV. These potential values fit with the chloride desorption process observed in the experiments with DBV molecules.

The structure of the DPV adlayer, the evidence proving the double layer when passing -250 mV, and the chloride desorption/readsorption processes will be represented in the next parts discussing STM results.

6.3 Structural determination

In the previous part, we have already discussed the redox behavior of DPV cations on chloride modified Cu(100), inferring that there might be 3 main processes or reactions of the system within the copper potential window. The aim of this part is to demonstrate the concommittant structural characteristics of the DPV adsorption.

Following the DBV experiment, after exchanging the pure supporting HCl electrolyte for the DPV^{2+} containing solution at potentials more positive than the main redox waves in the CV, we expected the presence of the dicationic DPV^{2+} species both in solution and at the surface. But with an initial starting potential at 0 mV, the DPV monolayer phases which are present on c(2 x 2)-Cl/Cu(100) differ significantly in their structural appearance, in that DPV adsorption leads exclusively to a stacking phase (Fig. 6.5). This observation appears surprising since this stacking motif has been identified as a structural 'fingerprint' for the presence of mono-reduced viologen species but not for the presence of adsorbed viologens in their di-cationic redox state [132, 133]. That stacking phase remains unchanged even when passing

P1 to more negative potential. Obviously, this DPV adlayer corresponds to mono-reduced viologen species. At the surface DPV^{2+} dications are so active that they are immediately reduced upon adsorption at potentials even above P1.

Due to symmetry reasons the DPV stacking phase occurs in two rotational domains rotated by 90^0. The nearest neighbor distance (NND) of DPV entities within these stacking chains amounts to NND_{DPV} = 0.36 ± 0.02 nm which is identical to the NND of the underlying chloride lattice of $NND_{c(2\times2)\text{-}Cl}$ = 0.362 nm and close to the intermolecular spacings of monoreduced DBV species on both the c(2×2)-Cl/Cu(100) surface and the chloride-free HOPG (see Sec. 5.6). Assuming that the redox-active bipyridinium groups are imaged brighter in the STM experiment than the phenyl groups are most likely located within the 'darker grooves' of the stacking phase (Fig. 6.5c). The inter-chain distance amounts to d = 1.88 ± 0.02 nm and compares well with the length of the DPV molecules (Fig. 4.5). An interdigitation of the phenyl groups of DPV entities of adjacent DPV stacking chains can therefore be ruled out. However, from the STM images alone it cannot be concluded whether the aromatic rings of the central bipyridinium unit are oriented perfectly perpendicular to the surface or whether their plane is slightly tilted.

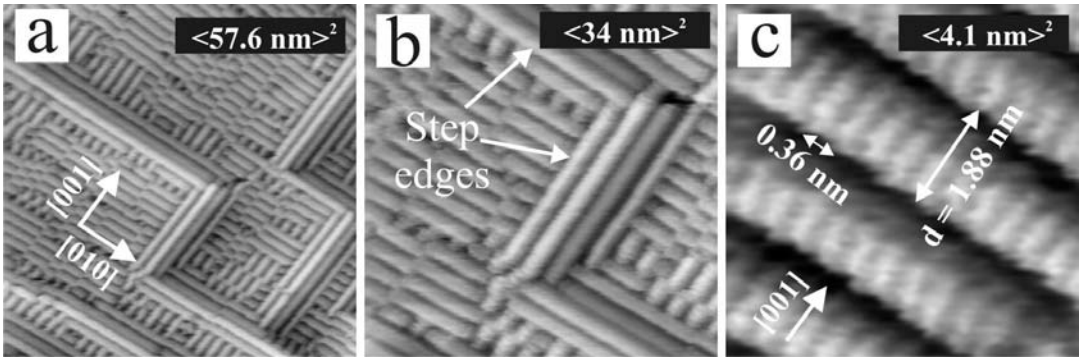

Figure 6.5: Surface morphology of the DPV stacking phase on c(2 x 2)-Cl/Cu(100) at high potentials, E = 0 mV: a) I_t = 0.6 nA, U_b = 250 mV; b) I_t = 0.6 nA, U_b = 250 mV, c I_t = 5.0 nA, U_b = 250 mV.

A distinct structural characteristic of this DPV phase is its typical behavior at step edges which is different from the DBV stacking phase (pointed out in Fig. 6.5b). The DPV stacking chains are preferentially oriented along the substrate [100] directions. The alignment of substrate steps along the [100] directions is clearly indicative for the presence of the c(2×2)-Cl layer underneath. It is worth mentioning that the lateral order of the DPV stacking phase is particularly well developed close to the mono-atomically high substrate steps. This results in two almost defect-free stacking chains running parallel on either side of these step edges, i.e. the upper and the lower side.

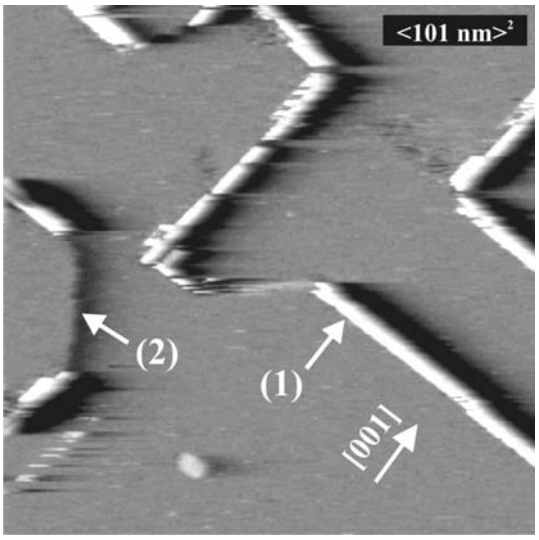

Figure 6.6: Selective decoration of [100] steps in the DPV submonolayer regime, I_t = 0.1 nA, U_b = 350 mV, E = -150 mV. The actual $DBVCl_2$ solution concentration was 10^{-6} mol/l.

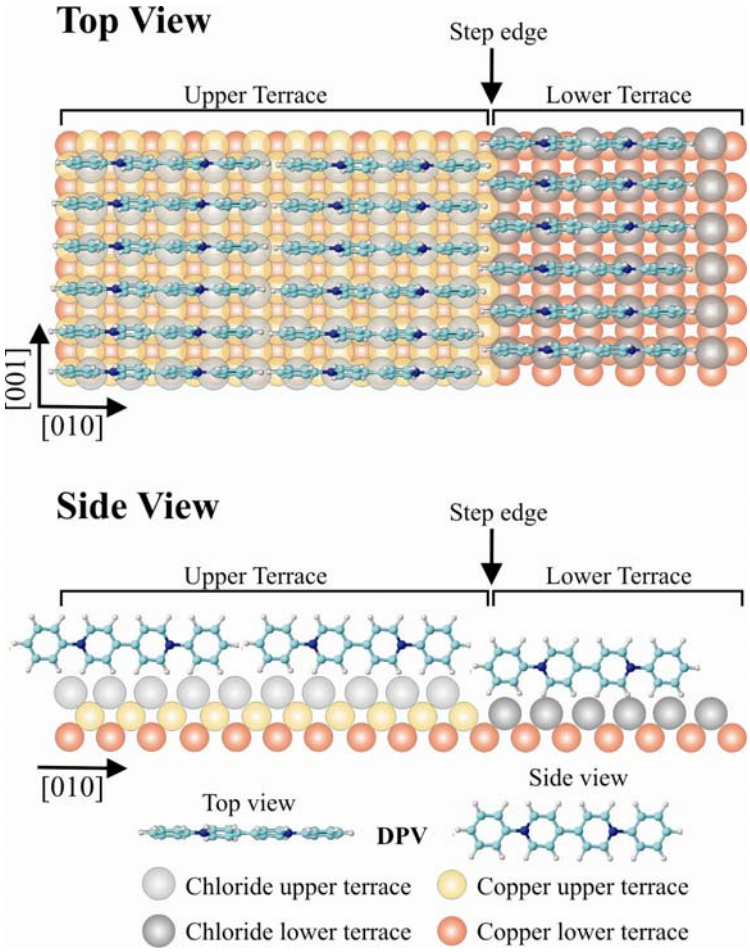

Figure 6.7: Structure model of the $(DPV^{\bullet+}_{ads})_n$ stacking phase on the c(2×2)-Cl/Cu(100) layer.

The specific affinity of DPV towards substrate step edges can further be demonstrated by using low concentration DPV solutions (Fig. 6.6). Under these experimental conditions no condensation and lateral ordering of DPV is observed on terraces. Only step edges that are oriented parallel to the substrate [100] directions are selectively decorated by DPV stacking chains (see white arrows '1' in Fig. 6.6), while step edges oriented along other crystallographic directions, e.g. [110], remain uncovered in this initial stage of the DPV phase formation (see white arrow denoted by '2' in Fig. 6.6). Each DPV chain in contact with a substrate [100] step contains DPV molecules that are oriented with their main molecular N–N axis perpendicular to the respective step edge and are therefore parallel to one of the [100] directions.

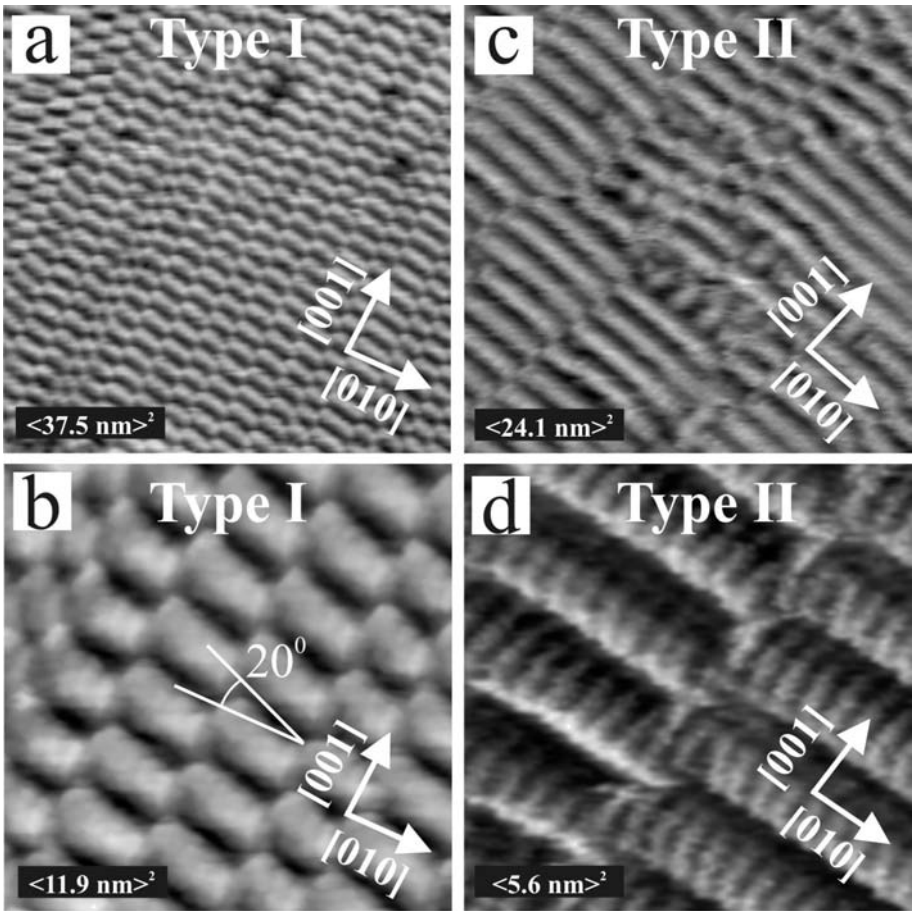

Figure 6.8: Different types of DPB stacking phases, (a)-(b) Type I: I_t = 0.2 nA, U_b = 300 mV, E = 0 mV; (c)-(d) Type II: I_t = 5.0 nA, U_b = 300 mV, E = 0 mV.

There is a clear preference of DPV for the lower sites at step edges which become decorated first before the corresponding upper sites of the step edges are populated (Fig. 6.6). The observed preference of the adsorbed DPV molecules for the substrate steps explains the strong inhibition effect of DPV on the copper dissolution and re-

deposition reaction as revealed by the voltammetry (Fig. 6.1). The structure model of the DPV stacking phase on the c(2×2)-Cl/Cu(100) layer is shown in Fig. 6.7.

The stacking phase in Fig. 6.5 is stable, remaining unchanged upon going towards more negative potentials until reaching the HER regime. However, there is an exception. Because at initial potentials higher than P1 (typically 0 mV), there can be found two structures of DPV stacking phase, namely Type I and Type II shown in Figs. 6.8a,b and c,d respectively. Normally, the coverage of Type I structure is much smaller than Type II and can be seen as small domains surrounded by Type II structure. In comparison with the typical step edges oriented in the substrate [100] directions, it appears that in both types of structures the bipyridinium groups are parallel to the [100] directions, however the orientations of the DPV stacking chains as a whole in the two structures are different. The dominant Type II stripe has a structure similar to the DPV stripes at step edges, therefore it is also parallel to the [100] directions of the Cl rows underneath (Figs. 6.10a,b). On the other hand, the Type I stripe propagation direction encloses a characteristic angle of $\alpha = 20^0 \pm 1^0$ with one of the main symmetry axes of the chloride lattice (Fig. 6.8b). Therefore, we propose structure models for both Type I and Type II that assume DPV entities being adsorbed in a so-called 'edge-on' geometry with the molecular N–N-axes parallel to the surface (Fig. 6.9). And since the preferential adsorption and orientation of DPV molecules at [100] oriented step edges even with very low DPV containing concentration is already known, we expect a higher electrochemical stability of Type II than that of Type I.

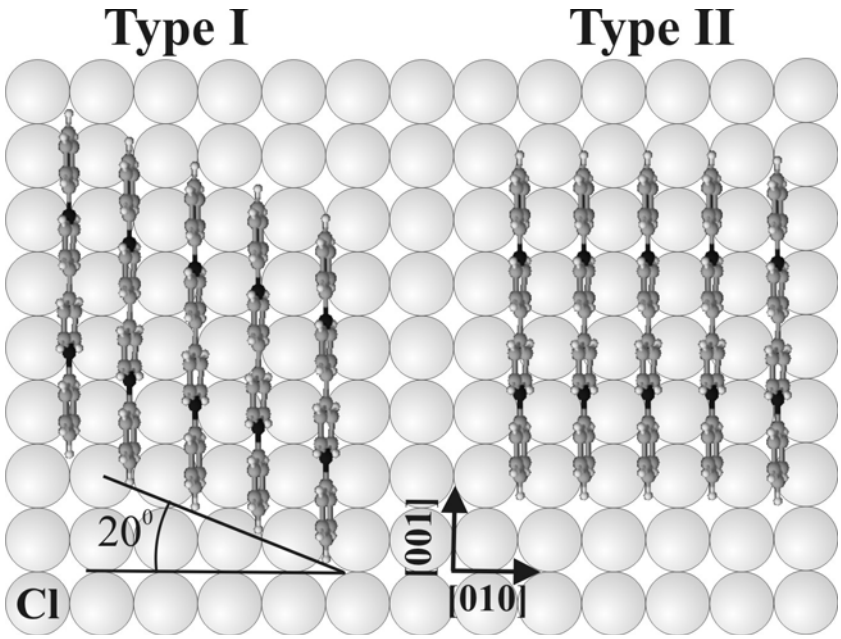

Figure 6.9: Preliminary structure models of both types of the DPV stacking phase.

The explanation for the presence of two stacking DPV structures in comparison to only one stacking phase of DBV adsorption takes into account their different conformations with respect to the chloride lattice. As mentioned above, the inter-DPV-chain distance amounts to d = 1.88 nm and that of DBV is only 1.82 nm (see Sec. 5.3.2) fitting well with the length of the molecules of 1.77 nm and 1.55 nm, respectively (Fig. 4.5), while the NND of the underlying chloride lattice is 0.362 nm. Therefore the distance between two DBV stripes is almost perfectly 5 times as much as the NND of the chloride lattice while that distance of DPV stripes is longer than the length of 5 adjacent chloride lattice atoms. Obviously, for the stacking phases the DBV stripes fit better with respect to the chloride lattice than the DPV ones explaining that the ordering of the monolayer DBV stacking phase (see Fig. 5.20) is found much better than that of DPV. The stacked DPV monolayer is divided in small domains and even the stripes of the Type II phase are not perfectly parallel to one another as seen inside the white dotted circle in Fig. 6.10. This imperfectly-ordered stacking phase structure is typical for DPV adsorption on the chloride modified Cu(100) substrate.

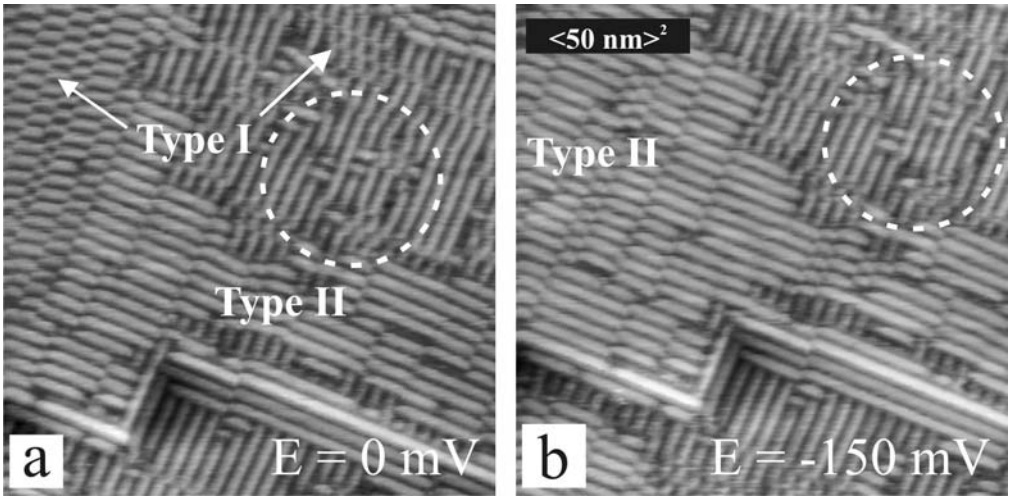

Figure 6.10: DPV stacking structures and the phase transition from Type I structure to more stable Type II phase upon passing P1, 50 x 50 nm, I_t = 0.2 nA, U_b = 300 mV, (a) Type I presence, E = 0 mV; (b) Type II mono layer, E = -150 mV.

Fig. 6.10a shows the STM results of DPV stacking phases at an initial adsorption potential of 0 mV. The structure represents both Type I and Type II phase. The surface morphology is not perfectly-ordered but is stable in the positive potential range before reaching the solution reduction peak P1 ($P1_{max}$ at about -120 mV). At the same area, passing P1, a phase transition only from Type I to Type II phase happens while surrounding Type II is still stable, forming a full monolayer of Type II stacking phase (Fig. 6.10b). Once transformed to Type II phase, the structure is stable even when scanning the potential back to the very positive regime above P'1. That means

this transition is irreversible and as expected the Type II phase has a higher electrochemical stability than the Type I stacking. After obtaining a full monolayer of Type II stacking phase, the surface morphology keeps stable in a broad regime from the onset of CDR as positive limit to the potential below P1 at -250 mV as negative limit.

As mentioned in the previous CV part, the potential value of -250 mV is critical in that it causes even a dramatic change of the reductive reaction peak system P1/P'1, which raises the question of what happens to the morphology of the DPV adsorption layer.

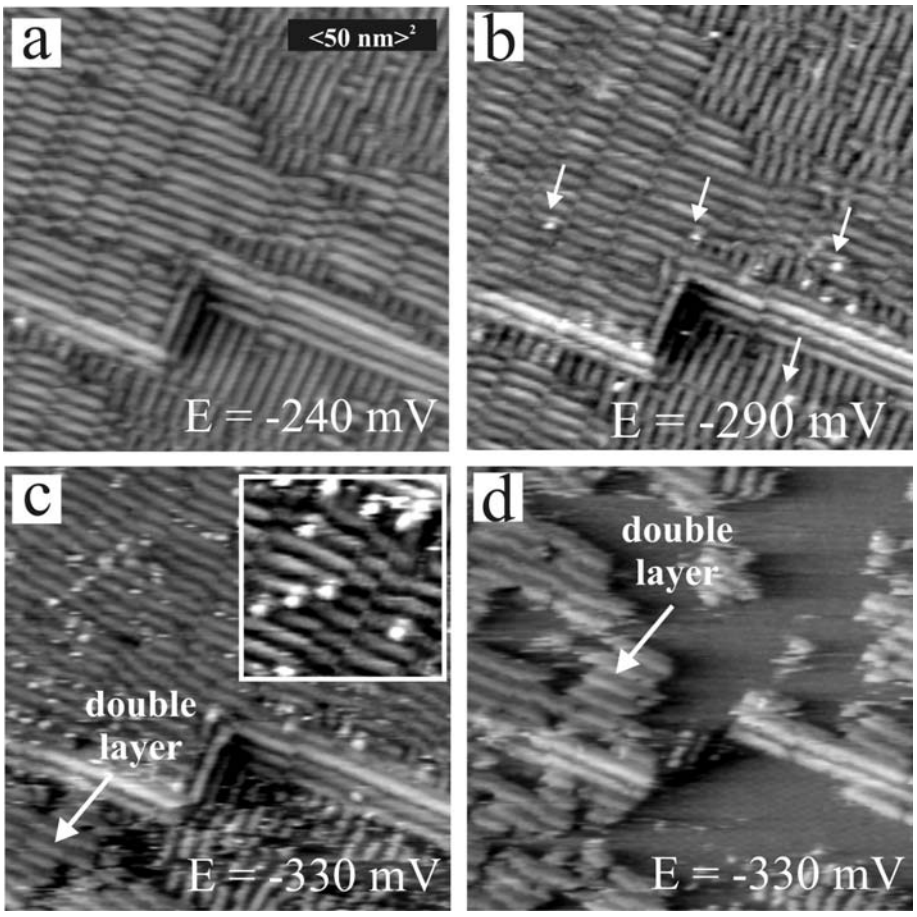

Figure 6.11: Potential-dependent series of STM images showing the structural change of the DPV stacking phase at potentials below -250 mV, (a)-(c) I_t = 0.2 nA, U_b = 300 mV, the in-set in (c) represents an enlargement of (c) showing the preferred second-layer adsorption of reduced DPV species in the 'darker' grooves of the DPV stacking monolayer phase

Fig. 6.11 shows the surface morphology of the DPV adlayer as a function of on-going potential changes to more and more negative potentials below -250 mV. At -240 mV (Fig. 6.11a), the DPV adlayer is still a full monolayer of Type II phase,

however when passing -250 mV, many bright dots on top of the previous Type II phase start to appear as indicated by white arrows in Fig. 6.11b. The lower the potential, the more dots appear. The in-set in Fig. 6.11c represents a zoom-in area of the surface, showing more details of these dots concerning their concentration, size and position on top of the previous DPV stacking monolayer phase. Obviously, the size of the dots is equal to the width of one DPV chain, and all dots stay in the darker grooves or the space between two adjacent DPV chains underneath. Therefore, these dots are assigned to be new reduced $DPV^{\bullet+}$ species adsorbed on top of the stable DPV stacking monolayer phase starting to form the second layer, and the preferred place of new second layer $DPV^{\bullet+}$ species is between DPV chains of the first layer. Fig. 6.11c also reveals an area indicated by a white arrow where there is a change of surface morphology in spite of the unchanged structure. That area denotes the formation of other reduced DPV chains above the first layer with the same structure as building blocks for the second layer. It is worth noting that in the STM image of Fig. 6.11c, the second layer area (marked by arrow) is on the down step terrace where the effect

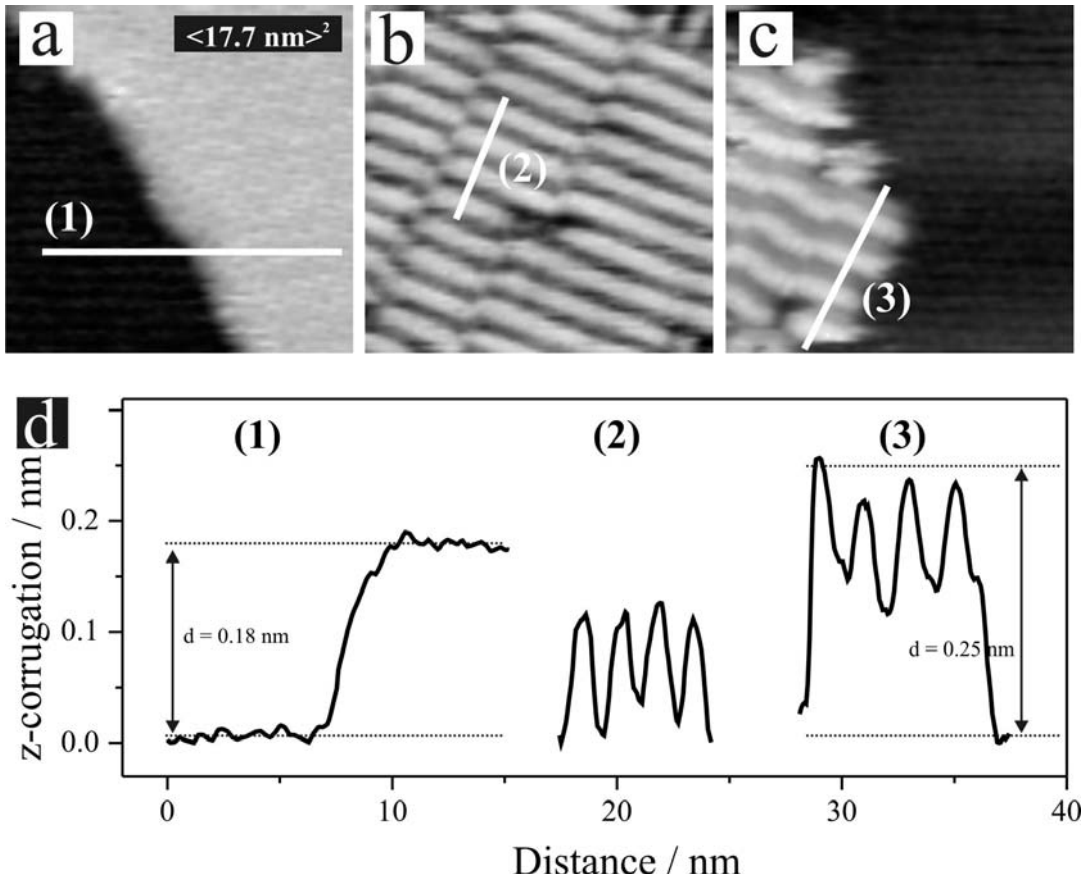

Figure 6.12: (a) Mono-atomically high step edge, (b) Periodicity of the stripe pattern in the full monolayer, (c) Periodicity of the stripe pattern in the sub-monolayer regime, I_t = 0.2 nA, U_b = 300 mV, (d) Cross sections along the white lines in (a)-(c).

of STM tip-removal is much less than on the upper one. Thus, it is supposed that at this potential the second DPV stacking adlayer should already grow to a full layer, but due to the STM tip-removal effect at the higher terrace step the new $DPV^{\bullet+}$ species cannot easily adsorb and the surface morphology cannot be imaged accurately in comparison with lower steps or surrounding areas. Fig. 6.11d shows only stripes in the second layer, but unfortunately due to the chloride desorption starting from the potential value of -330 mV, this double layer just appears as sub-layer.

The reduced DPV double layer can explain the change and shift of the peak system P1/P'1 of CV2 in Fig. 6.2. After passing -250 mV, the formation of the double layer on the surface leads to reconstruction of the structure of the interface layer (Fig. 6.4) enforcing the reduction or oxidation process of DPV molecules from solution to occur through this overlayer. Following the CV2 of Fig. 6.2, after passing -250 mV, even if the cathodic limit is set back to -250 mV, the peak pair P1/P'1 is stable and in steady state. Therefore, the DPV double layer is assumed to remain stable in a broad potential regime unless reaching the chloride desorption regime at negative potentials or CDR at positive ones.

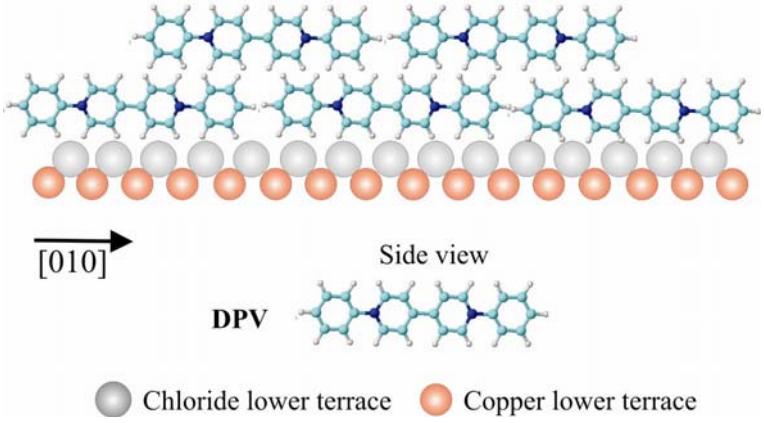

Figure 6.13: Side view structure models of the double layer DPV stacking phase.

Upon chloride desorption starting at a potential value of -330 mV towards negative potentials near the HER, the double layer decays step by step, revealing the bare surface underneath (Figs. 6.11d and 6.12a-c). This process actually provides more insight into the double layer structure. If reduced DPV adsorbs as a full double layer, the STM results show a surface morphology similar to the Type II stacking phase (Fig. 6.12b). Therefore it is difficult to conclude on the double layer structure. However, while decaying during the chloride desorption process (Fig. 6.12c), in comparison with the bare surface makes clear that the imaged DPV chains of this structure are twice as high as a single chain of the Type II monolayer phase (see

corrugation in Fig. 6.12d). In correlation with the height of an atomic step, obviously, the DPV stacking chains along the white line in Fig. 6.12c stay on top of the first DPV stacking layer underneath. Fig. 6.12c also shows besides the top bright DPV chains blurry grooves which are definitely not bare surface but underlying DPV chains. In fact, as seen in Fig. 6.12d, the down DPV chains are showing up as side shoulders of the maxima in profile 3. Therefore, it is concluded that the surface morphology of the double layer structure is almost the copy of the first DPV adlayer with only a very slight change and shift. After all, a structure model of the reduced $DPV^{+\bullet}$ double layer structure is proposed in Fig. 6.13.

6.4 Chloride desorption/readsorption

Previous STM studies already gave evidence for the decaying of the DPV double layer stacking phase (Fig. 6.11d) if the electrode potential decreases below -330 mV in the negative direction and reaches P2 (CV3 of Fig. 6.2) at the onset of HER.

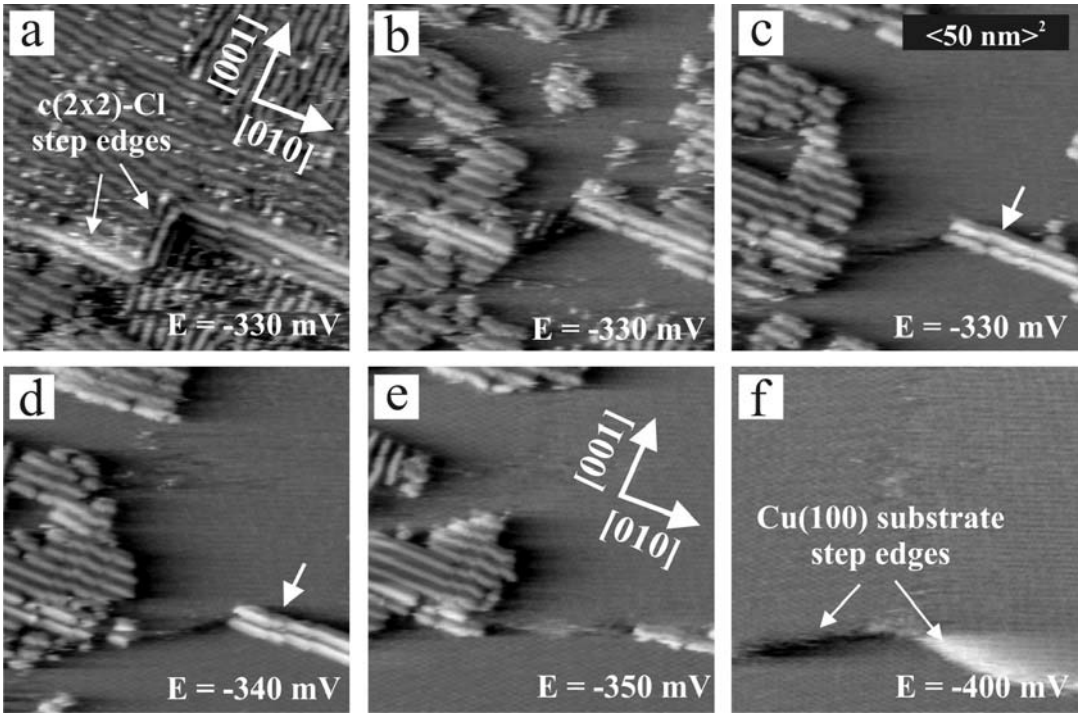

Figure 6.14: Potential-dependent series of STM images showing the chloride desorption process of the double layer DPV stacking phase, (a)-(f) I_t = 0.2 nA, U_b = 300 mV.

Fig. 6.14 represents more details in a potential dependent series of STM images showing the decaying process of the DPV double layer. The potential regime of this decaying process starts at potential of -330 mV and completes at about -400 mV. As

proved in part 5.4.2, also DBV adsorption on chloride modified Cu(100) showed a chloride desorption process in the potential regime from -320 mV to -430 mV (see Fig. 5.31). Therefore, in the similar potential regime, the decaying process of the DPV double layer stacking phase is also related to the chloride desorption process. However, in spite of an order/disorder phase transition in the case of DBV, the chloride desorption from the DPV covered surface results in a decaying process in which the DPV double adlayer phase is *removed* step by step from the surface revealing the bare substrate underneath (Figs. 6.14a-f). Thus, in comparison with the CV in this regime (CV3 of Fig. 6.2), it can be reinforced that the peak P2 corresponds to the chloride desorption process.

The surface morphology of the DPV adlayer before chloride desorption (Fig. 6.14a) shows step egdes with the typical 90^0 step edges of the c(2 x 2)-Cl lattice underneath (see Sec. 3.4.2 for more detail). However, during the chloride desorption process, not only the DPV stacking adlayer on terraces decays but also the straight step edges are removed gradually to become the step edges of the bare p(1 x 1)-Cu substrate as indicated by arrows in Fig. 6.14f. That means the c(2 x 2)-Cl template is lost causing the changes of the adsorbed viologen layers above, namely the disorder in the DPV phase or the total decaying of DPV layer.

Figs. 6.14c,d again prove the [100] oriented step edge being preferred for adsorption of DPV molecules as pointed out by the white arrow. The typical DPV stacking chains at step edges parallel to [100] direction seem to be stronger adsorbed and act as inhibitors even for the c(2 x 2)-Cl desorption process.

Although in CV3 of Fig. 6.2 only the reduction peak P2 appeared without its oxidation peak (or very small at HER if at all), the chloride desorption phase transition, demonstrated by STM results, is a reversible process. Fig. 6.15 represents the readsorption process when scanned back towards in the positive potential regime. Beginning with the bare substrate at very negative potential, and going back to the positive regime, the c(2 x 2)-Cl structure reappears together with the readsorption of DPV stacking chains. And the readsorbed DPV stacking phase is directly the stable double layer DPV structure (indicated by blurred chains aside the bright top ones). This process starts from step edges and defects, then spreading across the whole surface. It is worth noting that the process takes place at very low speed, starting at a potential value of -320 mV and completing at -110 mV, revealing a great hysteresis of ΔE = 210 mV, while the chloride readsorption process of DBV had a much smaller hysteresis of ΔE = 62 mV (see Sec. 5.2.1).

As mentioned in the CV part, by restricting the cathode potential limit to -500 mV, the CV3 of Fig. 6.2 shows surprisingly that the peak system P1/P'1 is now not the same as in CV2 but seems to be shifted back close to that of CV1 in respect to intensity and position. The low speed chloride re-adsorption process with DPV can explain that phenomenon. With the scan speed for the CV of dE/dt = 10 mV s^{-1} which is much

faster than the potential change of STM experiments, we suppose that until reaching the oxidation peak P'1, the surface is still not fully covered by the double layer DPV stacking phase or just fully covered by areas of both double layer and single layer phases. The interface region on the surface is somehow in between of a monolayer and a double layer DPV stacking phase. Therefore, in Fig. 6.2, the peak system P1/P'1 of CV3 is expected to appear in between of these of CV1 and CV2 with respect to intensity and position.

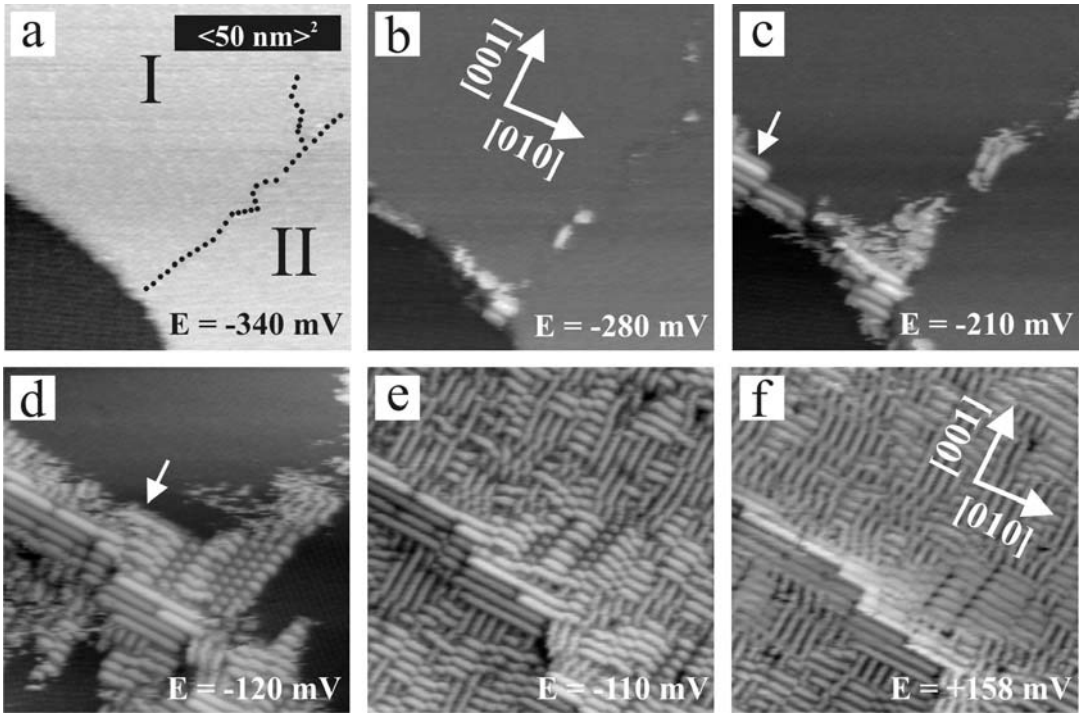

Figure 6.15: Potential-dependent series of STM images showing the chloride readsorption process of the double layer DPV stacking phase, (a)-(f) I_t = 0.2 nA, U_b = 300 mV.

With the low changing potential speed of STM experiments, the chloride readsorption process ends up with a fully-covered DPV double layer phase at a potential value of -110 mV (Fig. 6.15e). And this structure then remains stable even when passing the oxidation peak P'1 to very positive potentials and even in a broad range of the Cu potential window.

6.5 Copper dissolution in the presence of the DPV adlayer

As discussed in the CV parts, the DPV layer has a strong impact on the CDR, i.e. the potential of the dissolution reaction is considerably shifted to higher potentials

($\Delta E \approx 60$ mV) with respect to the CDR in the pure supporting electrolyte (see Fig. 6.1). That can be explained by the inhibiting effect of DPV on the CDR.

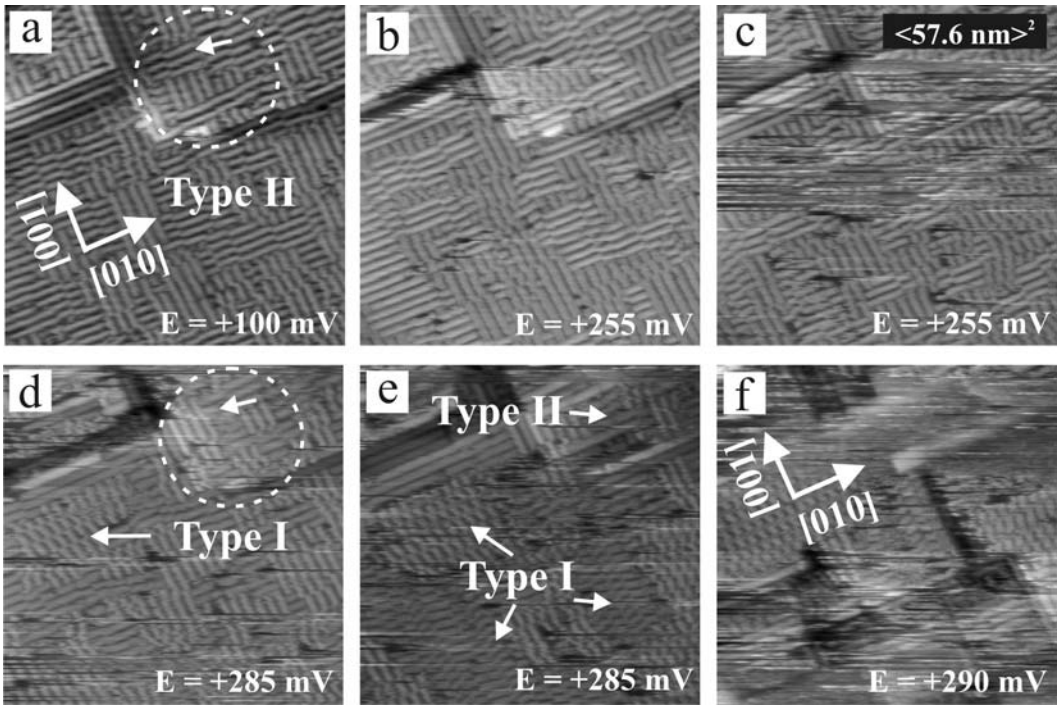

Figure 6.16: Potential-dependent series of STM images at the on-set of CDR, (a)-(f) I_t = 0.2 nA, U_b = 300 mV.

Fig. 6.16 shows a potential dependent series of STM images at the on-set of CDR, beginning with a full double layer of the stable DPV stacking phase (Fig. 6.16a). The copper dissolution reaction starts at the potential of +255 mV. It is worth to note that the copper dissolution reaction of a DBV covered surface started at the potential of just +120 mV (see Sec. 5.5). The huge difference of the inhibiting effect of the two molecules is related to the structural stability of the adsorption layers. At the on-set of CDR on the chloride modified Cu(100) template, the structure of the DBV adlayer is the rather open dication DBV^{2+} cavitand phase, while the more active DPV molecules in the form of the radical cations $DPV^{\bullet+}$ form the double layer stacking phase which is much denser and particularly stable at step edges.

However, similar to the DBV case, at the on-set of CDR, viologen molecules immediately re-adsorb on the newly created Cu areas thereby maintaining an always full adlayer in spite of the strong Cu dissolution reaction taking place underneath. Because of the new adsorption of viologen during the Cu dissolution reaction, the surface morphology can change. As marked by arrows inside the white dotted circles of Figs 6.16a,d, the same structure of the DPV stacking Type II phase is observed but the detailed arrangements are different. Interestingly, at some areas, the new DPV

adsorption forms the less stable DPV stacking Type I phase as indicated by arrows in Figs. 6.16d,e. Obviously, the Cu dissolution reaction causes the removal of the stable DPV stacking phase above, then DPV molecules in solution readsorb to form the less stable stacking Type I phase.

6.6 Summary

In this chapter the studies of DPV adsorption on a chloride modified Cu(100) surface was presented, using also the combination of CV and EC-STM methods.

The CV experiments indicate that there are 3 different reactions or phenomena taking place within the copper potential window:

- The first electron transfer reaction leading to the peak system P1/P'1 relates to the reduction/reoxidation between the dication DPV^{2+} and $DPV^{\bullet+}$ species in solution.
- After passing a critical potential value of -250 mV the peak system P1/P'1 increases and shifts to more positive potentials.
- The chloride desorption process related to the peak P2 in the HER regime.

The STM experiments provide complementary information about the corresponding surface structures and phase transitions related to these three processes.

With initial adsorption at high potential, surprisingly the DPV cannot be adsorbed and stabilized in its dicationic form on the chloride-modified electrode surface. Instead, DPV^{2+} species instantaneously react to the corresponding radical cation $DPV^{+\bullet}$ at the surface followed by the formation of a condensed $(DPV^{+\bullet})_n$ stacking monolayer phase. A distinct structural characteristics of this DPV stacking phase is its typical behavior at step edges. There the DPV stacking chains are always preferentially oriented along the substrate [100] directions, forming typical double rows along the edges. Furthermore, two modifications of the DPV stacking monolayer phase are found on the terraces, namely Type I and Type II, for which detailed structural models have been proposed. Of the two structures, Type I is found to be less stable than the Type II phase, because by passing the first reduction peak P1, all Type I structure transforms into Type II, creating a homogeneous DPV stacking monolayer surface.

Upon scanning even further cathodically and passing the critical potential value of -250 mV, more $DPV^{\bullet+}$ species adsorb on the surface and form another DPV stacking layer, resulting in a stacking double layer phase. The DPV chains of the second layer are proved to lie on the troughs between two chains of the first stacking layer. Once

formed the double layer structure is stable on the surface in the whole copper potential window despite the occurrence of electron transfer reaction through it. The stability of the double layer phase is also the reason for the strong inhibition effect for the copper dissolution reaction (CDR), which is shifted to much more positive potentials.

Scanning even further in the negative direction until reaching the chloride desorption peak P2, the DPV double layer phase co-desorbs together with the chloride leaving the bare substrate behind. This also explains that no inhibition effect is observed in the HER regime of the CV data. The co-desorption process of chloride and the DPV double layer is found to be quasi-reversible. However, the reverse phase transition for the readsorption of the double layer phase occurs at very slow speed, showing a great hysteresis of $\Delta E = 210$ mV.

Chapter 7

Comparison between DBV and DPV - “non-reactive” conditions

7.1 Cyclic voltammetry

In order to compare the redox behavior of DBV and DPV adsorbed on chloride modified Cu(100) under “non-reactive” condition, based on the differences of their CVs, we summarize here the information which was presented in the parts 5.2 and 6.2.

Fig. 7.1 displays the voltammetric behavior of Cu(100) in the absence (CV 1) and the presence (CVs 2 and 3) of viologens. CV 1 represents the standard CV of Cu(100) in pure 10mM HCl solution revealing the narrow copper potential window, which is confined at the anodic limit by the copper dissolution reaction (CDR) and the corresponding re-deposition reaction in the reverse potential scan. At the cathodic limit, it is the on-set of the HER which confines the copper potential window.

As described in previous parts, we could assign the peak systems P1/P’1 with the first electron transfer reaction from the dication to the corresponding radical cation species of both studied viologens (Eq. 4.1). The peak P1 of DBV appears at $P1_{max}$ = −290 mV (CV2a in Fig. 7.1), otherwise, the first reduction peak P1 of DPV already appears much earlier at $P1_{max}$ = −128 mV (CV3 in Fig. 7.1) with a resulting difference of ΔE = +162 mV between P1(DBV) and P1(DPV). The redox processes of DPV are shifted to higher potentials compared with those of DBV, including P’1 in the reverse scan of CV3 which corresponds to the re-oxidation of the $DPV^{\bullet+}$ species to the corresponding water-soluble DPV^{2+} species. Therefore, from a comparison of CV 2a and 3 in Fig. 7.1, it becomes obvious that DPV is electrochemically more reactive than DBV. Furthermore, STM experiments showed surprisingly different results for the adsorption of both viologens in the potential regime more positive than the first reduction peaks P1. In this regime the DBV adlayer appears as the dication DBV_{ads}^{2+}

cavitand phase, while the more active DPV directly adsorbs as the radical cation $DPV^{\bullet+}_{ads}$ stacking phase. We can also conclude that while the peak system P1/P’1 of DBV involves the first electron transfer reaction between dication DBV^{2+} and the corresponding radical cation $DBV^{\bullet+}$ in both the bulk solution and the adsorbed surface species, the peak system P1/P’1 of DPV relates only to the bulk process, maintaining the stable $DPV^{\bullet+}_{ads}$ stacking phase adlayer on the surface. Besides the shift of peak pairs P1/P’1 of the electrochemically more active DPV compared to DBV, a further difference which should be noticed between the two P1/P’1 peak pairs of DBV and DPV is the much higher current of P’1(DBV) than P’1(DBV) (CVs 2a and 3 in Fig. 7.1). The reason will be explained in the next section of STM results.

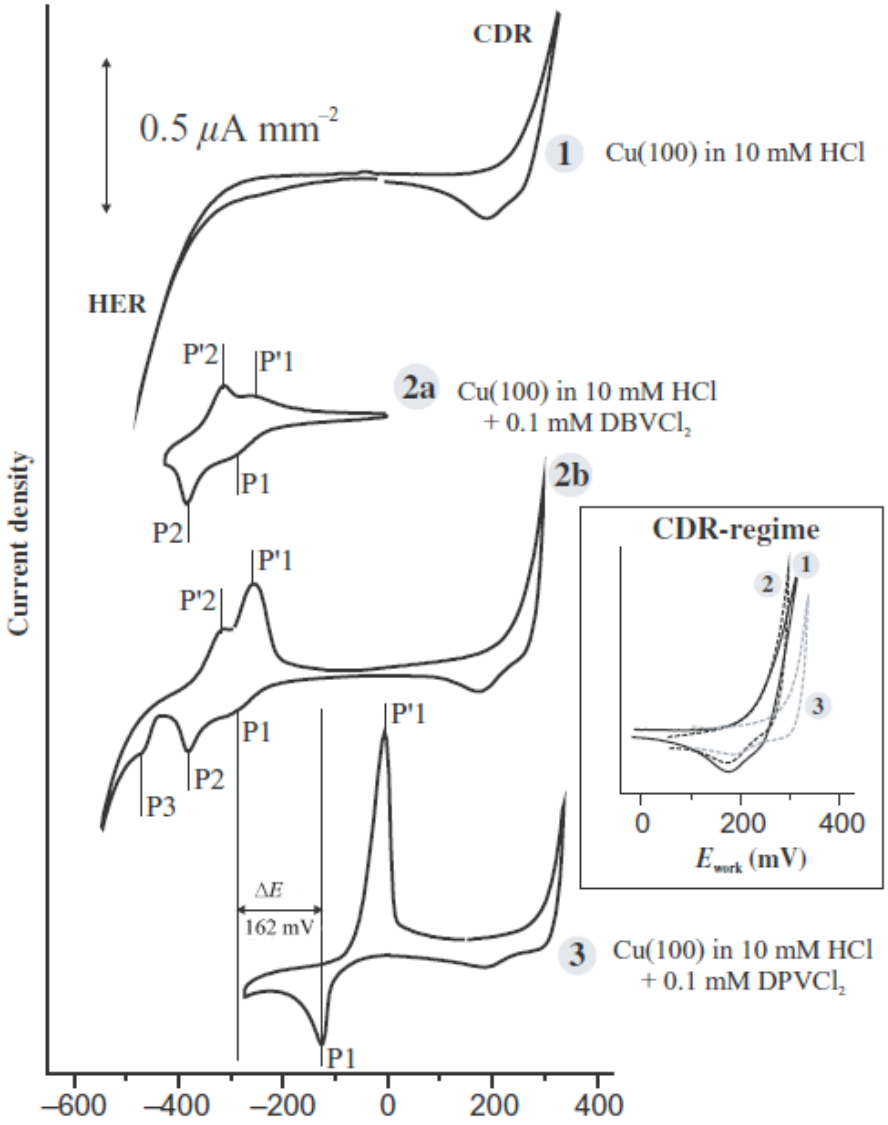

Figure 7.1: Overview of the electrochemical behavior of Cu(100) in the absence and presence of DBV or DPV.

Next we focus on the CVs at the on-set of the CDR regime which are illustrated in the inset of Fig. 7.1. While the CDR in DBV containing electrolyte (CV2) is almost not different from that in the pure supporting electrolyte (CV1), the DPV electrolyte (CV3) causes a big shift to the positive regime with ΔE = +65 mV. It is the strong adsorption of the DPV radical cation stacking phase that is assumed to cause the higher inhibition effect than the DBV dication cavitand phase adlayer at this regime.

Passing P1, in the scan to the negative regime, the CV of DPV soon reaches the HER regime (CV3 Fig. 7.1), while the CV of DBV (CV2b Fig. 7.1) extends much further to negative potentials revealing two more current peak systems P2/P'2 and P3/P'3 ($P2_{max}$ = -380 mV, $P3_{max}$ = -440 mV). As mentioned in Sec. 5.2.1, the peak pair P2/P'2 is assigned to the chloride desorption/readsorption processes and P3/P'3 corresponds to the second electron transfer between the radical cation $DBV^{\bullet+}$ species and the uncharged DBV^{0} molecules. It should be noted that in the CV3 of DPV in Fig. 7.1, the HER regime appears early (starting at the potential of about -330 mV) similar to the pure supporting electrolyte, but going further into the HER regime, the CV of DPV also shows a current wave of the chloride desorption process (P2 of CV3 Fig. 6.2) at the potential of -420 mV. Obviously, the chloride desorption occurs with both viologens, however following the STM results, it is found that in the case of DPV, the chloride adlayer desorbs together with the DPV adlayer revealing the bare substrate surface. Conversely, in the case of DBV, the chloride adlayer desorbs through the adsorbed DBV adlayer causing the structure of an amorphous phase. Indeed, at this negative regime, in contrary to the CDR regime, the DPV adlayer has here almost no inhibition effect, but on the other hand, the DBV adlayer now leads to a much stronger inhibition effect because of the chloride desorption process taking place underneath.

Following the CVs comparison displayed in Fig. 7.1, the surface morphology of DBV and DPV adsorption on chloride modified Cu(100) will also be compared in more detail in corresponding potential regimes listed in the order of potential from the CDR regime (positive) to the HER regime (negative) as below:

1. The potential regime which is more positive than the first reduction peak P1, namely dication regime, including the on-set of CDR regime comparison,
2. The potential regime between P1 and P2 (after passing the first reduction peak until reaching the chloride desorption process), namely radical cation regime,
3. The potential regime which is more negative than P2 of the chloride desorption process (before reaching P3 of DBV), namely chloride desorption regime.

It is noteworthy that with the DBV adsorption on c(2 x 2)-Cl/Cu(100), even the P3(DBV) appears in the CV, while for STM experiments, due to the strong hydrogen evolution reaction, no clear surface has been observed. Therefore there will be no *in-situ* STM comparison for this regime more negative than the second reduction peak P3(DBV).

7.2 *In-situ* STM results

7.2.1 Dication regime

The differences observed in the DBV and DPV redox chemistry find their correspondence also in related surface structure transitions. In order to illustrate this, we focus in the following on the different adsorption behavior of DBV and DPV at potentials above the main redox waves (P1). The DBV and DPV monolayer phases which are present on Cu(100) at potentials more positive than the main redox waves in the CV differ significantly in their structural appearance (see Fig. 7.2).

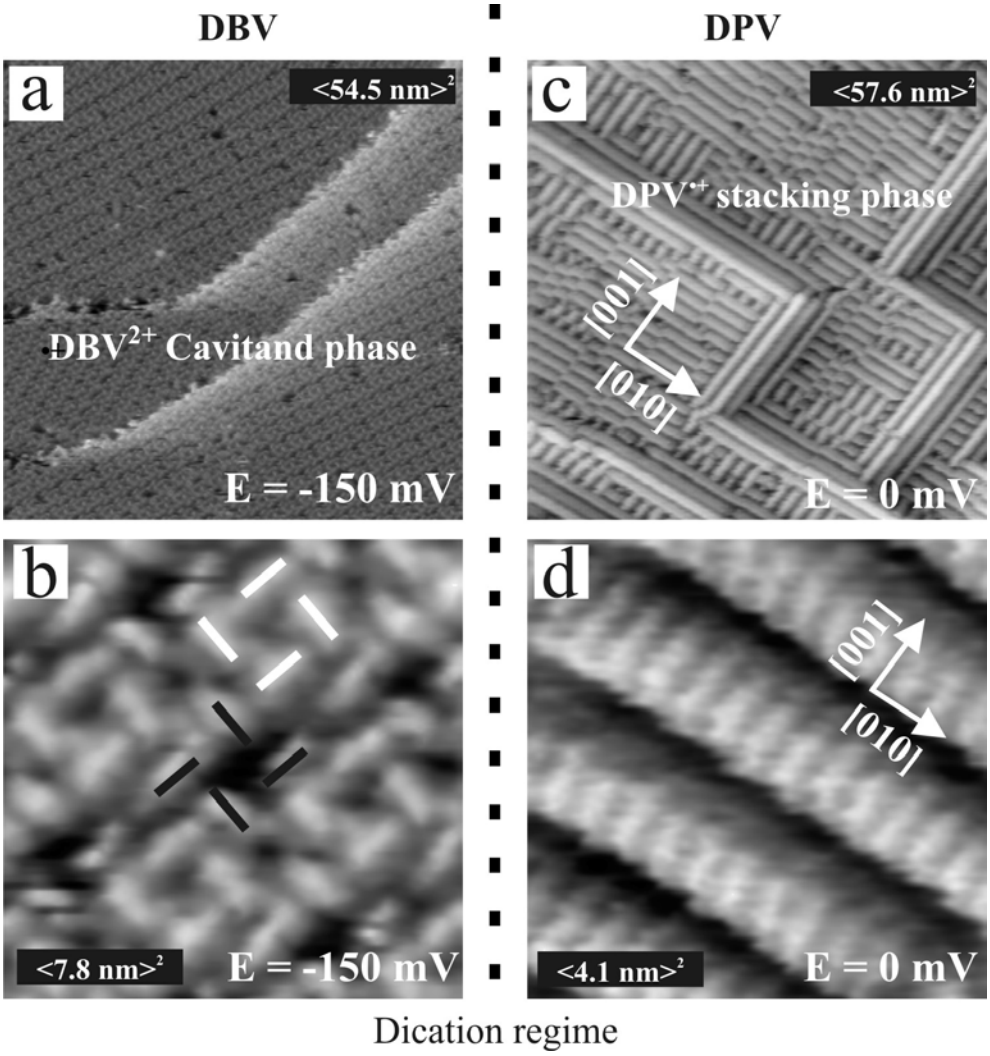

Figure 7.2: Overview of the DBV and DPV phases on the chloride modified Cu(100) surface at high potentials. (a)-(b) DBV^{2+}_{ads} cavitand phase, I_t = 1.1 nA, U_b = 350 mV; (c)-(d) $(DPV^{\bullet+}_{ads})_n$ stacking phase, (c) I_t = 0.6 nA, U_b = 250 mV, (d) I_t = 5.0 nA, U_b = 350 mV.

At a working potential at about -150 mV (before reduction to radical monocation species of both molecules), DBV^{2+}_{ads} appears as cavitand phase, but DPV adsorption leads exclusively to a stacking phase of mono-reduced species or $(DPV^{\bullet+}_{ads})_n$ (Fig. 7.2c and d) in this regime. This means that DBV^{2+}_{ads} cations are so active at the *surface* that they have the reductive reaction already at much higher potentials than the observed P1(DPV) even when their species in bulk solution is still stable DPV^{2+}_{aq}.

While adsorbed, the $(DPV^{\bullet+}_{ads})_n$ stacking phase is distinguished by the typical and strong double row at step-edges. The preferential adsorption of DPV double rows at step edges was described in more detail in the part 6.2. In one experiment, incidentally and inattentively, an STM measurement of DBV adsorbed on chloride modified Cu(100) was contaminated by a trace amount of DPV, resulting in the STM image in Fig. 7.3. With an extremely low concentration, DPV still adsorbed at step-edges as a double row, surrounded by a DBV^{2+}_{ads} cavitand monolayer. That affirms the higher reactivity of DPV than of DBV molecules.

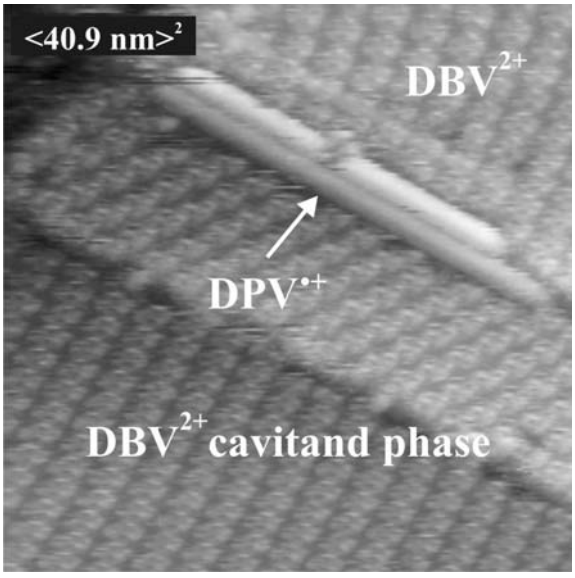

Figure 7.3: Co-adsorption of a trace amount of $(DPV^{\bullet+}_{ads})_n$ stacking phase surrounded by DBV^{2+}_{ads} cavitand monolayer showing the step-edge preferential adsorption of DPV molecules, I_t = 0.1 nA, U_b = 250 mV, E = +25 mV.

A further structural difference between the DPV- and the DBV/Cl/Cu(100) system concerns the inhibition effect at the onset of the CDR (see inset of Fig. 7.1). On the one hand, the cavitand structure of di-cationic DBV species, though perfectly ordered on extended terraces but not aligned parallel to the steps, reveals a large number of defects at step edges (Fig. 7.4a), which cause the di-cationic DBV phase to have almost no inhibition effect on the CDR. On the other hand, as a step-edge

preferential adsorbate, the $(DPV^{\bullet+}_{ads})_n$ adlayer effectively blocks reaction sites for the copper dissolution process, thereby causing the observed inhibition effect (Fig. 7.4b). It is noteworthy that in this positive regime of bulk dication species, the strong adsorption of the face to face $(DPV^{\bullet+}_{ads})_n$ stacking structure also contributes to the inhibition effect better than the open DBV^{2+}_{ads} cavitand phase. While there is no significant difference in the dissolution kinetics of Cu(100) in the pure supporting and the DBV containing electrolyte, we observe an upward shift of the CDR to higher potentials when DPV is present (see the inset CVs in Fig. 7.1). By STM, the CDR shift to positive potential is also observed. In Fig. 7.4a, the CDR of DBV adsorption starts at a potential of +125 mV, but a much higher potential of +290 mV is required to initiate the CDR of the DPV covered surface (Fig. 7.4b).

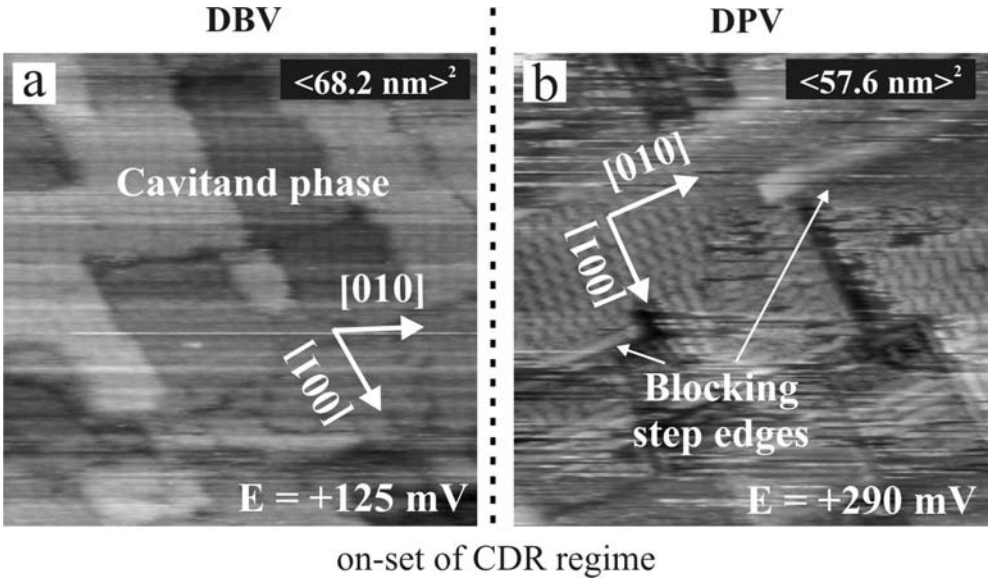

Figure 7.4: STM image comparison of DBV and DPV adsorption at the onset of CDR, (a) I_t = 1.1 nA, U_b = 290 mV; (b) I_t = 0.2 nA, U_b = 300 mV.

7.2.2 Radical-cation regime

Not only are the structural motifs different for the adsorbed DBV and DPV at high potentials (Fig. 7.2), also the potential dependence of the respective monolayer phases reveals distinct differences. While the di-cationic DBV^{2+}_{ads} phase undergoes a phase transition upon passing P1(DBV) resulting in a compact stacking phase similar to the one we observe for DPV already at higher potentials, there are no structural transitions within the observed DPV stacking phase when the main reduction peak P1(DPV) is passed (see Fig. 7.5a, b), indicating that while the P1(DBV) involves both solution and surface reduction, the P1(DPV) correlates with only the bulk solution process.

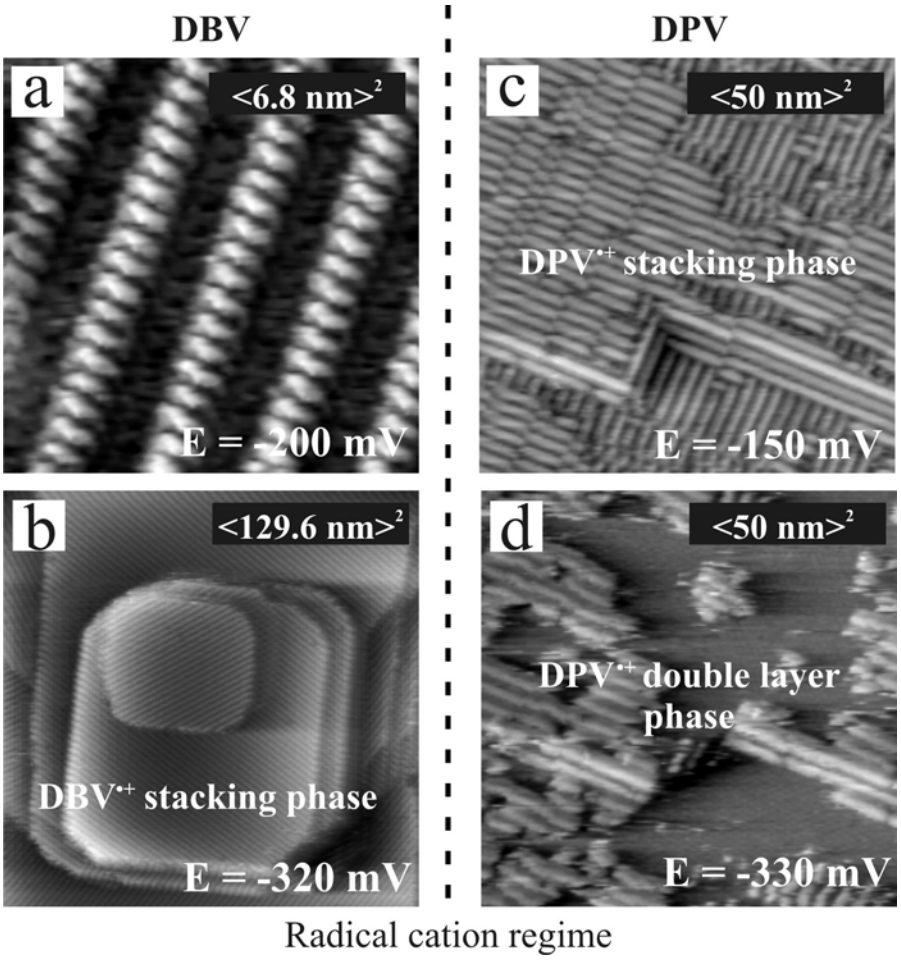

Figure 7.5: STM images showing the structural difference between radical cation DBV and DPV stacking phases at potentials lower than P1 of CVs 2a and 3 in Fig. 7.1: (a)–(b) $(DBV^{\bullet+}_{ads})_n$ stacking phase, (a) I_t = 40 nA, U_b = 28 mV, (b) I_t = 0.2 nA, U_b = 219 mV; (c) $(DPV^{\bullet+}_{ads})_n$ stacking phase, I_t = 0.2 nA, U_b = 300 mV, (d) $(DPV^{\bullet+}_{ads})_n$ double layer phase while passing -250 mV to the negative regime, I_t = 0.2 nA, U_b = 300 mV.

Passing P1, in the radical cation regime, the structures of DBV and DPV adlayer are both stacking phases of radical cation species (Figs. 7.5a,b and c,d). Generally, these structures are quite similar concerning the polymerization of radical cations to chains of face to face species. However, the main observable difference between these structures is at step edges. In the case of DPV, at step edges is the typical double row structure which is always parallel to step edges (or [100] orientation direction) closing the edges of every terrace (Fig. 7.5c), on the other hand, the DBV stacking phase has nothing special at the step edges (Fig. 7.5b). Another difference between the DBV and DPV adlayers is that while the well-ordered DBV stacking phase extends over the whole surface with only one structure, there are two types of DPV stacking phases in the potential regime higher than -250 mV which are described in more detail in Sec. 6.3. The interchain distances of DBV and DPV stacking phases are

different with 1.82 nm for DBV and 1.88 nm for DPV, which fit well with the length of the molecules of 1.55 nm and 1.77 nm (see Figs. 4.3 and 4.5), respectively. The relation between the different interchain distances and the ordering of DBV and DPV stacking phases has already discussed in Sec. 6.3.

The DBV stacking phase is stable in this radical cation regime, but within this regime, there is a critical potential of -250 mV which causes a change of the DPV stacking phase. By sweeping to negative potential below -250 mV, the DPV stacking phase transforms into the DPV double layer phase (Fig. 7.5d) which is a combination of two normal stacking layers (see Sec. 6.3 for detail). The double layer formation also causes an increase of the height of the oxidation peak P’1(DPV) in the reverse potential sweep back to positive potentials. Therefore, the phenomenon of the DPV double layer phase has been assumed to cause the height difference of P’1(DBV) and P’1(DPV) of CV2a and CV3 respectively in Fig. 7.1, as mentioned in the CV part.

7.2.3 Chloride desorption regime

Continuing sweeping to negative potentials, we find the peak system P2/P’2 in the CV2a (DBV) of Fig. 7.1 which could be attributed to the quasi-reversible desorption/readsorption of chloride anions through the viologen film being accompanied by order/disorder phase transition within the $(DBV^{\bullet+}_{ads})_n$ stacking phase, but on the other hand, the CV3 (DPV) already reaches the hydrogen evolution regime. The difference is also observed in STM results.

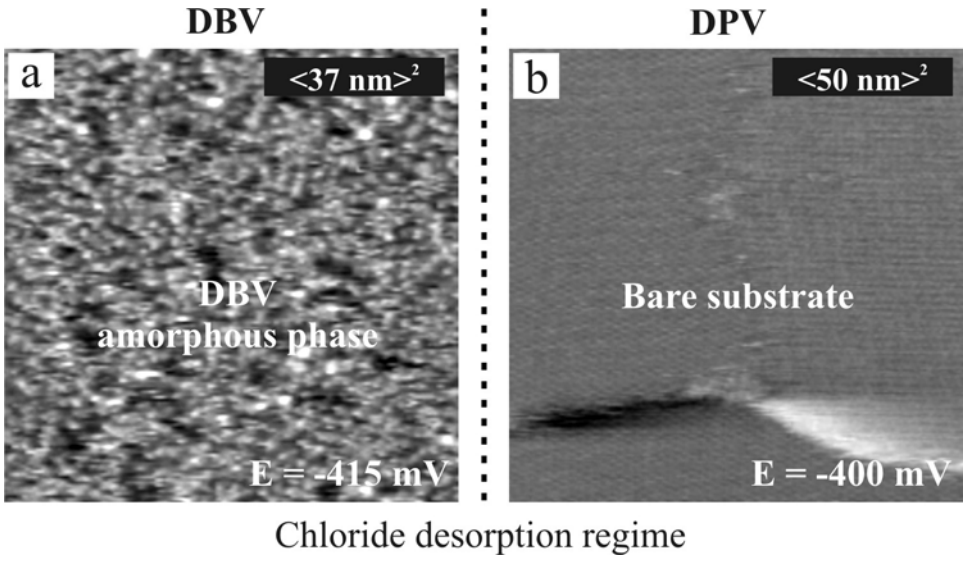

Figure 7.6: STM images show the surface morphology after chloride desorption in the negative regime: (a) amorphous $DBV^{\bullet+}_{ads}$ phase, I_t= 0.2 nA, U_b = 286 mV; (b) bare surface after codesorption of DPV and chloride, I_t= 0.2 nA, U_b = 300 mV.

Fig. 7.6 is the structural comparison of DBV and DPV adsorption at potentials below the chloride desorption peak P2. While the $DBV^{\bullet+}_{ads}$ species still arranges disordered on the surface in the form of an amorphous phase (Fig. 7.6a), the $(DPV^{\bullet+}_{ads})_n$ adlayer is already completely removed by chloride desorption revealing the bare surface underneath (Fig. 7.6b). This explains the strong downward shift of the HER to lower potentials when DBV is present (see the CV1 and 2b Fig. 7.1). The amorphous phase, though mobile, still acts as an effectively blocker for the hydrogen evolution reaction, thereby causing the observed inhibition effect. The chloride desorption of both DBV and DPV adlayer are quasi-reversible. In the anodic potential sweep backwards, the amorphous phase of DBV transforms back to the $(DBV^{\bullet+}_{ads})_n$ stacking phase and also the stable $(DPV^{\bullet+}_{ads})_n$ double layer phase adsorbs again on the substrate.

7.3 *Ex-situ* XPS results Comparison

In this part, we exclusively focus on the chemical nature of the respective viologen monolayers at high potentials above the main redox waves.

7.3.1 N1s photoemission spectra of DBV and DPV

The chemical shift of the N1s emission, which is sensitive to the redox state of the adsorbed viologen species, receives a particular interest in the *ex-situ* XPS experiments. Note that the interpretation of the obtained XPS data relies on the assumption that the chemical composition of the interface and, in particular, the viologen redox state remains unaltered upon emersion of the electrode out of the electrochemical environment. This assumption, however, appears very much justified with the results shown in Figs. 7.7–7.9 and their consistency with the electrochemical behavior discussed above.

The main question to be answered by the photoemission experiment is whether DPV exists in its di-cationic form on the chloride-modified copper surface at high potentials or whether it gets instantaneously reduced to the corresponding radical mono-cations even at potentials where the DPV^{2+}_{aq} solution species is still stable. Both the structural motif of the DPV phase at high potentials above the main reduction peak in the CV and the missing phase transition upon reaching P1 described above point to an instantaneous reduction of the di-cationic DPV^{2+} to the respective radical mono-cations upon adsorption. A similar phenomenon has been reported for various di-alkylated viologens adsorbed on HOPG [116, 133-135], or Hg [113] electrodes, where spike-like pre-peaks appear in the CVs at potentials more positive than the corresponding main redox waves. Their origin was explained in terms of Faradaic

processes involving the surface-confined viologen species coupled with surface phase transitions transforming ‘expanded’ phases of viologen di-cations into more compact phases of the corresponding radical mono-cations at potentials above the main redox waves [116, 134-136]. In accordance with the structural differences between adsorbed DBV and DPV seen in the *in-situ* STM experiments at positive potentials (Fig. 7.2) we, indeed, observe significant differences between both adsorbed species in the *ex-situ* photoemission experiment.

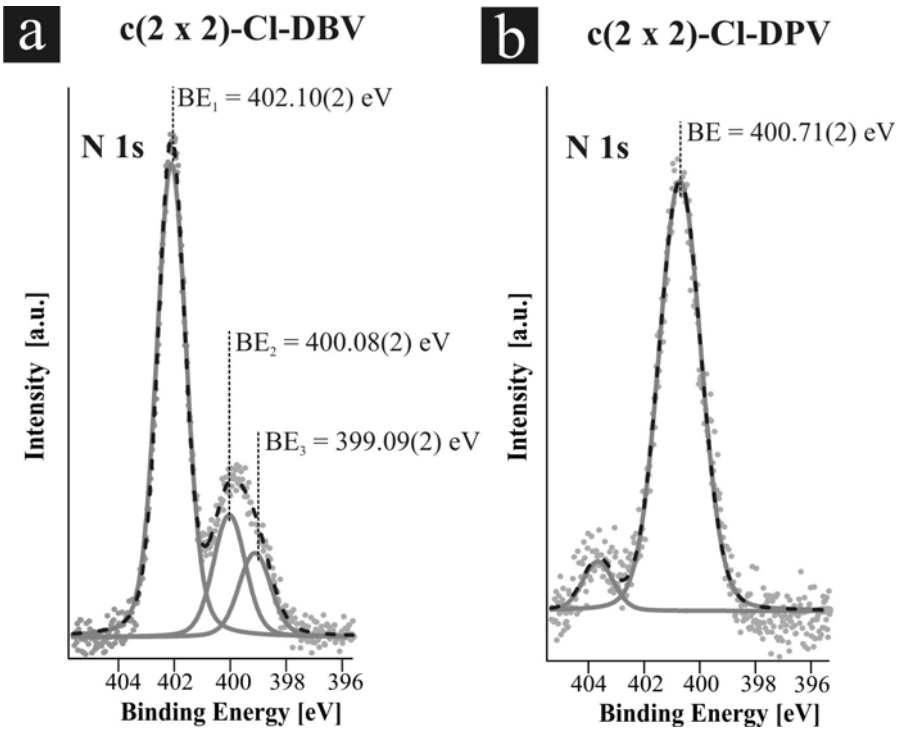

Figure 7.7: (a) N1s photoemission spectrum of the DBV monolayer phase after emersion at E_{emers} = +100mV, E_{photon} = 720 eV; (b) N1s photoemission spectrum of the DPV monolayer phase after emersion at E_{emers} = +130mV, E_{photon} = 720 eV, (E_{emers} indicates the emersion potential where the copper sample was transferred from the electrochemical environment into the UHV).

Fig. 7.7a represents the N1s photoemission spectrum obtained from the DBV cavitand layer (Fig. 7.2a) emersed out of the electrolyte at E_{emers} = +100 mV. The best fit was obtained assuming three individual viologen species with their main N1s component at BE_1 = 402.10(2) eV and two further components at the lower binding energies BE_2 = 400.08(2) eV and BE_3 = 399.09(2) eV, respectively. These latter components have to be assigned to reduced viologen species. Similar multi-component N1s spectra were reported for various solid di-chloride salts of viologens. For instance, Liu *et al* [137] assign the main peak in their N1s spectrum of 1,1’-bis(4-vinyl-benzyl)-viologen at BE = 401.7 eV to the positively charged nitrogen of the viologen species (V^{2+}), a satellite

feature at BE = 399.5 eV to the mono-reduced species ($V^{+\bullet}$) and a further satellite at even lower binding energy BE = 398.6 eV to the fully uncharged viologen (V^0). The presence of reduced viologen species in the viologen di-chloride salt has been rationalized in terms of an instability of the di-cationic viologen species against irradiation with x-rays. It appears most likely that such a transformation of di-cationic into the corresponding reduced viologen species is caused by slow photoelectrons and secondary electrons interacting with the di-cationic viologens which act as strong electron acceptors. In this respect, one could call this slow transformation a ‘dry’ reduction of di-cationic viologens under UHV conditions.

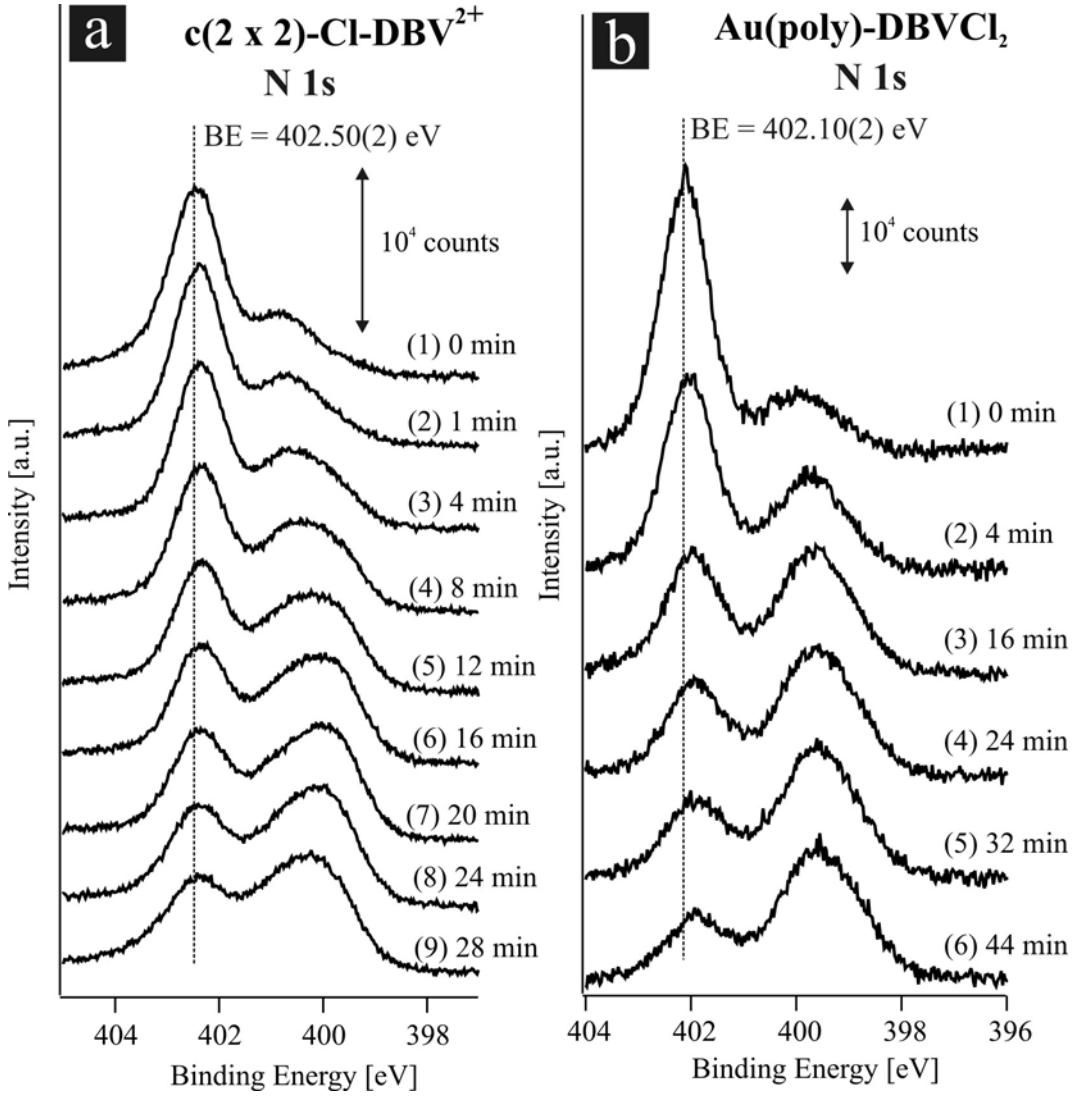

Figure 7.8: (a) Time-dependent N1s photoemission spectra of the DBV^{2+}_{ads} monolayer phase adsorbed on the chloride modified copper electrode, E_{photon} = 720 eV, E_{emers} = +100 mV, E_{emers} = +100mV; (b) time dependent N1s photoemission spectra of the $DBVCl_2$ salt deposited on an inert gold foil.

Adapting the interpretation of e.g. Liu et al., we do not expect any reduced DBV species present at the electrode at these high potentials of E = +100 mV and we therefore assign the main peak at BE_1 = 402.10(2) eV to di-cationic DBV. It is most likely that the satellite peaks observed in the N1s spectrum (Fig. 7.7a) are also experimental artifacts due to the transformation of the adsorbed di-cationic to the corresponding mono-reduced viologen species upon irradiation as suggested by Liu *et al* for the 1,1'-bis(4-vinyl-benzyl)-viologen di-chloride salt [137]. This hypothesis becomes experimentally substantiated by time-dependent XPS measurements of the emersed DBV^{2+}_{ads} monolayer (Fig. 7.8a) and of the corresponding $DBVCl_2$ salt deposited on an inert gold foil (Fig. 7.8b). The latter is to serve as reference for the identification of the DBV in its di-cationic state on the chloride modified surface at high potentials. We find the di-cationic DBV^{2+} in the di-chloride salt with an N 1s binding energy of BE = 402.5 eV (Fig. 7.8b) which is slightly higher (0.4 eV) than the value observed for the adsorbed DBV^{2+}_{ads} (Fig. 7.7a). Both spectra show the same time dependence upon irradiation. While the main component decreases with irradiation time we observe an increase of the satellite peaks at lower BE which are attributed to the reduced DBV species (Fig. 7.8). Note, however, that the satellite features are already present in the first spectrum of a time-dependent XPS series (spectra at t = 0 min in Fig. 7.8). From these observations we conclude that the DBV cavitand layer observed at potentials more positive than the main reduction wave indeed contains di-cationic DBV^{2+}_{ads} species in full agreement with our conclusions from the previous CV- and STM-results (see Figs. 7.2a,b).

Interestingly, the N1s emission of the DPV layer (Fig. 7.2c and d) emersed at similarly high potentials above the respective main reduction peak in the CV (E_{emer} = +130 mV) behaves significantly different than the one of the DBV^{2+}_{ads} monolayer. The dominant N1s emission at BE = 400.71(2) in Fig. 7.7b points to the presence of reduced $DPV^{\bullet+}_{ads}$ species at the electrode surface although DPV^{2+}_{aq} solution species are stable in their di-cationic form at these high electrode potentials (CV3 in Fig. 7.1). Our assignment of the main N1s peak in Fig. 7.7b to the mono-reduced $DPV^{\bullet+}_{ads}$ species is clearly supported by measurements on the N1s binding energy of the di-cationic DPV^{2+} species in solid $DPVCl_2$ salt (Fig. 7.9). The latter was also deposited on an inert Au foil as the $DBVCl_2$ salt before.

As expected, we found E_B(N1s) of di-cationic DPV^{2+} at high binding energies of BE = 402.53(2) eV (see XPS spectrum (1) in Fig. 7.9) as the main component. A similar BE was obtained for the di-cationic DBV^{2+} in the respective di-chloride salt with BE = 402.10(2) eV (see XPS spectrum (1) in Fig. 7.8b). Similar to the DBV^{2+} in the $DBVCl_2$ salt also the DPV^{2+} suffers reduction upon irradiation. In line with the disappearance of the di-cationic DPV^{2+} species in the solid salt a broad satellite feature emerges with time in the N1s photoemission spectrum like the value in the adsorbed case, i.e. BE = 400.71(2) eV, representing reduced DPV species as reaction products of the 'dry' DPV

reduction. The emergence of this reduced DPV species again serves as reference for the identification of the mono-reduced $DPV^{+\bullet}_{ads}$ species on the halide-modified copper surface. For comparison we have included the N1s spectrum from Fig. 7.7b obtained for the DPV film on the chloride-modified copper in Fig. 7.9 (spectrum 7). Interestingly, we observe the reduced $DPV^{\bullet+}_{ads}$ species not only on the c(2×2)-Cl but also on the c(2×2)-Br phase on Cu(100) [138]. Although chloride and bromide form the same lateral structure on Cu(100) their charge state on Cu(100) is different; recent *in-situ* x-ray scattering experiments point out that bromide is more discharged in the adsorbed state [139]. Therefore, the nature of the specifically adsorbed anion has apparently no significant impact on the instantaneous reduction of adsorbed DPV on the halide-modified copper surface, at least for chloride and bromide.

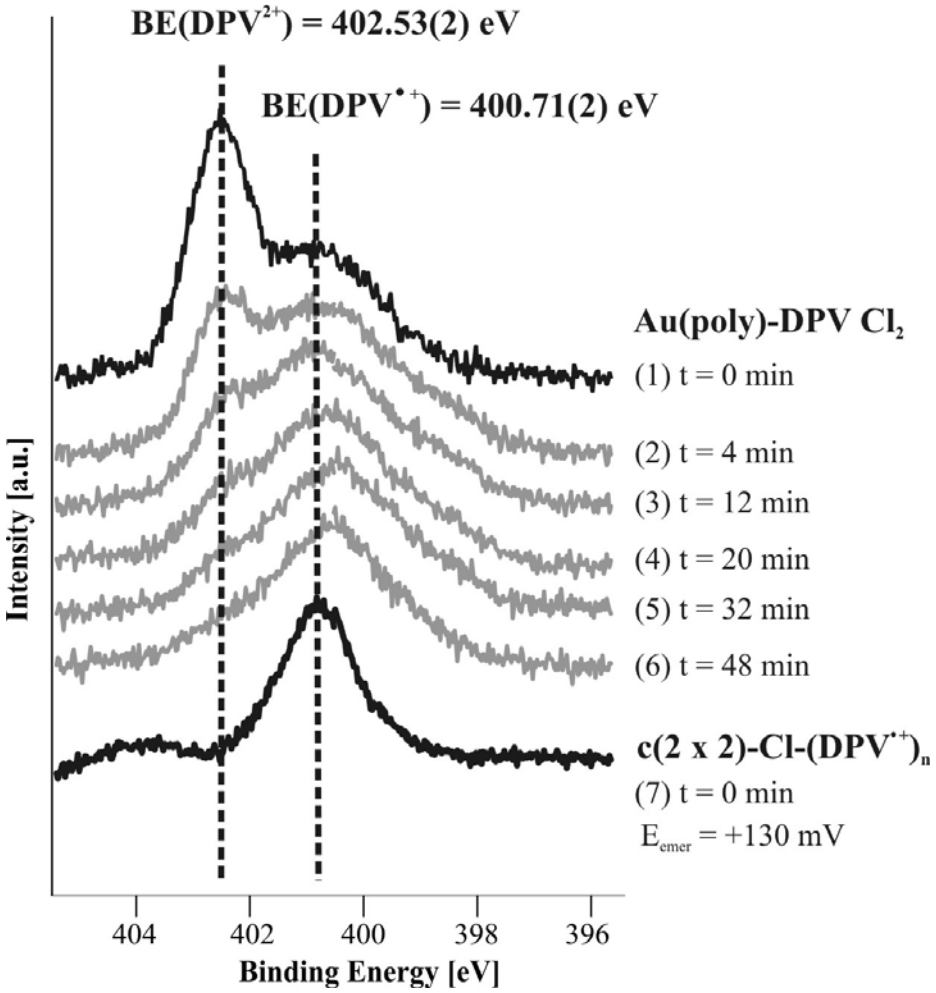

Figure 7.9: Time-dependent N1s photoemission spectra of the $DPVCl_2$ salt deposited on an inert gold foil compared with the N1s photoemission spectra obtained from the DPV monolayer on c(2x2)-Cl at high potentials, E_{photon} = 720 eV.

7.3.2 O1s photoemission spectra

Similar profound differences between DBV and DPV as noted for the N1s emissions are observed in the O1s spectra of the respective viologen monolayers at high potentials. Due to the absence of other oxygen containing species in the electrolyte we assign the observed O1s emissions to water. Since water tends to desorb rapidly from metal surfaces at RT under UHV conditions the O1s spectra obtained under *ex-situ* conditions cannot represent the ‘pristine’ state as in the electrochemical environment. However, these data can help to characterize the adsorbed viologen monolayers on a qualitative basis as being either hydrophobic or hydrophilic.

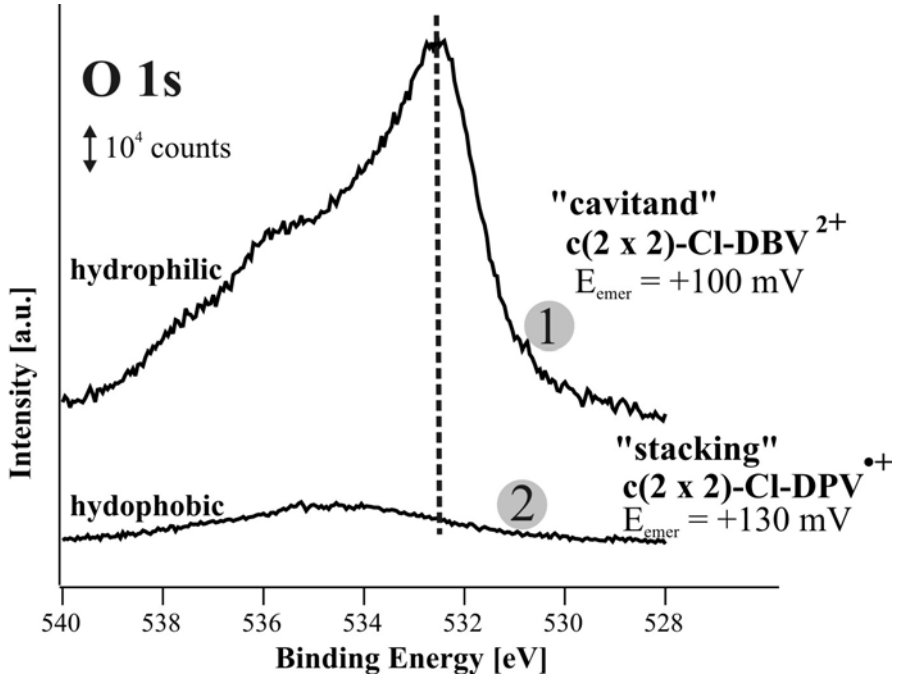

Figure 7.10: Overview of the O1s photoemission spectra of the viologen-covered c(2 x 2)-Cl/Cu(100) phase, E_{photon} = 720 eV.

Fig. 7.10 displays the O1s region of the DBV or DPV covered electrode after emersion and transfer into UHV. It is important to note that at the used excitation energy of E_{photon} = 720 eV the small peak in spectrum 2 coincides with a chloride-derived Auger transition which also contributes to the more complex spectrum 1. In order to circumvent a tedious deconvolution of the intensity at BEs higher than 534 eV in spectrum 1 into this chloride contribution and O1s components from possible water species, we base the following discussion only on the main O1s peak at BE = 532.51(2) eV in spectrum 1. This O1s binding energy is identical to that of water on the c(2×2)-Cl/Cu(100) surface without organic adsorbates (not shown here). The

first observation which strikes the eye is that this peak is missing in spectrum 2. Thus, the DBV covered surface retains water after transfer into UHV, while the DPV covered surface does not; the c(2×2)-Cl-DBV^{2+} behaves hydrophilic, the c(2×2)-Cl-$DPV^{\bullet+}$ surface hydrophobic.

Relating the integrated intensities (I) of the N1s and the O1s emissions (corrected for the respective energy depending cross sections (σ)) one can estimate the ratio of co-adsorbed water to di-cationic DBV^{2+}_{ads} within the cavitand layer (Fig. 7.2a, b) to be

$$\frac{n_{(O)}}{n_{(N)}} = \frac{I_{(O1s)}/\sigma_{(O1s)}}{I_{(N1s)}/\sigma_{(N1s)}} = \frac{2.2}{1}$$

with σ_{O1s} = 0.28 and σ_{N1s} = 0.19 at E_{photon} = 720 eV [140]. The ratio of water to DBV, thus, amounts to $n_{(H2O)}/n_{(DBV)} = \frac{4.4}{1} \approx \frac{4}{1}$ considering that one viologen molecule contains 2 nitrogen atoms.

Note that this number represents only the lower limit of co-adsorbed water on and within the DBV^{2+}_{ads} film since a certain amount of water may yet have desorbed before the photoemission experiment was started. It should be further noted that the lateral order of the DBV^{2+}_{ads} film may not be conserved upon emersion out of the electrolyte phase. From adsorption phenomena of oxo-anions it is well known that the lateral order breaks down immediately when volatile co-adsorbed water species partly desorb from the electrode surface under UHV conditions. However, for the identification of the viologen redox state it does not appear crucial whether the adsorbed species are laterally ordered or disordered.

While the DBV^{2+}_{ads} monolayer according to the above finding has to be considered as hydrophilic, the compact $(DPV^{\bullet+}_{ads})_n$ phase (Figs. 7.2c,d) is hydrophobic, no water is left on the surface after emersion of the $DPV^{\bullet+}_{ads}$ covered sample (spectrum 2 in Fig. 7.10). This can be seen as a further experimental hint for the presence of mono-reduced $DPV^{\bullet+}_{ads}$ species on the chloride lattice even at these high electrode potentials. The hydrophobicity of the $(DPV^{\bullet+}_{ads})_n$ monolayer is not only the result of the transition of the individual viologen di-cation to the radical monocation, it is also the result of the oligo- and polymerization process of individual $DPV^{\bullet+}_{ads}$ species that releases water from the surface.

All in all, the structural motifs of the viologen films observed by *in-situ* STM at positive potentials, the behavior of the viologen monolayers as a function of potential and the *ex-situ* XPS data, registered after emersion at positive potentials, point to a non-reactive DBV^{2+} adsorption resulting in a loosely packed and hydrophilic DBV^{2+}_{ads} film on c(2×2)-Cl/Cu(100), while DPV^{2+} undergoes a reactive adsorption giving rise to the formation of a densely packed and hydrophobic $(DPV^{\bullet+}_{ads})_n$ monolayer. In this respect, the DPV behaves similar to various di-alkylated viologens on the basal plane

of HOPG [134, 135]. The characteristic pre-peaks as indicators for the reaction of the adsorbed viologen species, however, are missing in the CV of the chloride-modified Cu(100) exposed to the DPV containing electrolyte (CV3 in Fig. 7.1). The reason for that could be the narrow potential window of copper.

7.3.3 Cl2p photoemission spectra

A final topic that has to be addressed concerns a possible co-adsorption of chloride anions within the 2D viologen films. Both the hydrophilic DBV^{2+}_{ads} film and the hydrophobic $(DPV^{\bullet+}_{ads})_n$ film are ‘multi-cationic’. The main question to be answered in this context is whether further chloride anions are required to stabilize the multi-cationic 2D viologen monolayers (see Fig. 7.2) besides those which are already specifically adsorbed on the metallic copper underneath the organic layer.

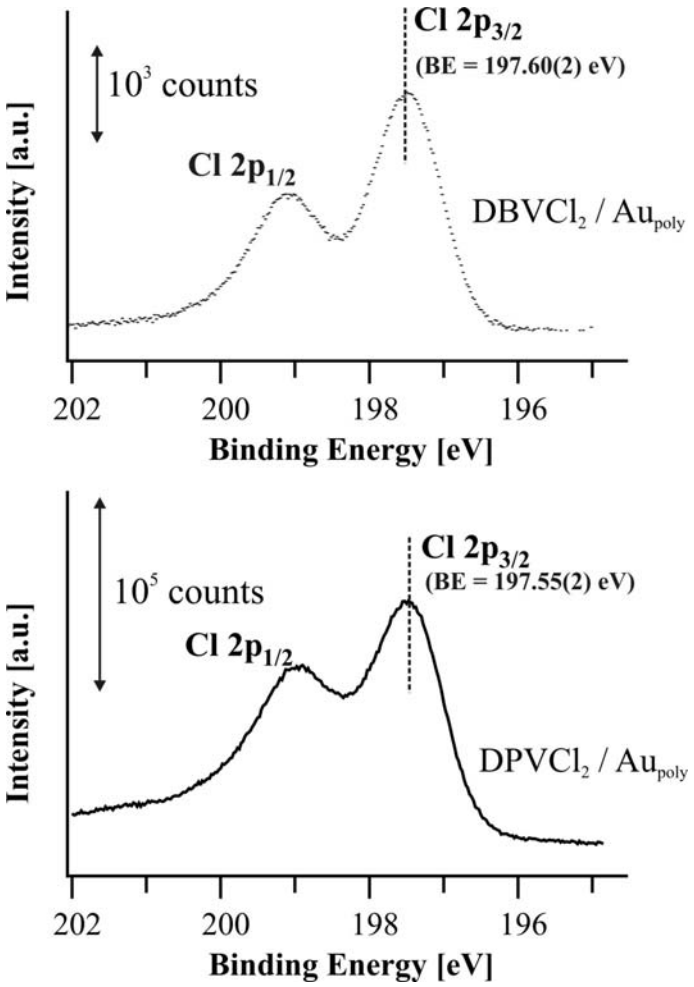

Figure 7.11: Cl2p photoemission spectra of the $DBVCl_2$ and $DPVCl_2$ salts deposited on inert gold foils, E_{photon} = 720 eV.

Using the Cl2p photoemission it should be possible to differentiate between specifically adsorbed chloride in direct contact with the copper and additional co-adsorbed chloride within the viologen layer. As an internal reference, we refer to the Cl2p spectra of the $DBVCl_2$ and $DPVCl_2$ salts that were deposited on an inert gold foil (Fig. 7.11). The $Cl2p_{3/2}$ emissions of the $DBVCl_2$ and the $DPVCl_2$ di-chloride are observed at BE = 197.70(2) eV and BE = 197.65(2) eV, respectively. The chloride species within the viologen salt can be considered as ionic. For comparison, chloride species within the largely ionic CsCl salt reveals a comparably low binding energy of the $Cl2p_{3/2}$ photoelectrons of BE_{CsCl} = 197.8 eV [42, 141].

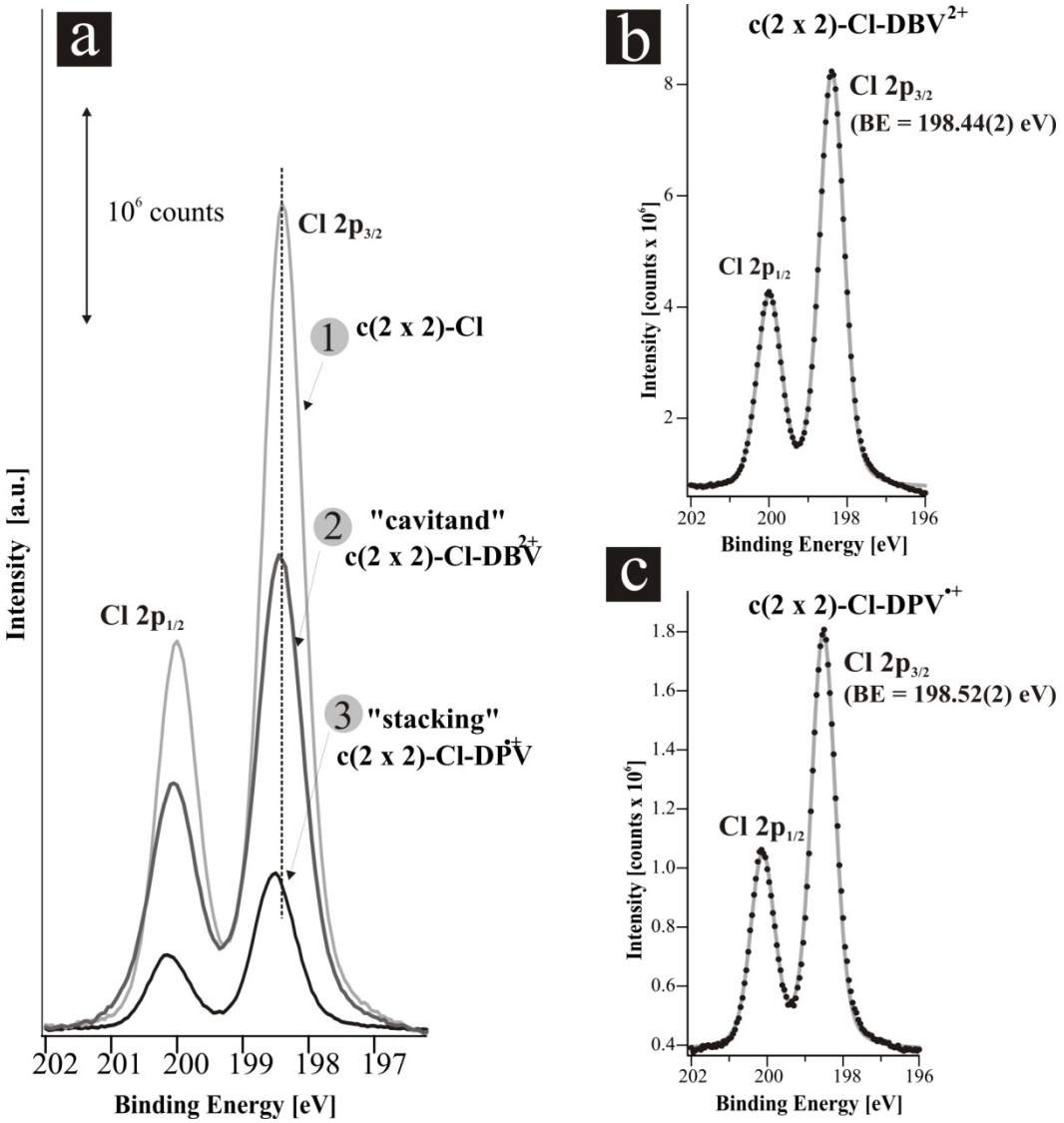

Figure 7.12: (a) Overview of the Cl2p photoemission spectra obtained for the viologen-free and viologen-covered Cu(100)-c(2x2)-Cl phase, E_{photon} = 245 eV; (b) fitted Cl2p photoemission spectrum of the DBV^{2+} monolayer phase; (c) fitted Cl2p photoemission spectrum of the $DPV^{\bullet+}$ monolayer phase.

It can be assumed that chloride which might be co-adsorbed within the DBV^{2+}_{ads} cavitand layer reveals a similar Cl2p binding energy as the one in the respective viologen salt. The Cl2p emissions obtained from the viologen-free (spectrum 1) and the viologen-covered chloride modified electrode surfaces (spectra 2 and 3) are presented in Fig. 7.12a. At first, one realizes a significant decrease in intensity by going from spectrum 1 to spectrum 3. Since these spectra were obtained using an excitation energy of only E_{photon} = 245 eV these differences in intensity do not reflect changes in the chloride surface concentration as a consequence of the viologen adsorption, but are due to 'damping' effects caused by the viologen overlayers on-top of the specifically adsorbed chloride layer. Note, that at this photon energy the kinetic energy of the Cl2p photoelectrons ranges only from 48–43 eV. Obviously, the observed damping effect is more pronounced in case of the more compact $(DPV^{\bullet+}_{ads})_n$ stacking layer (Figs. 7.2c,d) than for the more open DBV^{2+}_{ads} cavitand structure (Figs. 7.2a,b).

For the viologen-free and the viologen-covered surfaces, we find peak maxima of the $Cl2p_{3/2}$ emission at binding energies of $BE_{c(2\times2)\text{-}Cl}$ = 198.44(2) (spectrum 1), $BE_{c(2\times2)\text{-}Cl\text{–}DBV}$ = 198.42(2) (spectrum 2) and $BE_{c(2\times2)\text{-}Cl\text{-}DPV}$ = 198.52(2) (spectrum 3). While the BE of the $Cl2p_{3/2}$ photoelectrons are almost identical for the viologen-free and the chloride layer covered with the water-containing DBV^{2+}_{ads} film there is a tiny shift of about 0.1 eV towards higher BE when the hydrophobic $(DPV^{\bullet+}_{ads})_n$ stacking layer is present. There is, however, a difference of up to ΔE = +0.97 eV between the $Cl2p_{3/2}$ emission observed for the chloride anions in the viologen salts (Fig. 7.11) and the $Cl2p_{3/2}$ emissions originating from the specifically adsorbed chloride on the copper (Fig. 7.12a). This increase can be attributed to the specific interaction of chloride with the metallic copper substrate which involves a small partial charge transfer from the anion to the electrode. However, it should be noted that the character of the specifically adsorbed chloride remains largely ionic. For instance, the $Cl2p_{3/2}$ binding energy of the specifically adsorbed chloride on Cu(100) compares well with the $Cl2p_{3/2}$ binging energy of the ionic $NaCl_{bulk}$ salt of BE_{NaCl} = 198.4 eV [42, 141]. These findings agree well with recent in-situ x-ray diffraction studies on chloride adsorption on Cu(100) also indicating largely ionic chloride species present on the copper electrode [74].

All Cl2p spectra can be perfectly fitted by assuming only one chloride species (Figs. 7.12b, c), which has to be attributed to the specifically adsorbed chloride in direct contact with the metallic copper electrode. Further co-adsorbed chloride anions within the viologen film are not suggested by the photoemission experiment. Obviously, additional chloride anions are not necessary to stabilize 2D viologen monolayers regardless of the particular viologen redox state. There might be a further accumulation of solvated anions on-top of the multi-cationic viologen film. These additional anions, however, are not transferred into the UHV in the emersion

experiment. All these findings point to quite stable arrangements of these paired chloride anion/viologen cation layers at the interface with a clear spatial separation of negatively charged and positively charged layers. The presence of the cationic viologen layers does not significantly affect the copper–chloride bonding. In agreement with this there are also no chemical shifts of the copper emissions (e.g. Cu2p, Cu3p) after viologen adsorption on the chloride lattice (data not shown here). In this respect, the chloride layer can be regarded as a structurally and chemically stable negative ‘buffer’ layer between the positive metal electrode surface and the redox-active viologen layer.

7.4 Summary

The surface redox chemistry and related phase transitions of DBV and DPV molecules adsorbed on chloride modified Cu(100) are compared by means of CV, *in-situ* STM and *ex-situ* XPS. The experiments clearly indicate that there are substantial differences in reactivity of both adsorbed redox-active viologens resulting from the structural and electronic differences of the DBV or DPV molecules under investigation. It is noteworthy that the *ex-situ* XPS experiments enable a comparison between the DBV and DPV adlayers at high potentials.

The main difference of the CV results between the two molecules is that the first redox process of DPV is shifted to higher potentials compared to that of DBV, resulting in a difference of ΔE = +162 mV between P1(DBV) and P1(DPV). That indicates a higher electrochemical reactivity of DPV than DBV species from solution.

Moreover, STM images show the surprising result that adsorbed on the surface DPV is even more reactive than DBV. While at potentials more positive than the first redox wave in the CV, the dicationic DBV^{2+} species from solution can adsorb and are stabil on the chloride template in dicationic form as cavitand phase, the DPV^{2+} species does not adsorb in its dicationic DPV^{2+} form on the chloride precovered Cu(100) surface. Instead, DPV^{2+} instantaneously reacts to the corresponding radical cation $DPV^{\bullet+}_{ads}$ at the chloride modified surface followed by the immediate formation of a condensed $(DPV^{\bullet+}_{ads})_n$ stacking phase. Note that the DBV^{2+} cavitand phase transforms into a similar stacking phase only at potentials lower than -250 mV, i.e. after passing the CV peak P1.

The comparison between the DBV^{2+}_{ads} cavitand phase and the $(DPV^{\bullet+}_{ads})_n$ stacking phase at high potential can be supplemented by the XPS experiments. Firstly, the N(1s) core level binding energies of both adsorbed species at these high potentials are consistent with the existence of $DPV^{\bullet+}$ radical cations but DBV^{2+} dications, respectively. Furthermore, the XPS data clearly indicate that, on the one hand, the dications DBV^{2+}_{ads} of the cavitand phase do not completely lose their solvation shell

upon adsorption on the chloride layer. The resulting loosely packed cavitand structure is *hydrophilic* and contains at least four water molecules per DBV^{2+}_{ads} molecule. However, on the other hand, the more densely packed $(DPV^{\bullet+}_{ads})_n$ stacking phase proves to be highly *hydrophobic* which completely removes all water species from the chloride lattice. Upon adsorption and phase formation the DPV releases completely its solvation shell as a pre-requisite to undergo strong inter-viologen interactions in the form of π- π interactions. These strong adsorbate–adsorbate interactions are considered to be the main driving forces for the $(DPV^{\bullet+}_{ads})_n$ phase formation.

At potentials less than -250 mV the radical cation stripe phases of both $DBV^{\bullet+}$ and $DPV^{\bullet+}$, however, display different structures. While the DBV species still remain as the $(DBV^{\bullet+}_{ads})_n$ stacking phase, the $(DPV^{\bullet+}_{ads})_n$ adlayer transforms into a $(DPV^{\bullet+}_{ads})_n$ double layer phase. Once formed the double layer phase is stable in the broad regime of copper potential window before reaching the chloride desorption peak P2(DPV) lying in the HER regime.

The chloride desorption process in the presence of DBV or DPV is also surprisingly different. While an amorphous phase of $DBV^{\bullet+}_{ads}$ species is formed on the bare Cu(100) surface due to the chloride desorption *through* the DBV adlayer, the $DPV^{\bullet+}_{ads}$ species desorb *together* with the chloride leaving the bare substrate behind. The difference of the chloride desorption processes can explain the shift of the HER in the DBV containing electrolyte to much more negative potentials than in the presence of DPV.

Part IV

“Reactive” adsorption of Viologen – Results and discussion

Chapter 8

"Reactive" adsorption of DBV on chloride modified Cu(100)

8.1 Introduction

Electron transfer reactions involve both the solvated viologens in solution as well as the pre-adsorbed species. The latter reaction can result in distinct phase transitions within the adsorbed monolayers as a consequence of positional, orientational and conformational changes of covalently [126, 143] or noncovalently bound [113, 115, 116, 131, 132, 143] viologens.

In chapter 5, the DBV was adsorbed under non-reactive condition, in which the DBV solution was added into the cell at the potential regime from -100 mV to +100 mV (the double layer regime). In this condition, the DBV^{2+} species is not yet reduced to the mono-cation $DBV^{\bullet+}$, no electrochemical reaction takes place. But if DBV^{2+} species are introduced into the electrolyte at potentials within the potential regime of peak P1, i.e. from -120 mV to -250 mV (Fig. 8.1a), so that the electron transfer can take place prior to or simultaneously with the 2D phase formation, new structures of DBV or metastable phases have been found. There are in fact two new metastable phases denoted A and B occurring within the potential regime in which the DBV was added into the electrolyte. At this potential regime from -120 mV to -250 mV, the phase transition from the cavitand to stacking phase has not yet taken place. And so the structural integrity of the two metastable phases is not affected by the on-going solution redox processes, at least on the time-scale of the STM experiment. Depending on the potential, in most cases type A generally appears at the regime from -120 mV to -200 mV and type B at more negative potentials from -200 mV to -250 mV. They are very well-ordered structures. However, occasionally the two metastable phases and the cavitand phase even exist together, as verified by Fig. 8.1b, in which structure 1 is the cavitand phase, while A and B are the two metastable phases. Obviously, they are different structures.

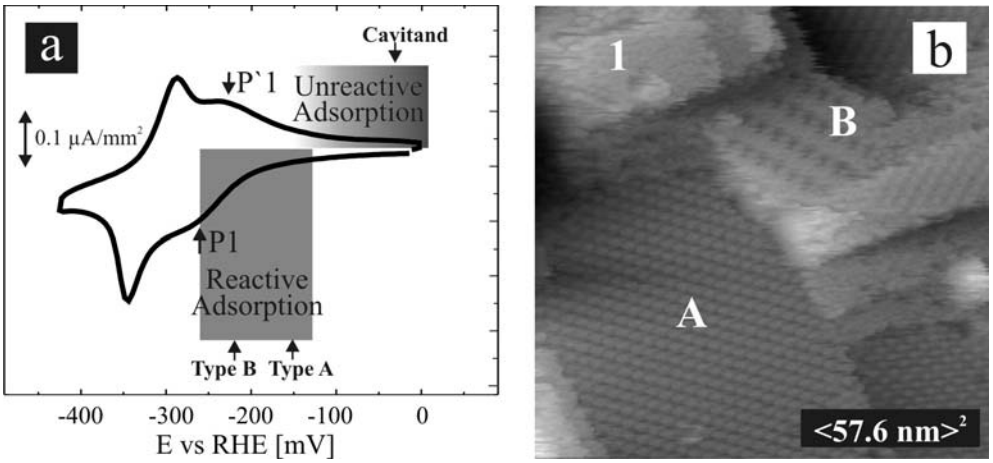

Figure 8.1: (a) Unreactive and reactive regimes related to the CV, (b) STM image of a three phase coexistence: 1. cavitand, 2. type A, 3. type B, I_t = 0.1 nA, U_b = 217 mV, E = -160 mV.

Besides the differences of structure and surface coverage, the two metastable phases have some unique properties: they can transform into the cavitand and the stacking phases but in an irreversible way and the transitions take place slower than the reversible ones from cavitand to stacking phase and vice versus, or in other words, there are high activation barriers to the other inactive phases with respect to potential dependence.

8.2 Structures

8.2.1 Metastable phase A - Dimers

The metastable phase A shows very well order in Fig. 8.2, it has typically 4 domains, two mirror and two further rotational domains, similar to the cases of cavitand and stacking phases (Fig. 8.2a). Figs. 8.2b,c are the zoomed-in images of the metastable phase A structure, illustrating separate building blocks. The corrugation of one building block shown in Fig. 8.2d proves that each block is built by two DBV molecules. At a defect (Fig. 8.3) we found that always both DBV molecules are lost, therefore they are likely to be a stable dimer and the metastable type A phase is therefore a dimer phase.

The key structural motif of the viologen film formed under these reductive conditions, i.e. simultaneous reduction and phase formation, is a dimer with radical mono-cations linked by π-bonding [124]. The elongated STM spots in Fig. 8.2b are assigned to the viologen redox moieties while the less conductive benzyl groups are supposed to lie in the dark areas with the lower imaging contrast. Both radical mono-cations constituting one dimer are slightly shifted against each other.

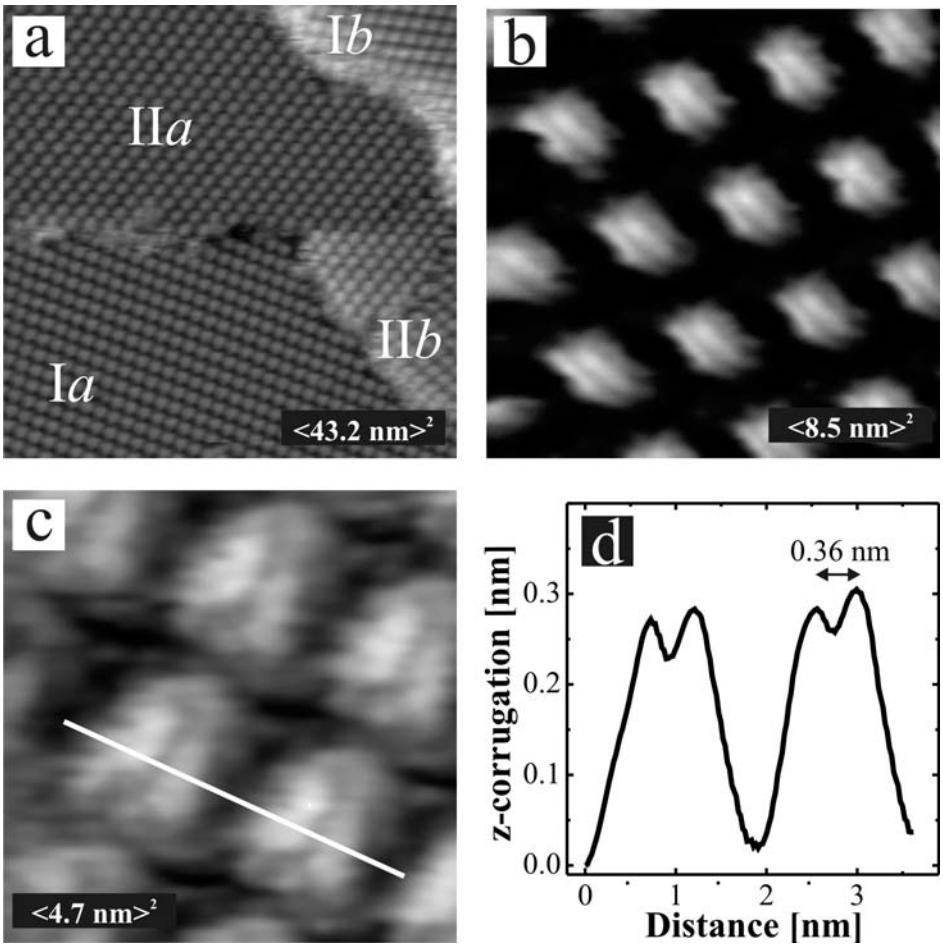

Figure 8.2: (a)-(c) STM images of the metastable viologen dimer phase: (a) I_t = 1.3 nA, U_b = 158 mV, E = -120 mV, (b) I_t = 0.4 nA, U_b = 204 mV, E = -130 mV, (c) I_t = 0.9 nA, U_b = 205 mV, E = -120 mV; (d) height profile across two dimers in (c) (white line).

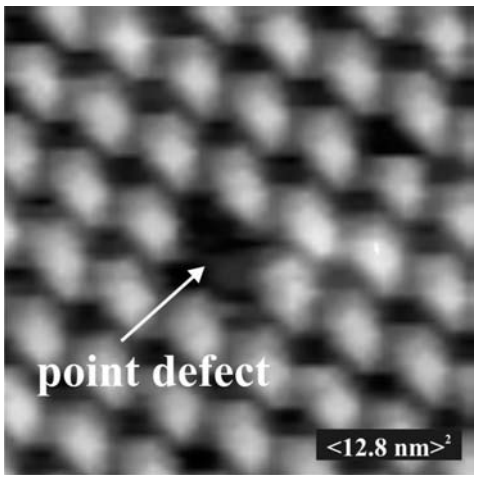

Figure 8.3: STM image of the viologen dimer phase with one missing dimer as a defect, I_t = 1.0 nA, U_b = 260 mV, E = -130 mV.

The value of the interviologen spacing within the dimer is 0.36 nm which is similar to that value of the radical cation $(DBV^{\bullet+}_{ads})_n$ stacking phase, indicating that the dimer building block is combined of two face to face radical $DBV^{\bullet+}$ species. Note that the regime for metastable phase formation from -120 mV to -250 mV is exactly the positive potential side of the reduction peak P1 (Fig. 8.1a) where the dication DBV^{2+} starts to be reduced into the corresponding radical cation $DBV^{\bullet+}$ species. Therefore, the formation of the dimer phase in particular or the two metastable phases in general can be assumed as follows. In the potential regime from -120 mV to -250 mV (the positive side of the reduction peak P1), the dication DBV^{2+} species in electrolyte come close to the surface for the first electron transfer reaction and are reduced to the corresponding radical cation $DBV^{\bullet+}$ species, then diffuse back to the solution, showing the increasing current peak P1. However, after being reduced, pairs of two $DBV^{\bullet+}$ species can combine immediately to form stable dimers (not trimer or oligomer). If the surface of the chloride lattice template is not yet covered (reactive condition), these dimers can adsorb on the chloride template. Depending on the potential or perhaps the concentration of dimers, the adsorption of dimers forms two different structures and coverages of two metastable phases. Therefore, the metastable phases are supposed to be phases of dimers. However, in the case if the surface of the chloride lattice template is already pre-covered by the cavitand phase of DBV^{2+}_{ads} species (non-reactive condition), the dication species from solution still come close to the surface, having the electron transfer through the cavitand phase adlayer, even forming dimers, but these dimers appear only in solution and cannot replace the cavitand phase to adsorb on the chloride lattice. Thus the DBV^{2+}_{ads} species of the cavitand phase at the surface is assumed to be less electrochemically active so that the cavitand phase remains stable in spites of the presence of radical cation species in solution. This assumption matches with the evidence in Sec. 5.2.1 which proved the reduction peak P1 was a solution peak.

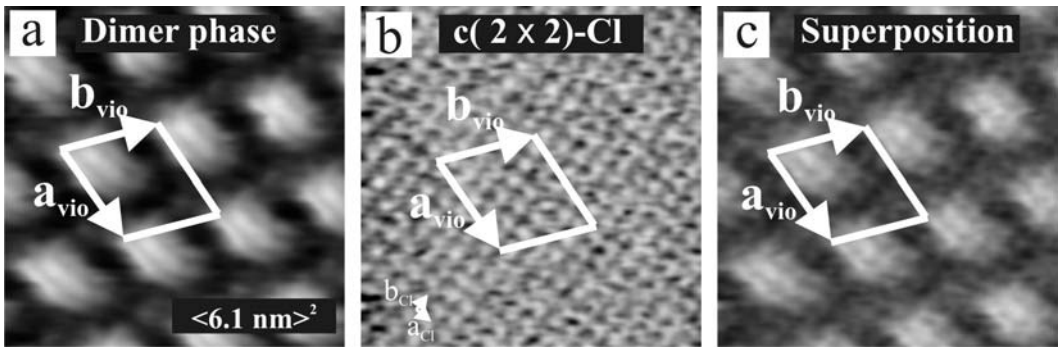

Figure 8.4: (a) STM image of the viologen dimer phase imaged under moderate tunneling conditions, I_t = 0.4 nA, U_b = 204 mV, E = -130 mV; (b) c(2x2) chloride lattice on Cu(100) imaged under more drastic tunneling conditions, I_t = 3.8 nA, U_b = 56 mV, E = -130 mV; (c) Superposition of panels (a) and (b).

The symmetry relation to the substrate is derived from a tip-induced removal of the viologen film (Fig. 8.4b) that allows the imaging of the chloride adlayer beneath [131, 132]. From a comparison of Figs. 8.4a and b it can be concluded that the dimer entities are oriented with their main molecular N–N axes parallel to the surface in an “edge-on” adsorption geometry. Such an orientation along the closely packed chloride rows indicate a “coordinative effect” of the chloride lattice that is facilitated due to the nearest neighbor chloride distance of d_{Cl} = 0.362 nm [72, 75] that perfectly matches the value of the interviologen spacing within the dimer of d_{dimer} = 0.36 nm. The translational symmetry of the dimer layer can be expressed using the matrix notation by relating the dimer lattice to the chloride lattice:

$$\begin{pmatrix} a_{vio} \\ b_{vio} \end{pmatrix} = \begin{pmatrix} 5 & -2 \\ 3 & 4 \end{pmatrix} \begin{pmatrix} a_{Cl} \\ b_{Cl} \end{pmatrix}$$

a_{vio} amounts to 1.95 nm, b_{vio} is determined to be 1.81 nm, enclosing an angle of 74.9° (Fig. 8.4). The oblique unit-mesh is the result of the structural anisotropy of individual dimer species. Assuming that there are no further viologen species within the unit cell besides those seen in the STM image or 2 DBV molecules per unit cell, we can determine the viologen coverage to be Θ_{vio} = 0.077 ML with respect to the chloride lattice.

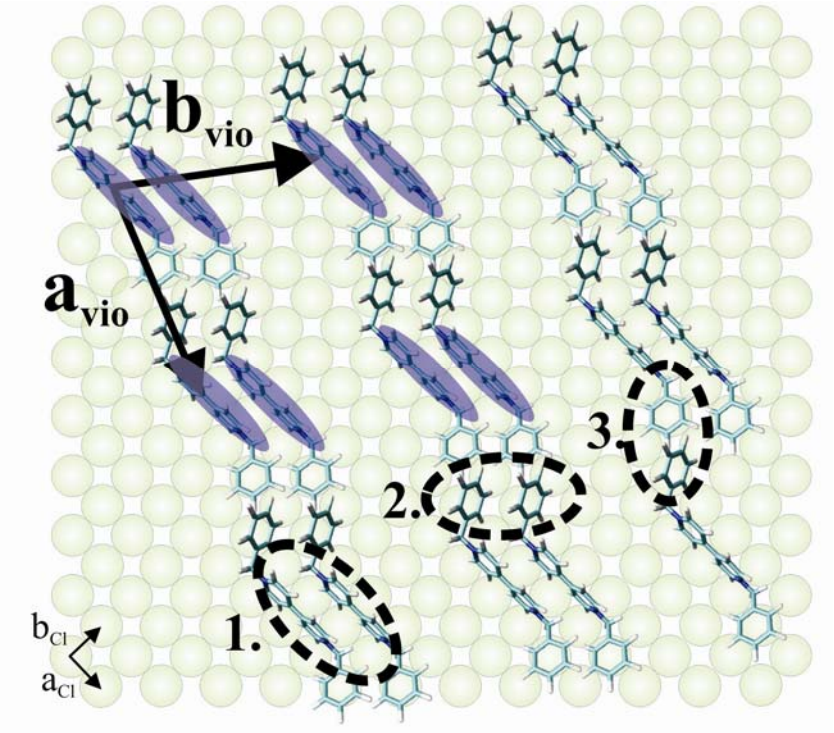

Figure 8.5: Proposed structure model of the dimer phase on the c (2x2) chloride lattice, showing the unit cell and proposed interactions.

Fig. 8.5 represents a structural model of the cationic dimer phase on-top of the anionic chloride lattice. It is assumed that both bipyridinium moieties of the dimer reside in neighboring grooves of the $(\sqrt{2} \times \sqrt{2})$R45-Cl lattice thereby minimizing the electrostatic repulsion between them. In the structure model of the dimer phase (Fig. 8.5), we propose 3 types of interactions:

- 1: bonding of two radical cations in a dimer,
- 2 and 3: bonding between two benzyl groups that connect dimers by each other in the dimer phase.

8.2.2 Metastable phase B

As mentioned in the introduction Sec. 8.1, the formation of the metastable phase B generally takes place at the potential regime from -200 mV to -250 mV, which is more negative than the regime of phase A (dimer phase) formation.

Similar to the dimer phase A, the metastable phase B also shows a very well ordered structure and has typically 4 domains (Fig. 8.6a). However different from the dimer phase, the type B phase is a more complex structure depending on the tunneling conditions, the STM of phase B gives different image contrast, but obviously the structure is combined of complex stripes and separated dots of DBV molecules (Fig. 8.6b). As explained in the previous section, the metastable phase B is also supposed to be a structural phase of dimers. But due to its complexity, not as clear as the separated dimer building blocks of phase A, this metastable phase is just denoted as "Type B" phase while the phase A is a true "dimer" phase.

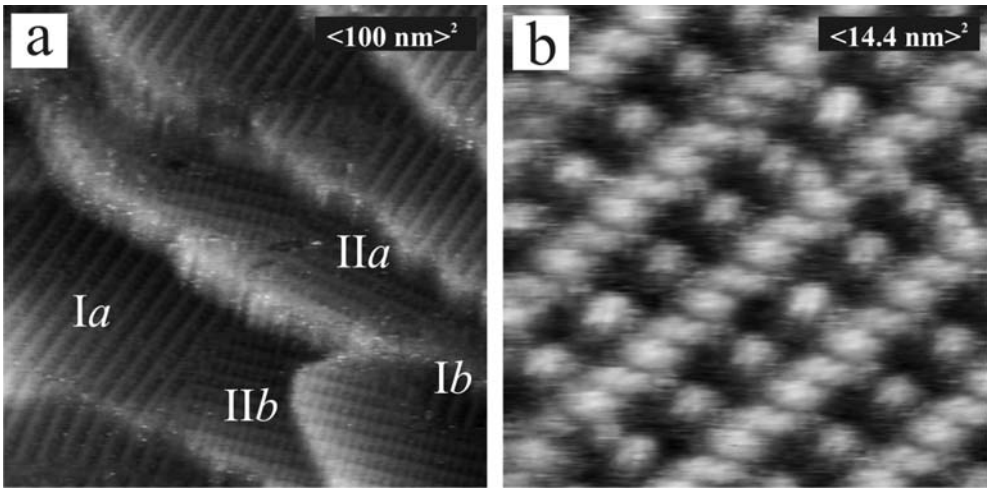

Figure 8.6: STM images of the metastable type B phase, (a) I_t = 0.9 nA, U_b = 173 mV, E = -230 mV; (b) I_t = 0.1 nA, U_b = 241 mV, E = -230 mV.

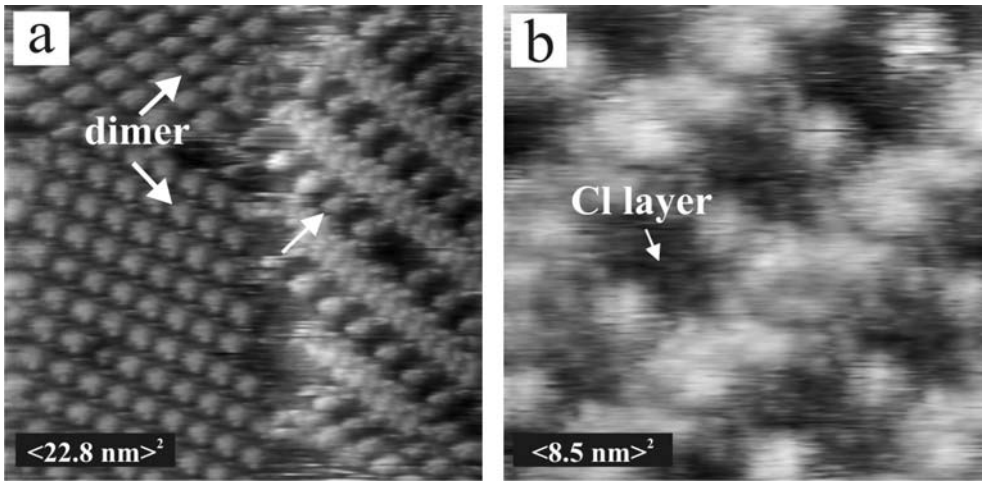

Figure 8.7: (a) STM image of the two-metastable phases coexisting, I_t = 0.9 nA, U_b = 205 mV, E = -230 mV; (b) STM image under more drastic conditions shows the type B phase with Cl adlayer underneath, I_t = 2 nA, U_b = 150 mV, E = -230 mV.

In order to define the structure of the type B phase, we should compare it with the dimer phase. Fig. 8.7a presents the STM image of both coexisting metastable phases. The arrows point out that the dimers in type A are similar to dots in type B phase. And under more drastic tunneling conditions, even the Cl adlayer beneath appears together with the structure of the type B phase, suggesting that there is no viologen molecule at the vacancy of type B phase. Therefore, the structure of type B phase is the combination of separated dimers and complex stripes composed by other dimers.

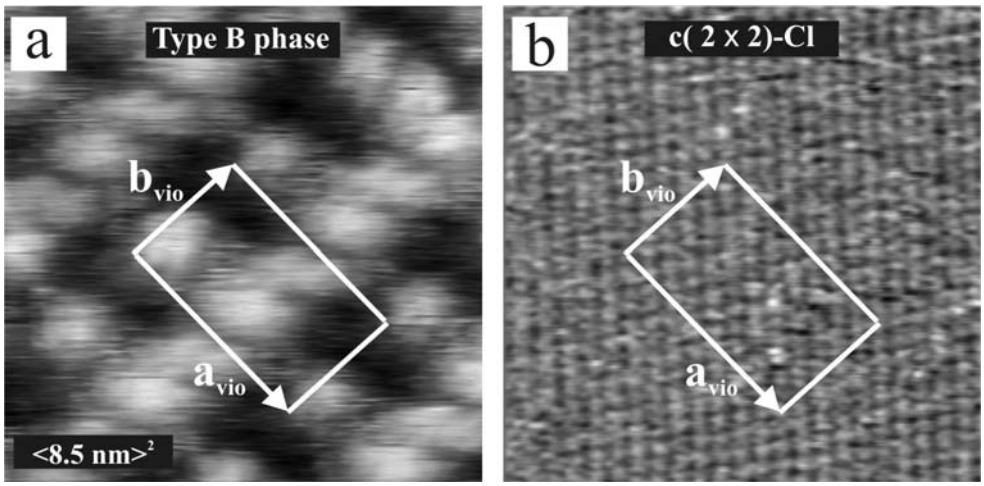

Figure 8.8: STM images of the metastable type B phase in comparison with the Cl adlayer underneath at the same position: (a) Type B phase under moderate tunneling conditions, I_t = 0.1 nA, U_b = 241 mV, E = -230 mV, (b) c(2x2) chloride lattice on Cu(100) imaged under more drastic tunneling conditions, I_t = 10 nA, U_b = 17 mV, E = -230 mV.

The symmetry relation to the substrate is derived from a tip-induced removal of the viologen film (Fig. 8.8) that allows the imaging of the chloride adlayer beneath. And the translational symmetry of the type B phase layer can be expressed using the matrix notation by relating the type B phase to the chloride lattice:

$$\begin{pmatrix} a_{vio} \\ b_{vio} \end{pmatrix} = \begin{pmatrix} 10 & -7 \\ 5 & 4 \end{pmatrix} \begin{pmatrix} a_{Cl} \\ b_{Cl} \end{pmatrix}$$

a_{vio} amounts to 5.69 nm, b_{vio} is determined to be 2.32 nm, enclosing an angle of 73.6°. The perpendicular-like appearance of a_{vio} and b_{vio} in Fig. 8.8 is supposed to be due to drift during the measurement.

In Fig. 8.9a individual DBV molecules are identified in the stripes of the type B phase structure only showing clearly 4 DBV molecules (denoted as 1 to 4 which are marked by white arrows in Fig. 8.9a) and some unknown other parts in the stripe within one unit cell. But by the similarity of the two metastable phases related to the reactive adsorption in the P1 regime of the CV (Fig. 8.1a) and the symmetry of the stripe structure, as explained in the previous section, we assume that the structure of type B phase is also composed by dimers. From that point of view and the STM results, we suppose that a stripe is a combination of dimers but in perpendicular orientation with separated dimers. By considering the intermolecular spacing of species within the stripe, we suppose that each entity consists of 3 dimers or 6 DBV radical cation species. The reason why in STM only 4 molecules per unit cell appear in the stripe is explained to be due to the 3D viewing of the STM images, and from the 6 molecules 4 ones can stand higher and can be seen brighter than the other 2 ones.

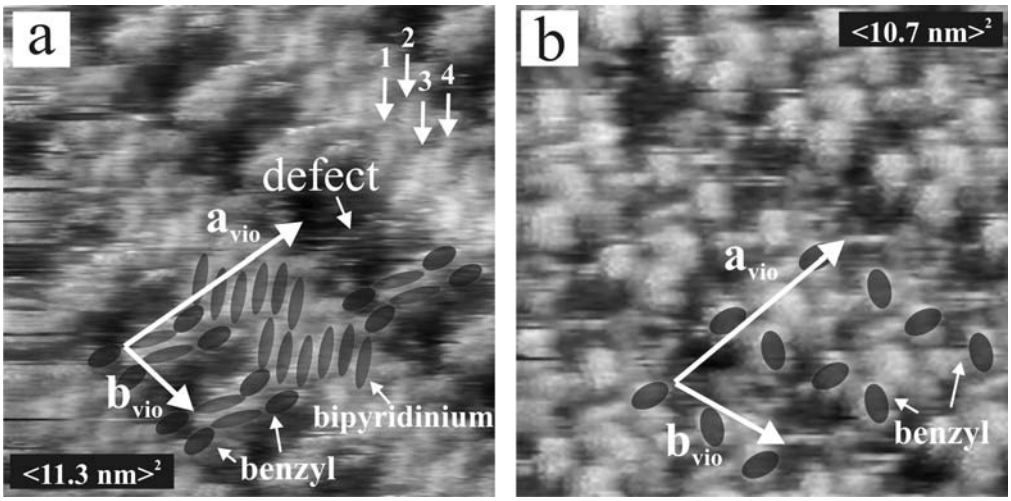

Figure 8.9: STM images of the metastable type B phase: (a) I_t = 0.3 nA, U_b = 141 mV, E = -230 mV, (b) benzyl groups appear enhanced under negative bias tunneling conditions, I_t = 0.6 nA, U_b = -43 mV, E = -230 mV.

The structure model of the type B phase suggests that the separated dimers and the stripes are connected by benzyl groups. Based on the flexibility of the benzyl group, in the separated dimer, the two benzyl groups rotate at different angles to connect with other benzyl groups in the stripe (shown in model Fig. 8.10).

Especially, if we apply a negative bias voltage for tunneling, occasionally STM results show the benzyl group brighter than the bipyridinium cores. In Fig. 8.9b for example, with the reverse bias of -43 mV, the STM image of type B phase appears totally different and the benzyl groups and their bonds are more obvious than the bipyridinium groups of DBV molecules. The comparison between Figs. 8.9a and b is consistent with the assumption of the structure model of type B phase consisting of separated dimers connected with perpendicular dimers in the stripe by benzyl groups.

Concluding from previous STM results, we propose the structure model for the type B phase as represented in Fig. 8.10, in which each unit cell has 8 DBV molecules resulting in a viologen coverage of Θ_{vio} = 0.107 ML with respect to the chloride lattice.

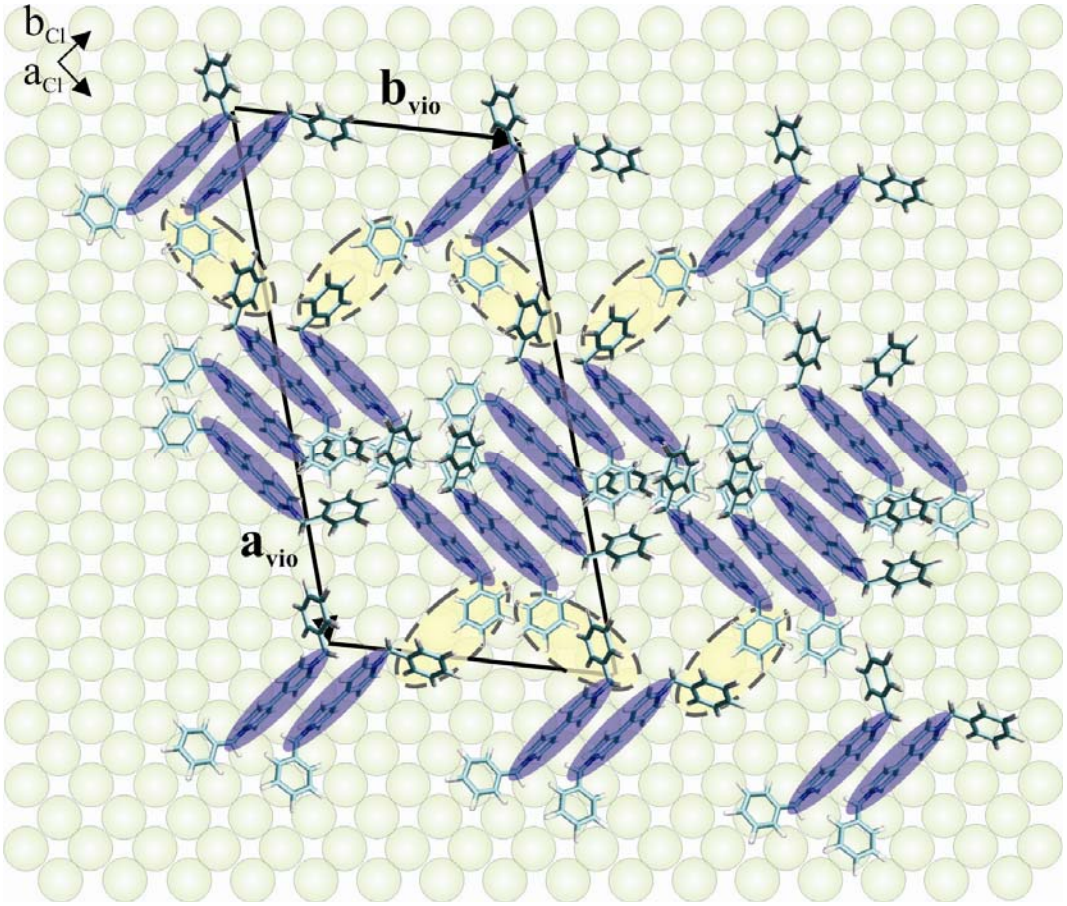

Figure 8.10: Proposed structure model of the metastable type B phase on the c(2x2) chloride lattice, combined of separated dimers and stripes of other dimers.

8.3 Irreversible phase transitions of metastable phases

As described in the sections, once formed under kinetic control, the two metastable phases can transform into cavitand or stacking phase by sweeping the working potential in anodic or cathodic direction, respectively. However, the transitions are irreversible, because in a subsequent opposite potential scan, only the cavitand and stacking phase transform into each other without appearance of the metastable phases, neither phase A (dimer) nor phase B (stripes and dimers).

Fig. 8.11 shows the two series of STM images of the transitions, both starting with the well-ordered dimer phase structure. By increasing or decreasing the working potential, in certain regimes, the dimer phase can transform into the two normal phases.

In a potential increase (anodic sweep), the dimer phase is stable only upto potentials of about +40 mV. Reaching the potential of about +40 mV, the dimer phase is replaced by the cavitand phase following a first order transition (Fig. 8.11a). The phase transition is fully completed at about E = +80 mV. This transition involves the oxidation of the radical-cation dimer species back to the dication DBV^{2+}. It appears that the orientation of domains of the cavitand phase does not depend on that of the previous dimer phase.

Although from the CV result (see Fig. 8.1a), the oxidation peak P1' of solution species ends much earlier at potential about -120 mV, on the surface, the transition takes place much slower and therefore reveals a considerable potential hysteresis which arises from additional activation barriers, considering that intermolecular π-π-bonds have to be broken for this phase transition. The explanation is similar as in the case of the stacking-cavitand phase transition, but there is one different thing related to the potential regime in which the transitions take place. While the transition from stacking to cavitand phase starts at potential of about -80 mV and completes at about +20 mV, the dimer-cavitand transition occurs much later, starting at even +40 mV, and is much faster, completing at about +80 mV. Obviously, the dimer phase represents a higher potential stability compared with normal stacking phase in term of phase transition. This phenomenon will be discussed more in the next part.

In the opposite potential scan direction (Fig. 8.11b), a potential decrease (cathodic sweep) into the regime below P1 (at a potential of about -300 mV) has to be performed in order to initiate the replacement of the dimer by the stacking stripe phase. The transition is completed soon, i.e. already around -320 mV. The biggest difference between the dimer-to-stacking- and the cavitand-to-stacking phase transitions is the growth behavior. The dimer-stacking phase transition takes place much faster and more ordered. It can be explained by the difference of building block species. The metastable phase consists of dimers as building blocks of radical cationic DBV with π-π bonds already, therefore in order to from a longer stripe of the stacking

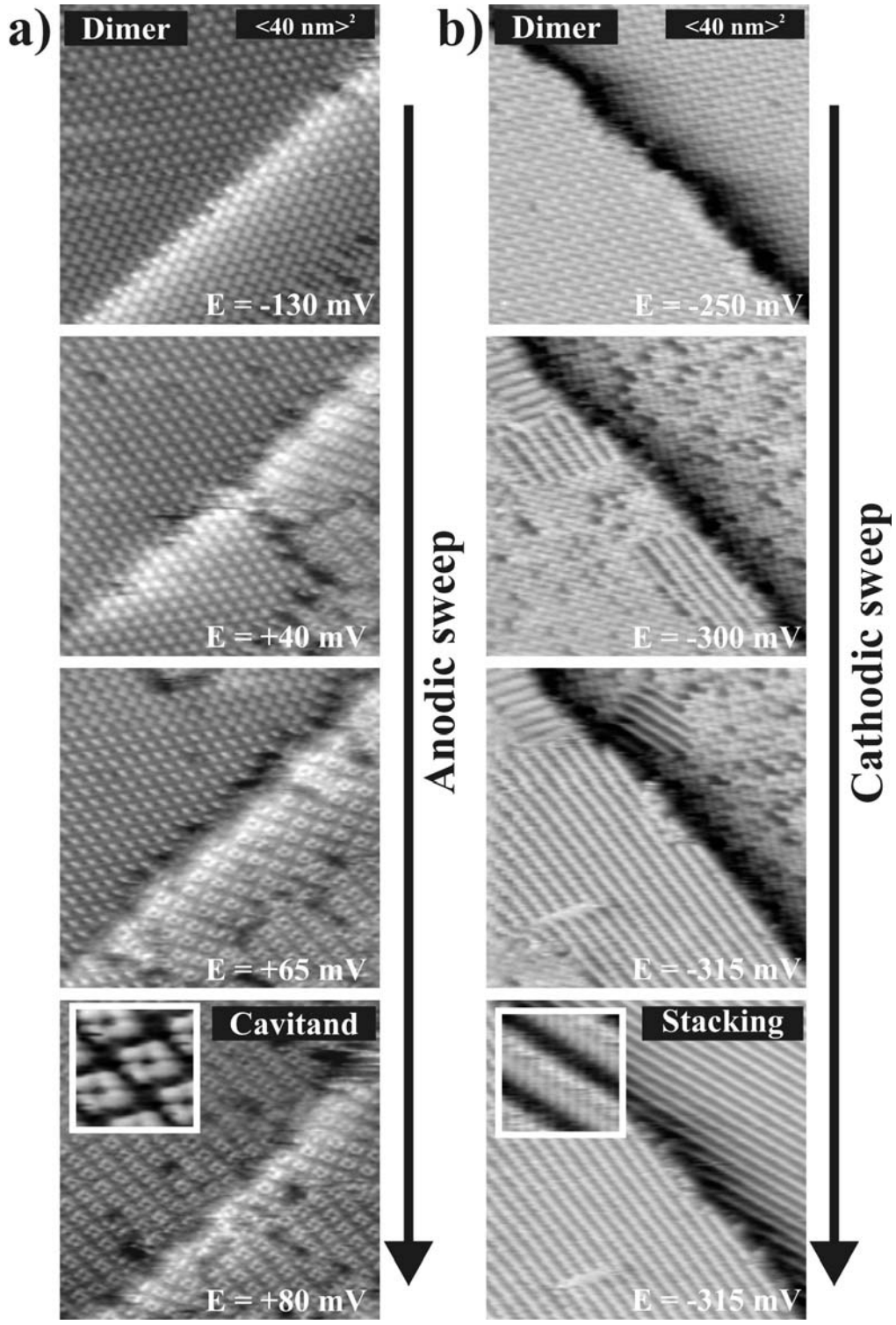

Figure 8.11: a) Irreversible transition of the dimer into the cavitand phase triggered by the oxidative one-electron transfer reaction (anodic sweep), I_t = 0.8 nA, U_b = -172 mV, b) Irreversible transition of the dimer into the stacking phase of radical mono-cations (cathodic sweep), I_t = 4.9 nA, U_b = 181 mV (the insets show molecularly resolved images of the respective phases).

phase, they seem to aggregate much easier and the ordering during the transition phase depends only on the ordering of the former metastable phase. Note that due to the irreversible transition of the metastable phases, in order to obtain the dimer phase structure in Figs. 8.11a and b, we carried out obligatorily two separate measurements under kinetic control.

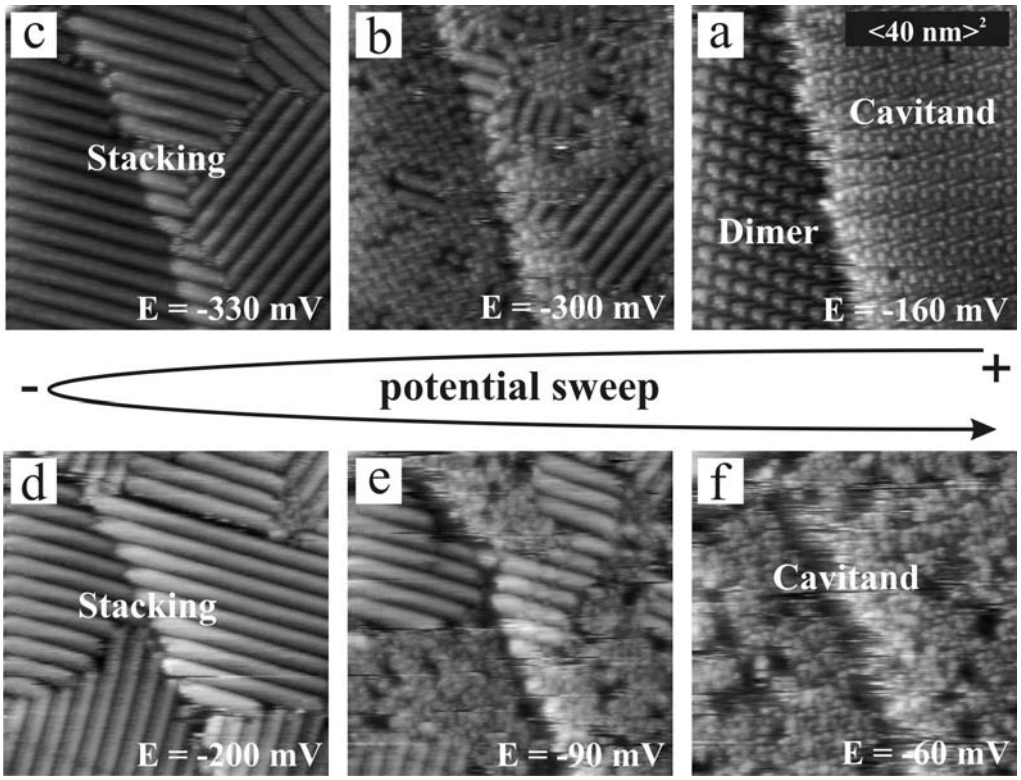

Figure 8.12: Irreversible transition of dimer, starting with co-adsorption of both dimer and cavitand phase: (a)-(c) Cathodic sweep, transition into stacking phase, I_t = 0.8 nA, U_b = -172 mV, (d)-(f) Anodic sweep, transition back to cavitand phase, I_t = 4.9 nA, U_b = 181 mV.

The STM image series of Fig. 8.12 was, however, registered at the same area. The structure in Fig. 8.12a is swept cathodically to 8.12b,c and later anodically swept back to 8.12d-f. The starting structure 8.12a consists of both dimer and cavitand phases. By decreasing the potential beyond P1, both phases are transformed into the stacking phase. After that, increasing the potential back, the stacking phases of the two parts are stable until -90 mV then reaching the potential regime of the phase transition back to the cavitand phase. The two parts are transformed into cavitand phase simultaneously without forming an intermediate dimer phase even at the place where it existed previously, proving the irreversibility of the transition from the dimer phase to the stacking phase. These phenomena are also applied for the other metastable phase transitions of dimer and type B phases to both stacking and cavitand phases.

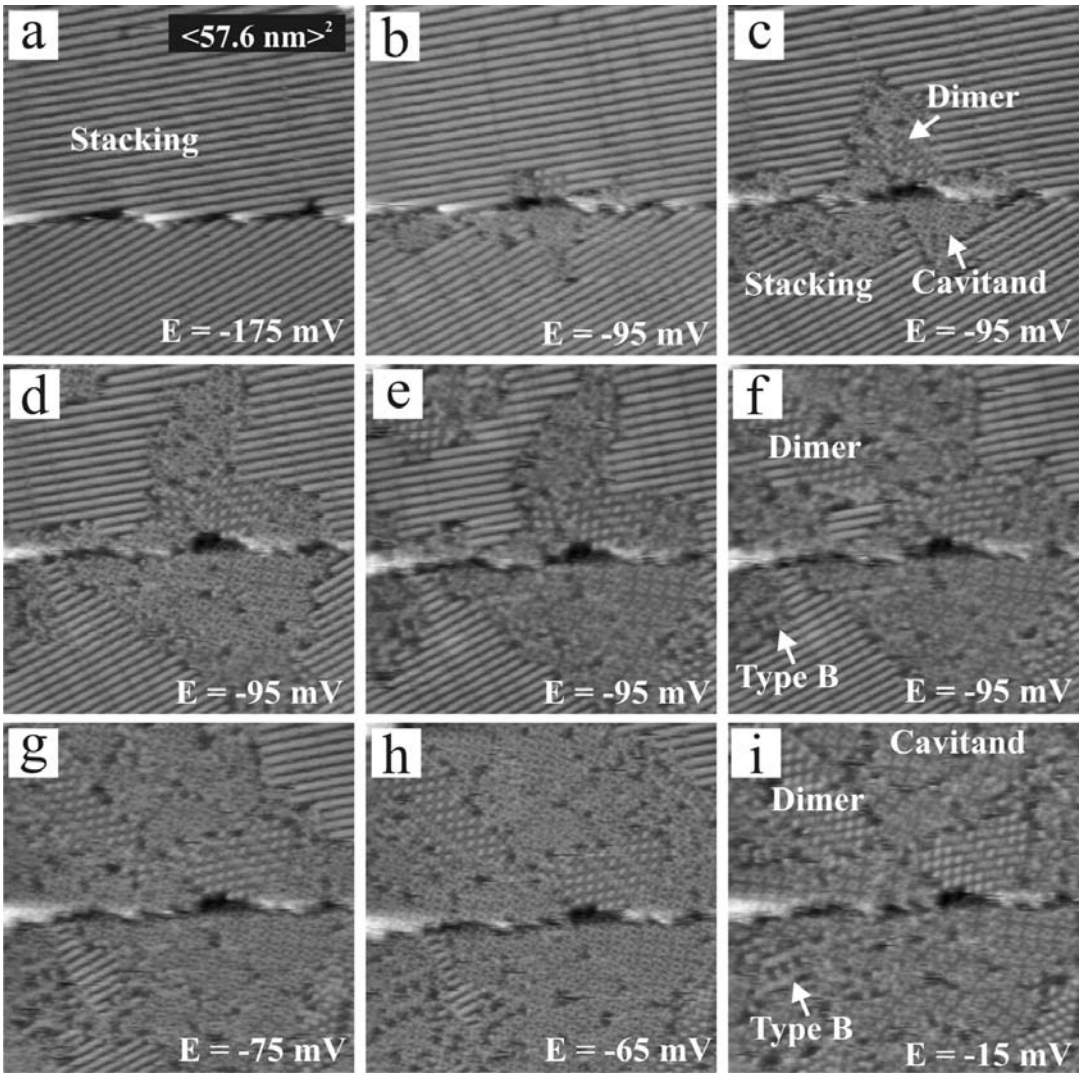

Figure 8.13: STM series showing the very exceptional occurrence of patches of metastable phases when following the phase transition from the stacking to the cavitand phase, (a)-(i) I_t = 0.1 nA, U_b = 143 mV.

As mentioned above, we can observe the metastable phases by adsorption of DBV molecules under reactive condition within the initial potential regime from -120 mV to -250 mV (the positive side of the reduction peak P1 in CV of Fig. 8.1a). Once formed the metastable phases are stable in a broad potential regime from -300 mV to +70 mV (see series in Fig. 8.11). Scanning further than that stable regime to more negative or positive potential, causes phase transitions from the metastable phases into stacking or cavitand phase, respectively. Then these metastable structures cannot be observed any more due to the irreversibility of the phase transitions. However surprisingly, in one STM experiment, when imaging the phase transition from the stacking phase back to the cavitand phase, we observed the presence of the two metastable phases within the phase transition, as shown in Fig. 8.13.

It is noteworthy that normally, the phase transition from the stacking phase back to the cavitand phase starts systematically at potential higher than -160 mV and completes at about -60 mV (see STM series in Figs. 5.28, 8.12d-f, 8.13). This regime is not completely out of the oxidation peak P'1 (CV in Fig. 8.1a) Therefore at the beginning of the phase transition, in solution, the $DBV^{\bullet+}_{aq}$ species or even dimers of $DBV^{\bullet+}$ are still present. In Fig. 5.28, the phase transition started very early at a potential of -160 mV, but the transition still ended up with a full monolayer of cavitand phase. On the other hand, in Fig. 8.13 the transition begins later at potential of -95 mV, but in some small areas indicated in Fig. 8.13, we find structures of the metastable phases. This can be explained by the fact that within the transition whenever moieties of $(DBV^{\bullet+}_{ads})_n$ stacking chains at the surface are oxidized into the dication DBV^{2+}, they generally adsorb almost simultaneously to form the DBV^{2+}_{ads} cavitand phase. However, in the special circumstances of Fig. 8.13, after oxidation the surface DBV species move out from the surface revealing the bare chloride lattice and then the dimers which are present close to the surface can readsorb to form the nucleation for the metastable phase adsorption as seen in Fig. 8.13. The removal of the pre-adsorbed DBV species is assumed to be tip-induced. Furthermore, because the dimer phase adsorbs partly in Fig. 8.13, we can observe the growth of its adsorption which is assumed to form row by row.

In spites of the observation of the metastable phase upon the phase transition from stacking to cavitand phase, the conclusion on the irreversibility of the transition from metastable phases into corresponding stacking or cavitand phases is still valid. The observation of the metastable phase is rather a non-equilibrium tip-induced effect.

8.4 Stability of metastable phases

The previous section illustrated the irreversible phase transitions from the metastable phases into the stacking or cavitand phase. Besides, Sec. 5.4.1 described already in detail the phase transitions between the stacking and the cavitand phase. However, it is noteworthy that these latter phase transitions (into the stacking or the cavitand phase) occur in different potential regimes.

Firstly, we compare the transition from the stacking to the cavitand phase with that of the metastable phases to the cavitand phase. The transition from the stacking phase to the cavitand phase was illustrated by the STM series of Figs. 5.28, 8.12d-f and 8.13, showing that the potential range of the transition depends strongly on the respective experiment. Generally, this transition starts at potentials ranging from -160 mV to -90 mV and completes at potentials ranging from -60 mV to 0 mV. That means above 0 mV, all surface $DBV^{\bullet+}$ species of the stacking phase are completely

transformed into the DBV^{2+} species of the cavitand phase. On the other hand, the metastable phase dimer once formed remains stable until +20 mV upon sweeping into the positive potential regime. Indeed, as exemplified in Fig. 8.11a, the phase transition from the dimer phase into the cavitand phase starts at a potential of +20 mV and completes at even higher potential of +80 mV. The transition from the metastable phase B to the cavitand phase was also studied (the result not shown here) representing on even higher stability in which the type B-cavitand phase transition starts at +90 mV and completes at +120 mV. Therefore, concerning the transition to the cavitand phase, the two metastable phases show a higher electrochemical stability than the stacking phase.

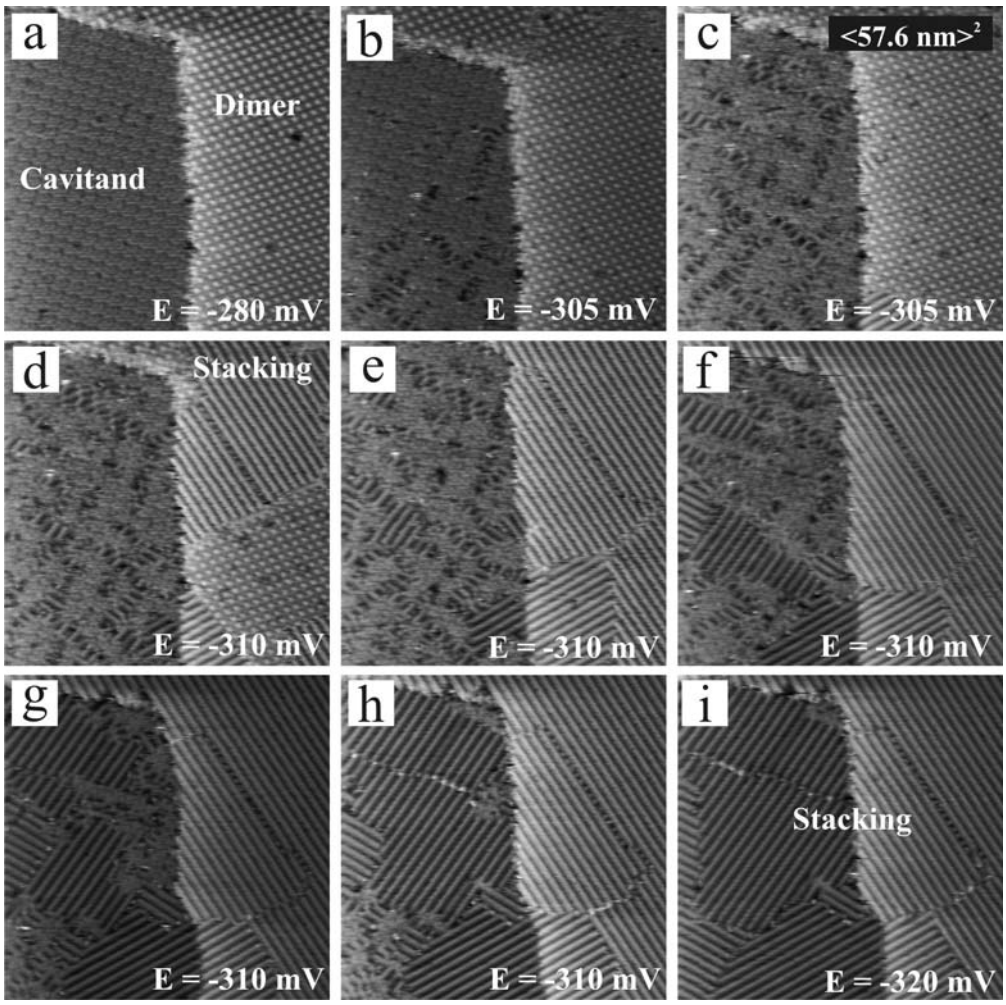

Figure 8.14: Characteristics of dimer-stacking and cavitand-stacking phase transitions, I_t = 0.2 nA, U_b = 286 mV.

Secondly, we compare the transition from the cavitand to the stacking phase with that of the metastable phases to the stacking phase. Although the dimer-stacking

phase transition was illustrated in Fig. 8.11b and the cavitand-stacking phase transition was discussed in Sec. 5.4.1 and illustrated in Fig. 5.22, the comparison is described in more detail in Fig. 8.14. Starting with the co-adsorption of both cavitand and dimer phase, on going to negative potentials, both phases transform into the stacking phase but with different behaviors. The cavitand-stacking phase transition starts at potential of -300 mV and completes at -320 mV. On the other hand, the dimer-stacking phase transition starts a bit later at -310 mV, this phase transition is so rapid that it completes at nearly the same potential of -310 mV. From all mentioned STM series, it is seen that for the cavitand-stacking phase transition, the nucleation starts at defects and spreads over the whole structure, the growth occurs slowly to the finally condensed stacking phase. However, as to the dimer-stacking phase transition, the nucleation starts from the step edges and the growth is much faster. It is noteworthy that from the STM series of Fig. 5.22, the cavitand-stacking phase transition started much earlier at potential of -240 mV because the starting cavitand phase is less ordered or has more defects. The type B-stacking phase transition was also carried out showing the same nucleation behavior as from the dimer phase but taking place later. It starts at potential of -320 mV and completes at -350 mV (the result not shown here).

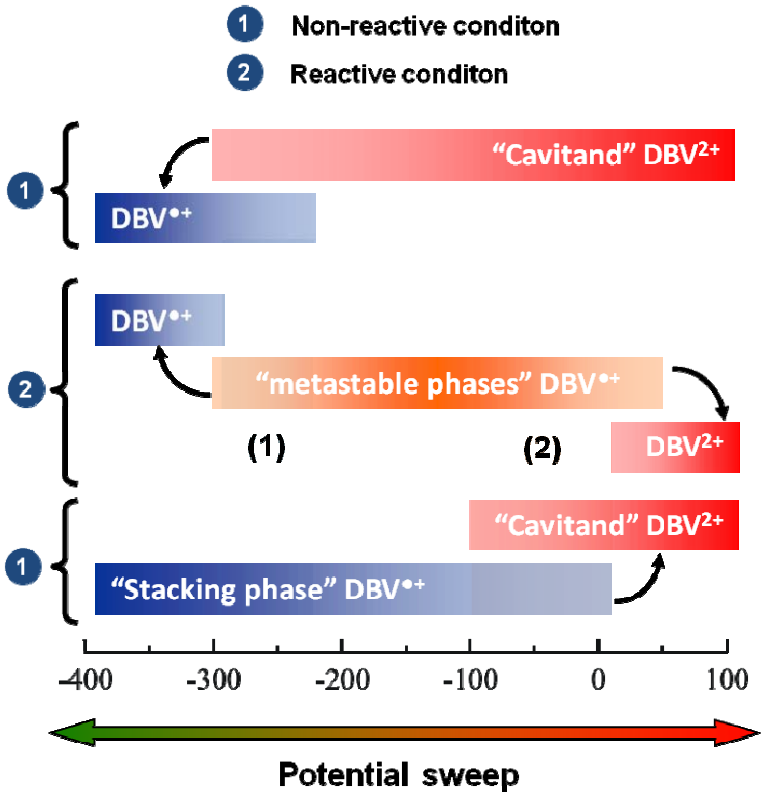

Figure 8.15: Phase diagram of irreversible *vs* reversible transitions, showing the different stability regimes of phases produced under reactive and non-reactive conditions, resp.

Fig. 8.15 shows the potential phase diagram of irreversible transition from metastable phases to cavitand and stacking phase in comparison with reversible transitions between cavitand and stacking phase. Obviously, the metastable phases produced under reactive conditions remain stable in a broad potential regime showing higher electrochemical persistence than the phases of cavitand and stacking which are formed under non-reactive conditions. The regimes (1) and (2) are potential regimes where the metastable phases persist and do not transform into the cavitand and stacking phase, respectively. This hindered transformation gives raise to interesting the tip-induced effects presented in the next section.

8.5 Tip-induced effect on metastable phases

By applying a drastic tunneling condition of high tunneling current and low bias voltage, the tip can penetrate deeper into the surface structure, thereby locally removing the top layer and revealing the lattice underneath. This tip-induced effect has been applied quite often throughout the thesis. It is normally used for the removal of the viologen adlayer in order to observe the chloride lattice underneath.

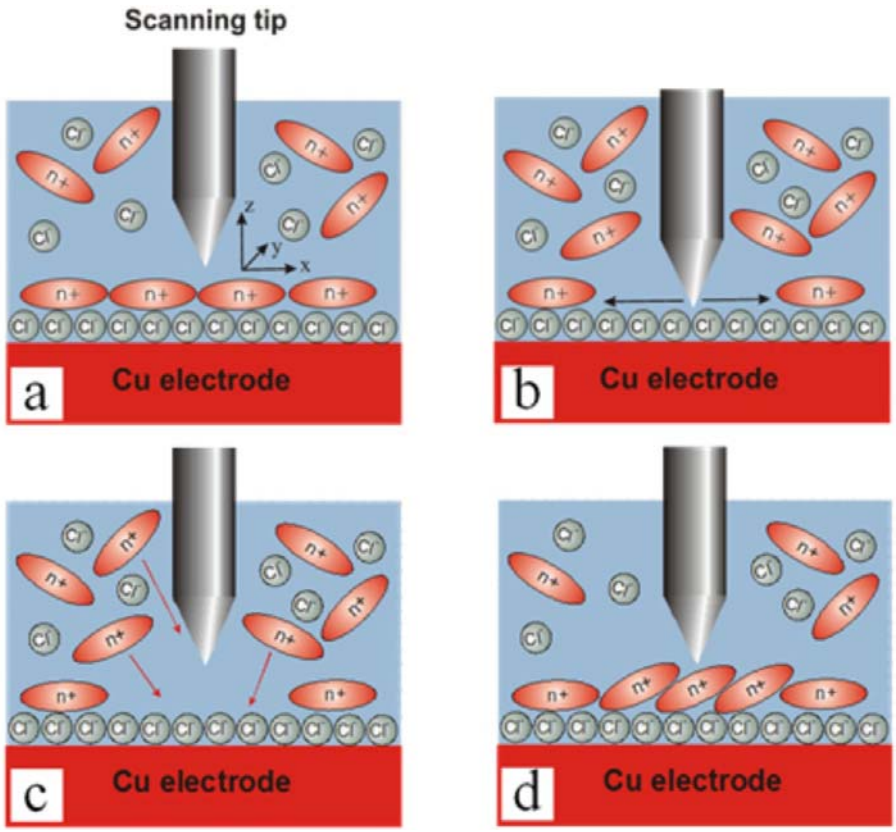

Figure 8.16: Model of the tip-induced effect on the metastable phases in the potential regime (1) of Fig. 8.15.

Generally, while returning to the moderate tunneling condition, the viologen readsorbs with the same structure as observed before. However, if we apply the effect to the metastable phases in the regime (1) or (2) of the phase diagram in Fig. 8.15, the readsorbed structure obtained inside the tip-induced area are different due to the metastability of the dimer- and type B phases compared to the cavitand or stacking phase. Within the regime (1), the model for the tip-induced effect on the metastable phases is illustrated in Fig. 8.16.

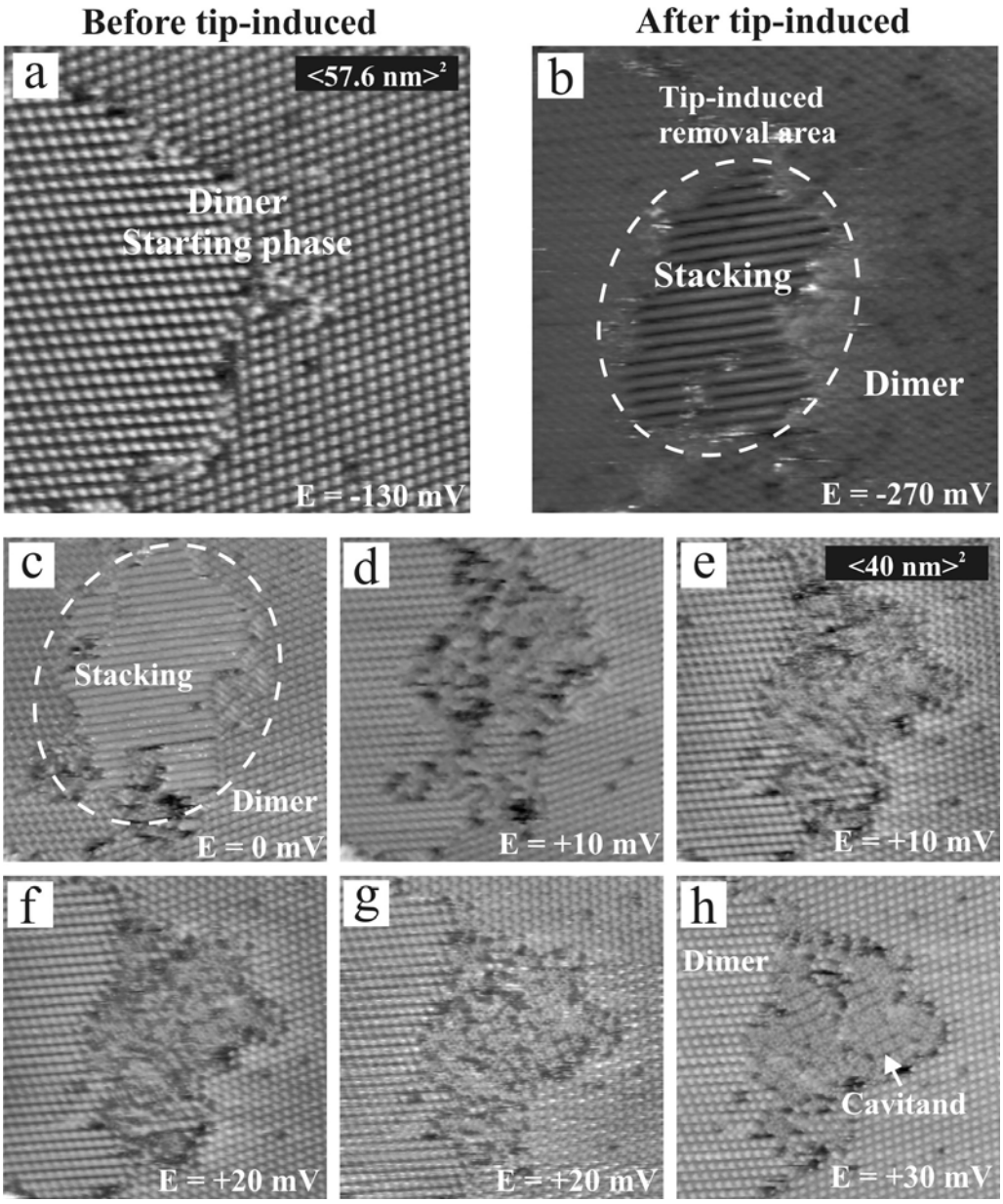

Figure 8.17: (a)-(b) Tip-induced effect on dimer phase applied in the regime (1) of Fig. 8.15, (c)-(h) STM series showing the stacking-cavitand phase transition within the local defect, I_t = 1.0 nA, U_b = 170 mV.

In the model of Fig. 8.16, the tip has been used to remove locally the metastable phase structure, forming a local defect within the viologen film (Figs. 8.16a and b). Subsequently, the tip was withdrawn by applying more moderate tunneling conditions (Fig. 8.16c). As a consequence the viologen species readsorb in the tip-induced local defect with different structures depending on the applied potential (Fig. 8.16d). If the tip-induced effect takes place within the regime (1) in Fig. 8.15, the final structure observed in that local area is the stacking phase, as shown in Figs. 8.17b and 8.18b.

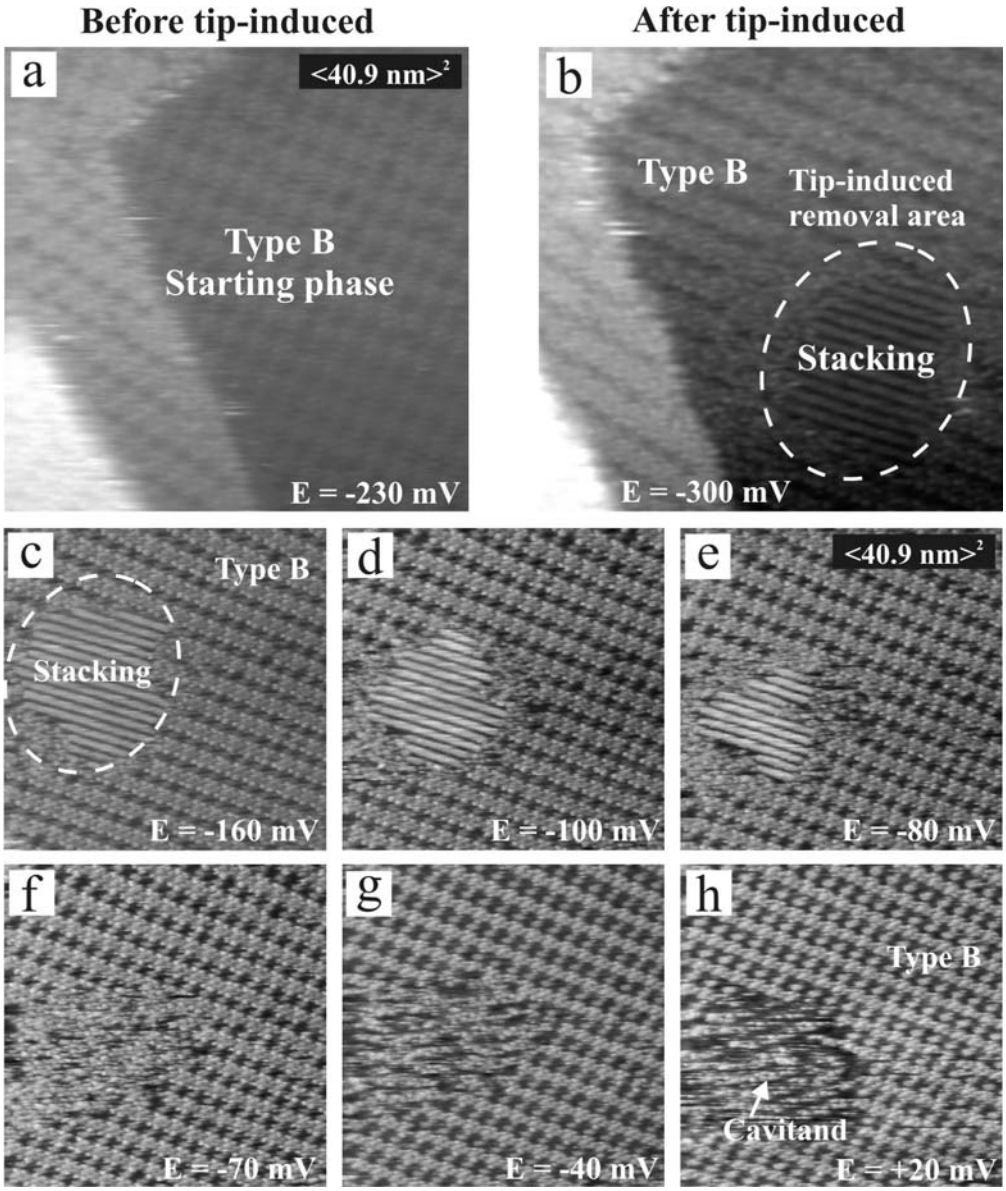

Figure 8.18: (a)-(b) Tip-induced effect on metastable type B phase applied in the regime (1) of Fig. 8.15, (c)-(h) STM series showing the stacking-cavitand phase transition within the local defect, I_t = 0.1 nA, U_b = 139 mV.

Fig. 8.17 starts with the dimer phase (Fig. 8.17a), then the potential is changed to -270 mV in the regime (1) of Fig. 8.15. After applying the tip-induced effect the structure within the local defect area appears as stacking phase (Fig. 8.17b). Sweeping the potential then to the positive regime causes a stacking-cavitand phase transition only within the tip-induced local area while the surrounding dimer structure remains unchanged (Fig. 8.17c-d). This phenomenon follows from the broader potential range of the metastable phase as shown in phase diagram of Fig. 8.15.

The same experiment was carried out by starting with the metastable phase B, and the same phenomenon was observed as described in Fig. 8.18.

Although in the frame of this thesis, the STM experiments of tip-induced effect on the metastable phases were only done within the regime (1) of Fig. 8.15 forming the stacking phase within the local removal area, it is expected that if we perform the experiment in the regime (2), the structure obtained in the tip-induced area should be the cavitand phase. However the phenomenon of cavitand-stacking phase transition within the local removal area with the surrounding metastable phase remaining stable can hardly be performed, because the metastable-stacking phase transition takes place almost together and coincides with the cavitand-stacking phase transition as discussed in the previous section.

8.6 Summary

In contrast to the *non-reactive* adsorption, in which the DBV solution was added into the cell at the potential regime from -100 mV to +100 mV within the double layer regime, the initial adsorption of DBV on chloride modified Cu(100) under *reactive* conditions is introduced at the potentials within the potential regime of the first reduction peak P1, i.e. from -120 mV to -250 mV. Therefore under the *reactive* condition, the adsorption of DBV species takes place *during* an ongoing electron transfer reaction.

The reactive viologen adsorption leads to two new structures, namely the type A, i.e. metastable dimer, and type B phase, which have considerably different potential-dependent surface structures and coverages than known from the non-reactive viologen adsorption. Especially, the surface morphology of these two new structures is always well-ordered. The two structures can be found to co-exist, however, in most cases, the dimer phase generally appears at the regime from -120 mV to -200 mV, while type B exists at more negative potentials from -200 mV to -250 mV. The structural models of the two metastable phases have been proposed to be both composed of $(DBV^{\bullet+})_2$ dimers, showing that the dimer phase has the smaller surface coverage than that of the type B phase.

By anodic or cathodic potential sweeps, the metastable phases can be transformed into the cavitand or the stacking phase already known from the non-reactive adsorption procedure, however in an irreversible way. The irreversible phase transitions of the metastable phases are different from the cavitand-stacking phase transition concerning not only the nucleation and growth, but also the potential regimes. In other words, especially the existence regimes of the metastable phases *overlap* with those of cavitand or stacking phase within the potential regimes denoted as (1) and (2) of the diagram in Fig. 8.15. Therefore, the transitions of metastable phases are accompanied by higher activation barriers than that between cavitand or stacking phase, giving rise to the interesting observation of a tip-induced effect which takes place within the regime (1). Namely after a local tip-induced removal of a metastable DBV structure DBV species readsorb but in the different structure of cavitand or stacking phase depending on the applied potential. A subsequent potential scan leads to a stacking-cavitand phase transition only within the tip-effected local area while the surrounding metastable structure remains unchanged.

Part V

Conclusion

Chapter 9

Conclusion

Organic layers play an increasingly important role in modern material science. Nowadays, organic chemistry can synthesize almost any kind of functional organic molecules, while surface physics on the other hand provides analytical techniques of high microscopic and spectroscopic resolution. Therefore, the symbiosis of organic chemistry and surface physics is a prerequisite to understand and design the physical and chemical properties of organic films. In this context especially supramolecular chemistry plays an important role to exploit all possible interaction mechanism for the self-assembly of the organic molecules. However, the fact that many organic molecules are not intact volatile makes their deposition in UHV impossible. Therefore, the deposition of organic layers from solution becomes a promising alternative route. Particularly in solution, by applying electrochemical techniques, the electrochemical potential is an additional parameter to control the deposition and growth of organic layers. Motivated by that approach, this thesis aimed at investigating the electrochemical deposition of redox active viologen species. In supramolecular chemistry, the role of viologens as molecular building-blocks is particularly interesting thanks to the intra-molecular conformational changes between their different redox-states. Hence, this work focuses on the surface *redox-chemistry* and the related structural *phase behavior* of electrodeposited viologens.

In order to achieve an atomistic understanding of the viologen adsorption both the *electrochemical engineering approach* and the *electrochemical surface science approach* are applied here. The "electrochemical engineering" is realized by varying

- the molecular structure,
- the nature of the substrate, and
- the external parameters like concentration, electrode potential etc.

The "surface science approach" is realized by using a combination of the following three methods:

- Cyclic Voltammetry (CV) as a traditional method for the redox chemistry of the viologen containing electrolyte under potential control,
- *In-situ* Electrochemical Scanning Tunneling Microscopy (EC-STM) as an atomistically sensitive techniques for surface structure determination and phase behavior of the viologen adlayer,
- *Ex-situ* X-ray Photoelectron Spectroscopy (XPS) as a supplement method for the correlation of the observed structures with the exact chemical state of the molecules.

In the framework of this thesis, the measured systems are the following:

- Dibenzyl-Viologen (DBV) adsorbed on a chloride modified Cu(100) surface under *non-reactive* conditions,
- DBV adsorbed on an HOPG substrate,
- Diphenyl-Viologen (DPV) adsorbed on a chloride modified Cu(100) surface, and
- DBV adsorbed on a chloride modified Cu(100) surface under *reactive* condition.

Not only is each of these systems investigated systematically and intensively, but also a careful comparison between them is presented. By far, most of the EC-STM investigations have been performed under potentiostatic and equilibrium (or *non-reactive*) conditions. However, it is for the first time that a system was also prepared under *reactive* conditions, i.e. *during* an ongoing electron transfer reaction. The main results of the thesis are summarized in the following.

First to be mentioned is the role of the preadsorbed c(2 x 2) chloride adlayer on the Cu(100) electrode surface which plays the role of a template for the viologen adsorption. This chloride layer is not only a potential binding partner for the viologen building-blocks, the anion modified surface as a whole can also act as a reactant in terms of an electron-donor or electron-acceptor in the electrochemical environment, and can even enhance the adsorption of the cationic viologen species due to electrostatic attraction.

On the chloride precovered Cu(100) template, the DBV species adsorb under non-reactive conditions at high initial electrode potentials as DBV^{2+} dication and form a so-called cavitand phase. Electrostatic interaction between the negatively charged chloride layer and these dicationic viologens is taken to be the major driving force for their adsorption and subsequent lateral ordering on the chloride modified electrode surface. In this thesis a new structural model of the cavitand phase is proposed which agrees with the obtained high resolution STM images and improves a previously published model considerably. This new model includes also a detailed explanation

for the two types of translational domain boundaries, namely “strong” and “weak” domain boundaries, observed in the STM images. Furthermore, this new structural model has the potential to be applied also for the interpretation of dicationic cavitand phases of other viologen species adsorbed on halide modified metal templates.

Passing the first reduction peak P1 in the cyclic voltammogram of Cu(100) in DBV containing hydrochloric acid in cathodic direction, a quasi-reversible phase transition from the dicationic DBV^{2+} cavitand phase to a radical cation $(DBV^{\bullet+})_n$ stacking phase is observed. The almost planar conformation of the bipyridinium cores in the reduced monocation radial state allows a small intermolecular distance and, hence, π-π stacking within the 1D polymer chains of the condensed DBV stacking phase. Therefore, the strong attractive intermolecular interactions play the dominant role as the driving force for the “polymerization” of that stripe structure.

Continuation of the cathodic scan until reaching the chloride desorption peak P2(DBV/Cl/Cu) initiates an order/disorder phase transition from the $DBV^{\bullet+}$ stacking phase to an amorphous phase. This process is driven by the chloride desorption through the viologen layer. The presence of the mobile amorphous phase is also responsible for an inhibition effect which shifts the hydrogen evolution reaction (HER) to more negative potentials. This order/disorder phase transition is reversible, the stacking phase reappears after readsorption of the chloride.

By contrast, on inert HOPG, without the presence of the preadsorbed anion layer, the dication DBV^{2+} species does not adsorb. The formation of an ordered structure is not observed until the radical cation regime of DBV is reached, then a double layer stripe phase of separated $DBV^{\bullet+}$ species is observed. Going to even more negative potentials and passing the second reduction peak P3(DBV/HOPG), a phase transition from the radical cation $DBV^{\bullet+}$ double layer stripe phase to an uncharged $(DBV^{0+})_n$ stacking phase occurs. The reason why on HOPG the polymeric stacking phase cannot appear in the radical cationic form is assumed to be related to the repulsive electrostatic interactions between $DBV^{+\bullet}$ species without the enhancement of the anion template.

In contrast to the adsorption of the dication DBV^{2+} cavitand phase, DPV^{2+} species adsorbing from solution instantaneously react to the corresponding radical cation $DPV^{+\bullet}$ on the chloride-modified surface followed by the formation of a condensed $(DPV^{+\bullet})_n$ stacking monolayer phase. Therefore, DPV can be regarded as prototype of a highly reactive viologen species. This stacking layer is highly hydrophobic which completely removes all water species from the chloride lattice. Upon adsorption and phase formation the DPV releases also completely its solvation shell as a pre-requisite to undergo strong inter-viologen interactions, most likely in the form of π-π interactions. The structure of this stacking phase is characterized by the preferential adsorption at steps of [100] orientation, forming typical double rows along the step-

edges on the chloride precovered template. It is noteworthy that there are two modifications of this DPV stacking monolayer phase, namely Type I and Type II, the former of which is less stable. Passing the first reduction peak of solution species P1(DPV), all Type I structure transforms into Type II, creating a homogeneous DPV stacking monolayer on the surface. Going to even more negative potentials, i.e. passing -250 mV, initiates a phase transition from the stacking monolayer phase to a stacking double layer phase of $DBV^{\bullet+}$ species. Once formed the double layer structure is stable on the surface in the whole copper potential window despite the occurrence of electron transfer reactions through it. Upon further negative scan until reaching the chloride desorption peak P2(DPV), unlike the amorphous phase of DBV, the DPV double layer phase co-desorbs with the chloride leaving the bare substrate behind. This phase transition can be reversed to form again the DPV double layer structure.

Returning to the interaction of DBV with the chloride template a very interesting observation could be made in experiments under reactive adsorption condition in which the DBV containing electrolyte is added into the electrochemical cell at initial potentials within the first reduction peak regime. Under these conditions the adsorption of the DBV^{2+} species takes place during an ongoing electron transfer reaction. Interestingly, the obtained adlayer structure under this condition is totally different from the previously observed DBV cavitand or stacking phases after non-reactive adsorption. Furthermore, there are even two new structures, namely type A, i.e. metastable dimer, and type B phase which may also coexist. The formation of the dimer phase is found at more positive potentials and has a smaller surface coverage than the type B phase. These two metastable phases are proved to be structures with $(DBV^{\bullet+})_2$ dimers as building-blocks. By anodic or cathodic potential sweep, the metastable phases can be transformed into the cavitand or stacking phase, respectively, however in an irreversible way. These irreversible phase transitions of the metastable phases differ from the cavitand-stacking phase transition not only concerning the nucleation and growth behavior, but also concerning the potential regimes of their occurrence. In other words, the transitions are accompanied by higher activation barriers than that between cavitand or stacking phase, especially in the high potential regime. That gives rise to the interesting observation of tip-induced effects which take place within the potential regimes where the existence regime of the metastable phases overlaps with the cavitand and stacking phase, respectively. Namely after a local tip-induced removal of a metastable DBV structure DBV species readsorb but in the different structure of cavitand or stacking phase depending on the applied potential. A subsequent potential scan leads to a stacking-cavitand phase transition only within the tip-effected local area while the surrounding metastable structure remains unchanged.

Outlook and Prospect

Obviously, CV and EC-STM are an excellent combination of methods for the *in-situ* investigation of both solution chemistry and phase behavior of adsorbed organic layers. Furthermore, the atomistically resolved results of the EC-STM promise successful future work with other building-blocks or more complex organic molecules. From this work, the chloride modified surface in particular and any anion modified surface in general proved to be an appropriate template for the adsorption of organic molecules in cationic form. Moreover, the thesis has successfully demonstrated that the adsorption of species under *reactive* conditions can possibly open a door to new phenomena in two-dimensional supramolecular chemistry at solid/electrolyte interfaces.

References

[1] Southampton Electrochemistry Group, *Instrumental Methods in Electrochemistry* (New York: Ellis Horwood in Physical Chemistry), (1990).

[2] F. Vögtle, *Supramolecular Chemistry: An Introduction*, John Wiley and Sons, Ltd, Chichester, UK, 1st edn, (1991).

[3] C. L. Bird and A. T. Kuhn, *Electrochemistry of the Viologens*, Chem. Soc. Rev., 10, p. 49-82, (1981).

[4] P. M. S. Monk, *The Viologens: physicochemical properties, synthesis and applications of the salts of 4,4'-bipyridines*, John Wiley and Sons, Ltd., Chichester, UK, 1st edn, (1998).

[5] C. Zörlein, *Supramolekulare Architekturen an fest/flüssig-Grenzflächen*, PhD thesis, University of Bonn (2005).

[6] J. Wang, *Analytical Electrochemistry*, Wiley-VCH, (Hardback) Manual, (2000).

[7] R. Guidelli and W. Schmickler, *Recent developments in models for the interface between a metal and an aqueous solution*, Electrochim. Acta, 45, p. 2317–2338, (2000).

[8] D. C. Grahame, *The electrical double layer and the theory of electrocapillarity*, Chem. Rev. 41, p. 441–501, (1947).

[9] O. M. Magnussen, *Ordered anion adlayers on metal electrode surfaces*, Chem. Rev., 102, p. 679–725, (2002).

[10] G. J. Gouy, *Constitution of the Electric Charge at the Surface of an Electrolyte*, Phys. 1910, 9, p. 457–468.

[11] D. L. Chapman, *LI. A contribution to the theory of electrocapillarity*, Phil. Mag. 1913, 25, p. 475–481.

[12] K. Kolasinski, *Surface science: Foundations of catalysis and nanoscience*. John Wiley & Sons, Ltd, (2001).

[13] http://www.virginia.edu/ep/SurfaceScience/electron.html (accessed Aug 2010).

[14] A. Groß, *Theoretical surface science - A microscopic perspective*. Berlin: Springer, (2002).

[15] J. E. B. Randles, *Cathode-ray polarograph. II. Current-voltage curves*, Trans. Faraday Soc., 44(5), p. 327-338, (1948).

[16] G. Binnig and H. Rohrer, *Scanning tunneling microscopy*, Surf. Sci., 126(1-3), p. 236–244, (1983).

[17] G. Binnig, H. Rohrer, C. Gerber and E. Weibel, *Tunneling through a controllable vacuum gap*, Appl. Phys. Lett., 40(2), p. 178–180, (1982).

[18] G. Binnig and H. Rohrer, *The Scanning Tunneling Microscopy*, Scientific American, 253(2), p. 50–56, (1985).

[19] R. Sonnenfeld and P. K. Hansma, *Atomic-resolution microscopy in water*, Science, 232(4747), p. 211–213, (1986).

[20] E. Meyer, H. J. Hug and R. Bennewitz, *Scanning Probe Microscopy – The lab on a tip, Introduction to Scanning Tunneling Microscopy*, Springer-Verlag Berlin Heidelberg, (2004).

[21] M. Tsukada, K. Kobayashi, N. Isshiki, and H. Kageshima, *First-principles theory of scanning tunneling microscopy*, Surf. Sci. Rep., 13(8), p. 265–304, (1991).

[22] J. Tersoff and D. R. Hamann, *Theory and application for the scanning tunneling microscope*, Phys. Rev. Lett., 50(25), p. 1998–2001, (1983).

[23] J. Tersoff and D. R. Hamann, *Theory of the scanning tunneling microscope*, Phys. Rev. B, 31(2), p. 805–813, (1985).

[24] M. Wilms, *Potentiodynamische Rastertunnelmikroskopie and Fest/Flüssig-Grenzplächen: Apparative Entwicklung and Untersuchung zur Sulfat-Adsorption auf Cu(111)*. PhD thesis, University of Bonn, (1999).

[25] K. Oura, V. Lifshits, A. Saranin, A. Zotov and M. Katayama, *Surface Science - An introduction*, Springer-Verlag Berlin Heidelberg, (2003).

[26] H. Bubert and H. Jenett, *Surface and Thin Film Analysis: Principles, Instrumentation, Applications*. Wiley-VCH Verlag GmbH, (2002).

[27] M. Wilms, M. Kruft, G. Bermes and K. Wandelt, *A new and sophisticated electrochemical scanning tunneling microscope design for the investigation of potentiodynamic processes*, Rev. Sci. Instrum., 70(9), p. 3641–3650, (1999).

[28] K. Besocke, *Characterization of films deposited by in-situ wall carbonization in TEXTOR*, Surf. Sci., 181(1-2), p. 145–153, (1987).

[29] In: K. Wandelt and S. Thurgate, *Solid-Liquid Interfaces*, Topic Appl. Phys. 85. Springer-Verlag Berlin Heidelberg, (2001).

[30] P. Broekmann, *Atomare Struktur und Dynamik von Kupfer/Elektrolyt-Grenzflächen*. PhD thesis, University of Bonn, (2002).

[31] D. Friebel, *In situ STM-Untersuchungen ultradünner Kupferchalkogenid-Filme auf Au(111)-Elektrodenoberflächen*, PhD thesis, University of Bonn, (2007).

[32] K. Itaya, *In situ scanning tunneling microscopy in electrolyte solutions*, Prog. Surf. Sci., 58(3), p. 121–247, (1998).

[33] J. Clavilier, R. Faure, G. Guinet and R. Durand, *Preparation of monocrystalline platinum microelectrodes and electrochemical study of the plane surfaces cut in the direction of the {111} and {110} planes*, J. Electroanal. Chem., 107(1), p. 205–209, (1980).

[34] J. Clavilier, *The role of anion on the electrochemical behavior of a {111} platinum surface; an unusual splitting of the voltammogram in the hydrogen region,* J. Electroanal., Chem., 107(1), p. 211–216, (1980).

[35] A. Hamelin, *In Modern Aspects of Electrochemistry*. No. 16, New York: Plenum Press, (1985).

[36] S. Motoo and N. Furuya, *Hydrogen and oxygen adsorption on iridium(111), (100) and (110) planes*, J. Electroanal. Chem., 167(1-2), p. 309–315, (1984).

[37] K. Sashikata, N. Furuya and K. Itaya, *In situ electrochemical scanning tunneling microscopy of single-crystal surfaces of platinum(111), rhodium(111), and palladium(111) in aqueous sulfuric acid solution*, J. Vac. Sci. Technol., B, 9(2), p. 457–464, (1991).

[38] J. H. Schott and H. S. White, *Halogen Adlayers on Ag(111)*, J. Phys. Chem., 98(1), p. 291–296, (1994).

[39] A. T. Hubbard, *Electrochemistry at well-characterized surface*, Chem. Rev., 88(4), p. 633–656, (1988).

[40] M. P. Soriaga, *Ultra-high vacuum techniques in the study of single-crystal electrode surfaces*, Prog. Surf. Sci., 39(4), p. 325–443, (1992).

[41] G. M. Brisard, E. Zenati, H. A. Gasteiger, N. M. Markovic and P. N. Ross, *Underpotential Deposition of Lead on Copper(111): A Study Using a Single-Crystal Rotating Disk Electrode and ex Situ Low-Energy Electron Diffraction and Scanning tunneling Microscopy*, Langmuir, 11(6), p. 2221–2230, (1995).

[42] D. Briggs and M.P. Seah, *Practical Surface Analysis by Auger and X-ray Photoelectron Spectroscopy*, New York John Wiley and Sons (1985).

[43] C.S Fadley, *in Electron Spectroscopy: Theory, techniques and applications*, C.R. Brundle, A.D Baker (editor), academic press, London, New York, San Francisco, (1978).

[44] http://www.chem.queensu.ca/people/faculty/horton/research.html (accessed Aug 2010).

[45] C. J. Powell, A. Jablonski, A. Naumkin, A. K-Vass, J.M Conny and J.R. Rumble, *NIST data resources for surface analysis by x-ray photoelectron spectroscopy and Auger electron spectroscopy*, J. Electron Spectrosc. Relat. Phenom., 114, p. 1097-1102, (2001).

[46] T. Mayer, M. Lebedev, R. Hunger and W. Jaegermann, *Elementary processes at semiconductor/electrolyte interfaces: perspectives and limits of electron spectroscopy*, *Appl. Surf. Sci.* 252, p. 31-42, (2005).

[47] http://nanoprobes.aist-nt.com/apps/HOPG 20info.htm (accessed Aug 2010).

[48] http://en.wikipedia.org/wiki/Copper (accessed Aug 2010).

[49] P. C. Andricacos, C. Uzoh, J. Dukovic, J. Horkans and H. Deligianni, *Damascene copper electroplating for chip interconnections*, IBM J. Kes. Develop., 12, p. 567–574, (1998).

[50] P. M. Vereecken, R. A. Binstead, H. Deligianni and P. C. Andricacos, *The chemistry of additives in damascene copper plating*, IBM J. Res. and Dev., 49, p. 3–18, (2005).

[51] D. Edelstein, J. Heidenreich, R. Goldblatt, W. Cote, C. Uzoh, N. Lustig, P. Roper, T. McDevitt, W. Motsiff, A. Simon, J. Dukovic, R. Wachnik, H. Rathore, R. Schulz, L. Su, S. Luce and J. Slattery, *Full copper wiring in a sub-0.25mm cmos ulsi technology, technical digest*, in IEEE International Electron Devices Meeting, p. 773, (1997).

[52] N. T. M. Hai, *Preparation and characterization of copper-iodide thin films and organic supramolecular layers at copper/electrolyte interfaces*, PhD thesis, University of Bonn (2007).

[53] D. Pletcher, R. Greef, R. Peat, L. Peter and J. Robinson, *Instrumental methods in electrochemistry*. Southampton Electrochemistry Group, University of Southampton, Horwood Publishing Limited, (2001).

[54] P. Broekmann, A. Spaenig, A. Hommes and K. Wandelt, *Influence of uniaxially incommensurate adlayers on the surface morphology: Iodide on Cu(100),* Surf. Sci., 517(1-3), p. 123–137, (2002).

[55] A. Hommes, A. Spaenig, P. Broekmann and K. Wandelt, *Low coverage p(2 x 2) iodide phase on Cu(100),* Surf. Sci., 547(1-2), p. 239–247, (2003).

[56] B. Obliers, P. Broekmann and K. Wandelt, *Uniaxial compression of iodide adlayers on Cu(111) studied under electrochemical conditions*, J. Electroanal. Chem., 554-555, p. 183–189, (2003).

[57] P. Broekmann, M. Anastasescu, A. Spaenig, W. Lisowski and K. Wandelt, *Atomic structures and dynamics of a Cu(100) electrode in dilute hydrobromic acid: An in situ STM study*, J. Electroanal. Chem., 500(1-2), p. 241–254, (2001).

[58] M. Kruft, B. Wohlmann, C. Stuhlmann and K. Wandelt, *Chloride adsorption on Cu(111) electrodes in dilute HCl solutions*, Surf. Sci., 377-379, p. 601–604, (1997).

[59] M. Wilms, P. Broekmann, M. Kruft, C. Stuhlmann and K. Wandelt, *STM investigation of step orientation and surface dynamics of Cu(111) in hydrochloric acid electrolyte*, Appl. Phys. A, 66, p. S473–S475, (1998).

[60] M. Wilms, P. Broekmann, C. Stuhlmann and K. Wandelt, *In-situ STM investigation of adsorbate structures on Cu(111) in sulfuric acid electrolyte*, Surf. Sci., 416(1-2), p. 121–140, (1998).

[61] M. Wilms, P. Broekmann, M. Kruft, Z. Park, C. Stuhlmann and K. Wandelt, *STM investigation of step orientation and surface dynamics of Cu(111) in hydrochloric acid electrolyte*, Surf. Sci., 402-404, p. 83–86, (1998).

[62] C. Safarowsky, A. Spaenig, P. Broekmann and K. Wandelt, *Reconstruction of a Cu(100) electrode in the presence of thiocyanate anions*, Surf. Sci., 538(3), p. 137–146, (2003).

[63] L. J. Wan and K. Itaya, *In situ scanning tunneling microscopy of Cu(110): atomic structures of halide adlayers and anodic dissolution*, J. Electroanal. Chem., 473(1-2), p. 10–18, (1999).

[64] P. Muller, S. Ando, T. Yamada and K. Itaya, *In situ scanning tunneling microscopy of Cu(110): atomic structures of halide adlayers and anodic dissolution*, J. Electroanal. Chem., 467(1-2), p.282–290, (1999).

[65] L. J. Wan, T. Suzuki, K. Sashikata, J. Okada, J. Inukai and K. Itaya, *In situ scanning tunneling microscopy of adsorbed sulfate on well-defined Pd(111) in sulfuric acid solution*, J. Electroanal. Chem., 484(2), p. 189–193, (2000).

[66] T. Yamada, N. Batina, and K. Itaya, *Interfacial structure of iodine electrodeposited on Au(111): studies by LEED and in situ STM*, Surf. Sci., 335(1-3), p. 204–209, (1995).

[67] M. Sugimasa, J. Inukai, and K. Itaya, *In situ STM studies of sulfur and thiocyanate adlayers on Cu(111) in alkaline solution*, J. Electroanal. Chem., 554, p. 285–291, (2003).

[68] M. T. M. Koper, *A lattice-gas model for halide adsorption on single-crystal electrodes*, J. Electroanal. Chem., 450(2), p. 189–201, (1998).

[69] A. Cuesta and D. M. Kolb, *The structure of bromide and chloride adlayers on Au(100) electrodes: an in situ STM study*, Surf. Sci., 465(3), p. 310–316, (2000).

[70] J. L. Stickney and C. B. Ehlers, *Surface chemistry of electrodes: Cu(111) in aquaous HCl*, J. Vac. Sci. Technol., A, 7(3), p. 1801–1805, (1989).

[71] W. Polewska, R. J. Behm, and O. M. Magnussen, *In-situ video-STM studies of Cu electrodeposition on Cu(100) in HCl solution*, Electrochim. Acta, 48(20-22), p. 2915–2921, (2003).

[72] M. R. Vogt, A. Lachenwitzer, O. M. Magnussen, and R. J. Behm, *In-situ STM study of the initial stages of corrosion of Cu(100) electrodes in sulfuric and hydrochloric acid solution*, Surf. Sci., 399(1), p. 49–69, (1998).

[73] M. R. Vogt, F. A. Moller, C. M. Schilz, O. M. Magnussen, and R. J. Behm, *Adsorbate-induced step faceting of Cu(100) electrodes in HCl*, Surf. Sci., 367(2), p. L33–L41, (1996).

[74] S. Huemann, N. T. M. Hai, P. Broekmann, K. Wandelt, H. Zajonz, H. Dosch, and F. Renner, *X-ray Diffraction and STM Study of Reactive Surfaces under Electrochemical Control: Cl and I on Cu(100),* J. Phys. Chem. B, 110(49), p. 24955–24963, (2006).

[75] D. W. Suggs and A. J. Bard, *Scanning Tunneling Microscopic Study with Atomic Resolution of the Dissolution of Cu(100) Electrodes in Aqueous Chloride Media*, J. Phys. Chem. 99(20), p. 8349-8355, (1995).

[76] S. E. Bae and A. A. Gewirth, *In Situ EC-STM Studies of MPS, SPS, and Chloride on Cu(100): Structural Studies of Accelerators for Dual Damascene Electrodeposition*, Langmuir, 22(25), p. 10315-10321, (2006).

[77] C. Y. Nakakura and E. I. Altman, *Bromine adsorption, reaction, and etching of Cu(100),* Surf. Sci., 370(1), p. 32-46, (1997).

[78] C. Y. Nakakura and E. I. Altman. *Scanning tunneling microscopy study of the reaction of Br2 with Cu(100),* Surf. Sci., 398(3), p. 281-300, (1998).

[79] J. M. Lehn, *Supramolecular Chemistry*, VCH, Weinheim, Germany, 1st edn, (1995).

[80] J. M. Lehn, *Supramolecular chemistry – Scope and perspectives. Molecules, supermolecules, and molecular devices*, (Nobel Lecture, 8.12.1987), Angew. Chem., Int. Ed. Engl., 27, p. 89-112, (1988).

[81] A. E. Kaifer and M. Gomez-Kaifer, *Supramolecular Electrochemistry*, VCH, Weinheim, Germany, 1st edn, (1999).

[82] V. Balzani, M. Venturi and A. Credi, *Molecular Devices and Machines*, Wiley-VCH, 1st edn, (2003).

[83] K. Ariga and T. Kunitake, *Supramolecular Chemistry - Fundamentals and Application*. Springer-Verlag Berlin Heidelberg, (2006).

[84] S. De Feyter and F. C. De Schryver, *Two-dimensional supramolecular self-assembly probed by scanning tunneling microscopy,* Chem. Soc. Rev., 32(3), p. 139–150, (2003).

[85] G. R. Desiraju, *The Crystal as a Supramolecular Entity - Perpectives in Supramolecular Chemistry, vol. 2*. Baffins Lane, Chichester, West Sussex PO19 1UD, England: John Wiley & Sons Ltd, (1996).

[86] P. S. Weiss, *Nanotechnology. Molecules join the assembly line,* Nature, 413(6856), p. 585–586, (2001).

[87] J. D. Hartgerink, E. R. Zubarev, and S. I. Stupp, *Supramolecular one-dimensional objects,* Curr. Opin. Solid State Mater. Sci., 5(4), p. 355–361, (2001).

[88] B. J. Holliday and C. A. Mirkin, *Strategies for the Construction of Supramolecular Compounds through Coordination Chemistry,* Angew. Chem. Int. Ed., 40(11), p. 2022–2043, (2001).

[89] D. L. Caulder and K. N. Raymond, *Supermolecules by Design*, Acc. Chem. Res., 32(11), p. 975–982, (1999).

[90] Q. H. Yuan, L. J. Wan, H. Jude, and P. J. Stang, *Self-Organization of a Self-Assembled Supramolecular Rectangle, Square, and Three-Dimentional Cage on Au(111) Surfaces,* J. Am. Chem. Soc., 127(46), p. 16279–16286, (2005).

[91] J. V. Barth, G. Costantini, and K. Kern, *Engineering atomic and molecular nanostructures at surfaces,* Nature, 437(7059), p. 671–679, (2005).

[92] R. G. Chapman and J. C. Sherman, *Templation and encapsulation in supramolecular chemistry*, Tetrahedron, 53(47), p. 15911–15945, (1997).

[93] M. S. Boeckl, T. Baas, A. Fujita, K. O. Hwang, A. L. Bramblett, B. D. Ratner, J. W. Rogers, and T. Sasaki, *Template-assisted nano-patterning of solid surfaces,* Biopolymers, 47(2), p. 185–193, (1998).

[94] G. M. Whitesides, J. P. Mathias, and C. T. Seto, *Molecular self-assembly and nanochemistry: a chemical strategy for the synthesis of nanostructures,* Science, 254(5036), p. 1312–1319, (1991).

[95] D. M. Vriezema, M. C. Aragones, J. A. A. W. Elemans, J. J. L. M. Cornelissen, A. E. Rowan, and R. J. M. Nolte, *Self-Assembled Nanoreactors*, Chem. Rev., 105(4), p. 1445–1489, (2005).

[96] H. Gleiter, *Nanostructured materials: basic concepts and microstructure,* Acta Mater., 48(1), p. 1–29, (2000).

[97] S. Leininger, B. Olenyuk, and P. J. Stang, *Self-Assembly of Discrete Cyclic Nanostructures Mediated by Transition Metals,* Chem. Rev., 100(3), p. 853–907, (2000).

[98] P. Laitenberger, C. G. Claessens, L. Kuipers, F. M. Raymo, R. E. Palmer, and J. F. Stoddart, *Building supramolecular nanostructures on surfaces: the influence of the substrate,* Chem. Phys. Lett., 279(3-4), p. 209–214, (1997).

[99] P. J. Thomas, N. Berovic, P. Laitenberger, R. E. Palmer, N. Bampos, and J. K. M. Sanders, *Room temperature manipulation of self-organized supramolecular nanostructures with a scanning tunneling microscope,* Chem. Phys. Lett., 294(1-3), p. 229–232, (1998).

[100] G. P. Lopinski, D. D. M. Wayner, and R. A. Wolkow, *Self-directed growth of molecular nanostructures on silicon,* Nature, 406(6791), p. 48–51, (2000).

[101] Y. He, T. Ye and E. Borguet, *Porphyrin Self-Assembly at Electrochemical Interfaces: Role of Potential Modulated Surface Mobility,* J. Am. Chem. Soc., 124(40), p. 11964–11970, (2002).

[102] R. Hoffmann, *Flexible Molecules with Defined Shape – Conformational Design*, Angew. Chem. Int. Ed. Engl. 31**,** p. 1124–1134, (1992)

[103] D. J. Searles and E.I. von Nagy-Felsobuki, *Ab Initio Variational Structure Calculations of Molecular Vibrational-Rotational Spectra*, Springer-Verlag, Berlin, (1993).

[104] K. Kobayashi, F. Fujisaki, T. Yoshimina and K. Nik, *An analysis of the voltammetric adsorption waves of methyl-viologen,* Bull. Chem. Soc. Jpn., 59(12), p. 3715-3722, (1986).

[105] K. Arihara, T. Ohsaka and F. Kitamura, *Characteristic cyclic voltammograms of alkyl-viologens at single crystal gold electrodes,* Phys. Chem. Chem. Phys., 4(6), p. 1002-1005, (2002).

[106] T. Lu and T. M. Cotton, *In situ Raman spectra of the three redox forms of heptylviologen at platinum and silver electrodes: counterion effects,* J. Phys. Chem., 91(23), p. 5978-5985, (1987).

[107] B. Kirchner and S. Kossmann, private communication.

[108] T. Lu, T. M. Cotton, J. K. Hurst and D. H. P. Thompson, *A Raman and surface-enhanced Raman study of asymmetrically substituted viologens,* J. Phys. Chem., 92(24), p. 6978-6985, (1988).

[109] S. H. Chen and X. M. Ren, *SERS studies of methylviologen on silver sol and the effect of halide ions*, Spectrochim. Acta, 51A(4), p. 717-725, (1996).

[110] X. Y. Tang, T. Schneider and D. A. Buttry, *A Vibrational Spectroscopic Study of the Structure of Electroactive Self-Assembled Monolayers of Viologen Derivatives,* Langmuir, 10(7), p. 2235-2240, (1994).

[111] X. Y. Tang, T. Schneider, J. W. Walker and D. A. Buttry, *Dimerized -Complexes in Self-Assembled Monolayers Containing Viologens: An Origin of Unusual Wave Shapes in the Voltammetry of Monolayers,* Langmuir, 12(24), p. 5921-5933, (1996).

[112] P. Crouigneau, O. Enea and B. Beden, *In situ investigation by simultaneous voltammetry and UV-visible reflectance spectroscopy of some viologen radicals adsorbed on a platinum electrode,* J. Electroanal. Chem., 218(1-2), p. 307-317, (1987).

[113] P. Crouigneau, B. Beden, A. M. Braun and O. Enea, *In situ spectroelectrochemical studies on N,N'-dibenzyl- and N,N'-diheptyl-viologen radicals adsorbed on metallic (platinum, gold) electrodes,* J. Electroanal. Chem., 234(1-2), p. 329-340, (1987).

[114] F. Kitamura, T. Ohsaka and K. Tokuda, *In situ infrared reflection absorption spectra of heptyl-viologen adsorbed on a mercury electrode surface*, J. Electroanal. Chem., 353(1-2), p. 323-328, (1993).

[115] K. Arihara, F. Kitamura, T. Ohsaka and K. Tokuda, *Adsorption structure of the heptyl-viologen cation radical on a mercury electrode surface: voltammetric and in situ infrared reflection absorption spectroscopic studies*, J. Electroanal. Chem., 488(2), p. 117-124, (2000).

[116] K. Arihara, F. Kitamura, K. Nukanobu, T. Ohsaka and K. Tokuda, *Voltammetric and spectroscopic study of the adsorption of alkyl-viologens on a HOPG electrode*, J. Electroanal. Chem., 473(1-2), p. 138-144, (1999).

[117] T. Sagara and K. Miuchi, *Double potential step chronoreflectometry approach to bi-stable potential region of the faradaic phase transition of heptyl-viologen at a HOPG electrode*, J. Electroanal. Chem., 567(2), p. 193-202, (2004).

[118] T. Sagara, H. Maeda, Y. Yuan and N. Nakashima, *Voltammetric and Electrodereflectance Study of Thiol-Functionalized Viologen Monolayers on Polycrystalline Gold: Effect of Anion Binding Viologen Moiety*, Langmuir, 15(11), p. 3823-3830, (1999).

[119] Th. Dretschkow and Th. Wandlowski, *An order-disorder-order adlayer transition of 2,2'-bipyridine on Au(111),* Electrochim. Acta, 45(4-5), p. 731-740, (1999).

[120] Th. Dretschkow and Th. Wandlowski, *Structural studies of 2,2'-bipyridine on Au(100),* J. Electroanal. Chem., 467(1,2), p. 207-216, (1999).

[121] K. H. Hausser and J. N. Murell, *Pi complexes between organic free radical,* J. Chem. Phys., 27, p. 500-504, (1957).

[122] S. I. Imabayashi, N. Kitamura, S. Tazuke and K. J. Tokuda, *The role of intramolecular association in the electrochemical reduction of viologen dimers and trimers*, Electroanal. Chem., 243(1), p. 143-160, (1988).

[123] F. J. Hirayama, *Intramolecular excimer formation. I. Diphenyl and triphenyl alkanes,* Chem. Phys., 42(9), p. 3163-3171, (1965).

[124] E. M. Kosower, *Free Radicals in Biology*, Pryor, W. A., Ed.; Academic Press: New York, (1976).

[125] Z. Li, B. Han, G. Meszaros, I. Pobelov, Th. Wandlowski, A. Blaszczyk and M. Mayor, *Two-dimensional assembly and local redox-activity of molecular hybrid structures in an electrochemical environment,* Faraday Discuss., 131, p. 121-143, (2006).

[126] N. T. M. Hai, S. Furukawa; T. Vosch, S. De Feyter, P. Broekmann and K. Wandelt, *Electrochemical reactions at a porphyrin-copper interface*, Phys. Chem. Chem. Phys., 11(26), p. 5422-5430, (2009).

[127] M. J. Blandamer, J. A. Brivati, M. F. Fox, M. C. R. Symons and G. S. P. Verma, *Solvation Spectra Part 17.-Water-Induced Dimerization of Various Dye and Related Paramagnetic Ions Studied by Optical and Electron Spin Resonance Spectroscopy*, Trans. Faraday Soc., 63, p. 1850, (1967).

[128] F. M. Hawkridge, H. L. Landrum and R. T. Salmon, *A surface-modified gold minigrid electrode which heterogeneously reduces spinach ferredoxin*, J. Am. Chem. Soc., 99, p. 3154, (1977).

[129] M. Hawkridge, J. F. Stargardt, H. L. Landrum and R. T. Salmon, *Reversible heterogeneous reduction and oxidation of sperm whale myoglobin at a surface modified gold minigrid electrode*, Anal. Chem., 50, p. 930, (1978).

[130] Th. Wandlowski, *Encyclopedia of Electrochemistry*, M. I Urbakh, E. Gileadi, Eds.; Wiley-VCH: Weinheim, (2002).

[131] C. Safarowsky, A. Rang, C. A. Schalley, K. Wandelt and P. Broekmann, *Formation of 2D supramolecular architectures at electrochemical solid/liquid interfaces,* Electrochim. Acta, 50(21), p. 4257-4268, (2005).

[132] C. Safarowsky, K. Wandelt and P. Broekmann, *Formation of Supramolecular Cavitands on Copper Electrode Surfaces,* Langmuir, 20(19), p. 8261-8269, (2004).

[133] T. Sagara, T. Fujihara and T. J. Tada, *Molecular Structure Dependence of the Phase Transition Spike Response of Viologens at an HOPG Electrode Using Bisviologen and Carboxylated Viologen,* Electrochem. Soc., 152(8), p. E239-E246, (2005).

[134] T. Sagara, S. Tanaka, Y. Fukuoka and N. Nakashima, *Study of the Voltammetric Spike Response of Heptyl-Viologen at a HOPG Electrode Horizontally Touched to a Gas/Heptyl-Viologen Aqueous Solution Interface,* Langmuir, 17(5), p. 1620-1629, (2001).

[135] T. Sagara, S. Tanaka, K. Miuchi and N. Nakashima, *Characteristics of faradaic phase transition of an adsorption layer of heptyl-viologen at a basal plane HOPG electrode*, J. Electroanal. Chem., 524, p. 68-76, (2002).

[136] Y. Tanaka and T. Sagara, *Phase transition behavior of two-component viologen adsorption layers on a HOPG electrode surface,* Electrochem. Comm., 9(4), p. 741-746, (2007).

[137] X. Liu, K. G. Neoh, L. P. Zhao and E. T. Kang, *Surface Functionalization of Glass and Polymeric Substrates via Graft Copolymerization of Viologen in an Aqueous Medium,* Langmuir, 18(7), p. 2914-2921, (2002).

[138] K. Gentz, K. Wandelt and P. Broekmann in preparation.

[139] H. Keller, M. Saracino, N. T. M. Hai and P. Broekmann, *Templating the near-surface liquid electrolyte: In situ surface x-ray diffraction study on anion/cation interactions at electrified interfaces ,* Phys. Rev. B, 82(24), p. 245425/1-245425/7, (2010).

[140] J. J. Yeh and I. Lindau, *Atomic subshell photoionization cross sections and asymmetry parameters,* Atom. Nucl. Data Tables, 32(1), p. 1-155, (1985).

[141] http://www.lasurface.com (accessed Oct 2010).

[142] D. I. Gittins, D. Bethell, D. J. Schiffrin and R. J. Nichols, *A nanometre-scale electronic switch consisting of a metal cluster and redox-addressable groups*, Nature, 408, p. 67–69, (2000).

[143] F. Kitamura, T. Ohsaka and K. Tokuda, *Adsorption behavior of viologen derivatives on hanging mercury electrode surfaces*, J. Electronal. Chem., 347(1-2), p. 371–381, (1993).

Acknowledgement

I would like to express my gratitude to all those who gave me the possibility to complete this thesis.

My greatest appreciation and thanks go to Prof. Dr. Klaus Wandelt, my supervisor, for accepting me as a Ph.D student and giving me an opportunity to conduct scientific research in the Institute of Physical and Theoretical Chemistry, University of Bonn. I am really grateful for his financial support, his valuable advice and his enthusiastic supervision during the preparation of the dissertation. In addition, I would like to express my deeply thanks to the unconditional support, the continued encouragement and especially, the 'superhuman' patience he devoted to me during my hard time to complete the thesis.

I would like to express my special thanks to Dr. Peter Broekmann for his direct guidance in experimental work, thoughtful comments, fruitful discussions and rich ideas during the whole period of my research as well as acting as second referee.

My sincere thanks go to Frau Kirschfink for helping me all of document things and especially for editing my thesis.

I would like to thank Hamed Alaei helping me to solve some problems with the computers as well as the STM apparatus.

For XPS measurements in BESSY, I want to thank Dr. Ralf Hunger, Sasha Hümann and Stephan Breuer.

I wish to express my sincere thanks to the Daimler Benz Foundation, the organizer and supporter of the Vietnamese-German Seminar on Physics and Engineering, which at first gave me the opportunity to have contact with Prof. Dr. Klaus Wandelt and then granted me the scholarship that enabled my staying in Germany.

My sincere thanks go to my two Vietnamese colleagues Nguyen Thi Minh Hai and Phan Thanh Hai, who supported me in research work as well as in social life. I wish them all the best for their future.

Finally, I owe deepest appreciation and thanks to my wife for her unconditional supports and continuous efforts without those I could not successfully complete this

work. She has not only always sympathized with me but also helped me by taking care of our daughter Linh Dan whose lovely images became the motivation for my hardest times. For the family, I would like to express my special gratitude to my parents and my sister.

Publication list

1 Duc Thanh Pham, Knud Gentz, Caroline Zoerlein, Hai Nguyen Thi Minh, Sung-Lin Tsay, Barbara Kirchner, Simone Kossmann, Klaus Wandelt, Peter Broekmann, *Surface redox chemistry of adsorbed viologens on Cu(100),* New Journal of Chemistry, 30(10), p. 1439-1451, (2006).

2 Duc Thanh Pham, Sung-Lin Tsay, Knud Gentz, Caroline Zoerlein, Simone Kossmann, Jyh-Shen Tsay, Barbara Kirchner, Klaus Wandelt, Peter Broekmann, *Quasi-Reversible Chloride Adsorption/Desorption through a Polycationic Organic Film on Cu(100),* Journal of Physical Chemistry, 111(44), p. 16428-16436, (2007).

3 Duc Thanh Pham, Klaus Wandelt, Peter Broekmann, *2D ordering phenomena under non-equilibrium conditions: an in situ STM approach*, ChemPhysChem, 8(16), p. 2318-2320, (2007).

4 Stephan Breuer, Duc Thanh Pham, Sascha Huemann, Knud Gentz, Caroline Zoerlein, Ralf Hunger, Klaus Wandelt, Peter Broekmann, *Organic layers at metal/electrolyte interfaces: molecular structure and reactivity of viologen monolayers*, New Journal of Physics, 10, (2008).

5 Duc Thanh Pham, Hubert Keller, Stephan Breuer, Sascha Huemann, Hai Nguyen Thi Minh, Caroline Zoerlein, Klaus Wandelt, Peter Broekmann, *Anion/cation layers at electrified interfaces: a comprehensive STM, XRD and XPS case study*, Chimia, 63(3), p. 115-121, (2009).